Statistical analyses of galaxy catalogues

Shanks, Thomas

STATISTICAL ANALYSES OF

GALAXY CATALOGUES

by

Thomas Shanks

September, 1979

An account of work done at the Department of Physics and submitted to the University of Durham in accordance with the regulations for admission to the degree of Doctor of Philosophy.

"There are more things in Heaven and Earth, Horatio,

than are dreamt of in your philosophy".

Hamlet, Act I, Scene V.

CONTENTS

PREFACE

The work presented in this thesis was carried out between 1976 and 1979 while the author was a research student under the supervision of Dr. R Fong, in the Physics Department at the University of Durham.

Some of the research was carried out in collaboration with Dr. R S Ellis and Dr. Fong but the majority is the author's own work. This work has not been submitted for any degree, diploma or other qualification at any other university.

Certain results have appeared in the following paper :

Shanks, T, 1979. Mon.Not.R.astr.Soc., 186, 583.

ABSTRACT

STATISTICAL ANALYSES OF GALAXY CATALOGUES

Galaxy catalogues, complete over a wide range of limiting magnitude, are statistically analysed to test theories of formation of galaxies and clusters of galaxies.

Statistical measures used in the past to investigate the galaxy distribution in these catalogues are reviewed and the results therefrom summarised.

From applying statistical techniques new to extra galactic astronomy to shallower catalogues it is found that the evidence supporting the hierarchical distribution of galaxies at small scale lengths is not as strong as previously believed. The results are more consistent with a model for galaxy distribution where galaxies are found in clusters with power-law profiles. The implications of this result for theories of galaxy formation are discussed.

New, extensive catalogues, complete in J and R to faint limits are obtained from machine measurements of U.K. Schmidt photographs at the South Galactic Pole. The techniques required to produce these catalogues are described. Number magnitude counts and colour magnitude diagrams for these samples are presented and found to be consistent with the work of other authors. These results are used to investigate the selection effects operating in the samples. Tentative evidence for galaxy luminosity evolution is discussed.

The strength of galaxy clustering in these deep catalogues is statistically measured and compared with the results from shallower surveys.

From this comparison good evidence is found for the homogeneity of the galaxy distribution over the large scales 50-700 h^{-1} Mpc. None of the discrepancies of previous studies are found. The possibility of testing theoretically predicted clustering growth rates with such data is discussed.

Statistical analysis of galaxies in the deep samples also shows evidence for a feature in the 2-point galaxy correlation function like that found in the analysis of shallower catalogues. However, the position of the feature corresponds to a spatial separation of 3 h^{-1} Mpc instead of 9 h^{-1} Mpc as found locally. The reasons for the discrepancy are discussed and the implications for galaxy formation theory described.

Finally the faint stellar catalogues produced alongside the deep galaxy catalogues are statistically analysed. Evidence is found for two distinct populations of stellar types at the South Galactic Pole. The spatial distribution of stars within these populations is investigated.

CHAPTER ONE

INTRODUCTION

1.1 GENERAL

In the recent past great efforts have been made to discover the nature of the distribution of galaxies. The underlying motivation for these efforts lies in the hope that galaxies are good'tracers' of the mass of the Universe. On this assumption the study of the distribution of galaxies becomes the study of the large scale distribution of matter itself. Many cosmological theories have been developed which make predictions for this distribution. The broad aim of this thesis is to present original observational results on the distribution of galaxies against which tests of these predictions can be made.

These observational results will almost exclusively arise from the statistical analyses of galaxy catalogues that are complete to some brightness limit. The statistical approach is relevant here because we wish to make statements which apply generally (in some approximation) to most of the matter in the Universe and not just to particular objects. The work presented here includes the results from statistical analyses applied to new and extensive galaxy catalogues measured from U.K. Schmidt plates by the COSMOS machine at The Royal Observatory, Edinburgh. It also contains the results of analysing shallower "eyeballed" catalogues by statistical techniques new to extragalactic astronomy.

1.2 THEORIES AND PREDICTIONS FOR STATISTICAL TEST

To motivate more particularly the work that follows let us now concentrate on the two most popular theories of galaxy formation and clustering - what I shall call here the isothermal and adiabatic theories, (see Jones, 1976a, for a review). Both these theories use gravitational

instability as the basic mechanism for the growth of structure. However, they make different assumptions about conditions in the pre-recombination universe and these lead to radically different predictions for the way galaxies formed. Also, although both attempt to explain the well known tendency for galaxies to be found in clusters, they make distinct predictions for the distribution of galaxies within these clusters. In the isothermal theory galaxies form first and attract each other under gravity to form clusters with detailed substructures. This theory therefore predicts a present day galaxy distribution consisting of clusters of many sizes showing no "preferred scales". The adiabatic theory, however, predicts that a preferred scale of clustering will exist. This is because in this theory cluster sized masses are preferentially the first to grow with galaxies forming subsequently when these "protoclusters" collapse. Thus if a preferred scale of galaxy clustering were to be observed, this would be taken as strong evidence for the adiabatic theory and against the isothermal theory. Thus one way to test between the theories is to devise statistical analyses which are sensitive to preferred scales of clustering. The difficulty here is that the statistics must retain their sensitivity in applications to catalogues that, in general, contain only 2-dimensional, projected galaxy positions, and that are complete to a brightness rather than a volume limit.

With the isothermal theory it is also relatively simple to theoretically predict the rate of growth of clustering, (e.g. Peebles, 1957). This prediction has been checked using N-body calculations (Groth and Peebles, 1976, Efstathiou, 1979) and has been found to be reasonably accurate. An observational test of this prediction is possible through the statistical analysis of galaxy catalogues that are complete to faint limits. Such deep catalogues contain information, not only on galaxies at long distances but also on the galaxy distribution at earlier epochs (because of the "look-back" time associated with galaxies at large redshift). The observed clustering

growth rate might therefore be found by comparing statistical measures of galaxy clustering for the deep samples with those measured locally. The possibility of thus constraining the dynamical evolution of galaxy clusters is a strong motivation for obtaining deep galaxy catalogues. The production of such catalogues will be a major objective of this thesis.

Another motive for producing these catalogues is to check the reproducibility of a feature found in the correlation analysis of the Lick Catalogue (Groth and Peebles, 1977). This feature is a prediction of both the isothermal and adiabatic theories though its interpretation in each case is different. In the former theory the feature corresponds to the transition between linear and non-linear regimes of clustering (Davis et al, 1977) whereas in the latter it is a relic of the early preferred scale of clustering. Both theories make q_o dependent predictions for the position of this feature. In the Lick sample the estimation of the correlations at large angle is difficult because of plate to plate variations and the effects of variable observation by our own galaxy. These difficulties make the reality of the Groth and Peebles feature uncertain. In the deep samples any such feature is moved to smaller angular scale because of projection effects and so its estimation can be reliably carried out using only a single Schmidt plate. This forms a very good test from an independent sample of the reality of this important feature.

1.3 STATISTICAL MEASURES

Many statistical investigations into the distribution of galaxies have been carried out using a wide variety of statistical measures. It is of interest to see which if any of these has a bearing on the questions raised above (e.g. do any indicate a preferred scale of clustering ?). Also, the large number of statistical measures used often leads to confusion over how the different results from each fit into an overall picture of galaxy clustering. Therefore we begin in Chapter 2 with an up-to-date

review of the statistical measures that have been used together with the main results obtained from their application. Foremost among these measures is the 2-point galaxy covariance function, $\xi(r)$, which has been used in many forms over the years but most successfully by P.J.E.Peebles and co-workers at Princeton.

In Chapter 3 are presented the results from applying some of these statistics to computer simulated models of galaxy distribution. These consist of a hierarchical model which has no preferred scales of clustering and a power-law cluster model which does. These are reasonable approximations to distribution that may arise in the isothermal and adiabatic theories respectively. By comparing the statistical results from data and simulations we can test which model gives the best agreement with the actual galaxy distribution. I shall also apply the new statistical analysis, Mead's Analysis, to both simulations and data. The results from this analysis have some very important implications for whether a preferred cluster scale exists or not. These implications will be discussed in the conclusions for Chapter 3 where I shall attempt to incorporate both these new results and the old into a simple picture of galaxy clustering.

1.4 DEEP GALAXY CATALOGUES

Even using machines such as COSMOS (see Pratt et al, 1975), many problems are encountered in compiling deep galaxy samples for the purposes outlined above. These mainly arise from the requirement to base statistical results on representative or "fair" samples of galaxies. This means that large samples are needed even at deep depths. Here we shall use the entire unvignetted area of U.K. Schmidt plates which corresponds to over 14 sq.deg. of sky. Over areas this large there are problems in detecting images consistently because of uneven sensitivity in the emulsion of photographic plates and uneven absorption by galactic and extragalactic clouds.

COSMOS's high speed and on-line reduction makes the measurement of such large areas feasible. This speed has to be paid for to some extent by less accurate photometry but as we shall see this accuracy is quite adequate for the statistical/survey work of interest here. The large areas required also lead to problems with automatic star galaxy separation and details of how this and other problems are overcome are given in Chapter 4.

1.5 ANALYSIS OF DEEP GALAXY CATALOGUES

In Chapter 5 we move on to the analysis of the galaxy samples produced in Chapter 4. Here the approach is similar to that of Ellis et al (1977) and Phillipps (1979). To do the correlation evolution test of the isothermal theory as outlined above, we need a knowledge of the selection effects that define our sample so that its average depth can be estimated. These selection effects depend on the galaxy luminosity function, galaxy K-correction and galaxy luminosity evolution. Constraints on these parameters can be obtained through number-magnitude relations from COSMOS data, supplemented from other sources. Other constraints can be obtained from colour-magnitude diagrams obtained from the J-R plate pairs. The power of correlation analysis to test for clustering evolution depends on how precisely such considerations can define these selection effects. Of course, topics such as luminosity evolution are of astronomical interest in their own right and the implications of the present results for these parameters will be fully discussed in Chapter 5.

Almost as a by-product we have produced star catalogues in 2 colours as well. These are of interest since they contain information on stellar populations and, of course, quasars. The number-magnitude and colour-magnitude relations for these are also discussed in Chapter 5.

In Chapter 6 the correlation functions are computed for the deep samples. The small angle results are compared with those found in the

shallower samples, using selection parameters obtained from the number count considerations of Chapter 5 (see also Phillipps et al, 1978). This checks the applicability of a single model of galaxy clustering out to large distances in addition to testing for correlation evolution. The correlations at large angles are inspected to check for the existence of a feature and the results are compared with those of Groth and Peebles(1977). The significance of these results are discussed in terms of galaxy formation theory.

Chapter 6 concludes with the correlation results for stellar images, obtained from both the complete samples and from colour sub-samples.

Chapter 7 contains a summary of the conclusions from the present results and also a discussion of prospects for future work.

CHAPTER TWO

REVIEW OF STATISTICS USED TO INVESTIGATE GALAXY DISTRIBUTION

2.1 INTRODUCTION

Since galaxies were first discovered statistical methods have often been used to examine the properties of their spatial distribution. These statistical investigations have played a large part in forming our present day notions of galaxy clustering. The purpose of this chapter is to provide a list of the statistics that have been employed in these investigations and to give a review of their properties. Past reviews of this type have been given by Abell (1962) and also by de Vaucouleurs (1971).

In reviewing each statistic's properties a major consideration will be how much interpretation of its results is affected by projection problems. At the moment inference about the 3-dimensional distribution of galaxies is largely made from only 2-dimensional angular positions on the sky. It is important, therefore, that the effects of projection on a particular statistic can be accounted for. Where possible an assessment will be given of each statistic's power to discriminate between various models of galaxy clustering. The aim here will not be to say that any one statistic is more powerful than any other but to indicate what particular aspect of galaxy clustering is best highlighted by each.

Some of the statistical problems encountered in galaxy work are, of course, not unique to extragalactic astronomy. Galaxy clustering can be looked on as a 3 -dimensional point process and therefore a subsidiary aim of the review will be to join together, where possible, the notations of statistical astronomy to the conventional point process notation of statistics.

Therefore Section 2.2 gives a brief historical outline. Since the basic material for any statistical analysis comes from a consistent galaxy catalogue, Section 2.3 reviews the galaxy catalogues at present available. Sections 2.4 to 2.8 comprise the main body of the review of the statistical techniques. Section 2.9 gives a summary of the results from their application.

2.2 HISTORICAL BACKGROUND

Statistical methods were first used in galaxy work in the 1930's by Hubble, Bok, Zwicky and Mowbray. These early investigators, despite being handicapped by poor catalogues, obtained good evidence that the distribution of galaxies was non-random.

In the 1950's, with more consistent catalogues available, J. Neyman, E.L. Scott, D.N. Limber, G.O. Abell, D. Layser and F.Zwicky, among others, laid the foundation for the modern techniques of statistical astronomy. In this period two general approaches were adopted. The approach pioneered by Neyman and Scott involved comparing complete stochastic models of clustering using various statistical tests. Typically the models might have consisted of all galaxies being members of randomly placed clusters with Gaussian number density fall-offs. Limber and Layser, however, preferred another approach which consisted of finding only the low order moments of the distribution even though these could not uniquely define a model. These low order moments were of importance in the theoretical, statistical machine treatment of galaxies as a "galaxy gas". This latter approach, though limiting what could be learned, had the advantage of providing simple measures of clustering which subsequently could be "scaled" to different catalogues' depths. This "scaling with depth" was to be a crucial test of whether the clustering of galaxies was intrinsic or merely induced by the presence of foreground, obscuring material. Since in general, users of this second approach have ultimately interpreted their

results as evidence for a particular stochastic model, the effective difference between these two approaches is small.

With the advent of high speed computing techniques the way was opened in the early 1970's for the very thorough statistical analyses of the newly completed Zwicky, Lick and Jagellonian catalogues by P.J.E.Peebles and his collaborators at Princeton. As we shall see, interpretation of these analyses still dominate thinking on galaxy clustering today.

2.3 GALAXY CATALOGUES

There are 3 principal sources giving the positions of individual galaxies complete to a specified limiting magnitude. These are the catalogue of Zwicky (1961-68), the Lick Catalogue (Shane and Wirtanen, 1967, but see Seldner et al (1977) for a new reduction), and the Jagellonian Catalogue (Rudnicki et al,1973). Table 2.1 gives details of these and other catalogues. These three catalogues were all obtained by observers inspecting plates by eye and selecting galaxies for inclusion by comparing theirbrightness with standard objects. This procedure is subject to inconsistencies such as differences in the selection criteria of various observers. Although the greatest possible care was taken by the observers to minimise such effects it was realised that to obtain galaxy samples to even fainter limiting magnitudes only machines would be able to reach the required level of detection consistency (see Chapter 4).

The presence of galactic or extragalactic obscurring material is always a problem for consistent detection in any catalogue. The only solution is to avoid areas in the catalogues that have had obvious absorption problems (e.g.by restricting samples for analysis to high galactic latitude).

The other catalogues of Table 2.1 give more information about each galaxy but are only complete to brighter limiting magnitudes. For instance, the Nilson catalogue (Nilson., 1973) covers the sky to the north of

TABLE 2.1

Galaxy Catalogues

Catalogue	Completeness limit (Mpg)	Galaxy Number (/□°)	Area of Sky Covered	References
Zwicky	14.9	0.57	$\delta > 0^{\circ}$ $b_{\pi} > 40^{\circ}$	Zwicky(1961-68)
Lick	18.6	53.0	$\delta > -23^{\circ}$ $\lvert b_{\pi} \rvert > 40^{\circ}$	Shane & Wirtanen (1967)
Jagellonian	∿20.3	330.0	6 sq.deg.	Rudnicki et al (1973)
Nilsson	14.5	0.29	$\delta > -02^{\circ}\ 30'$	Nilsson (1973)
Shapley-Ames	13.2	-	all sky	Shapley & Ames (1932)
Huchra	13.2	-	all sky	Huchra et al (1978)
RCBG	∿ 16	-	all sky	de Vaucouleurs et al (1976)

All magnitudes are photographic magnitudes.

declination, δ, $\delta > -02^{o}\ 30'$, and is complete to a limiting magnitude, m_{pg}, of 14.5. As well as information on the positions, diameters, Hubble types and radial velocities (incomplete) of galaxies, it also contains information on their shapes and orientations. It thus allows statistical analyses of a complete sample of elliptical galaxies, for example.

The Reference Catalogue of Bright Galaxies (RCBG) (de Vaucouleurs et al, 1976) covers the whole sky and is an updated version of the older Shapley-Ames Catalogue (1932). It consists of 4364 galaxies mainly brighter than 16^{m} and bigger than 0.5' in diameter. It contains incomplete information on galaxies' positions, magnitudes, diameters, colours and redshift.

Catalogues with complete information on redshift are important for 3-dimensional statistical studies of galaxy clustering. At present these are only complete to very bright limiting magnitudes. For example, Huchra et al, (1979) was able to produce a catalogue with redshift information on all galaxies brighter than 13.2^{m}. Redshift catalogues such as these are the subject of much present day effort and it is hoped there will soon be published a catalogue complete (in the Northern Hemisphere) to limiting magnitude 14.5.

Another class of catalogue gives the positions of clusters of galaxies. The most famous example of these is the catalogue of Abell (1958). This catalogue contains information on rich clusters north of $\delta = -27^{o}$. Abell estimated for each of his clusters a distance ($D = 1 \rightarrow 6$) and a richness ($R = 1 \rightarrow 6$). The depth of his catalogue is estimated to be 600 Mpc (with $H_{o} = 50$ km s^{-1} Mpc^{-1}).

The Zwicky catalogue (Zwicky 1961-68) also contains information on clusters of galaxies to 16^{m}.

More recently Turner and Gott (1976) have produced a group catalogue (for galaxies north of $b_{II} = 40^{o}$) wherein groups were detected

by their surface density contrast on the sky and then "cleaned up" for projection effects using incomplete velocity information. Turner and Gott thus obtained a group catalogue complete to 14^m with an estimate of the redshift for each group. This enabled them to carry out analyses of the distribution of groups of galaxies in 3-dimensions.

2.4 CORRELATION ANALYSIS

We now move onto the review of individual statistics, the first of which is the correlation function. This statistic is called also by the name of covariance analysis, autocorrelation analysis and fluctuation theory. Broadly, it is a statistic which gives an idea of the average degree of irregularity as a function of scale. Because it is the most widely used of the statistics of galaxy distribution I shall review it in slightly more detail than some other statistics.

2.4.1 Theory

Here we follow the treatment of Dautcourt (1977). Firstly, the probability density function f_N' is defined such that

$$\delta P = f_N' (\underline{x}_1, \ldots, \underline{x}_N) \, d\underline{x}_1 \ldots d\underline{x}_N \qquad (2.1)$$

is the probability of there being a galaxy in volume $(\underline{x}_1, \underline{x}_1 + d\underline{x}_1)$ and also galaxies in $(\underline{x}_2, \underline{x}_2 + d\underline{x}_2)$, ..., $(\underline{x}_N, \underline{x}_N + d\underline{x}_N)$. (assuming N galaxies are distributed in a finite volume V).

From f_N' ( ) the functions f_1( ), f_2( ).... are defined as

$$f_1(\underline{x}_1) = V \int f_N' (\underline{x}_1, \ldots \underline{x}_N) d\underline{x}_2 \ldots d\underline{x}_N \qquad (2.2)$$

$$f_2(\underline{x}_1, x_2) = V^2 \int f_N' (\underline{x}_1, \ldots x_N) d\underline{x}_3 \ldots d\underline{x}_N \qquad (2.3)$$

etc.

It is convenient here to write

$$f_2(\underline{x}_1, \underline{x}_2) = f_1(\underline{x}_1)\ f_1(\underline{x}_2) \quad + \quad \xi(\underline{x}_1, \underline{x}_2) \tag{2.4}$$

Thus distinguishing the separable and non-separable parts of f_2. Making the assumptions of homogeneity and isotropy means that $f_1(\underline{x})$ is 1 everywhere and ξ is only a function of r ($= |\underline{x}_1 - \underline{x}_2|$). So

$$f_2(\underline{x}_1, \underline{x}_2) \quad = \quad 1 \quad + \quad \xi(r) \tag{2.5}$$

Equation (2.5) defines the 2-point covariance function $\xi(r)$. This is seen from eqn.(2.3) and eqn.(2.5) to be equivalent to another definition of $\xi(r)$ whereby

$$\delta P_2 \quad = \quad \frac{N(N-1)}{V^2} \quad f_2\ (\underline{x}_1, \underline{x}_2) d\underline{x}_1\ d\underline{x}_2 \quad = n^2\ (1 + \xi(r)\ ) d\underline{x}_1\ d\underline{x}_2 \tag{2.6}$$

and δP_2 is the probability of there being one of the N galaxies in $(\underline{x}_1, \underline{x}_1 + d\underline{x}_1)$ and another in $(\underline{x}_2, \underline{x}_2 + d\underline{x}_2)$.

Higher order covariance functions can be defined similarly (see Peebles and Groth, 1975).

To form an estimator for $\xi(r)$ it is necessary to consider the secondary random variable $\rho(\underline{x})$ where

$$\rho(\underline{x}) \quad = \quad \sum_{i=1}^{N} \quad \delta\ (\underline{x} - \underline{x}_i) \tag{2.7}$$

and $\delta(\ )$ is the delta function. (Note that the randomness of ρ arises not through its argument $\underline{x}$ but through the random $\underline{x}_i$'s).

Thus

$$<\rho(\underline{x})> \equiv \int f_N' (\underline{x}_1, \ldots\ldots \underline{x}_N) \rho(\underline{x})\, d\underline{x}_1 \ldots . d\underline{x}_N \qquad (2.8)$$

$$= n$$

where $n = N/V$, the mean galaxy density.

Similarly

$$<\rho(\underline{x})\ \rho(\underline{x}')> = n^2(1 + \xi(r)) + n\,\delta(\underline{x} - \underline{x}') \qquad (2.9)$$

All these equations can also be obtained for the 2-dimensional, projected density distributions. If $n(\underline{x})$ represents the projected number density at $\underline{x}$, the angular separation of two galaxies at $\underline{x}$ and $\underline{x}'$, $\mathcal{N}$, the average projected number density and $w(\theta)$, the 2-point angular covariance function then eqn. is recast as

$$<n(\underline{x})\ n(\underline{x}')> = \mathcal{N}^2(1 + w(\theta)) + \mathcal{N}\,\delta(\underline{x} - \underline{x}') \qquad (2.10)$$

Thus the expected number of pairs of projected galaxies $<M_p>$ in areas $\Delta\,\Omega_1$ and $\Delta\,\Omega_2$ which are θ apart is thus given by

$$<M_p> = <n(\underline{x})\ n(\underline{x}')>\, \Delta\,\Omega_1 \Delta\,\Omega_2$$

$$= \mathcal{N}^2\,(1 + w(\theta))\ \Delta\,\Omega_1\ \Delta\,\Omega_2 \qquad (2.11)$$

if $\theta \neq 0$.

This approximation forms the basis for estimating $w(\theta)$. (To relate this notation to the usual notation of point processes (taken from Cox and

Lewis (1966). Their

$$m_f(\tau) = n\,(1 + \xi(\tau)),$$

$$\gamma_+(\tau) = n^2\,\xi(t)$$

and their $\Delta N_t \rightarrow \rho(\underline{x})$)

2.4.2 Estimators

Since galaxy catalogues only cover parts of the universe, biases in estimators of $w(\theta)$ can occur at the edges of samples. In practice this means that estimators with different edge corrections are required in different catalogues. Sharp (1979) gives an account of these. Three estimators making use of eqn. (2.11) are summarised below.

(a) The estimator $\hat{w}(\theta)$ used by Phillipps et al, 1978, was

$$\hat{w}(\theta) = \frac{N_p(\theta)}{N_c A} - 1 \qquad (2.12)$$

Here $N_p(\theta)$ is the number of galaxies counted in a half annulus bin $\sim \theta$ away from other galaxies called "centres" in the sample. A galaxy is a centre for a separation θ if it occurs more than θ away from the edge. N_c is the number of centres in the sample and A is the area of the half annuli. This is a good estimator if the only interest is in $w(\theta)$ at small θ.

(b) When the edges are more than just simple boundaries (e.g. if there are "holes" in the sample- see Chapter 4) then another estimator can be defined as

$$w(\theta) = \frac{N_p^D(\theta)}{N_p^R(\theta)} - 1 \qquad (2.13)$$

Here $N_p^D(\theta)$ has the same meaning as N_p in (a) above. $N_p^R(\theta)$ is also the same as N_p but computed for a random (Poisson) simulated distribution with the same edges. This estimator works well for all scales of θ but is expensive in computing time at the largest scales. This type of estimator is also used to estimate the 3-point function (see Peebles and Groth, 1975)

(c) Frequently galaxy positions are given in the form of counts of galaxies in contiguous square bins. Here it can be shown (e.g. Peebles 1976) that if N_i and N_j are random variables representing the number of galaxies in bins i and j then

$$\hat{w}(\theta) \simeq \frac{\langle N_i N_j \rangle}{\langle N_i \rangle \langle N_j \rangle} - 1 \qquad (2.14)$$

θ is now the distance between bin centres.

The usual name given for this estimator is a serial correlation estimator of $w(\theta)$. It is useful because even when dealing with unbinned data it is sometimes computationally faster to bin and use this estimator.

2.4.3 Limitations of Covariance Analysis

A well known problem of interpreting covariance function results is that the covariance function estimate at any particular scale length is a product of clustering on many different scales. (Blackman & Tukey, 1959, Peebles, 1973). For instance, a large scale gradient in galaxy counts due to obscuration will affect values of the covariance function even on scales much smaller than the obscuration scale length. Therefore data must be prefiltered before estimation of $w(\theta)$ if such unphysical trends are suspected because once the covariance function has been calculated a difficult deconvolution is needed to separate out real effects from the trend.

2.4.4 Simple Model Predictions for $\xi(r)$

It is possible to predict the behaviour of $\xi(r)$ for some simple clustering models.

A general class of models have cluster centres randomly distributed (with density α) with cluster members distributed in a secondary, "daughter" process around them. If the probability distribution of the distance between 2 arbitrary cluster members is denoted by $h(r)$ then we have that

$$n = \alpha \langle N \rangle \tag{2.15}$$

(where n, as usual, is the average density and N is the random number of objects per cluster)

and

$$\xi(r) = \frac{\alpha}{n^2} \quad \frac{\langle N(N-1) \rangle}{C(r)} \quad h(r) \tag{2.16}$$

where $C(r) = 2\pi r$ for a 2-d process

and $C(r) = 4\pi r^2$ for a 3-d process (e.g. Ripley 1977).

For a daughter process consisting of points being uniformly distributed in a 3-d sphere of radius, a,

$$h(r) = \begin{cases} \left(1 - \frac{r}{2a}\right)^2 \left(2 + \frac{r}{2a}\right) \frac{r^2}{2a^3}, & 0 < r \leq 2a \\ 0 \quad r > 2a \end{cases} \tag{2.17}$$

For a similar process with circles in 2-d

$$h(\theta) = \begin{cases} \frac{4\theta}{\pi a^2}\left[\cos^{-1}\left(\frac{\theta}{2a}\right) - \frac{\theta}{2a}\sqrt{1-\theta^2/4a^2}\right] & 0<\theta\leq 2a \\ 0 & \theta > 2a \end{cases} \qquad (2.18)$$

(Besag and Diggle,1977).

These are exact results. There also exists some approximate results very relevant for galaxy clustering. The first is for the case where the daughter process is a power-law number density fall-off from the cluster centre. It has been shown (Peebles,1974a) that in this power-law cluster model (PLC Model) where the number density, g(r), runs as

$$\begin{aligned} g(r) &\alpha r^{-\varepsilon} & r &\leq R \\ g(r) &= 0 & r &> R \end{aligned} \qquad (2.19)$$

then

$$h(r) \alpha \begin{cases} r^{-\gamma} & r << 2R \\ 0 & r > 2R \end{cases} \qquad (2.20)$$

where $\gamma = 2\varepsilon - 4$

Another result due to Soneira and Peebles (1977) is that for the hierarchical model. In this model several levels of nested sub-clusters are distributed around each cluster centre. The number density of objects in a level of the hierarchy is always a constant factor λ.

bigger than in the next lowest level. If the expected number of sub-clusters per cluster at each level is $\langle\eta\rangle$ then it can be shown that the typical density, d(r), inside clusters of size r_1 is

$$d(r_1) \quad \alpha \quad r_1^{-\gamma} \quad \text{(approximate)} \tag{2.21}$$

where $\gamma = 3 - \log \langle\eta\rangle / \log \lambda$

and therefore

$$\xi(r) \quad \alpha \quad r^{-\gamma} \quad \text{(approximate)} \tag{2.22}$$

These last two models will be further investigated in Chapter 3.

2.4.5 Projection Properties

The projection properties of $\xi(r)$ are well known and given a form for $\xi(r)$ the form for $w(\theta)$ can be predicted from Limber's formula (Limber 1953).

$$w(\theta) \quad \int_0^\infty dx\, x^4\, \phi^2(x) \int_{-\infty}^{\infty} dy \quad \xi\left[(x^2\theta^2 + y^2)^{\frac{1}{2}}\right] \Big/ \left[\int_0^\infty dx\, x^2 \phi(x)\right]^2 \tag{2.23}$$

where $\phi(x)$ is the selection function (i.e. the probability that a galaxy at a distance x will be included in the sample.

A relativistic version of this formula was derived by Phillipps et al (1978) and Groth and Peebles (1977) and this is used for deep samples.

Following directly from Limber's equation is the result that if

$$\xi(r) \quad \alpha \quad r^{-\gamma}$$

then $w(\theta) \quad \alpha \quad \theta^{1-\gamma}$ (Peebles, 1973) (2.24)

Also, if the selection functions of 2 samples are similar and differ only in characteristic depth D^* then,

$$\frac{w_1(\theta)}{w_2(\theta)} = \frac{D_2^*}{D_1^*} \; F\left(\theta \; \frac{D_1^*}{D_2^*}\right) \qquad (2.25)$$

(Peebles, 1973)

This is known as the simple scaling relation.

Fall and Tremaine (1977) give formulae which, when certain conditions hold, can deproject $w(\theta)$ to give $\xi(r)$.

2.4.6 Three Point Function

All the above procedures can be generalised to the case of 3 point and the higher order correlation functions. The relevant results are summarised below.

Analagously to eqn. 2.6 the usual definition of the 3 point function comes from

$$\delta P_3 = n^3 \left[1 + \xi(x) + \xi(x') + \xi\left(x''\right) + \zeta\left(x, x' x''\right) \right] dV_1 dV_2 dV_3 \qquad (2.26)$$

where δP_3 is the joint probability of finding galaxies in the 3 volumes dV_1, dV_2 and dV_3 and ξ is the 3 point covariance function.

The angular 3-pt function, $Z(x,x',x'')$ is similarly defined and thus

$$\langle n(x)\, n(x')\, n(x'') \rangle = n^3 \left(1 + w(x) + w(x') + w(x'') + Z(x,x',x'') \right) \qquad (2.27)$$

and it is on approximations to this eqn. that estimators for Z are based, (see Peebles & Groth, 1975).

Usually the spatial 3 point function is reparamaterised so that

$$\zeta(x,x',x'') \equiv \zeta(r,u,v) \tag{2.28}$$

where $r = x$, $u = \frac{x'}{x}$ and $V = \frac{x'' - x'}{x}$

and $x \leq x' \leq x''$.

Thus r is a size parameter, u measures triangle elongation and v ranges from 0 for an isosceles triangle to 1 for a straight line. Similarly the angular 3-point function becomes $z(\theta,u,v)$.

There exist results for the 3-point function in special cases of clustering models.

For the PLC model of section 2.4.4 it can be shown (Peebles & Groth, 1975) that

$$\zeta(r) \alpha \quad r^{-(3\varepsilon - 3)} \qquad r << R. \tag{2.29}$$

at fixed u, v and

$$\zeta(u) \alpha \quad u^{-\varepsilon} \tag{2.30}$$

at fixed r and v.

For the <u>hierarchical model</u> also of section 2.4 it can be shown that

$$\zeta(r_1,r_2,r_3) = Q\left(\xi(r_1)\,\xi(r_2) + \xi(r_2)\xi(r_3) + \xi(r_3)\,\xi(r_1)\right) \tag{2.31}$$

where Q is a constant. This result is due to Soneira and Peebles (1977). Finally, a similar relationship to Limber's formula can be obtained relating ζ to Z. This is given in Groth & Peebles, (1977). A consequence of this

formula is that if ζ has a power law form i.e.

$$\zeta \quad \alpha \quad r^{-\beta}$$

then $$z \quad \alpha \quad \theta^{-(\beta-2)} \tag{2.32}$$

and if $\zeta \quad \alpha \quad u^{-\varepsilon}$ (2.33)

then $z \quad \alpha \quad u^{1-\varepsilon}$

2.4.7 Other Related Statistics

There are other statistics derived directly from the covariance function which I shall note briefly here.

(a) It is sometimes convenient (Groth and Peebles, 1976, Fall 1978 and Phillipps et al, 1978) to consider the integral covariance function, $\bar{\xi}(r)$, where

$$\bar{\xi}(r) = 4\pi n \int_0^r ds\, s^2\, \xi(s) \tag{2.34}$$

This measure is equivalent to the K(t) measure of Ripley (1977).

(b) If Δ is now the number excess of particles in a randomly sampled volume, V', then it is sometimes useful to consider the r.m.s. relative dispersion in Δ, $\sigma^2(r)$. Thus

$$\sigma^2(r) = \frac{\langle \Delta^2 \rangle}{nV'} \tag{2.35}$$

It can be shown that

$$\sigma^2(r) = 1 + \frac{n}{V'} \int_{V'} \xi(r)\, d\underline{x}_1\, d\underline{x}_2$$

$$\approx 1 + \bar{\xi}(r) \quad \text{(Groth \& Peebles, 1976, Fall, 1978).} \tag{2.36}$$

The first expression arises by considering Δ as the sum of elemental volumes and the last approximation only holds if $\xi(r)$ is small when r is comparable to the dimensions of V'.

(c) 2 point covariance function techniques can also be used to cross correlate 2 separate data sets (for instance Lick galaxies and Abell clusters, as in Seldner and Peebles,1977). The spatial cross correlation function, ξ_{ab}, for objects of types a and b is defined by

$$\delta P_{ab} = n_a n_b (1 + \xi_{ab}(r) \quad dV_a dV_b \tag{2.37}$$

where δP_{ab} is the joint probability of finding objects of types a and b respectively in the volumes dV_a and dV_b deparated by distance r when the mean densities are n_a and n_b. It can be shown that ξ_{ab} is equivalent to the number density run of objects of type b around objects of type a.

2.5 POWER SPECTRAL ANALYSIS

A general point process has been shown to be representable by a sum of delta functions, $\rho(\underline{x})$ (eqn. 2.7). In this form the point process resembles a conventional Time Series and so it is worthwhile to see whether the methods of Time Series Analysis can be of any help in the analysis of point processes. One of the most powerful statistics used in Time Series analysis is the Power Spectrum.

2.5.1 Background

Power Spectral Analysis (P.S.A.) in Time Series can be looked upon as the determination of the Fourier frequencies that contribute most to the variation of a stationary random variable with time. Since in point processes we are not interested in detecting periodicities, the intuitive appeal of PSA here is not as strong. But because the power spectrum retains some of its powerful Time Series properties and also because it arises

naturally in the physical theory through the solution of equations governing the growth of density perturbations, it is still a very useful function to try and estimate. Bartlett (1964) first developed this statistic's use in point processes. Peebles (1973) first applied it to galaxy clustering.

2.5.2 Theory

For our purposes here we now assume that space is divided into large boxes each of volume V (= L^3) with periodic boundary conditions.

Now as in eqn. (2.7)

$$\rho(\underline{x}) = \sum_{i=1}^{N} \delta(\underline{x} - \underline{x}_i)$$

so $\rho(\underline{x})$'s Fourier Transform, $\delta_{\underline{k}}$, is given by

$$\delta_{\underline{k}} = N^{-\frac{1}{2}} \sum_{i=1}^{N} \ell^{i\underline{k}\underline{x}_i} \quad \text{with } \underline{k} = \left(\frac{2\pi n_1}{L}, \frac{2\pi n_2}{L}, \frac{2\pi n_3}{L} \right) \tag{2.38}$$

Since $\rho(\underline{x})$ is a random variable, so is $\delta_{\underline{k}}$.

$$\text{Define } C(\underline{r}) = N^{-1} \int_V \rho(\underline{x})\ \rho(\underline{x} + \underline{r})\ d^3\underline{x}. \tag{2.39}$$

$C(\underline{r})$ is a random number representing the number of pairs in volume V separated by a distance $\underline{r}$.

Thus

$$C(\underline{r}) = V^{-1} \sum_{\underline{k}} |\delta_{\underline{k}}|^2 \ e^{i\underline{k}.\underline{r}} \tag{2.40}$$

Now from equations (2.7) and (2.9)

$$\langle C(\underline{r}) \rangle = n\,(1 + \xi(r)) + \delta(\underline{r}) \tag{2.41}$$

Assuming that

$$\langle |\delta_{\underline{k}}|^2 \rangle = 1 + P(k) \tag{2.42}$$

(P(k) is defined here as the power spectrum)

then by taking expected values in eqn (2.40) and equating to $\langle C(\underline{r}) \rangle$ in eqn. (2.41) it is seen that

$$\xi(\underline{r}) = n\,V^{-1} \sum_{k \neq o} P(\underline{k})\, e^{i\underline{k}.\underline{r}} \tag{2.43}$$

Thus we have the important result that the power spectrum P(k) is the Fourier Transform of $\xi(\underline{r})$. Thus no new information is contained in P(k) over that contained in $\xi(\underline{r})$. However, it is still worthwhile to measure the PS since, in general, estimates of $\xi(\underline{r})$ and $P(\underline{k})$ will not be equivalent. For the P.S. has the important advantage over $\xi(\underline{r})$ that at a particular $|k| \alpha \frac{1}{\lambda}$, $|\delta_k|^2$ only depends on clustering with a scale length λ. Large scale gradients in the data caused by obscuration, for instance, do not affect the values of the spectra at small scales. This is because the $|\delta_k|$'s are approximately orthogonal (see Blackman and Tukey, 1959, Peebles, 1973). This result still holds in point processes as it did in Time Series.

2.5.3 Point Process Spectra

The spectra of interest in point processes differs from those of interest in Time Series. When looking for periodic behaviour in a Time Series the interesting features are peaks in the spectrum. Here we

investigate the interpretable features of point process spectra.

It is instructive to first restrict attention to a 1-dimensional point process. Consider the data given as only n_b binned counts, n_i, along the x axis (see Figure 2.1).

From the defn. of δ_k (eqn. 2.38)

$$\delta_k = N^{-\frac{1}{2}} \sum_{i=1}^{n_b} n_i \, e^{ikx_i} \tag{2.44}$$

where x_i is the position of the centre of each bin and N is the total number of counts.

Thus the real and imaginary parts of e^{ikx_i} can be looked upon as weighting functions for the n_i's. Typically these weights will act like cosk'x (see Figure 2.1). This means for δ_k', that

$$\delta_k' = (n_1 - n_2) + (n_3 - n_4) + \ldots + (n_9 - n_{10}) \tag{2.45}$$

If these brackets were replaced by moduli then δ_k would provide a direct test of clustering because then the sum of differences would be large if clusters occurred on the scales of the bin size (e.g. in the shaded bins of Figure 2.1) and small otherwise. This procedure, in fact, does form the basis for a different test, Mead's Analysis, full details of which are given in Chapter 3. However, with the P.S. formulation the larger differences in eqn. (2.45) tend to cancel out and so the direct test is not possible.

A more indirect test of clustering can be formed by regarding the δ_k's as a random walk with step $(n_i - n_{i+1})$. Using random walk theory it can be shown (Webster 1976, Peebles & Yu, 1970) that for an underlying

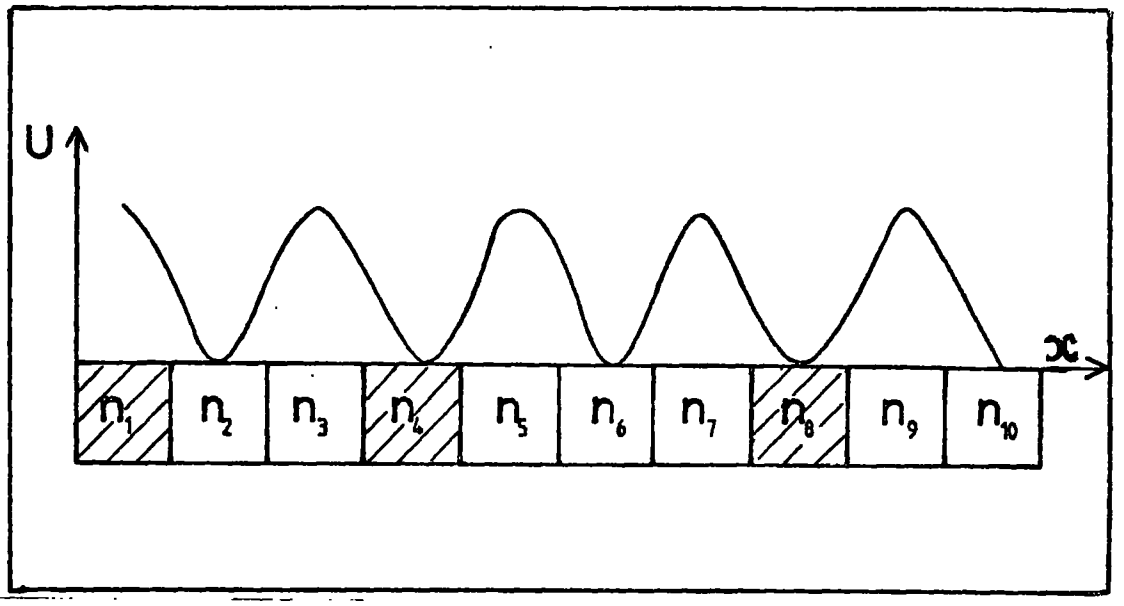

Figure 2.1 1 dimensional binned data. n_i represents the number of points in bin i. Shaded bins indicate a higher density of points. u is a weighting function used in P.S.A.

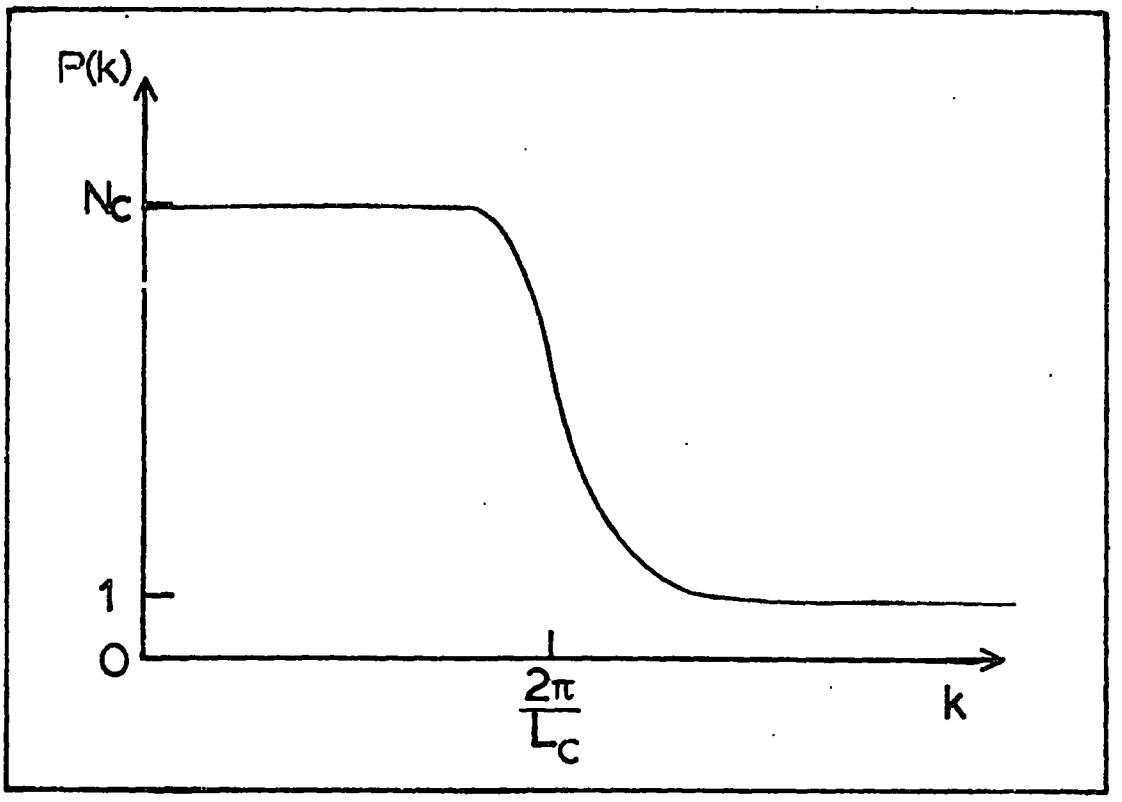

Figure 2.2 Predicted power spectral analysis results for a typical spatial clustering process. N_C is the average number of points inside clusters of diameter L_C.

random distribution of points along the line

$$< |\delta_k|^2 > \; = \; 1 \tag{2.46}$$

and

$$p\,r\left(|\delta_k|^2 \; > \; x \right) \; = \; e^{-x} \tag{2.47}$$

It can also be shown that if the underlying distribution consists of points uniformly distributed inside clusters of scale length L_C which are themselves randomly distributed along the line then for $\frac{2\pi}{k} >> L_C$,

$$<|\delta_k|^2> \; = \; N_C \tag{2.48}$$

where N_C^{-1} is the number of points/cluster and

$$p\,r\left(|\delta_k|^2 > x \right) \; = \; e^{\frac{-x}{N_C}} \tag{2.49}$$

For $\frac{2\pi}{k} << L_C$ the points inside the cluster are resolved by the cosine fitting algorithm of spectral analysis and the results for a random distribution hold.

For a point process such as this the spectrum will therefore look like that given in Figure 2.2. Thus in point processes the features of interest are <u>dips</u> in the spectrum, rather than <u>peaks</u>, for these can indicate a characteristic clustering size. Also the height of the spectrum before the dip allows an estimate of average cluster membership.

2.5.4 Useful Relationships

(a) It can be shown (Fall 1978) that

$$P(k) \simeq 1 + \Xi\left(\pi/k\right) \tag{2.50}$$

where Ξ is as defined in Section 2.4.

Thus, again the value of $<|\delta_k|^2 - 1>$ is shown to be approximately equal to the number of points in excess of random within a radius $\pi/_k$ of a random point

(b) There also exists a relationship between the quantity $\sigma^2(r)$ (defined in Section 2.4.5) and the P.S.

Peebles (1974b) showed that, approximately

$$\sigma^2(r) \propto \sum_{|k| \leq k_o} <|\delta_k|^2> \quad \text{if } k_o \lesssim \frac{2\pi}{r} \tag{2.51}$$

(c) In the notation of Cox and Lewis (1966), Bartlett (1964), the power spectrum P(k) is represented by g+(w).

(d) If the form $\xi(r)$ is a power law then it can be shown that if

$$\xi(r) \propto r^{-\gamma}$$

then approximately

$$P(k) \propto k^{3-\gamma} \tag{2.52}$$

(Fall, 1979)

(e) The projection properties of the P.S. are as well known as the covariance function. These are derived in full in Peebles (1973).

2.6 TESTS OF A POISSON NULL HYPOTHESIS

Here we describe 2 tests which were more fashionable in the early days of analysing galaxy clustering when the major interest was in whether galaxies were clustered rather than how they were clustered. First, however, I shall show how the Poisson distribution relates to the probability density functions of Section 2.4.

2.6.1 Poisson Distribution

Assuming that all high order correlations are zero the probability density function, f_N of Section 2.4 becomes

$$f_N\ (\underline{x}_1 \ldots\ldots \underline{x}_N) \;=\; \frac{1}{V^N} \tag{2.53}$$

Now let us calculate the probability, $P(N_1)$, that a volume V_1 contains just N_1 galaxies.

From eqns (2.3) and (2.53) this is given by

$$P(N_1) \;=\binom{N}{N_1} \int_{V_1} d\underline{x}_1 \ldots d\underline{x}_{N_1} \int_{V-V_1} d\underline{x}_{N_1+1} \ldots\ldots d\underline{x}_N \cdot \frac{1}{V^N} \tag{2.54}$$

Assuming $V >> V_1$ and $N >> N_1$ this gives

$$P(N_1) \;=\; \frac{\bar{N}_1^{\,N_1}\ \exp\ (-\bar{N}_1)}{N_1!} \tag{2.55}$$

where $\bar{N}_1$ is the average number of points in V_1.

This is just the definition of the Poisson probability density function and so a distribution is Poisson if all high order correlations are set to zero.

2.6.2 Chi-Square Test

This test is used on data, say, on a square photographic plate from which galaxy counts have been obtained in $N_T \times N_T$ square bins. If N galaxies have been recorded then the average count for each bin is $\bar{N} = \frac{N}{N_T^2}$. To test if the underlying distribution of galaxies is Poisson the fraction of bins, P(i), containing i counts out of the N_T^2 bins is computed for i = 1,...,N. The frequency, $P_o(i)$, expected for a Poisson distribution with mean intensity $\bar{N}$ is also computed. A χ^2-test is carried out in the usual manner to compare the observed P(i) with the expected $P_o(i)$

Thus

$$\chi^2 = \sum_{i=o}^{N} \left[P_o(i) - P(i) \right]^2 \Big/ P_o(i) \qquad (2.56)$$

can be tested against a χ^2_{N-1} distribution. It can be shown that when the tested distribution is non-Poisson, the χ^2 statistic depends on <u>all</u> moments of the distribution (Dautcourt 1977).

The same criticism can be made of this statistical test as applied to the covariance function in Section 2.4. Since this is a "blanket" goodness-of-fit test, deviations from the null result may be produced by effects not necessarily related to galaxy clustering, the most obvious of which is obscuration. Therefore interpretation of the non-randomness found in the early results from this test was not simple. Moreover, since the projection properties of the statistics were unknown, it was impossible to check for contamination by scaling the results to deeper and deeper samples. These are very serious drawbacks to the application of this test.

2.6.3 Dispersion - Subdivision Tests

This test is known by other names including the Index of Dispersion Test (Zwicky, 1957) and Binning Analysis (Webster, 1976). Again, this was used on the same binned galaxy counts as the chi square test. Historically it predates the covariance function but as we shall see the two contain similar kinds of information. If N is the count of galaxies in one small square cell of size $\theta x \theta$ then the test is applied by comparing the usual estimate of variance of the counts, S,

$$S = \frac{1}{n-1} \sum_{i=1}^{n} (N_i - \langle N \rangle)^2 \quad \text{where } n = N_T^2 \tag{2.57}$$

with the expected variance for a Poisson distribution, $\langle N \rangle$.

Defining U as

$$U = \frac{(n-1)S}{\langle N \rangle} \tag{2.58}$$

then by the Central Limit Theorem, for large n, U is a sum of approximately Gaussian distributed random variables. Thus under the null hypothesis of a Poisson distribution, U can be tested against a χ^2 distribution with n-1 degrees of freedom. This is tantamount to calculating the sample variance of the distribution of P(i) and comparing it with the variance of the relevant Poisson distribution. This entire procedure is to be repeated on scales of 2 x 2 and upwards of the original $\theta x \theta$ cells and what is usually looked for is the maximum deviation from the null hypothesis which is sometimes suggested as a characteristic cluster size.

It will now be shown that there is no new information contained in this statistic over that continued in $w(\theta)$. From Peebles (1975) it can be shown by considering arbitrarily small elemental areas in the original

$\theta x \theta$ cell that

$$\langle N^2 \rangle = \langle N \rangle + \langle N \rangle^2 + \mathcal{N}^2 \int_{\text{cell}} w(\theta i_j) d\Omega_i \, d\Omega_j \qquad (2.59)$$

Here $\mathcal{N}$ and w are the average number density and the 2-point covariance function respectively. θ_{ij} is the distance between elemental areas $d\Omega_i$ and $d\Omega_j$ and the integral is done over the interior of each cell.

From this it is shown, assuming a -0.8 power law for w that

$$\frac{\langle (N - \langle N \rangle)^2 \rangle}{\langle N \rangle} - 1 = \langle N \rangle \, w(0.36\theta) \qquad (2.60)$$

Thus the first term on the R.H.S. is the Dispersion statistic and contains no more information than w.

The test is subject to the usual criticism (applying to $w(\theta)$ also) that it tests only deviation from Poisson and takes no account of the source of these deviations. Also the significance tests are invalid at larger scales once clustering has been found at a smaller scale, since the null hypothesis can nevertheless hold.

More complicated versions of this test do exist to test for various types of obscuration. Here $\langle N \rangle$ is replaced by many individual row and column averages and the test repeated, with care being taken over the degrees of freedom allowed for the new χ^2.

2.7 NEAREST NEIGHBOUR ANALYSIS

We now move further away from the object of fluctuation theory statistics - the estimation of the low order moments - over to statistics which may depend on many moments of a distribution. These types of tests are useful in the cluster modelling approach providing means of comparing

an actual distribution of galaxies and, for instance, a computer simulated model.

2.7.1 Theory

The nearest neighbour analysis consists of computing the histogram of the number of galaxies whose nearest neighbour lies a distance θ away, for all θ. This is then compared with the same histogram computed for a Poisson distribution.

Dautcourt (1977) gives a derivation of the probability distribution, $D(\theta)$, of the nearest neighbour distances for various point processes in terms of their moments. For a random distribution

$$D(\theta) = 2\pi \sin\theta\mathcal{N} \exp(-\Omega\mathcal{N}) \qquad (2.61)$$

where $\Omega = 2\pi(1-\cos\theta)$

For $2\pi\mathcal{N} >> 1$ $D(\theta)$ has a maximum at $\theta = 1/\sqrt{2\pi\mathcal{N}}$. Dautcourt also gives formulae assuming weak clustering and general formulae which involve moments of all orders. Formulae can also be derived for the distribution of 2nd nearest neighbour distances which is sometimes also of interest.

2.7.2 Application

Bogart and Wagoner (1973) found that the most sensitive way of applying NNA to distributions where obscuration was a problem was to randomly split the data into halves and use one half as "sources", the other half as "objects". The nearest neighbour of each source among the objects was found and the distance histograms computed. Random sets of sources are then produced and the procedure repeated. In this way the mean separation and empirical standard error can be found for the random

case and this makes possible comparisons with the data. To guard against the usual difficulty of obscuration being the source of non-random results the random sets were sometimes produced by merely rotating the data sources in galactic longitude. Since there is a relationship between obscuration and galactic latitude this provided a control experiment where obscuration was present and the reality of the non-random results could be checked.

2.7.3 Criticisms

Again this is a test where non-random results can be caused by many effects. Even when contaminating effects are not present, NNA has a reputation of being good at testing for non-random distributions but less good as a discriminator between models. It can be shown that when the clustering is weak there is not much more information in NNA than in covariance function analysis. Also the projection properties of NNA have never been properly derived.

2.8 THE MULTIPLICITY FUNCTION

2.8.1 Definition

With this statistic a surface density enhancement is chosen and the corresponding number density contour is drawn on the sky, using an algorithm such as that described by Turner and Gott (1976). Any objects lying within a closed, connected contour are defined as a group. The multiplicity function, $N(n_G)$, is simply defined as the frequency histogram of the number of members, n_G, of each group. It can be shown that this function can be calculated in the same amount of computational time it takes to calculate $w(\theta)$ and that this function contains information on all moments of the surface distribution (see Gott and Turner (1977)).

2.8.2 Projection Problems

The 3-dimensional multiplicity function is a statistic of great interest to cosmology for it is simply related to the mass distribution of clusters. But because of magnitude limited sampling and the shortage of redshift data, all that can presently be observed is a 2-dimensional multiplicity function. The projection equations relating the 3-dimensional multiplicity function to its 2-D equivalent are difficult to handle (Efstathiou et al, 1979), and this makes comparison of theoretical predictions for the 3-dimensional mass spectrum with the observation very difficult. However, in common with other statistics with bad projection properties, the simple M.F. can still be used on actual galaxy data as long as interpretation is aided by comparison of results with simulated skies, (see Chapter 3). Also there is the future possibility of reducing problems by use of new redshift data but this still leaves an awkward projection problems in the deconvolution of the galaxy luminosity function.

2.8.3 Bhavsar's Statistic

Another criticism of the multiplicity function, even in 3-dimension, is that it tells nothing about the internal structure of the groups it detects. Thus for large values of n_G, $N(n_G)$ will be very small and noisy although the contributing groups here will contain large numbers of galaxies.

A statistic which is a close relative of the multiplicity function and which does tell us something about the internal structure of clusters was described by Bhavsar (1978). Essentially it consists of going through the procedure outlined above and fitting some arbitrary functional form to the 2-dimensional multiplicity function over a set range of scales. If this functional form say is a power law then the amplitude of that power law can be plotted as a function of the density contrast used to define the multiplicity function. However, this statistic too has bad projection properties.

2.9 RESULTS

To conclude this chapter I shall summarise the results from applying these statistics to present day galaxy catalogues. Interpretation of the results, though, will be left to Chapter 3.

The major result comes from the 2 point covariance function analyses of the Zwicky, Lick and Jagellonian catalogues (Groth and Peebles, 1977 and references therein). It was found that over a large range of separation $w(\theta)$ had a smooth variation and was consistentwith a form for $\xi(r)$ such that

$$\xi(r) = 15(hr)^{-1.77} \qquad r \lesssim 9h^{-1} \text{ Mpc} \tag{2.62}$$

(see Figure 2.3)

The magnitude of $w(\theta)$ scaled well between the catalogues indicating that this result was reasonably independent of obscuration effects. This result is consistent with those obtained from power spectrum analyses of these catalogues (Peebles and Hauser, 1974).

After $\theta = 2.0^{\circ}$ the $w(\theta)$ from the Lick Catalogue falls well below its small scale power law behaviour. This indicates some evidence for a feature in $\xi(r)$ at $r = 9\ h^{-1}$ Mpc whose consequences for cosmology would be large. However, this result depends to some extent on preliminary data smoothing and therefore this result is less well established. In Chapter 5 we investigate new evidence relating to this feature in ξ, from deep, machine measured samples.

3-point covariance function analyses of these samples, also by Groth and Peebles (1977 and references therein) indicated that ξ too

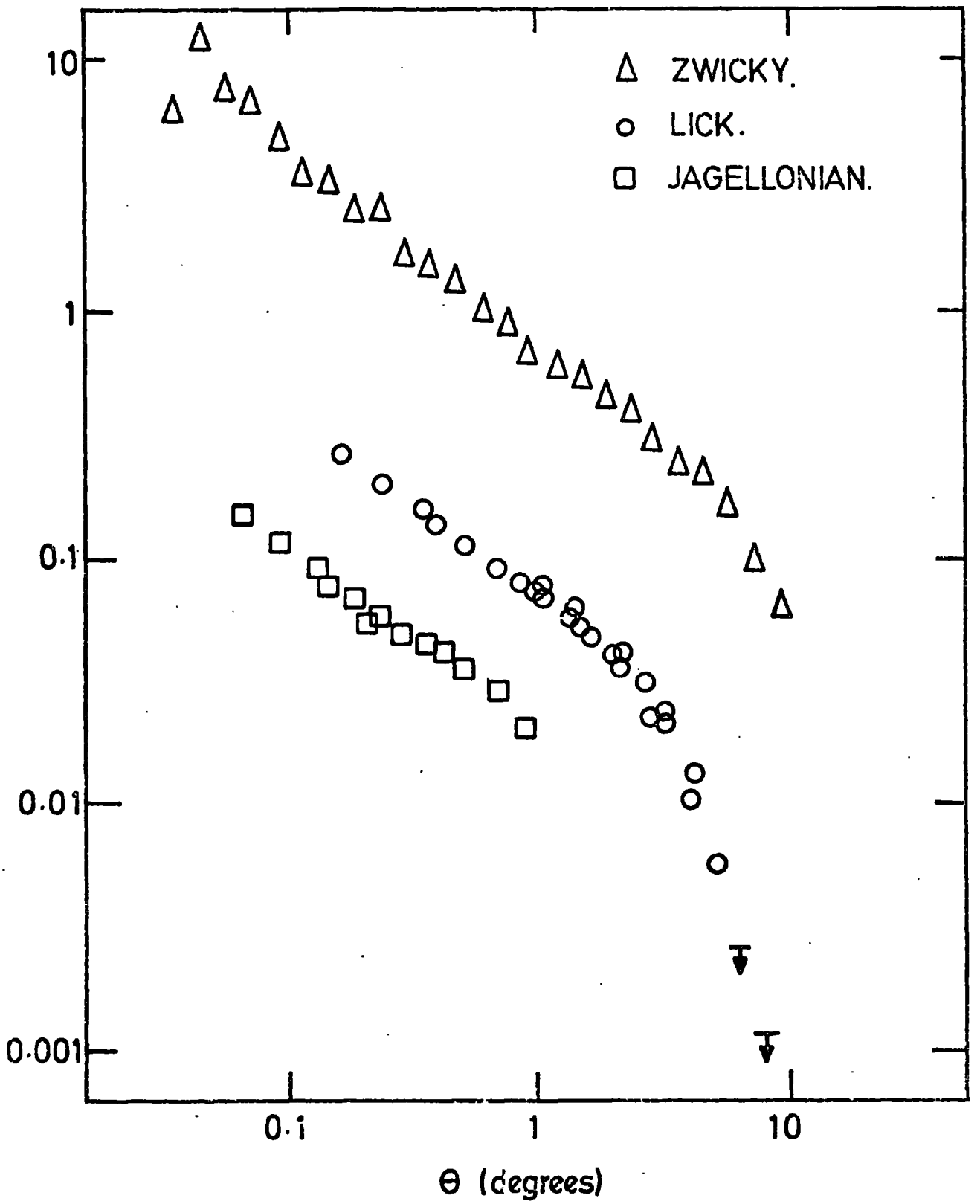

Figure 2.3 2 point covariance function results from the Zwicky Lick and Jagellonian catalogues (taken from Groth and Peebles 1977). These can be represented by -0.75 power-laws in separation, θ.

followed power law behaviour. For $\theta \lesssim 3^{\circ}$ it is well represented by the model

$$\zeta(r_1,r_2,r_3) = Q\left[\xi(r_1)\ \xi(r_2) + \xi(r_2)\ \xi(r_3) + \xi(r_3)\ \xi(r_1)\right] \quad (2.63)$$

with

$$Q = 1.29 \pm .21$$

These 3-point function analyses showed little or no evidence for linear features in the galaxy distribution.

Nearest neighbour analysis was applied to the Abell Catalogue of Rich Clusters by Bogart and Wagoner (1973) to test whether these clusters were superclustered. This analysis produced good evidence that they were. This result was confirmed by a 2-point covariance analysis of the same catalogue (Hauser and Peebles, 1973), and the angular covariance function is shown in Fig. 2.4. The corresponding spatial cluster cluster covariance function was found to be an order of magnitude larger than the galaxy-galaxy covariance function.

The cross-correlation function, ξ_{gc}, was found between this Abell cluster catalogue and the Lick catalogue. (Seldner and Peebles (197) and references therein). They found that the average galaxy number density run, g(r), around Abell cluster centres was well fitted by

$$g(r) = 165\ \langle n \rangle\ (hr)^{-2.4} \qquad 0.5\ \text{Mpc} < hr \lesssim 15\ \text{Mpc}. \quad (2.64)$$

$\langle n \rangle$ here is the overall, mean galaxy number density.

Finally the multiplicity function was applied to the Turner and Gott (1976) group catalogue by Gott & Turner (1977). A smoothly varying multiplicity function was obtained.

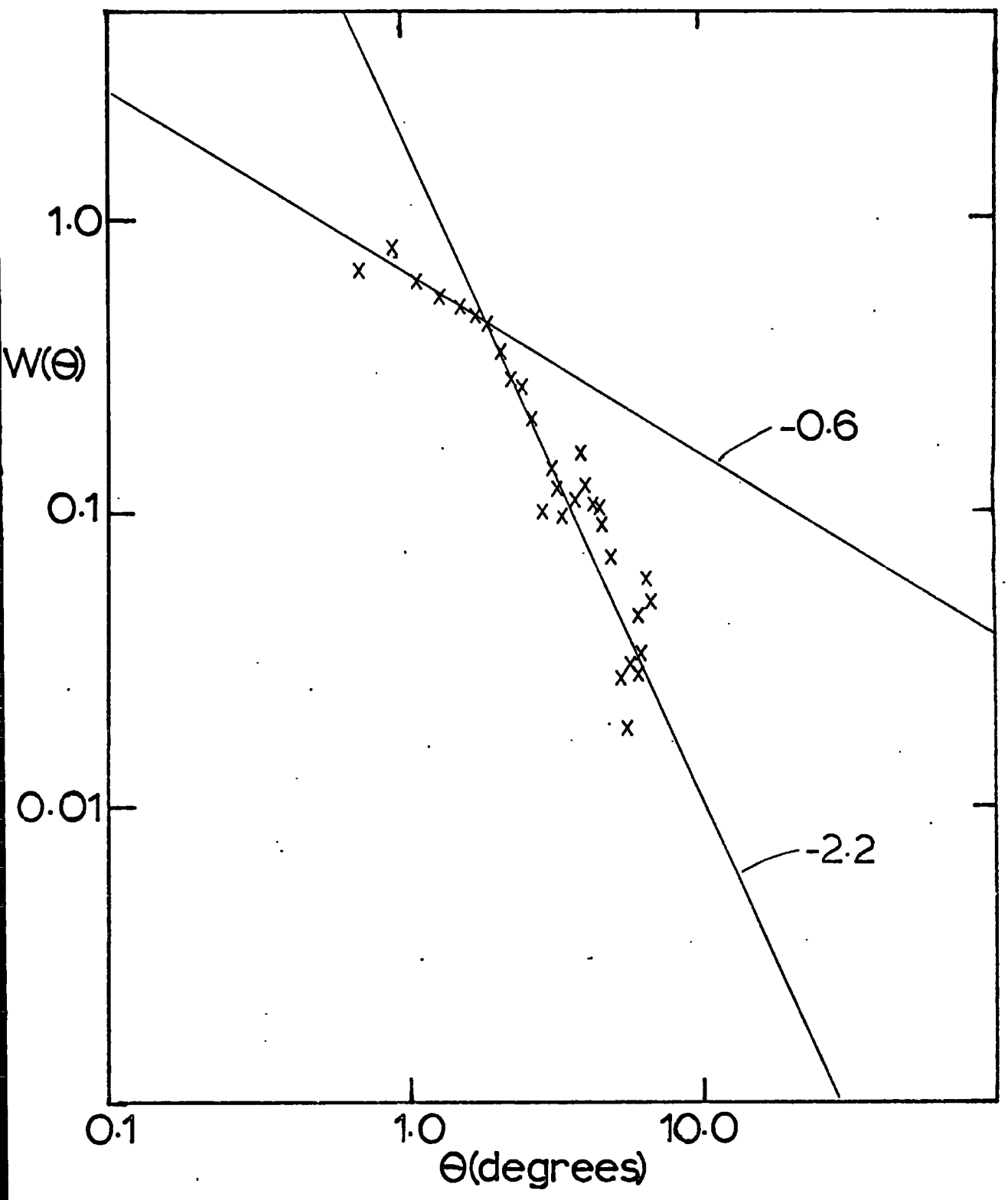

Figure 2.4 2 point covariance function results for the Abell (1958) cluster catalogue. The asymptotic slope here is -2.2

CHAPTER THREE

DISCRIMINATING BETWEEN MODELS OF GALAXY CLUSTERING USING STATISTICAL MEASURES

3.1 INTRODUCTION

We continue now by checking how well these various statistics discriminate between the different theories of galaxy clustering. This will be done by simulating two static models of galaxy clustering and comparing statistical results from these with those obtained from the data. One of the models has no preferred scales of clustering and is often identified with isothermal theory. The other is a model with one (large) preferred scale of clustering and could possibly be identified with adiabatic theory.

We look first at the usual theoretical interpretation of the statistical results summarised at the end of Chapter 2. The smooth behaviour of the best established result, the 2-point covariance function, is always taken as evidence supporting the isothermal theory, (Peebles 1974c). This smoothness is seen as the result of "continuous" galaxy clustering with all scales of clusters contributing to form a $\xi(r)$ that falls off slowly as a power law with r. The absence of features at small scales is said to argue against the presence of a preferred scale and therefore also against the adiabatic theory.

The validity of this interpretation is reinforced by statistical mechanic calculations where galaxies were treated like gravitating gas particles. Here an approximate solution for $\xi(r)$ was found from the BBGKY equations (Montgomery, and Tidman, 1964). . . . Under the assumptions that

$\Omega = 1.0$ and that galaxies were initially randomly distributed this was found to agree with the observed -1.8 power-law small scale form for $\xi(r)$, (Davis, et al, 1977). N-body simulations provided a check on this result with a more direct approach to the problem (Aarseth, Gott and Turner (1979), Efstathiou, 1979). In these simulations the equations of notion of typically 1000 point mass galaxies are numerically integrated taking into account the effects of gravity and the Hubble expansion. $\xi(r)$ was measured after clustering had been allowed to develop and was again found to be in rough agreement with observation. Moreover, the measurement of the three-point function for these simulations was also reasonably consistent with the data. Thus there seems little doubt that isothermal theory can reasonably well explain the 2-and 3-point covariance functions associated with the actual distribution of galaxies.

The multiplicity function of Gott and Turner (1977) also gave a smooth result when applied to shallow samples. Theoretical predictions based on N-body simulations have been made for the 3-dimensional form of the multiplicity function expected in the isothermal picture (Efstathiou et al., 1979, Press and Schechter, 1974) It is difficult to relate these to the observed multiplicity function because of the function's bad projection properties. However, the lack of features is again usually taken as evidence for the absence of a preferred scale of clustering.

By all the above considerations it was concluded that the observed distribution of galaxies was good evidence for isothermal theory. We now go on to test how strong this evidence really is by applying the above statistics to simulated models. This provides the most effective test of the statistics' performance since it tests how their power to discriminate between models is affected by random fluctuations present in the simulations. It also provides a method of empirically determining, in simple

situations, the 2-dimensional behaviour of statistics with difficult projection properties.

The favourite "continuous" model of galaxy clustering and the one we identify in the simulations here with isothermal theory is the clustering hierarchy (CH) model. This model has a long history of popularity in the gravitational instability theory (Carpenter, 1938 , Layser 1974, Kiang, 1967 , and Soneira and Peebles, 1977). In it, all galaxies are found inside many, large (but of finite dimensions) clusters which contain a nested hierarchy of subclusters. Thus the galaxy isodensity contours inside the large clusters look like those shown in Figure 3.1a. This distribution arises naturally in isothermal theory where galaxies form early, and are distributed almost randomly in space. Mutual gravitational attraction first of all brings pairs of galaxies together to become bound, virialised groups. These groups then come together to form small bound clusters and this process repeats itself up to a maximum scale determined only by the age of the universe. This is the physical interpretation of the result from the simple linear theory for the growth of density enhancements in an expanding universe that, in time, ever-larger masses condense out of the Hubble flow because of their gravitational instability. The accuracy of this interpretation is borne out by tests on the distribution arising from the N-body simulations which give results consistent with its clusters having hierarchical structure (Fall, 1978, Peebles, 1978). As we have seen in Chapter 2 this model shows smooth, power law behaviour on small scales for both its 2- and 3-point functions and therefore is in agreement with the BBGKY predictions as well as with the observations. The simulations of the Lick catalogue by Soneira and Peebles (1978) which used the hierarchical model confirmed these results. Here we apply these and other statistical tests to simulated CH models.

In contrast to the hierarchy, our other simulated model does have a very definite, preferred scale of clustering. This is the power law cluster (PLC) model and here models are distributed in clusters of a single size, each having a power law number density fall-off from the centre out to some fixed radius. The density contours for these clusters are like those given in Figure 3.1b and are thus very different from the hierarchical contours of Figure 3.1a. The connections of this model to the adiabatic theory are much less firm than those of the hierarchical model to isothermal theory, since exact predictions in this case are more difficult. The main connection lies simply in identifying the model's single sized clusters with the predicted preferred scale. It could also be argued that after the collapse of the protocluster in which galaxies formed, relaxation processes could lead to a power law cluster denity profile (Binney, 1976). But even ignoring these theoretical considerations, it is still of great interest to see how strongly this definitely non-hierarchical model can be rejected by the statistics usually quoted as evidence for the hierarchical clustering of galaxies.

We know already that this model gives rise to a power law $w(\theta)$, (see Chapter 2). The covariance properties of this model were first discussed by Peebles (1974a) with the point of investigating whether just a few rich clusters could produce the observed $w(\theta)$ for the Zwicky catalogue. Two arguments against the PLC model were given in this paper discussion of which is postponed to Section 3.4 when this new version of the model will have been described. A third argument proposed by Peebles and Groth (1975) was that the PLC model would give the wrong behaviour for the 3-point function, $z(\theta,u,v)$. It was argued that the power law fall-off of z with θ would be faster than is observed (see Chapter 2). Thus the PLC model, indistinguishable from the observed distribution by its second moment

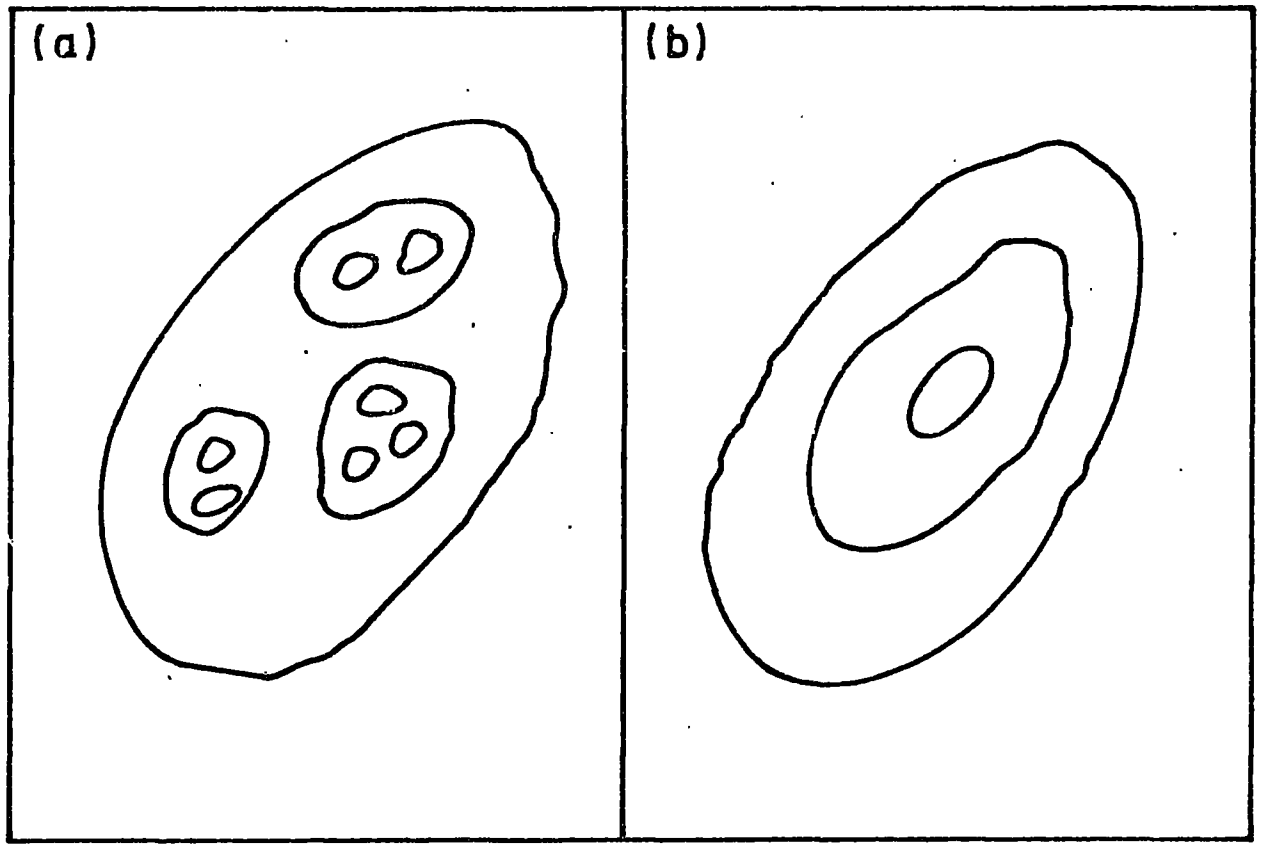

Figure 3.1 Density contours of a galaxy cluster in (a) the hierarchical model (b) the power-law cluster model.

properties is supposedly distinguishable by its third moment properties. We check from the simulations how these and other arguments (e.g. the multiplicity function) apply to the new version of the PLC model described in Section 3.2.

So in Section 3.2 we describe the method of simulating the two model skies. In Section 3.3 we apply the 2- and 3-point analyses and the multiplicity function to the simulations and data and in Section 3.4 we discuss the implications of the results. In Section 3.5 we go on to describe a statistical analysis called Mead's Analysis, which is new to extragalactic astronomy. The results of applying this analysis to various galaxy catalogues, static simulations and N-body simulations, are presented in Sections 3.6 and 3.7. Finally, in Section 3.8 we try to incorporate the results from all the above analyses into a simple picture of galaxy clustering and discuss its implications for galaxy formation theory.

3.2 METHOD OF SIMULATION

The computer simulation of each three-dimensional cluster in the CH models was done in a similar manner to Soneira and Peebles (1977) except that exactly two points were distributed at each level of the hierarchy instead of an average of two points per level. This means that around each cluster centre two points are distributed uniformly at random to form the first level. Another 2 points, the second level, are generated uniformly in each of two spheres of radius R/1.76 around the points of the first level and this process is continued for say N levels. The parameters choices of R and N were determined by best fitting the observed $w(\theta)$ amplitude.

The simulation of PLC clusters was done using the definition given below :

(i) All galaxies are distributed in clusters.

(ii) These clusters are distributed uniformly at random throughout space.

(iii) There is a constant number of galaxies, m, inside each cluster, distributed spherically symmetrically with a power law number density fall off n(r) up to some constant cut-off radius R i.e.

$n(r) = A\, r^{-\varepsilon}$ $\quad r \leq R$ $\quad A, \varepsilon$ constants

$n(r) = 0$ $\quad r > R$

It should be noted that in this version of the PLC model all galaxies are distributed in clusters and not just some in a few rich clusters. The values of A and ε were determined empirically by fitting to the $w(\theta)$ amplitude and slope.

Apart from these different internal structures of the clusters the simulations were done in a similar manner for the CH and PLC models. It was decided to simulate mainly at the Zwicky level, $m_{lim} = 15.0$, since the 2- and 3-point functions are furthest above the noise in the shallow samples. Cluster centres were generated randomly in a cone in three-dimensional space corresponding to $b_{II} \geq 45^{o}$. Galaxies were then generated in the cluster according to either the hierarchical or PLC prescriptions. Cluster centres were generated far enough out to ensure that the $b_{II} \geq 45^{o}$ boundary or the magnitude limit did not affect the sample. Galaxies were then assigned absolute luminosities using the Schechter luminosity function (Schechter, 1976). Schechter's parameter M^{*} was taken to be - 20.5 (H_o = 50 km s^{-1} Mpc^{-1} here and throughout). Magnitudes were generated in the range $M^{*} \pm 4.0$ as in the paper by Ellis, et al (1977). Reasonable variations in M^{*} and α did not affect the results. The absolute number density of galaxies was normalised to give the same number density as that of the Zwicky catalogue ($m_{lim} = 15.0$) in the sky. This meant that the

absolute space density of clusters was 4×10^{-6} Mpc^{-3}. Within the errors involved, this is in rough agreement with the estimated space density of Abell clusters ($\sim 6 \times 10^{-7}$ Mpc^{-3}). Apparent magnitudes were then calculated for the galaxies. Galaxies fainter than $m_{lim} = 15.0$ were removed from the survey and the rest projected on to the sky to give a data set like the Zwicky catalogue.

3.3 STATISTICAL COMPARISON OF SIMULATIONS AND DATA

3.3.1 Correlation Analyses of Simulated PLC Model

For reference purposes, we present first as (1) in Figure 3.2 the recalculated $w(\theta)$ results for the corrected list of 3767 Zwicky catalogue galaxies with $b_{\pi} \geq 40^{o}$, $\delta \geq 0^{o}$ and $m_{lim} = 15.0$ taking galactic extinction into account in the usual way (see Peebles and Hauser, 1974). The straight line has a slope of -.74, the slope obtained by a least squares fit to the $w(\theta)$ calculated from the Lick catalogue (Groth and Peebles,1977). The possible suggestion in Fig.3.2(1) of a break-away from power law behaviour at $\theta \sim 6^{o}$ has been confirmed by this $w(\theta)$ analysis of the Lick catalogue where a similar reproducible future was found.

The results for the 2-point covariance analysis on the PLC simulations are presented as (2) in Figure 3.2. These are the averaged results from an ensemble of four simulations with R = 25 Mpc, $\varepsilon = 2.3$ and m = 525. These were the parameter choices which gave best agreement in (2) with the data. The density fall-off parameter ε has been slightly affected by the cut-off at R = 25 Mpc. Since the $w(\theta)$ slope is determined over scales in θ that correspond to R, the lack of pairs at $r > R$ steepens the $w(\theta)$ slope at large θ. Whereas $\varepsilon = 2.4$ is needed with very large values of R to produce roughly the observed slope (see Chapter 2) $\varepsilon = 2.3$ is found by trial and error to be a suitable power for the radius of cluster used here.

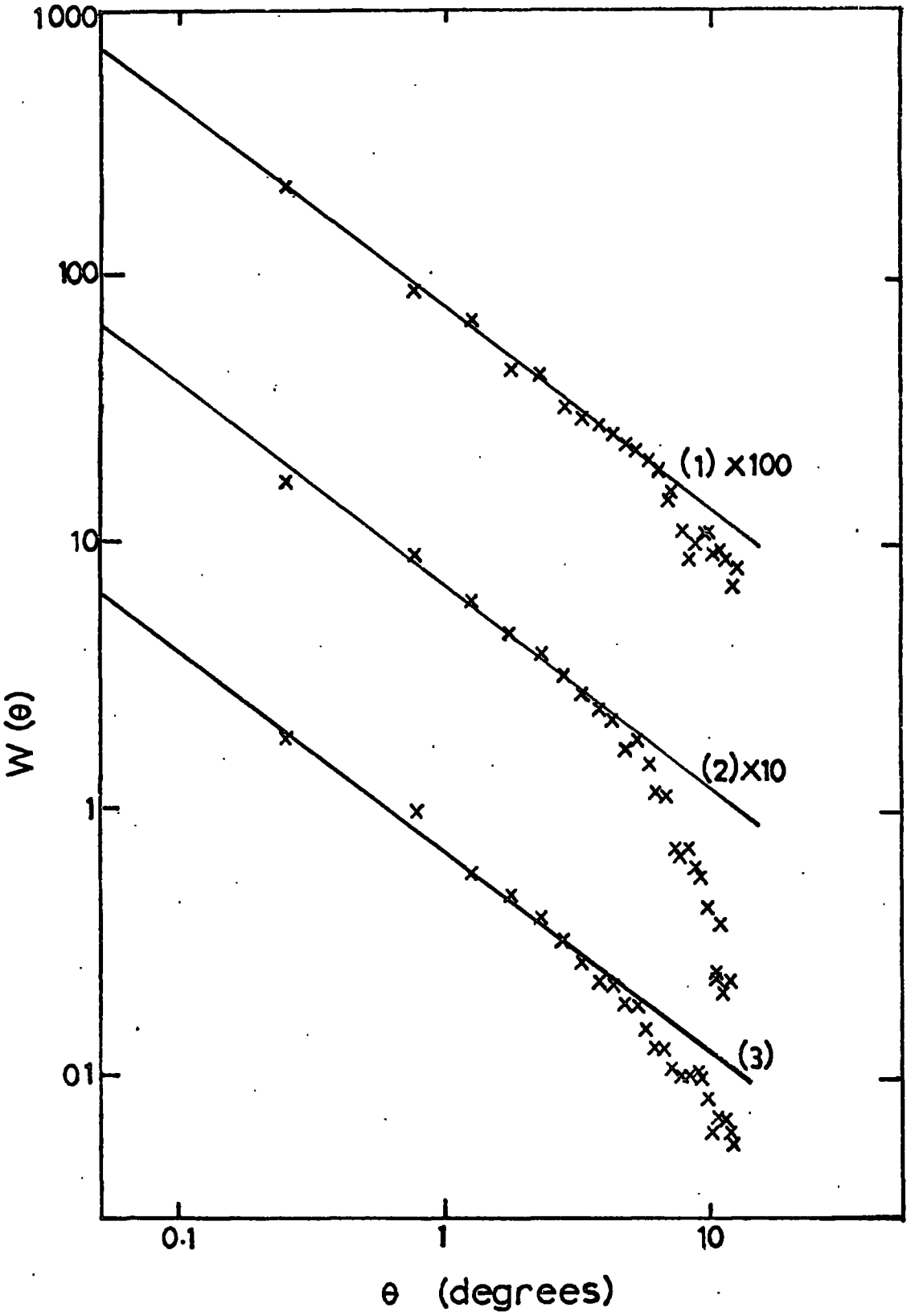

Figure 3.2 (1) $w(\theta)$, $\theta \leq 12^{\circ}$, for Zwicky catalogue, $\delta \geq 0^{\circ}$, $b_{II} \geq 40^{\circ}$, $m_{lim} = 15.0$.

(2) ensemble average $w(\theta)$ for four power-law cluster simulations with R = 25 Mpc, $\varepsilon = 2.3$, n = 525.

(3) ensemble average $w(\theta)$ for four hierarchical simulations with R = 25 Mpc and 9 levels.

The hardest feature to fit was the apparent break in the observed $w(\theta)$ at $\theta \sim 6^{\circ}$. The results from this and a variety of other simulations show that only at R = 25 Mpc do the clusters consistently keep $w(\theta)$ a power law as far as is observed. Superclustering of smaller R = 9 Mpc clusters was tried to see if that would also keep $w(\theta)$ high long enough, but it did not. The only conclusion is that for a model of this type to work the clusters must be of conventional supercluster size. The line fitted by eye in Figure 3.2(2) corresponds to the observed -0.74 power law. The power-law amplitude too corresponds to the observed amplitude. Therefore this PLC model reproduces well the observed $w(\theta)$.

Considering now the galaxy 3-point covariance function $z(\theta,u,v)$, we present first for comparison as the closed circles in Figure 3.3 the results for the statistic applied to the Zwicky catalogue. This was computed for exactly the same sample of galaxies as above. It was computed in a similar manner to Peebles and Groth (1975) except that due to computer time limitations I could only calculate it up to a maximum separation of 3°. Also, here the bins are linear in θ and u. Table 3.1 gives the range of u and v for each graph in Figure 3.3. Briefly θ is a parameter defining the size of a particular galaxy triangle whose shape is defined by u and v. A full description of these and of the computational details are set out clearly in Peebles and Groth (1975). The known -1.6 power-law variation of Z with θ while u and v are held constant is shown in Figure 3.3 in agreement with Peebles and Groth. The fitted amplitude of this power law would be a factor of 2 higher than that reported by the above authors but agrees with the corrected amplitude in Groth and Peebles (1977).

The results for the 3-point covariance function for the PLC model are presented as the open circles in Figure 3.3. The results shown are based on one simulation because of computer time limits. As can be seen

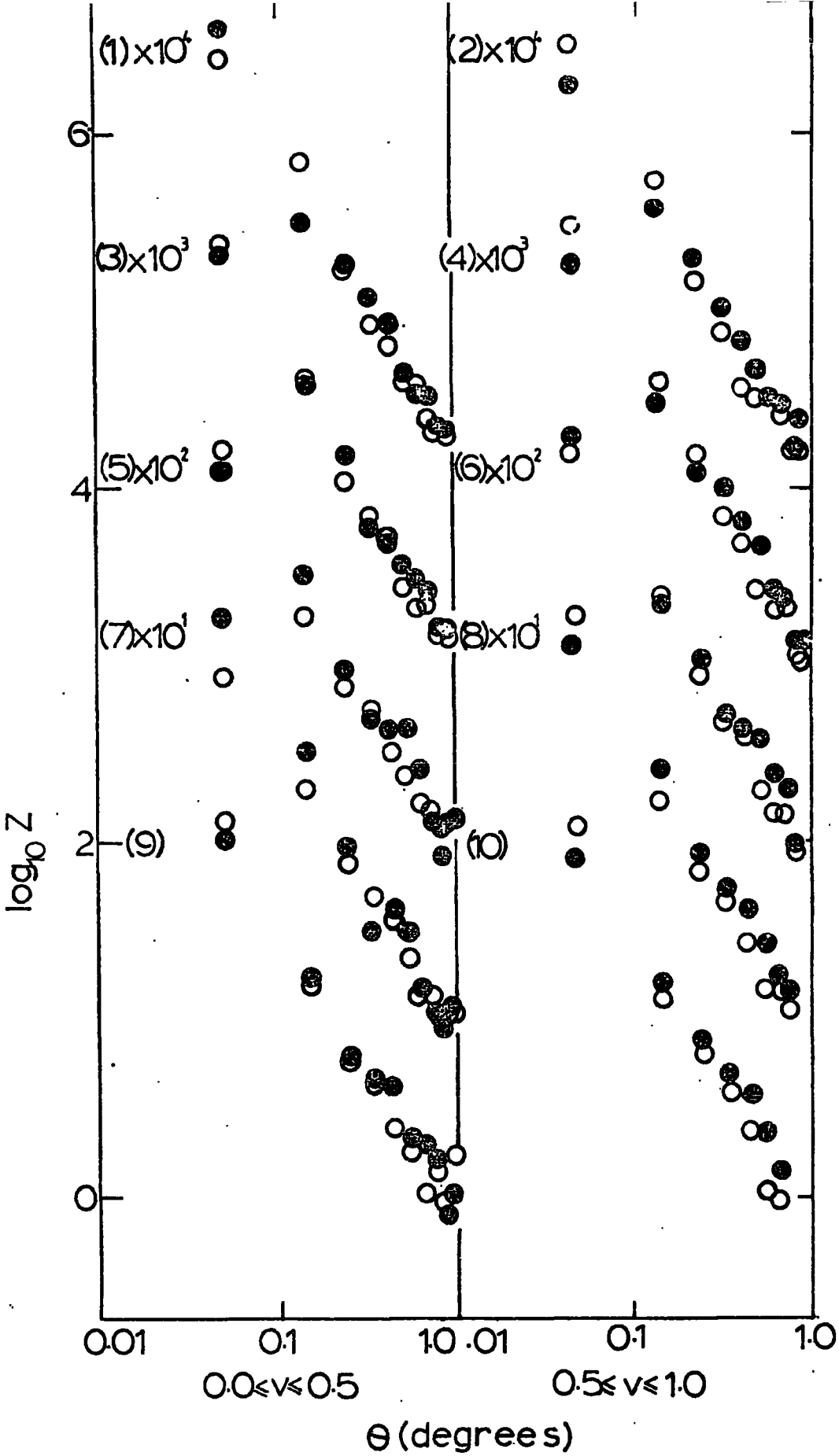

Figure 3.3 $z(\theta, u, v)$ v. θ for u, v bins as in Table 3.1. Filled circles are the $z(\theta, u, v)$ for the Zwicky catalogue galaxies, $\delta \geq 0^{\circ}$, $b_{II} \geq 40^{\circ}$, $m_{lim} = 15.0$, open circles are the $z(\theta, u, v)$ for the power-law cluster simulation ($R = 25$ Mpc, $\varepsilon = 2.3$, $n = 525$).

TABLE 3.1

u, v bins for $z(\theta,u,v)$ in Figure 3.3

		u				
		1.0 ↓ 1.44	1.44 ↓ 1.88	1.88 ↓ 2.32	2.32 ↓ 2.76	2.76 ↓ 3.2
v	0.0–0.5	(1)	(3)	(5)	(7)	(9)
	0.5–1.0	(2)	(4)	(6)	(8)	(10)

the simulated distribution (one of the ensemble of four whose $w(\theta)$'s were presented earlier) gives a reasonable approximation to the observed $z(\theta,u,v)$. The observed slopes here are -1.77 ± 0.05 (in reasonable agreement with the predicted -1.9 for very large R clusters) and not significantly different from the observations. If it were required the agreement could be made exact by making the model slightly more sophisticated. For instance, we could adopt a model with a core-halo cluster structure with the core reverting to a marginally flatter power law fall-off. This would make the z variation with θ exactly -1.6 and not affect the $w(\theta)$ slope too much since it is determined over a larger range of scales. This modification would mean an increase in the number of parameters involved in the model but this in itself is not too serious since such fall-off's are observed in the cores of individual clusters. Also hierarchical simulations need similar modifications before full agreement with the correlations is obtained. With even our simple model showing such reasonable agreement it seems clear that the 3-point function may not be as strong evidence against the PLC model as had previously been believed.

3.3.2 2-Point Results for Crude Hierarchy

The parameters which best gave the 2-point function amplitude for this model with the Schechter luminosity function were R = 25 Mpc and N = 9. This means that in 3-dimensions there are always 512 galaxies per R = 25 Mpc cluster. The average $w(\theta)$, $\theta < 12^{\circ}$, is shown for an ensemble of four such hierarchical models as (3) in Figure 3.2. $w(\theta)$, $\theta \lesssim 3^{\circ}$, is shown for one of the ensemble in Figure 3.4. A drop off at $\theta \sim 0.1^{\circ}$ is immediately visible. The drop off, caused by the simple hierarchy was noted by Soneira and Peebles (1977) and is not removed by introducing probability distributions into the numbers per level. If the drop-off is removed to acceptably small θ by raising the number of levels in R = 25 Mpc to 10 then the

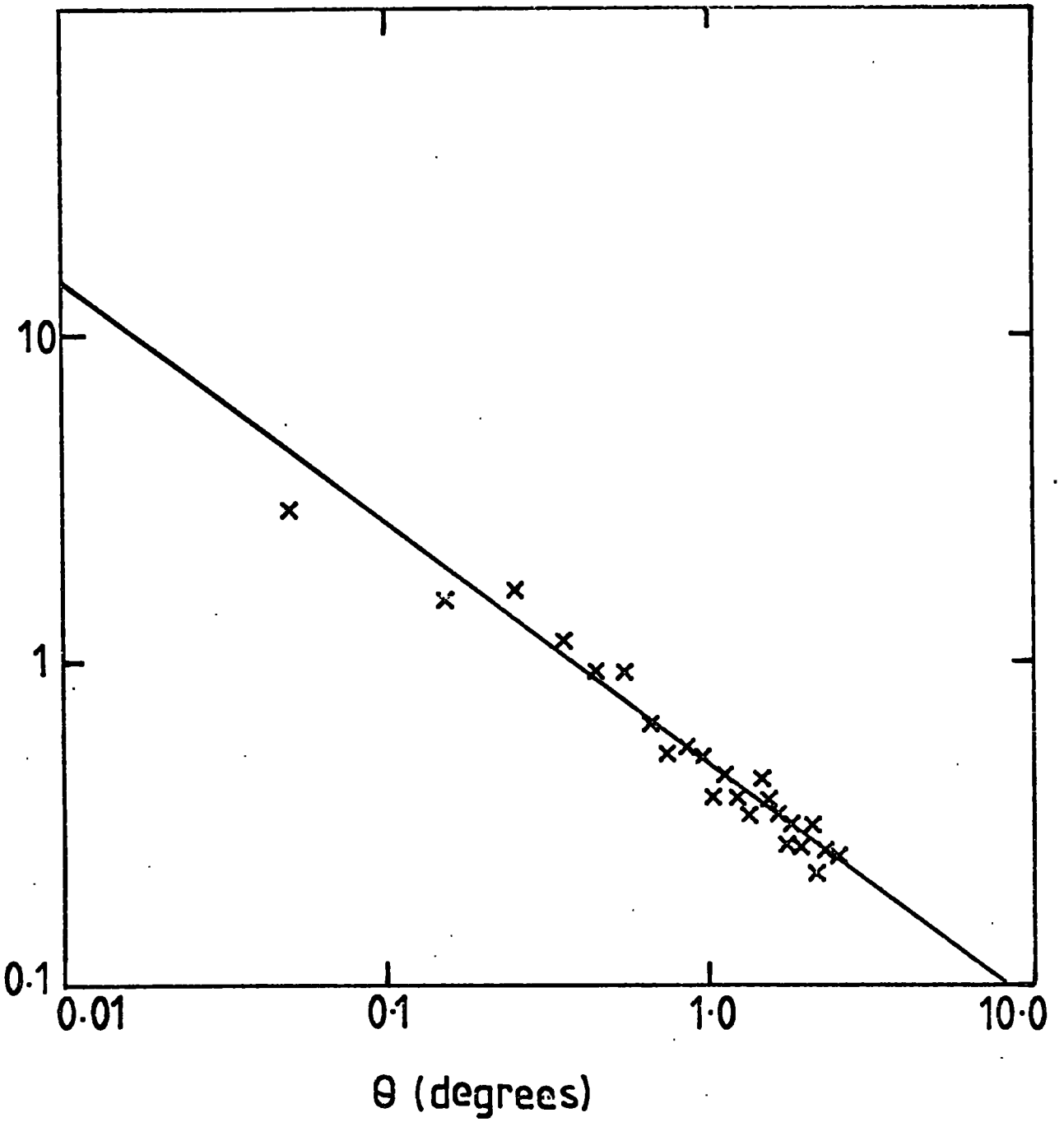

Figure 3.4 $w(\theta)$, $\theta \lesssim 3^{o}$, for a hierarchical simulation, R = 25 Mpc and 9 levels.

model 2-point covariance function disagrees with the observed amplitude by a factor of 2. However, the drop-off can probably be removed by introducing varying numbers of levels for cluster (Groth et al, 1977) with a small percentage of clusters having 11 or 12 levels which hopefully can fill out this drop-off without disturbing the amplitude of $w(\theta)$ too much. The varying numbers of levels is also required to produce the correct amplitude for the 3-point covariance function. These difficulties all mean that the hierarchical models needs at least as many parameters to fulfil the 2- and 3-point function criteria as the PLC model.

3.3.3 Multiplicity Function Results for Hierarchical and PLC Models

The results for the multiplicity function applied to the Zwicky catalogue are presented as the crosses in Figure 3.5. The surface density contrast used here to define the groups is which corresponds roughly to a 3-dimensional density contrast of 10% (see Gott and Turner, 1977). These broadly reproduce the results of the analysis of the 14^m limited sample of Gott and Turner in that the fraction, f, of mass associated with groups seems to vary smoothly with n, the group size. This is the smooth variation without features at any scale which has been interpreted as evidence for the galaxies being continuously distributed in a hierarchy. However, marked as the closed circles in Figure 3.5 are the average results for the multiplicity function applied to the 4 PLC simulations which were presented earlier. In 3-dimensions this model would give a 3-dimensional multiplicity function as a delta function at the constant membership size of the cluster. However, it can be seen that in projection it produces a multiplicity function as smooth as the observed. The reason for this is that the magnitude limit makes more distant clusters look smaller since, at large distances, only the brighter end of the luminosity function is being sampled. This smooths

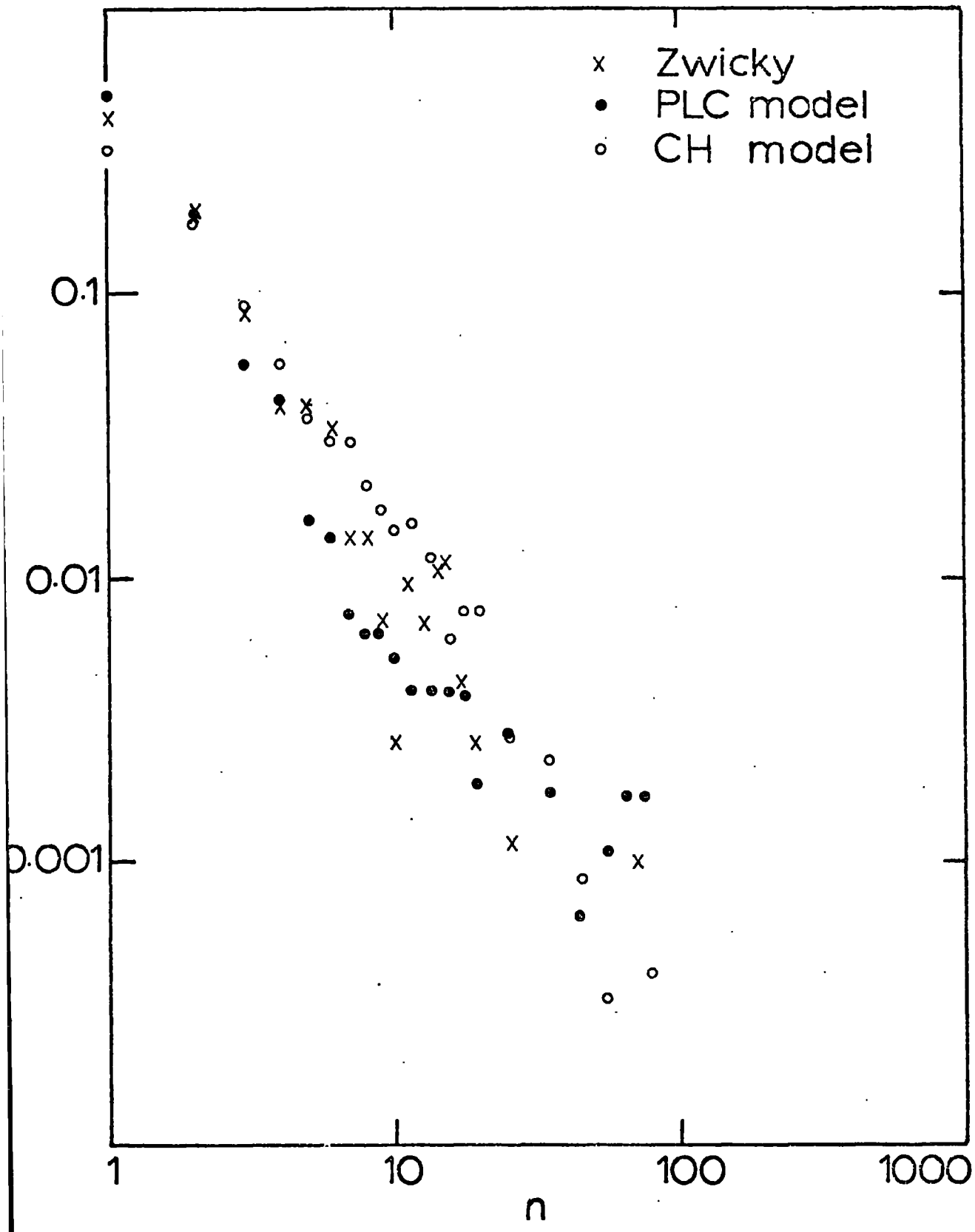

Figure 3.5 The multiplicity function result for the Zwicky catalogue and ensemble average results of 4 PLC and 4 CH simulations. Here f is the fraction of galaxies involved in clusters of size n, with a 10% density contrast.

any features caused by the preferred scale. Thus the smoothness of a projected multiplicity function is not straightforward to interpret. This fact is emphasised by the open circles in Fig.3.5. These represent the average multiplicity function from 4 simple hierarchical simulations. Again a smooth variation of mass fraction, f, with number, n, is seen similar to the observed. But this model, constructed to give "no preferred scales", shows in 2-dimensions, less power at small scales than a model which in 3-dimensions has all its power at large scales.

Going on now to a straight comparison of the 2 models with the data indicates that both models give reasonable fits to the data. At intermediate scales the hierarchical model possibly better fits the data whilst at larger scales possibly the PLC does better. The important point is that it can hardly be said that the PLC model is being more firmly rejected by multiplicity function analysis than the hierarchical model.

Thus similarly to the 2-and 3-point functions the multiplicity function does not seem to provide as much evidence for the hierarchical model as is generally believed. Again this throws open the question of whether a preferred scale of clustering exists or not.

3.3.4 Visual Impression

Another non-statistical and more subjective justification for hierarchical galaxy clustering is the claim that many scales of galaxy clustering are apparent when pictures of galaxy distributions are inspected by eye (see Soneira and Peebles 1978). This is certainly confirmed by Figure 3.6a, where dots depict the positions of Zwicky catalogue galaxies, $m_{\ell im} = 15.0$, $\ell_\pi > 40^o$, $\delta > 0^o$. However, Figure 3.6b shows that in a similar dot plot of a typical PLC simulation many scales of clustering are also apparent, although in this case we know that, in 3-dimensions, only one large scale of clustering exists. The 2-dimensional projection and

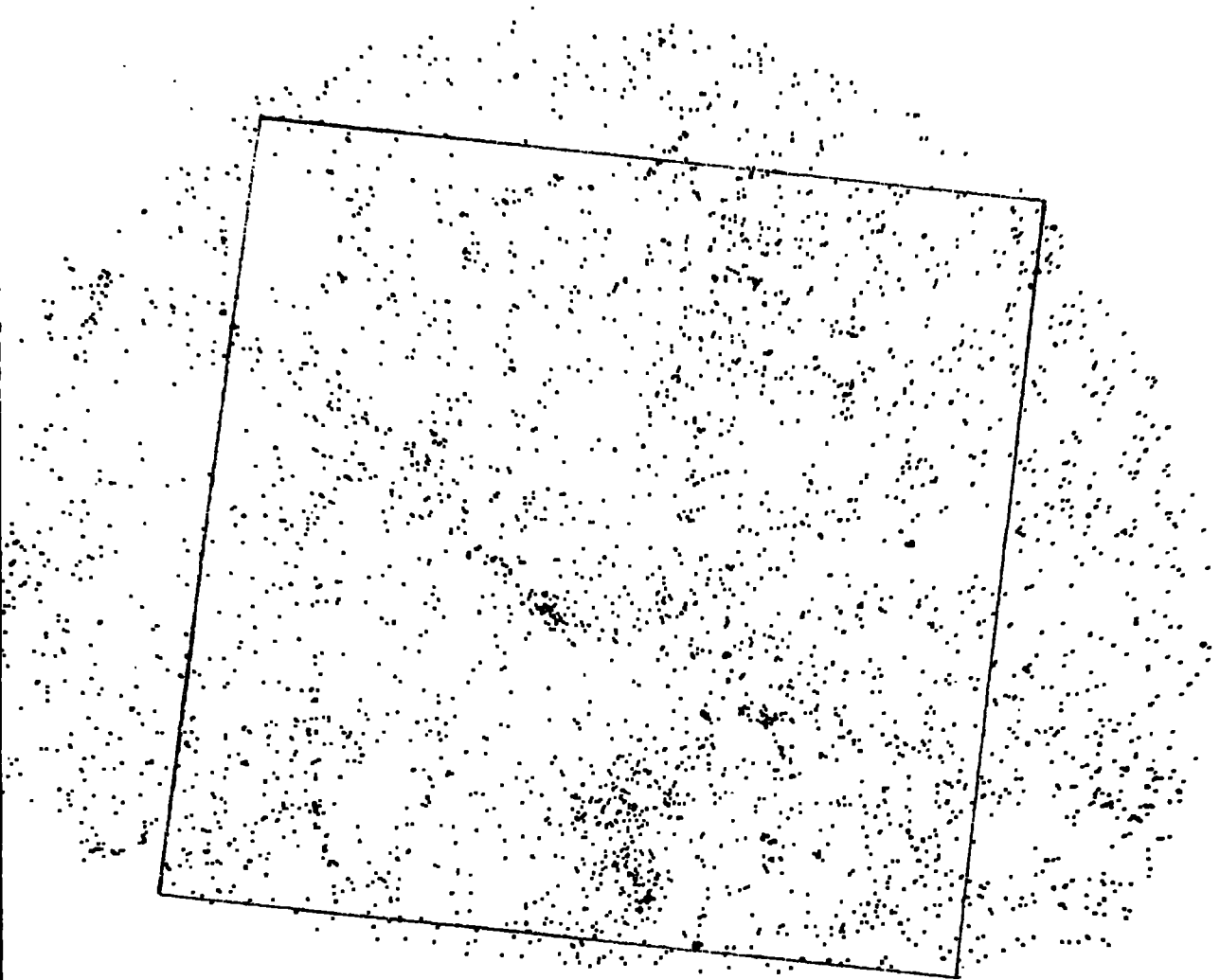

Figure 3.6 (a) Equal area projection of galaxies in Zwicky catalogue $\delta \geq 0^{\circ}$, $b_{II} \geq 40^{\circ}$, $m_{lim} = 15.0$. Mead's analysis was carried out on galaxies inside the square.

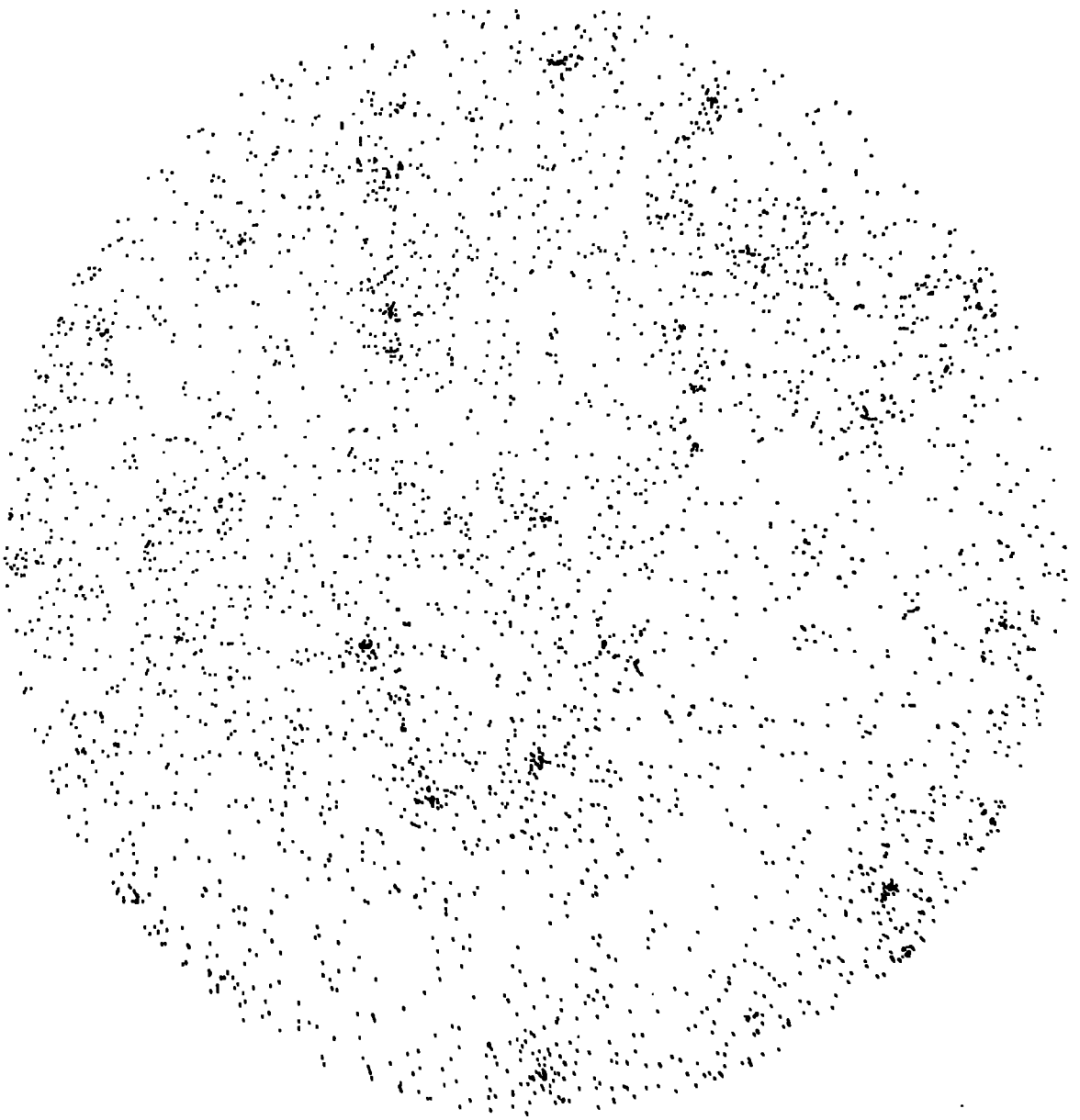

Figure 3.6 (b) Distribution of galaxies arising from a typical PLC simulation.

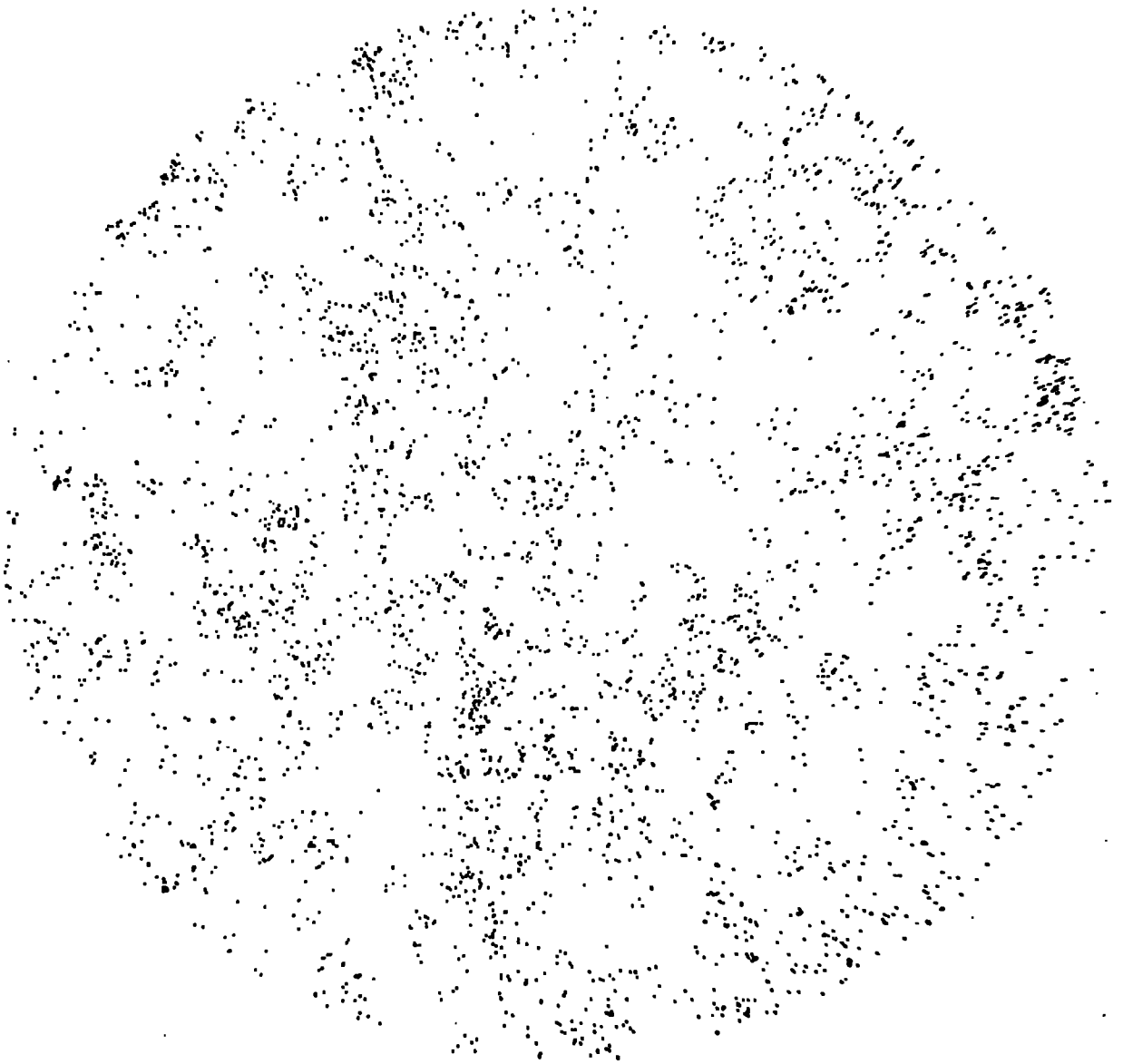

Figure 3.6 (c) Distribution of galaxies from a typical CH simulation.

magnitude limit have combined to produce a visual impression that all scales of cluster exist. Finally, a dot plot produced by a hierarchical simulation is presented in Figure 3.6c. Comparisons between the simulations and the Zwicky catalogue show that it is difficult to visually reject either of the models even though the structure of clusters in each is entirely different.

3.4 DISCUSSION

3.4.1 Other Arguments Concerning Power Law Model

As mentioned in Section 2.1 there were offered in Peebles (1974a) two "serious arguments" against the original PLC model, where a few rich clusters were giving rise to the power-law $w(\theta)$. The first point was that since superclustering is an observed phenomenon (Hauser and Peebles, 1973) why did it not produce a feature in $w(\theta)$? It was suggested that superclustering was not a feature of only one preferred scale but that it carried on continuously down to small scales. This continuity filled out $w(\theta)$ in a smooth way. (It was also argued (Peebles, 1974c) that this lack of features was surprising if adiabatic theory was relevant since no preferred scale was being picked out). However, the subsequent discovery of the break in the galaxy $w(\theta)$ from the analysis of the high resolution Lick counts (Groth and Peebles, 1977) solves both these problems at once. The suggestion is that this break is the required feature produced by preferred scale of supercluster size. The smoothness of $w(\theta)$ before the break point comes from the "on the average" smooth supercluster power-law density fall-off. The validity of this interpretation is borne out by the simulations.

The second argument in Peebles (1974a) does not really apply to this new version of power-law clustering. It concerned the observation that clusters that blatantly exhibit power-law number density fall-off's

(and that might be considered examples of the "few rich clusters" discussed in Peebles (1974a) e.g. Coma, do in fact display deviations from power-law behaviour by flattening off at up to 200 kpc from the centre. This effect was modelled in the PLC simulations, indeed leaving a spherical hole at the middle of all the superclusters and no deviation from the $w(\theta)$ power-law was produced. This is to be expected since few of the pairs measured by $w(\theta)$ at small θ come from the nearest rich clusters in the simulations.

A main piece of evidence for the general power-law distribution of galaxies in clusters comes from the cross-correlations of Abell cluster centres and the Lick catalogue galaxies (Seldner and Peebles, 1978). The cross-correlation function directly measures the projected number density run around Abell cluster centres and $n(r) \propto r^{-2.3}$ was fitted to the curve after de-projection. $n(r) \propto r^{-2.3}$ fits almost as well. This is a strong piece of evidence supporting the above PLC model. Furthermore, the cross-correlation function of Seldner and Peebles continues out to a radius of more than 20 Mpc.

It is important also to point out that the power-law cluster model treats clusters like Coma and Virgo in a natural way and not as statistical fluctuations. Jones (1976b) analysed the galaxy distribution around the Virgo cluster using de Vaucouleur's (1974) distance determinations. He found that a power-law fitted the number density fall-off from the centre of Virgo out to a distance of over 20 Mpc. Also, Chincarini and Rood (1976) found that a power-law of index -2.27 fitted the number density run of the Coma cluster out to a radius of 35 Mpc.

3.4.2 Theoretical Consequences

Firstly, such a simple model also giving rise to the observed 2 and 3 point covariance functions means that the basis for the assumption of a heirarchical distribution is not as strong as previously thought.

As the hierarchical model is a model usually associated with isothermal perturbation theory this means that the case for pure isothermal fluctuations in the early universe is less convincing as well.

Secondly, it may now be possible to argue that the observed 2- and 3-point covariance functions do not totally exclude the adiabatic theory of galaxy formation. Doroshkevich and Shandarin (1978) predict that in an $\Omega = 0.1$, $H_o = 50$ km s^{-1} Mpc^{-1} universe the preferred scale of supercluster (or "pancake") is between 40-50 Mpc. Assuming 10^{12} $M_\odot$ as the mass of a galaxy it can be seen that the mass involved in the power-law cluster simulations is of a comparable order of magnitude. A power-law density fall-off in the supercluster, of index $\varepsilon \sim 2$, could result by relaxation processes as indicated by Binney (1976). As shown above the resulting distribution could well represent the observed 2 and 3 point galaxy covariance functions at small separations.

Finally, making the assumption that collective relaxation effects play a role in forming clusters of galaxies, Press and Lightman (1978) find that a power-law density cluster (index of density fall-off between 2.0 and 2.5) will result. Again the above result shows that this process may also be consistent with the 2- and 3-point covariance functions.

Thus, by these considerations, it is important to test whether hierarchical or power-law clustering better models the present day galaxy distribution. There is an evident need for a new statistical analysis that can discriminate between hierarchical and power-law clustering. Such an analysis is described in the next section.

3.5 MEAD'S ANALYSIS

3.5.1 Description

Mead's analysis was originally suggested for one-dimensional transect problems in ecology (Mead, 1974). However, the two dimensional version described here was first suggested by Besag and Diggle (1977).

Mead's analysis in two dimensions is carried out on gridded data in a square area. Thus, if galaxy positions on a square photographic plate are recorded as (x,y) co-ordinates then, as a preliminary to Mead's analysis, each position is counted into one of NxN square bins on the plate. N must be a power of two and for the galaxy catalogues N usually took the value 128.

The smallest area Mead's analysis tests for clustering is the area covered by 2 x 2 (e.g. area A_1 in Figure 3.7) of the raw 128 x 128 counts, a_1. Mead's analysis tests this scale by the following procedure. Firstly, the sub-totals $A_1 = a_1 + a_2 + a_3 + a_4$, A_2, A_3 and A_4 are obtained in cell B_1. (Here the capital letters indicate the total number of galaxies in a square area and they also reference that particular square area on Figure 3.7). Then the test statistic $T_{B_1}^{(1)} = |A_1 - A_2| + |A_1 - A_3| + |A_1 - A_4| + |A_2 - A_3| + |A_2 - A_4| + |A_3 - A_4|$ is computed for square B_1. This is repeated for all the 1024 (N = 128) "B size" squares on the grid and $T_B^{(1)} = \sum_i T_{B_i}^{(1)}$ is computed. In some sense $T_B^{(1)}$ is expected to be large if there are clusters present "on the average" of a size A. (Note that $T_B^{(1)}$ is testing scales of size A - to prevent confusion the B is now dropped and thus $T^{(1)} = T_B^{(1)}$). To obtain quantitative significance levels for the size of $T^{(1)}$ the procedure of Besag and Diggle (1977) is then followed. A randomisation of the a_i's in Square B_1 is performed and $T_{B_1}^{(2)}$ computed for the new permutation of a_i's. This is repeated for all

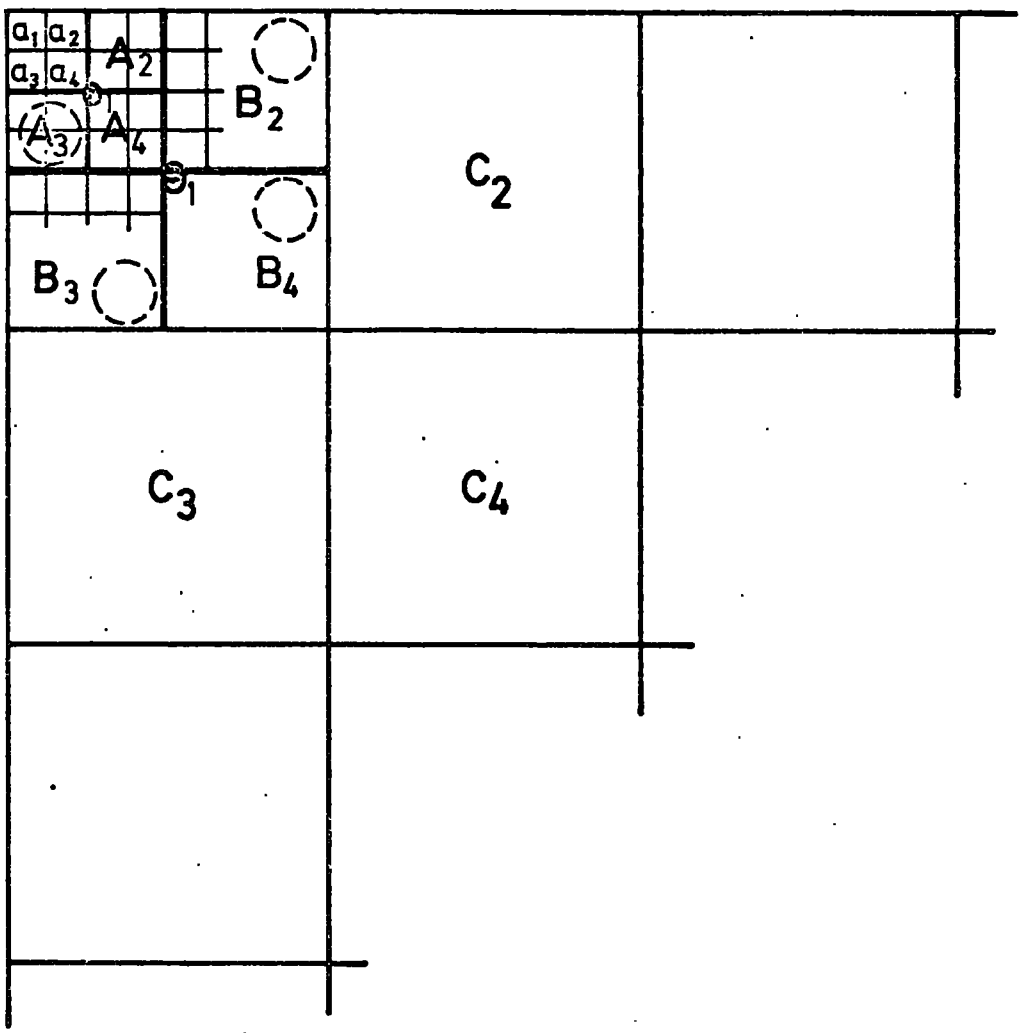

Figure 3.7

the 1024 "B size" squares in the area and a new statistic $T^{(2)} = \sum_i T^{(2)}_{B_i}$ is formed on the randomised data. This process is repeated 99 times so that by the end there is $T^{(1)}$, the statistic computed on the raw data and $T^{(2)}$, $T^{(3)}$, $T^{(4)}$,....., $T^{(100)}$, the statistics computed on the 99 different randomisations of "4's within 16's" of the data. If $T^{(1)} > T^{(2)}$, $T^{(3)}$,....., $T^{(100)}$ then there is evidence for clustering on scale A at the 1% level. If exactly one of the randomised statistics $T^{(j)}$ is larger than $T^{(1)}$ then the above statement can be repeated about scale A but this time at the 2% level etc. The complete procedure is repeated on the B totals ($B_1 = A_1 + A_2 + A_3 + A_4$, etc.) to test for clustering at scales of size B and all scales up to 64 x 64 of a 128 x 128 grid (i.e. 6 scales in all). In Figure 3.8a are shown the results of such a Mead's analysis with a 128 x 128 grid on a 2-dimensional 128 x 128 unit area with 600 simulated uniformly distributed cluster centres each with 6 points uniformly distributed around them inside a circular cluster of diameter 16 units. A scale is picked out somewhere between the 8 unit and 16 unit scales of clustering at the 1% level which is sensible since 16 units is the maximum scale of correlation in this simulation.

Mead's analysis' advantages over other similar types of analyses e.g. binning analysis (Webster, 1976) are as follows :-

(1) Getting significant results at small scales does not invalidate the test at larger scales.

(2) Similarly large scale inhomogeneities in the data do not affect the tests at smaller scales since the Mead's analysis always contrasts density enhancements with just the density locally and not the global density.

(3) Mead's analysis is sensitive to clustering of clustering. For instance, in Figure 3.7, if the pattern of clusters (dashed circles) displayed

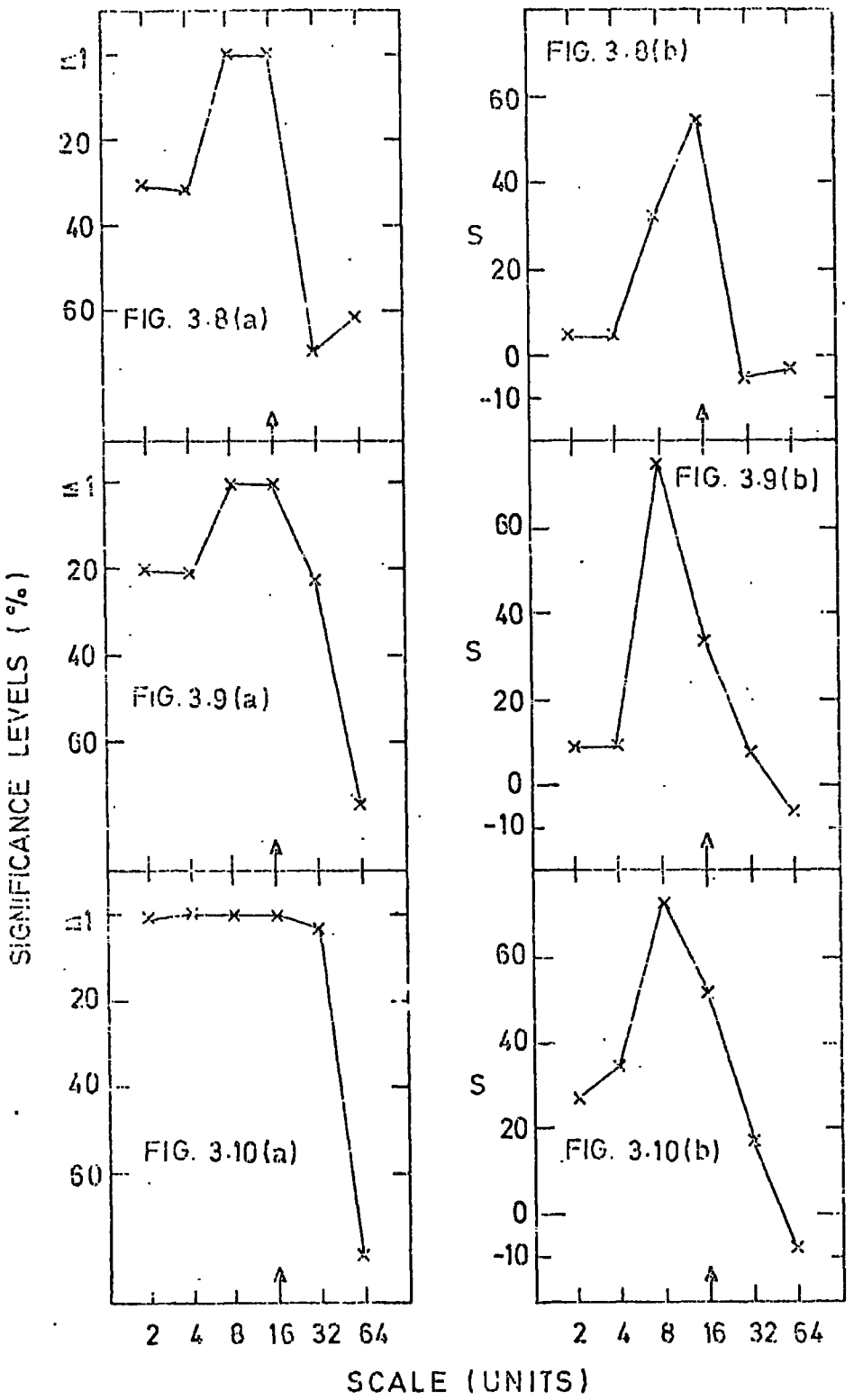

Figure 3.8 (a) Mead's analysis for a 2-D simulation on a square 128x128 unit area with 600 clusters of 16 units diameter each containing 6 points distributed uniformly at random. (b) Mead's analysis for the 2-D simulation as in Figure 3.8a. Here , S , the no. of standard errors the data statistic is away from the mean of the randomised statistics, is plotted as the ordinate.

Figure 3.9(a) As Figure 3.8a for a simulation of 180 clusters of 16 units diameter with 20 points per cluster. (b) As Figure 3.8b for the simulation of Figure 3.9a.

Figure 3.10(a) As Figure 3.8a for a simulation of 180 clusters of 16 units diameter with 20 points per cluster. (b) As Figure 3.8b for the simulation of Figure 3.10a.

here were to be repeated over the whole area, then Mead's Analysis would give evidence for clustering at the A size and C sise but not the B size.

(4) Mead's analysis tests only one type of deviation from randomness (unlike binning analysis) which makes interpretation of its results easier.

The main disadvantage of Mead's analysis is the small and discrete number of scales tested - it only tests 6 scales on a 128 x 128 grid.

3.5.2 Modified Mead's Analysis

As experience with Mead's analysis was gained it became obvious that the method of picking out scales of clustering described above would not work in cases where the clustering was, in some sense, strong. In tests on two-dimensional simulations like the one mentioned already (Figure 3.8a) but where the 2-point covariance function was higher (i.e. where the overall density remained the same but the numbers in each cluster were higher) scales lower than the preferred scale were also raised to the 1% significance level in a Mead's analysis. This is an effect of testing for circular clustering with a necessarily square grid. Figures 3.9a and 3.10a show Mead's analysis applied to 3600 points distributed in circular clusters of 16 units as before but now in turn with 10 and 20 points per cluster. The effect on the Mead's analysis is obvious. To resolve this problem and find the most significant scale, the first suggestion was to do the randomisations more times, allowing a finer scale of significant levels. However, computer time limits make this impractical. So an approximation had to be made which turned out to be extremely successful. At scale A the mean of the $T^{(i)}$'s, $T^{mean} = \sum_{i=2}^{100} T^{(i)}/99$ and its standard error $S_A = \left(\frac{1}{99.98} \sum_{i=2}^{100} (T^{(i)} - T^{mean})^2\right)^{\frac{1}{2}}$, were calculated and then the quantity $S = (T^{(1)} - T^{mean})/S_A$ - the number of s.e.'s $T^{(1)}$ lies from T^{mean}. As can be seen from Figures 3.8b, 3.9b and 3.10b, these have a fairly

consistent relationship with the percentage levels. This can also be seen from Figure 3.15 , the Mead's results for 3 actual deep galaxy datasets where the clustering is relatively weak. Here S has been plotted as the ordinate and the consistent percentage levels are the numbers in the brackets beside each point. Knowledge of the effect of "strong clustering" makes the interpretation of the relative heights of the Mead's analysis peaks more important than the quoting of the absolute significance levels. The size of the covariance function at small θ for the Zwicky and Jagellonian catalogues indicates that there the standard error representation will be required to allow interpretation of peaks past the 1% level. The relative heights of the "S" peaks would allow some interpretation of the data to be made even without the three-dimensional simulations with which to compare. With the three-dimensional simulations an unambiguous interpretation of the data is possible.

Figures 3.8b, 3.9b and 3.10b show that although the 2-point covariance functions of these simulations falls from 2 units to 8 units, the Mead's results are lower at the 2 unit scale than at the 8 unit scale. In Figure 3.11 the results of a Mead's analysis on a simulation with 2 different scales is presented (450 clusters of 4 units diameter with 4 points per cluster plus 180 clusters of 16 units diameter with 10 points per cluster). Two peaks can be clearly seen and that the first is much higher than the second is expected due to the increased density in the smaller clusters. That the Mead's analysis of the larger scale is unaffected by the presence of the smaller scale is shown in Figure 3.12 where the simulation consisted of 180 clusters of 16 units diameter with ten points per cluster plus 1800 random points.

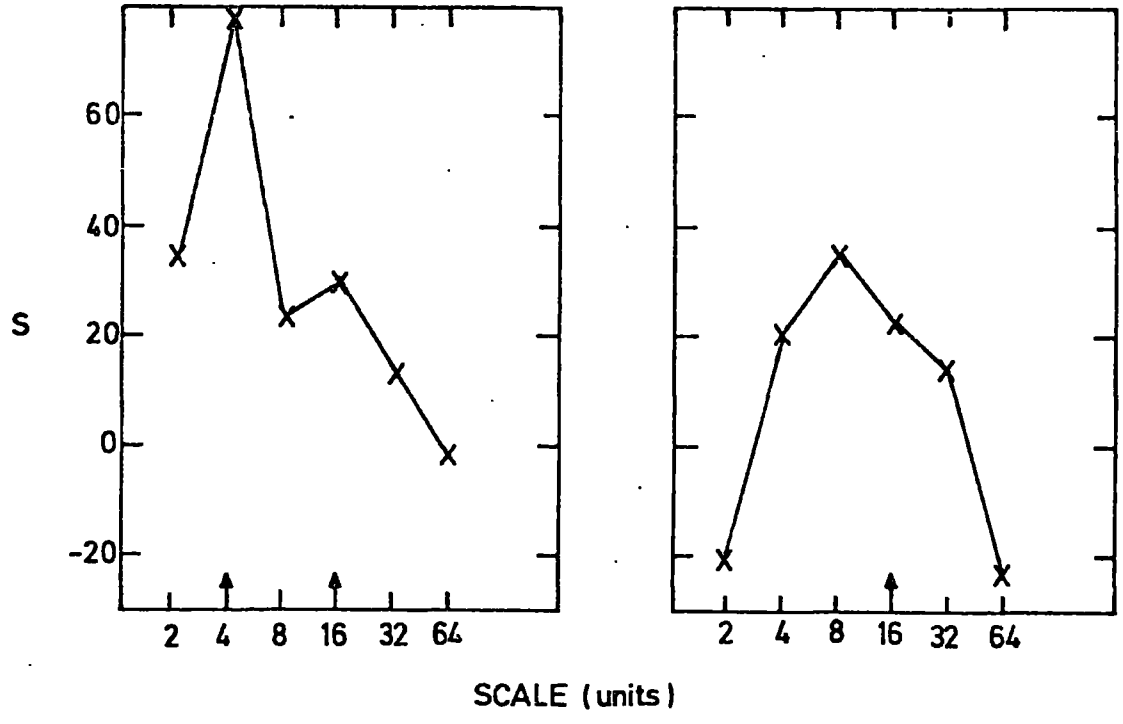

Figure 3.11 As Figure 3.8b for simulation of 180 clusters of 16 units diameter with 10 points per cluster plus 450 clusters of 4 units diameter with 4 points per cluster.

Figure 3.12 As Figure 3.8b for simulation of 180 clusters of 16 units diameter with 10 points per cluster plus 1800 random points.

3.6 COMPARISON OF MEAD'S ANALYSES FOR DATA AND SIMULATION

3.6.1 Zwicky Catalogue

The Zwicky catalogue, of course, lists galaxy positions as spherical coordinates on the sky. It is not possible to do Mead's analysis in spherical coordinates (unlike covariance analysis) so the galaxies had to be projected first, using the usual equal area projection. The large square area in Figure 3.6.a was used for the Mead's analysis (a total of 2670 galaxies). The projection, being an equal area one, will only distort the shapes of density inhomogeneities and not their density contrasts. This should not affect the Mead's analysis too much, certainly not at the most interesting first few scales. Exactly the same procedure and size of area (of similar number density) was used for the Mead's analysis on the simulations. The results are presented in Figure 3.13. The solid line in Figure 3.13a represents the data, the dashed line in Figure 3.13b the average Mead's results for the ensemble of four power-law cluster simulations whose $w(\theta)$'s were presented earlier ($R = 25$ Mpc, $\varepsilon = 2.3$, $n = 525$). The dot-dash line in Figure 3.13c represents the average Mead's result for the four hierarchical simulations (9 levels, $R = 25$ Mpc). As these stand it can be seen that at the second scale ($\theta \sim 1.4^{\circ}$) at least, the hierarchical simulation gives a much higher peak than either the observed data or the power-law simulation (the standard errors are the empirical ones). However, it must be remembered that this hierarchical simulation's $w(\theta)$ showed a drop off at small θ (i.e. there were too few close pairs in the hierarchy) and therefore the Mead point at scale 1 ($\theta \sim 0.7^{\circ}$), high as it is, is artificially too low. So also presented as the dotted line in Figure 3.13c is the result for 10 hierarchical levels in 25 Mpc radius clusters although it is known that this gives a factor of 2 too high a covariance function. The idea here is to show that the result does not only depend on just one

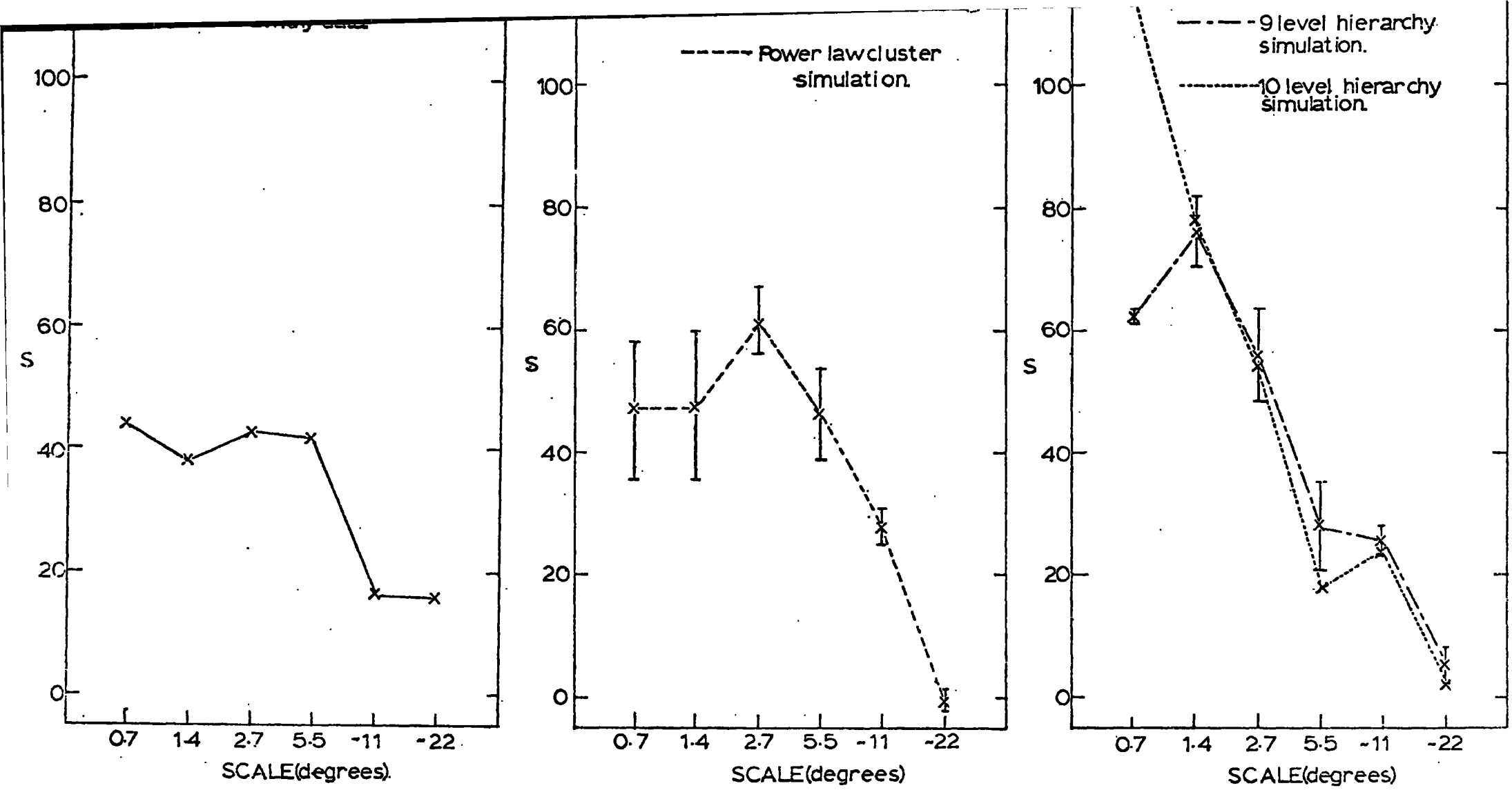

Figure 3.13 (a). Mead's analysis for the projected Zwicky catalogue. (b) Mead's analysis for the ensemble of 4 PLC simulations (R = 25 Mpc, ε = 2.3, n = 525, m_{lim} = 15.0) (c) Mead's analysis for the ensemble of 4 CH simulations (R = 25 Mpc, 9 levels and m_{lim} = 15.0). Empirical standard errors are given.

scale being different from the observed but that the basic shape of the Mead's results for the crude hierarchy is different from the observations. As expected the tenth level makes the first scale join the general trend for the rest of the scales. This trend is definitely downwards unlike the trend for the power-law cluster simulations which is marginally upwards for the first 3 scales and for the data which is basically flat up to the third scale. The Mead's results seem to give decisively different results for the crude hierarchy compared to the data. The results for the power-law cluster simulations while giving an unobserved peak at scale 3 ($\theta \sim 2.7^{\circ}$) seems to represent the data much better. Note also that the Mead's results for the data begin to drop off at scale 4 ($\theta \sim 5.5^{\circ}$) roughly corroborating the break in $w(\theta)$ at about 6°.

3.6.2 Jagellonian Catalogue

Mead's analysis was also carried out on the Jagellonian catalogue. This was a more straightforward exercise than for Zwicky - the galaxy positions here are recorded as (x,y) counts on a $6^{\circ} \times 6^{\circ}$ area and no equal area projection is needed. The catalogue comes as 96 x 96 counts in 3.75' x 3.75' cells. For the purposes of the Mead's analysis the area was divided up into one 64 x 64 area and five 32 x 32 areas and the Mead's statistics were totalled up to the fifth level. The Mead's analysis results for the distribution are presented as the solid line in Figure 3.14. Also presented are the results of a Mead's analysis for a power-law cluster simulation carried out on a $6^{\circ} \times 6^{\circ}$ square area using exactly the same method, luminosity function etc., as for the 15^{m} limited Zwicky simulation. m_{lim} was taken to be 20^{m} after Phillipps et al (1978) and the number density to be 330 galaxies/sq. degree to match the observed. This simulation with the usual cluster radius of 25 Mpc, $\varepsilon = 2.3$ and $n = 525$ gave a -0.75 power-law in $w(\theta)$ with approximately the same amplitude as observed. The

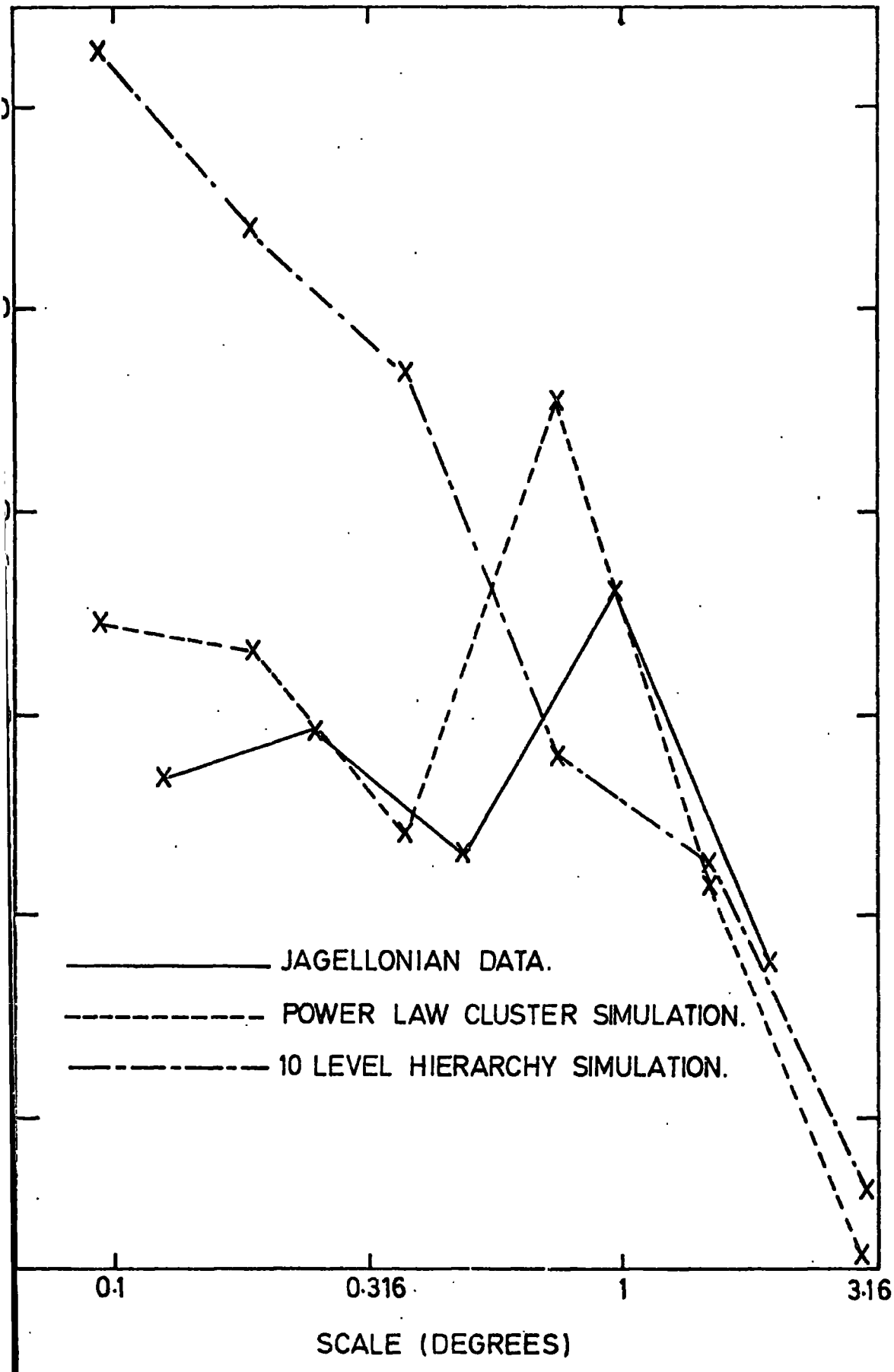

Figure 3.14 Mead's analysis for the Jagellonian catalogue, for a power law cluster simulation (R = 25 Mpc, ϵ = 2.3, n = 525, m_{lim} = 20.0) and a hierarchical simulation (R = 25 Mpc, 10 levels and m_{lim} = 20.0).

agreement between the model Mead's results and the data results is good. The preferred scale on both is at the same place as the drop-off from their respective power-law $w(\theta)$'s ($\sim 1^{\circ}$). The simulation shows the danger there would be in interpreting these peaks and drop-offs in terms of maximum correlation lengths. Both the simulation and the data show a Mead's analysis peak in the region of 10 Mpc (using a typical angular diameter distance D^{*}_{A} = 800 Mpc with this luminosity function). But we know that in the simulation at least the maximum correlation length is 5 x this. The Mead's peak (and the $w(\theta)$ break) only corresponds to the diameter outside which the cluster density contrast, at D^{*}_{A}, is too small to be picked up by the statistics. The important point is not the size of the preferred scale but the shape of the Mead's results. A suggested reason for the more pronounced peak produced by the Jagellonian data than by the Zwicky data is that it is a limiting magnitude effect. As the limiting magnitude increases not only does the sample go deeper but it also goes fainter. Thus at D^{*}_{A} a cluster core might be better defined by inclusion of fainter members than in the Zwicky catalogue. A justification for this is that the power-law cluster simulation shows the same effect.

However, the major result again comes from the comparison with a crude hierarchical simulation. This simulation's Mead's analysis is shown by the dot-dash line in Figure 3.14. Again there was trouble with the 9-level hierarchy because of its $w(\theta)$ drop off at small θ - this time only a -0.5 power-law $w(\theta)$ came through the projection instead of the -0.75 that might be expected with the hierarchy's 1.76 "thinning factor". This is in accordance with the work of Dautcourt (1977) who predicts this as the effect on $w(\theta)$ of a drop-off in $\xi(r)$ - the 3-D equivalent of $w(\theta)$ - at small r. The 10-level hierarchy upon which the results in Figure 3.14 are based gave a -0.7 power-law but gave an amplitude of $w(\theta)$ two times as high

as the actual Jagellonian data. So care must be taken when comparing these Mead's results with the other two. Even with this proviso, the hierarchy's Mead's results again seems to have a completely different shape from the data and the power-law cluster Mead's analyses. On the basis of both Figure 3.14 and Figure 3.13 it can be firmly said that the power-law cluster model is more consistent with the data than the hierarchical model.

3.6.3 Deep Data

Mead's analysis was also carried out on even deeper data samples than the Jagellonian field. In Figure 3.15 are shown the Mead's results for the field of Dodd et al (1976) (dashed line), and for the field of Ellis et al (1977) measured by COSMOS from J and R Schmidt plates. Both Dodd's and Ellis' fields measure approximately 2 sq. degrees with roughly 4000 galaxies identified on each. No simulations were carried out at these depths because these are not magnitude limited samples. These samples can roughly be compared, though, to samples limited at around 21-22 J magnitudes (see Ellis et al, 1977). The basic shape of the earlier Mead's results is again observed - the highest peak for all the samples occurs not at the first couple of scales where Phillipps et al (1978) showed that $w(\theta)$ is high but at a third scale ($\sim$ 0.1°) where $w(\theta)$ is lower. The reason for the later highly significant Mead's results at scales 5 and 6 (0.36° and 0.72° respectively) on the J149 area is the known large scale inhomogeneity in the galaxy counts on this plate due to variations in its photographic emulsion (see Phillipps et al,1978). To a lesser extent inhomogeneities are also visible on the R field and the Dodd field. Roughly, the Mead preferred scale and the $w(\theta)$ break point convert to approximately 2 Mpc (with $D^{*}_{A} \sim$ 1200 Mpc). However, as in section 3.6, 2 Mpc is a maximum clustering contrast length not a maximum possible correlation

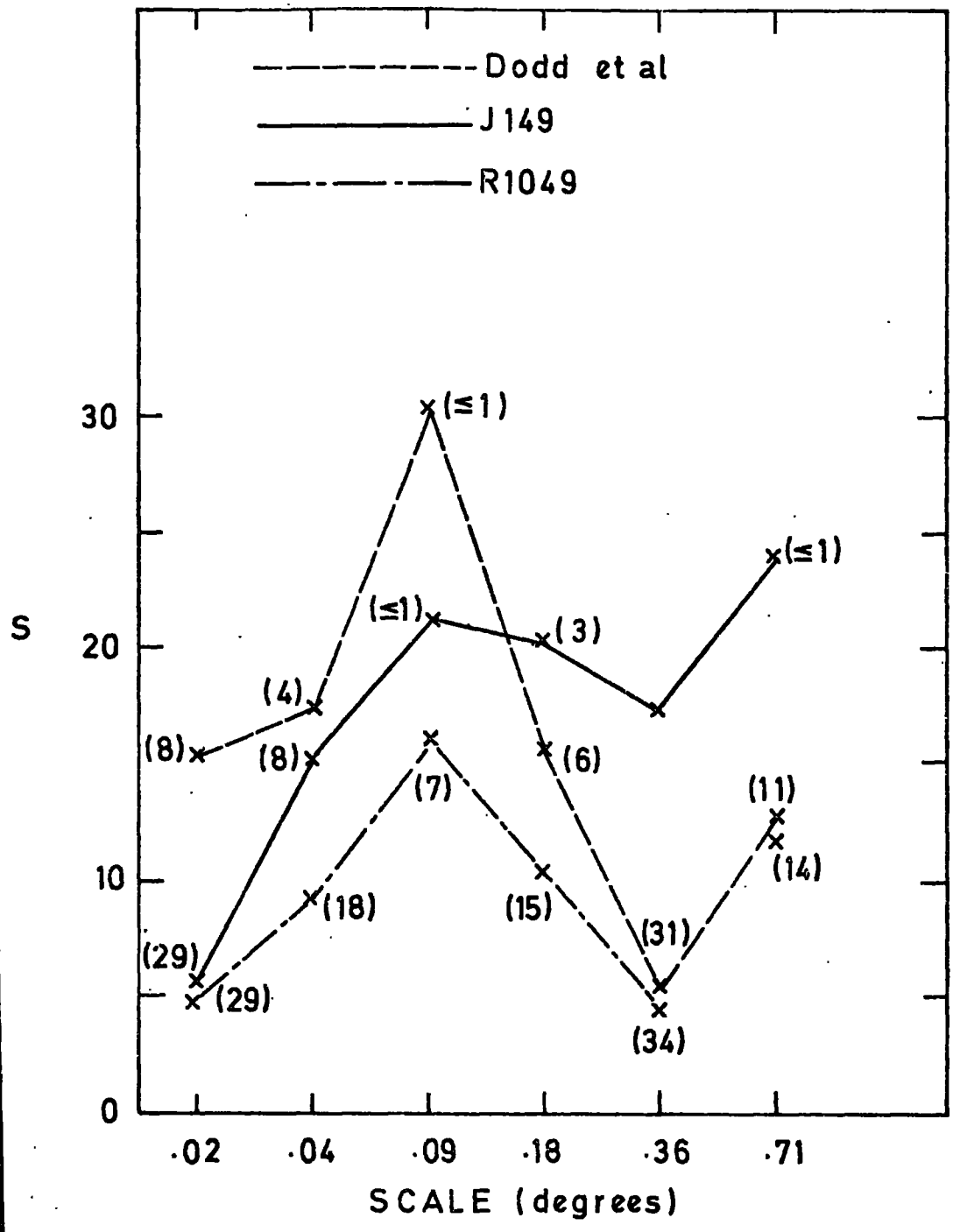

Figure 3.15 Mead's analysis for the area in J and R of Ellis, et al , (1977) and for the data of Dodd et al. (1976). The percentage levels that correspond to the S values are given as the numbers in brackets.

length - at these depths only the very core of a cluster will stand out against the background of galaxies from even more distant clusters. The shape of the Mead's results is again the important point - their behaviour resembles that now expected from galaxies distributed in power-law clusters rather than in a crude hierarchy. This indicates that the results found in the last section are reproducible from datasets independent of the Jagellonian catalogue.

3.7 MEAD'S ANALYSIS ON N-BODY SIMULATIONS

A major experimental boost for isothermal perturbation theory is the result that in N-body numerical experiments starting from a random galaxy distribution $\xi(r)$ can be interpreted as a -1.9 power-law, (Aarseth, Gott and Turner, 1979 Efstathiou, 1979, Fall, 1978) which roughly agrees with the observed $w(\theta)$. The hierarchical model is supposed to approximate the distribution of galaxies that results from a Hubble expansion with gravity acting i.e. the distribution expected from a perfect N-body simulation. It was of interest, therefore, to find out the results of applying Mead's analysis to the projected distribution from an N-body run. These results, from a simulated universe of 1000 bodies with $\Omega = 1$ at an expansion factor of 2 (dashed line) and 12 (solid line) are shown in Figure 3.16. The scales are given as fractions of the radius, R, of the N-body sphere. The area the Mead's analysis was carried out on was a square inside with the N-body sphere fitted and onto which the mass points from the simulations were projected. This differs from the projected Zwicky catalogue in that no luminosity function was involved in the projection. So detailed comparisons with the Zwicky catalogue Mead's analysis would be invalid. However, the shape of the Mead's results, particularly in the case of the expansion factor of 12, is highly suggestive of a hierarchical distribution in the light of section 5's results.

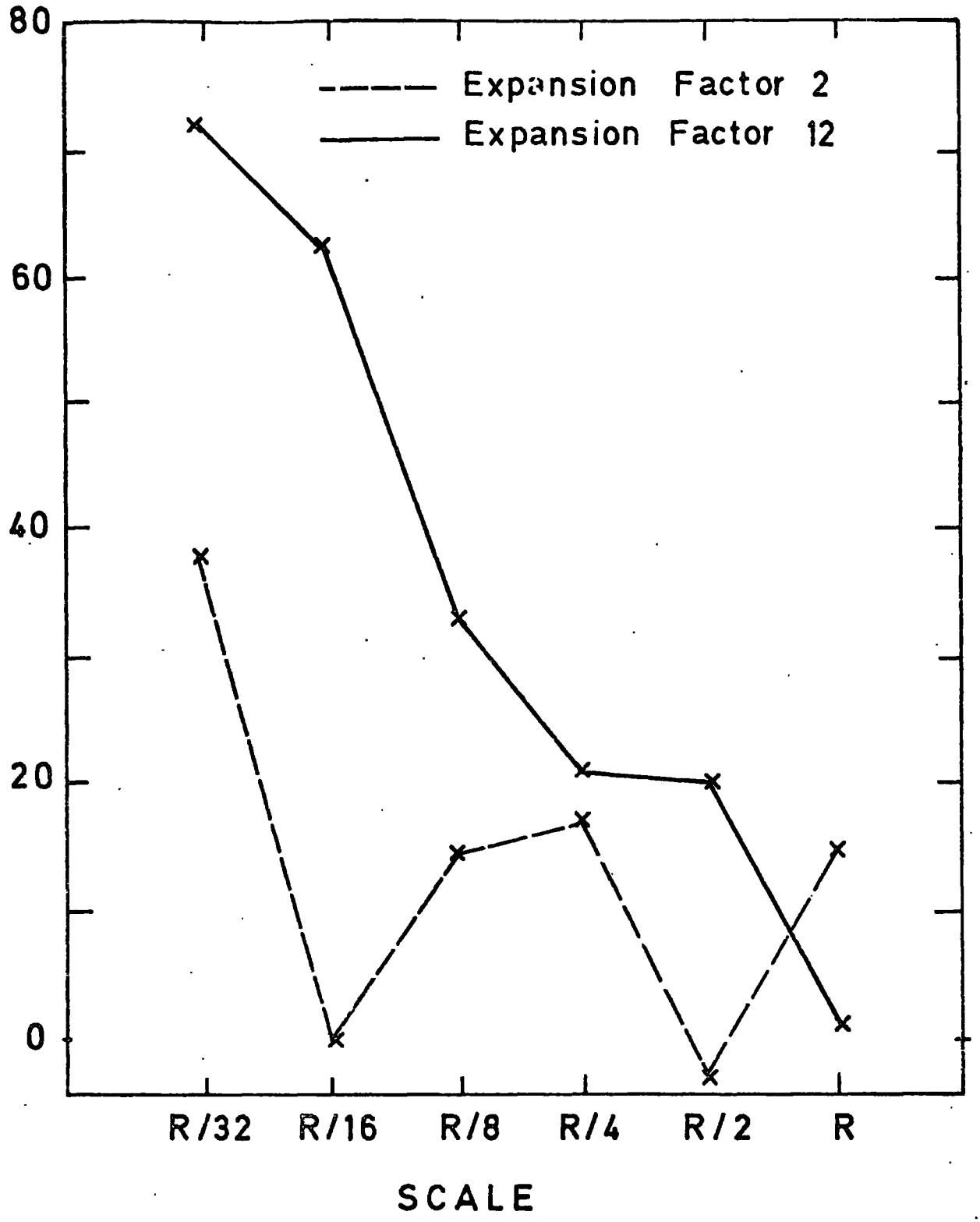

Figure 3.16 Mead's analysis for the N-body simulations in an $\Omega = 1.0$ universe at expansion factors of 2 and 12. The scales are given as fractions of the radius, R, of the N-body sphere.

This indicates that the hierarchical model may be a very good approximation to the distribution arising from the N-body experiments. However, there is a question-mark over the relationship between these experiments and the process which gave rise to the actual distribution of galaxies. Any reformulation of the crude hierarchical model that results in eliminating its inconsistent Mead's analysis behaviour has also to come up with an answer as to how the new hierarchical model relates to the N-body simulations.

3.8 CONCLUSIONS

It has been demonstrated that neither correlation functions nor the multiplicity function can very powerfully discriminate between the hierarchical model and the simple power-law cluster model. Since the latter model has a definite preferred scale of clustering this shows that the usually quoted evidence for a continuous pattern of galaxy clustering (and thus for the isothermal theory of galaxy formation) is less strong than previously thought. The new statistical analysis, Mead's analysis of galaxy catalogues points strongly away from the hierarchical model and, tentatively, towards the power-law cluster model. N-body simulations suggest that the hierarchical model can approximate well the behaviour of initially random points clustering under gravity. However, Mead's analyses on the observations indicate that some process other than gravity alone could be a major factor in producing galaxy clusters. It will be interesting to see how more sophisticated versions of the hierarchical model stand up to Mead's analyses of the data and N-body simulations. If another version of the "continuous clustering" model cannot be found that resolves these problems then the consequences for isothermal theory may be serious.

On the other hand, the possibility of interpreting the 2-point covariance function's feature and the behaviour of Mead's statistic at small angle as evidence for a preferred scale of galaxy clustering is encouraging for proponents of the adiabatic theory of galaxy formation. A problem raised for the theory by this interpretation is that the large size of the preferred scale may make it difficult to understand how galaxies could have formed in the way the theory suggests (Fall and Bonnometto, in preparation). However, we shall see in Chapter 6 that correlation analyses of the deep samples indicate a preferred scale of smaller size, which may solve this problem.

An interesting further project will be to apply Mead's analysis technique to the Abell cluster catalogue. In a similar manner to the above, it could thus be investigated whether clusters are distributed hierarchically or not. If it so happened that they were, then this would indicate that a different process (most probably the isothermal mechanism) formed clusters of clusters than formed clusters of galaxies. This would be taken as further evidence for the adiabatic theory.

CHAPTER FOUR

PRODUCING GALAXY CATALOGUES USING U.K. SCHMIDT PLATES AND COSMOS

4.1 INTRODUCTION

In the future many galaxy catalogues will be produced by automated plate measuring machines. Examples of such machines already in existence are the COSMOS machine at the Royal Observatory, Edinburgh and A.P.M. at the Institute of Astronomy, Cambridge. In the detection and measurement of faint images on photographic plates these machines have the important advantages of being quicker and more objective than even the most highly skilled human eye. However, as we shall see, the machine production of galaxy catalogues raises its own problems and these have to be understood and overcome before any meaningful astronomical interpreation of the data can be made. In this chapter there will be described the data reduction techniques developed to produce galaxy catalogues from COSMOS measurements. Particular reference will be made to the techniques required to produce consistent samples from large areas of wide field photographs. These techniques were developed in the course of obtaining galaxy catalogues in two colours from U.K. Schmidt plates of the S.G.P. field. The results of statistical analyses of these new catalogues will be described in Chapters 5 and 6.

4.2 PHOTOGRAPHIC MATERIAL

The basic photographic material for our investigations here are five wide-field plates taken with the U.K. Schmidt Telescope at Siding Springs. Table 4.1 gives full details of these plates and Figure 4.1 shows a map of the S.G.P. field. Some of these plates form part of the S.R.C. "J" survey of the southern hemisphere. The S.G.P. was the field

TABLE 4.1

Photographic Material

Field	RA	Dec	UKST No	Date	Exposure
SGP	$0^h\ 53^m$	$-28^\circ\ 03$	J 3721	Nov. 4 1977	80 min
			R 2775	Dec. 19 1976	90 min
SRC 412	01^h09^m	$-30^\circ\ 00$	J 1920	Nov. 25 1975	60 min
			R 3780	Dec. 4 1977	90 min
SRC 475	01^h06^m	$-25^\circ\ 00$	J 1916	Nov. 25 1975	60 min

Notes: J = Kodak IIIa - J plus Schott GG 395

R = Kodak IIIa - F plus Schott RG 630

(in Paper I the Kodak 098 emulsion was used)

Co-ordinates are plate centres for 1950.0 epoch.

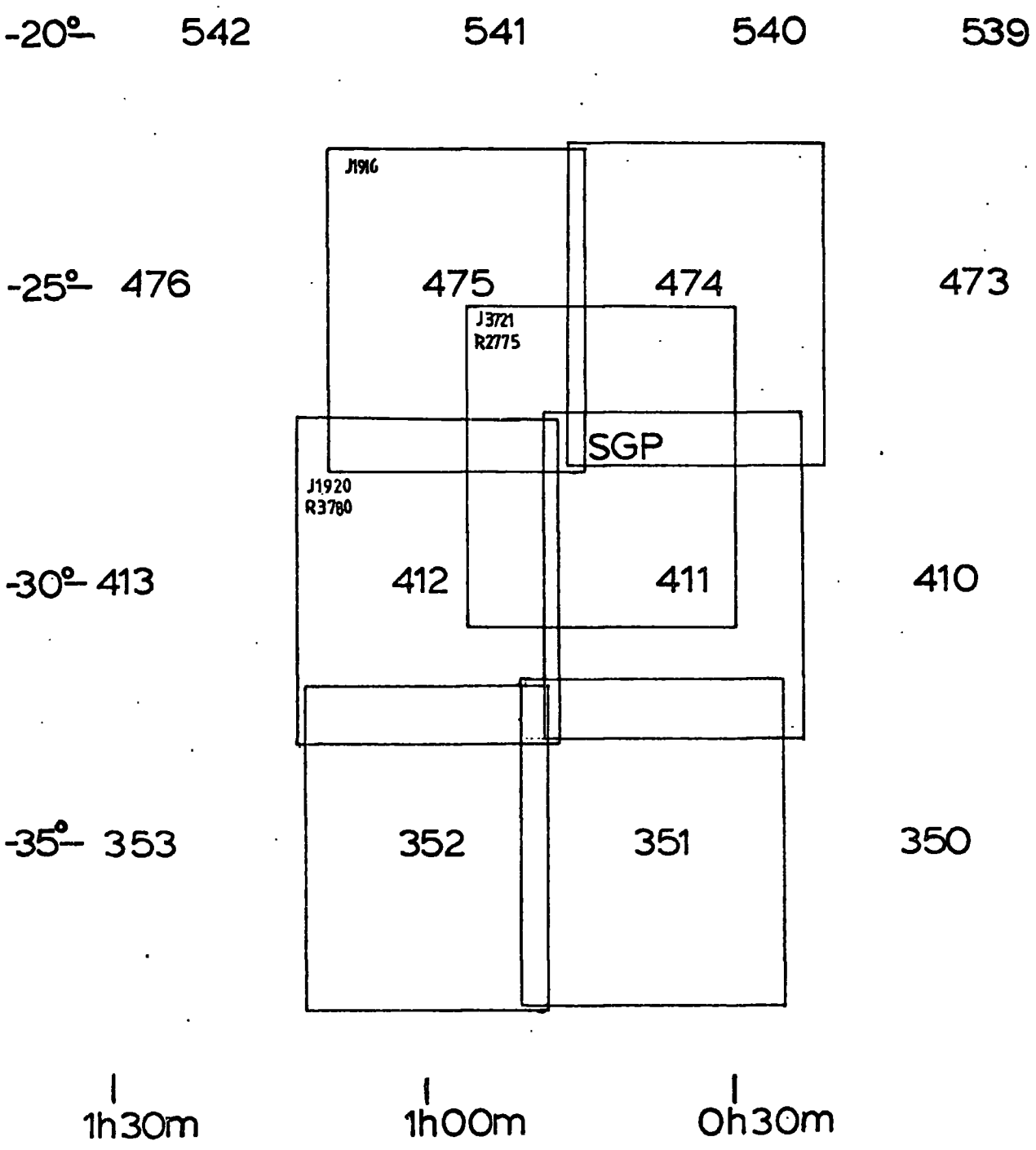

Figure 4.1 Map showing $6^{\circ}x6^{\circ}$ SRC fields in the immediate vicinity of the South Galactic Pole (SGP). SRC field numbers are given. The numbers of the UKST plates used here are also shown in the appropriate field.

chosen for these analyses because it was hoped that obscuration effects caused by our own galaxy might be less likely to occur there. All the plates chosen for analysis were of high quality (taken in good seeing conditions) and only the central unvignetted portions of the plates were used in the analysis.

4.3 THE COSMOS MACHINE

4.3.1 Description

COSMOS (CO-ordinates, Sizes,Magnitudes, Orientations and Shapes) is basically a fast, raster scanning microdensitometer with computing facilities and software which allow on-line data processing. Full details of the machine's hardware are given in Pratt (1977) and only a brief description of the relevant points is given here. The machine is designed to work in one of three modes - Mapping Mode (MM) which outputs pixel transmissions over an area with no on-line reduction ; Coarse Mode (CM) which outputs fully on-line reduced data giving the positions of images above a certain isophote plus some 8 other parameters ; and Fine Mode (FM) which gives on-line reduction over small areas with many more parameters per image than CM. Data used here will derive mainly from COSMOS's CM output. However, data has also been obtained from MM and reduced using alternative off-line software (McGillivray and Dodd, 1979) to provide consistency checks on results obtained using CM.

In both CM and MM COSMOS measures in steps across a 1024 μm "lane" down which the machine raster scans before starting the next "lane". The size of these steps determines the COSMOS pixel size. For CM runs the step was taken to be 8 μm but for MM runs it was constrained to be at least 16 μm because of the amount of output which would otherwise be involved.

COSMOS measures at each step in CM and MM using a cathode ray tube whose "spot" has an effective width of 32 μm. This measures light

transmitted through the plate on a transmission scale quantised into 128 levels. This transmission scale, on any particular run, may be converted into relative intensity units via the "characteristic curve" obtained from the "wedge" provided on most astronomical photographs. This provides the meachine with a relative photometric scale. In this way the machine photometrically measures each pixel of the area to be scanned. The machine's speed is such that it is capable of doing 10^8 such measurements per hour.

4.3.2 Primary Data Reduction

This stage of the data reduction may be split into two equally important parts - consistent image detection (or definition) and then the measurement of the selected images (see also Kron 1978). The major part of the primary reduction procedures was done using packages developed by the COSMOS team at the Royal Observatory, Edinburgh. Since much depends on the efficiency of these packages a description of them will be given now.

First of all the reduction procedures changed between the first COSMOS CM runs (e.g. the runs used by Ellis et al (1977)) and the CM runs used here. Improvements have been made, mainly in the background following routines, to enable much larger areas to be consistently scanned. These larger areas were found to be necessary to ensure that the catalogues of faint images obtained are representative samples and therefore suitable for statistical analysis.

The problem with this new requirement is that over large areas of a single Schmidt plate, the "sky" brightness varies considerably. These variations are mainly due to unevenness in the sensitivity of the plate emulsion but they can also be caused by "real" sky variations due to the presence of interstellar or intergalactic clouds. By choosing the areas

for study away from the galactic plane, at the SGP, it is hoped to minimise the latter effect (but see Chapter 6). However, to obtain consistent brightness measurements of two truly similar objects from two areas of plate that have different emulsion sensitivities, a procedure equivalent to background subtraction is required.

Of course, this background subtraction (or background following) cannot be left just to the later measurement/photometry stage. It must enter into the image detection stage as well. If the only pixels considered as possible candidates for photometry as images were those above some fixed isophote, this would bias the numbers and brightnesses of images detected towards the more sensitive areas of the plate. A badly inconsistent image detection stage cannot be righted by even the most sophisticated subsequent measurement procedure. With COSMOS CM the background subtraction was therefore done on-line. This also has the advantage that "noise" pixels which fall below the detection threshold can be rejected quickly thus reducing data handling problems.

The background subtraction algorithm is based on the assumptions that :-

(a) All observed sky variations are caused by variations in emulsion sensitivity.

(b) This sensitivity depends only on the emulsion thickness at a particular point.

(c) Whatever the thickness of the emulsion, its characteristic curve remains constant.

Thus it can be shown that for 2 truly similar objects in 2 separate areas of plate.

$$I_1^C = I_2^C \times I_1^{Sky} \; / \; I_2^{Sky} \qquad (4.1)$$

where I_1^C , I_2^C are the central intensities of images 1 and 2 and I_1^{Sky}, I_2^{Sky}

are the average background intensities around these images.

Similar equations hold for other "truly" comparable isophotes. We are interested here in setting consistently a local threshold intensity level above which pixels are to be regarded as signal and below which pixels are to be regarded as noise. This "threshold cut" must therefore be set always at the same true isophote independent of variations in the photographic emulsion thickness. From (1) this isophote I^{th} is given by

$$I_1^{th} = I_1^{Sky} (1 + f) \qquad (4.2)$$

where f is a constant fraction. Here the threshold intensity is said to be f x 100 % of sky.

To obtain I^{Sky} the frequency histogram of pixel transmission across every raster of each lane is obtained. The median value of this distribution is found. These values are smoothed in 1024 μm x 1024 μm bins and a low order polynomial fitted down each lane. The fitted value of T at a particular bin is then defined as the sky background transmission level for that bin. This is converted to intensity units, I_{sky}, via the characteristic curve, $I_{thresh} = (1 + f) I_{Sky}$ calculated and I_{thresh} converted back to transmission units, T_{thresh}. The lane is then remeasured and only pixels with transmission lower than T_{thresh} are taken as signal. Figure 4.2 shows the sky background contour map obtained for the plate J3721.

COSMOS then on-line (in CM) pattern analyses each pixel into its parent image. To ease data handling problems images which then have less than 10 pixels are rejected. From eyeball comparisons the pattern analysis has been seen to be working well for all images except for very bright stellar images which it tended to break up into many smaller images (see Figure 4.3). The area around such images has to be drilled out as "holes".

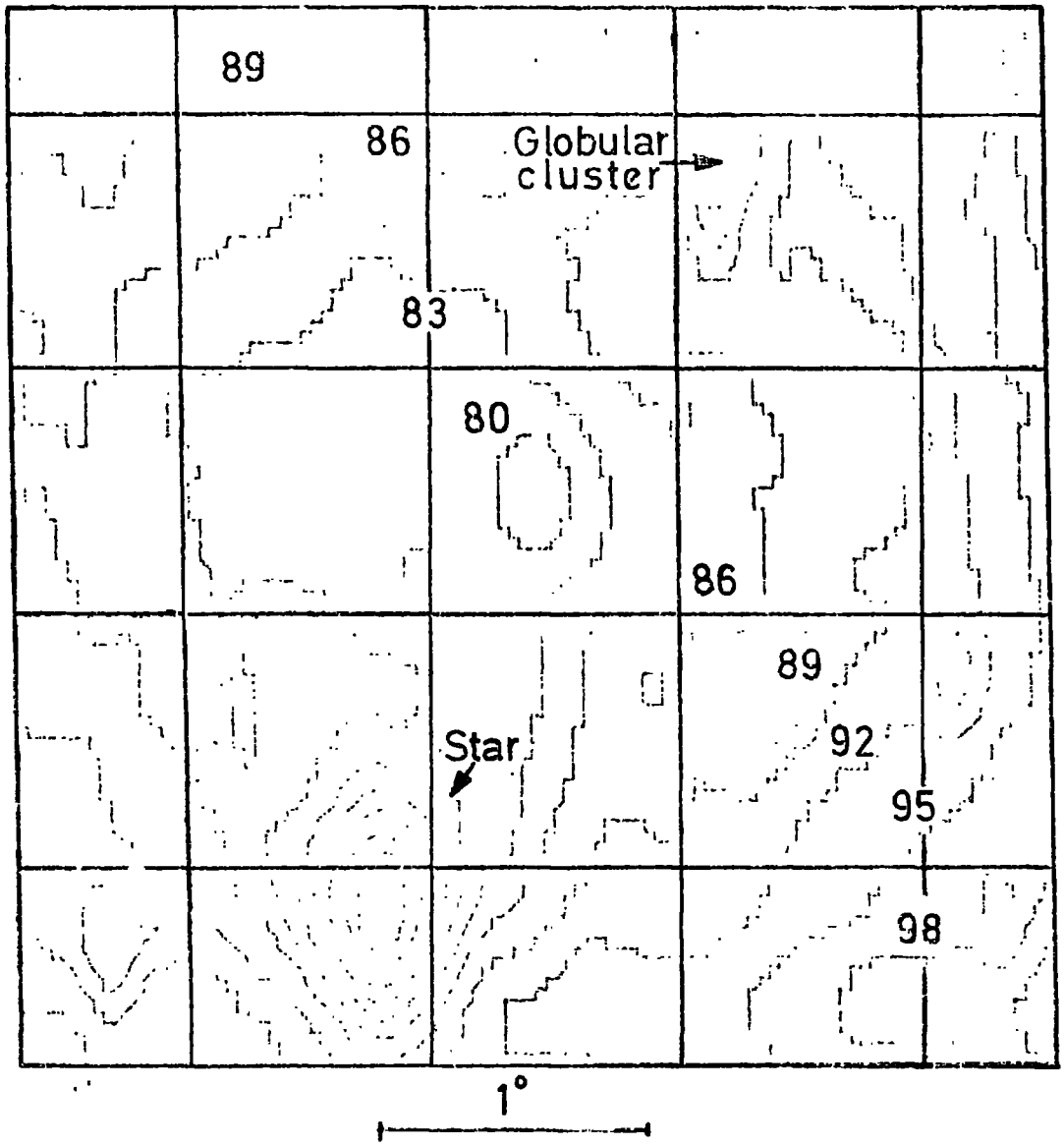

Figure 4.2 Sky background brightness map as outputted for plate J3721 by COSMOS. The contours represent areas of constant background transmission. The variations are thought to be mainly due to differences in emulsion thickness.

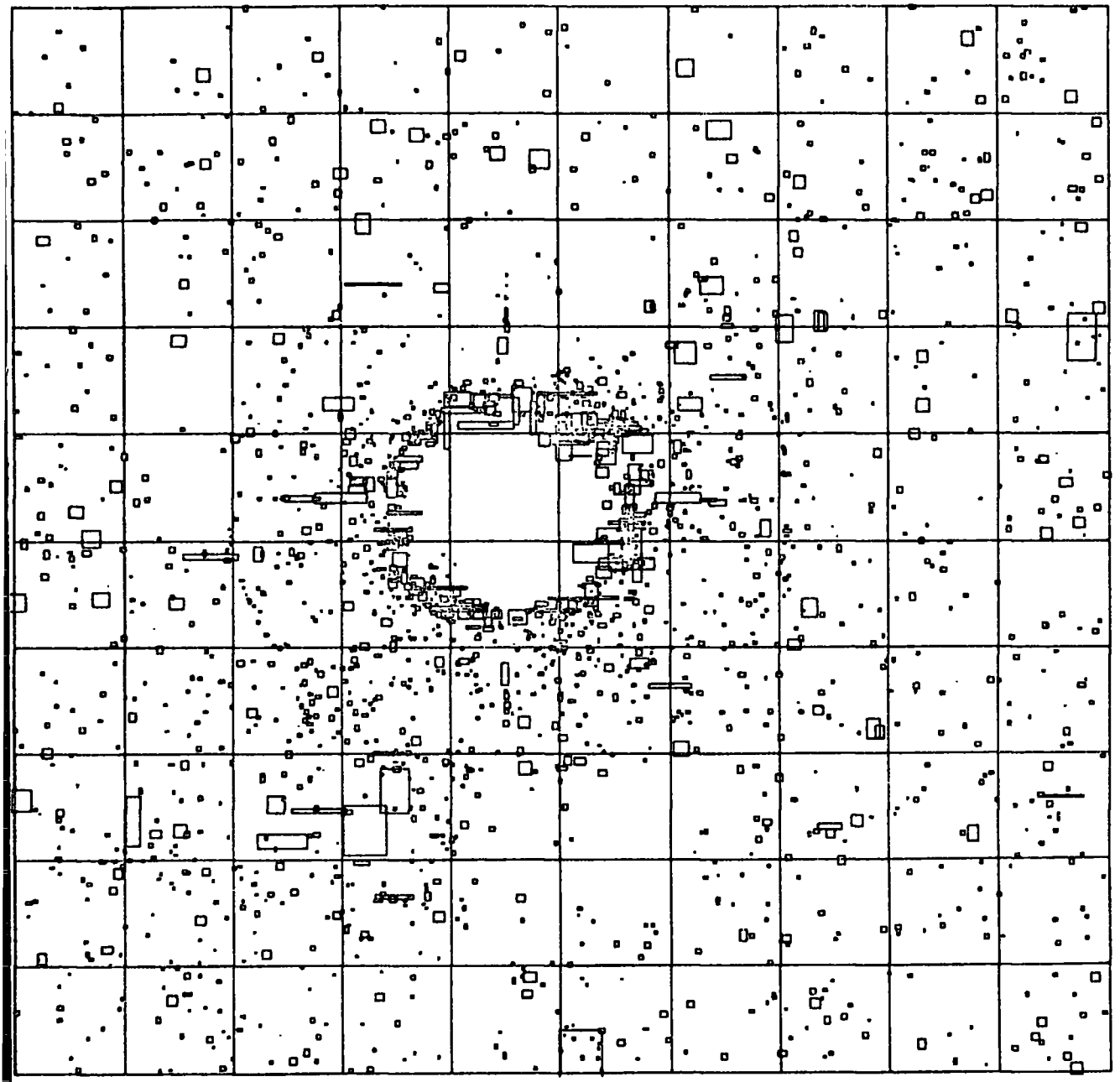

Figure 4.3 Large images are broken up by the COSMOS pattern analyser. Therefore areas such as that shown here have to be removed (or "drilled") from the COSMOS datasets (see Figure 4.10). These "holes" are ignored in the subsequent statistical analyses.

Details of these holes are given for each plate in Table 4.2

Unfortunately, no indications are given by the COSMOS pattern analyser of the probability that a particular image is a merged image. However, at the threshold cuts we are using here loss of images due to merging is not expected to be a serious problem.

For each image the required parameters can now be measured and recorded on magnetic tape. The parameters measured in CM are given in Table 4.3. No more sophisticated photometric procedures were used in this measurement stage than were used in the detection stage. It will be seen that this accuracy of measurement is adequate for our purposes here.

4.4 OBTAINING RELATIVE MAGNITUDES FROM COSMOS CM DATA

It can be seen from Table 4.3 that for CM runs the integrated pixel intensity, Σ_I, was not outputted as an image parameter. This was because the hardwiring of the machine CM software was too inflexible to allow its computation. This inflexibility was one of the reasons why Ellis et al resorted to selecting their galaxy samples on the basis of isophotal image angular diameter, d, which can be computed from the outputted parameters, instead of selecting by brightness. However, it is more desirable to select on the basis of integrated pixel intensity, Σ_I, and the reason for this is because the errors on Σ_I are less than those on d. This can be clearly seen by considering the errors in A, the total number of pixels above threshold for a particular image. For a circular image with a centrally peaked profile the major contribution to A will be from pixels whose intensities are very close to the threshold value. Because sky has random noise imposed on it and because machine measurement is imperfect and subject to error, these pixels are the ones with which it can be said with least certainty that they truly lie above the threshold isophote. Indeed assuming $\sqrt{A}$ as an estimate of the standard error in A

TABLE 4.2

The Data

Plate No.	Sky Brightness (mag.arcsec^{-2})	Threshold (% sky)	Threshold (mag.arcsec^{-2})	Area Scanned (deg^2)	Area Drilled (deg^2)	Number Galaxies (deg^{-2})	Density Stars (deg^{-2})
J 3721	23.0	9	25.7	14.25	1.07	1311	1463
R 2775	21.75	7	24.6	14.15	1.14	1105	999
J 1920	22.5	7	25.4	14.88	0.44	1553	1338
R 3780	21.75	7	24.6	13.61	1.63	1361	1016
J 1916	22.5	7	25.4	13.35	1.97	1571	1592

Notes : The threshold values are based on COSMOS measurements of the North calibration wedges on UKST plates.

The number densities refer to limiting magnitudes J = 21.5 and R = 19.75.

The area drilled refers to portions of the data removed because of detection problems around bright stars.

TABLE 4.3

COSMOS IMAGE PARAMETERS

1. X - coordinate of image centroid.
2. Y - coordinate of image centroid.
3. Maximum X coordinate of image.
4. Minimum X coordinate of image.
5. Maximum Y coordinate of image.
6. Minimum Y coordinate of image.
7. Area.
8. Minimum Transmission of Image.
9. Local Threshold Transmission.
10. Code relating to orientation of image.

All coordinates measured in units of $\frac{1}{10}$'s of microns.

Area is quantised in 8 μm x 8 μm pixels.

Transmissions are digitised into 127 levels (0 → 127).

it can be seen that when A is small the fractional error in A can be very large indeed. These arguments apply with even greater force to the measurement of the angular diameter, d.

On the other hand with Σ_I the pixels near the threshold are weighted less and the central, high intensity pixels weighted more. The latter are less subject to fluctuations because they lie higher above the sky noise. Thus if Σ_I were available it would be possible to right some of these errors made in the detection procedure by doing a secondary selection within the detected images based on rejecting images whose Σ_I's were too faint.

Although Σ_I was not available, a method was devised to obtain image magnitudes from the COSMOS CM data parameters. The errors on this estimated magnitude were greater than on Σ_I but less than on A or d.

The method involved using M.M. to first find the areal intensity profile of a number of CM measured images. Six such profiles are shown in Figure 4.4. Also shown are the Gaussians

$$I(r) = I_o e^{-r^2/\alpha^2} \qquad (4.3)$$

which pass through the central intensity $I_o(r = 0)$ and the threshold intensity I_{th} $(r = a)$. These Gaussians give reasonably good fits to the MM profiles and therefore by integrating under this profile relative magnitudes can be obtained for all images. Indeed the magnitudes obtained were technically total magnitudes since the integration was done to infinity but in practice the difference between total and isophotal magnitudes is found to be small at the threshold cuts of sky used here. The smaller errors on the magnitude, m, then, say, on area A, arise because the weighting has been taken, to some extent, away from peripheral pixels

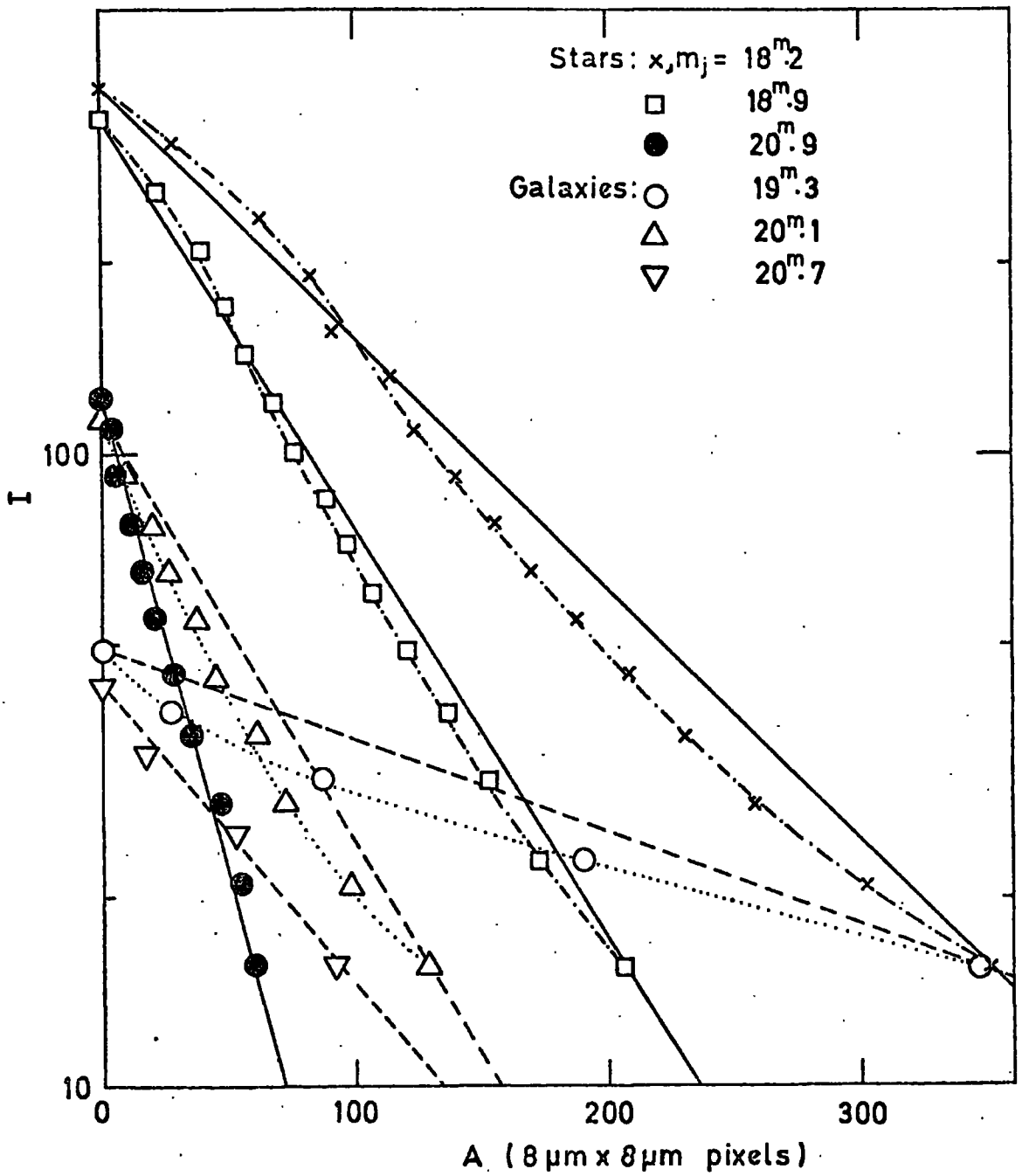

Figure 4.4 Profiles from COSMOS MM data of images on plate J1920 in terms of intensity, I (arbitrary units), as a function of area A. Straight lines are Gaussian fits to the central intensity and area at threshold. The isophotal magnitudes, obtained by pixel addition, differ from the Gaussian fitted isophotal magnitudes by only $0^m.01$ for the $18^m.2$ star and $0^m.14$ for the $19^m.3$ galaxy. As total magnitudes are used in the analysis, this difference is lessened by the obvious tendency of the Gaussian fit to underestimate the amount of light in the wings below the threshold.

towards the central pixel and its transmission, T_{min}. The error in T_{min} is small because it lies high above sky noise and it is constrained in one direction because it is a minimum value. Of course, the errors are still higher than if Σ_I were available. However, we are still able to make a secondary selection of objects by estimated brightness to improve the selection accuracy of our samples.

Also to improve the photometry low percentage threshold cuts of sky were used (see Table 4.2). This meant that a larger number of pixels were measured per image thus reducing errors. In the secondary selection procedure care was taken to define our sample limits sufficiently bright so that not more than a few percent of images had less than 50 measured pixels. This also was done to reduce photometry errors.

We used the small overlap area between plates J3721 and J1920 to compare magnitudes obtained using the above techniques for images detected on both plates. The standard error on our magnitudes was found to become slightly worse as the images reached fainter limits. Averaging these errors over magnitude bins (weighting towards those bins with more images) gave an estimate of the average standard error in our samples to be $\pm 0.25^m$.

This error estimate, of course, represents only random error. It will be argued in Section 4.5 that comparison of COSMOS and standard photometry shows systematic COSMOS photometric errors only affect bright stellar images. Efforts are being made to confirm this result by comparing faint COSMOS galaxy magnitudes with more accurate PDS magnitudes.

This detection procedure as described above should be consistent in each part of the plate with the only effect of this residual photometric error being towards including more truly faint objects everywhere. This small bias will not affect the angular homogeneity of detection and thus will not restrict the statistical analyses of galaxy distribution used in Chapter 6.

4.5 ABSOLUTE CALIBRATION OF COSMOS MAGNITUDES

The relative magnitudes obtained above have now to be calibrated on an absolute scale. There existed 2 possible sources of calibration - the U.K.S.T. night sky photometer-readings on the night each plate was taken and stellar and galaxy photometry already available on these fields. Unfortunately, the UKST night sky photometer is immoveable and takes simultaneous readings at the South Celestial Pole introducing an unknown correction when transferring to the field concerned. We also have evidence for substantial variations in the night sky brightness at Siding Spring over the 2 year period between the taking of plates J1916/1920 and that of plate J3721 ; small overlap regions show the sky for plates J1916/1920 to be $0^{m}.5$ brighter than that for J3721. This makes it impossible to use any subsequent photometry of the sky brightness in these regions.

Certain deficiencies in COSMOS photometry at bright light levels also put restrictions on how this calibration can be done using stellar sequences. Firstly, the COSMOS photomultiplier has a poor dynamic range. This means that a bright measured transmission will generally correspond to a wide range in intensity. The resulting inaccuracy is worsened due to large quantisation errors in the transmission due to their being digitised.

Secondly, the COSMOS photomultiplier "spot" has a wide $\frac{1}{2}$ width of 32 μm. This means that when stepping with an 8 μm increment COSMOS measurements smooth over a large number of 8 μm pixel elements. This has the effect of smoothing many noisy pixel intensities which would have to be smoothed anyway. However, by smoothing in this way, COSMOS is averaging in transmission and therefore is smoothing non-linearly in intensity. This approximation does not matter for faint intensities where the relationships with transmission is almost linear anyway but it

will be important for bright stars.

Thirdly, the COSMOS spot also has a "halo" which extends for perhaps 200 μm in radius. This exists because the speed of COSMOS' scan makes it impossible to use "stops" to cut down this halo's size. Again this halo makes COSMOS transmission measurements underestimate true values and makes the photometry of bright, sharply profiled,objects even less reliable. For faint images, however, this error becomes less and less important.

These problems mean a substantial scale error exists in COSMOS magnitudes for brighter images and therefore only faint stellar sequences can be used to calibrate COSMOS readings. Unfortunately, reliable faint sequences are at present rare in the Southern Hemisphere. We have used an unpublished electronographic sequence from Dr. M.R.S. Hawkins (Royal Observatory, Edinburgh) and one unpublished Racine prism sequence from Dr. J Graham (Cerro Tololo).

Each of these sequences has its own possible scale errors. There was known to be problems with non-linear response of the nuclear emulsion used to obtain the electronographic sequences. With the Racine sequence a 6^m prism step was used to proceed from calibrated bright stars to faint images. This large step was unsupported by any faint photoelectric photometry. Therefore care must be taken in the comparisons below between COSMOS photometry and these sequences.

It is first useful to find from the more reliable bright sequence members the extent of the scale error in COSMOS magnitudes for bright images. From COSMOS measurements of the SGP2 sequence stars find the parameters α of eqn. 4.3 for each star. This gives a measure of the width of the image. Since stars are point sources spread ideally only by atmospheric effects their intensity profiles should be fitted by Gaussians which vary in

amplitude but not in width whatever the magnitude of the star. Figure 4.5 shows these α's plotted against magnitude as recorded by Hawkins. As expected on the basis of the above COSMOS scale error arguments, the width of stellar images is correlated with brightness to about as faint limits as 19J mag. Fainter than this stellar widths are roughly constant with increasing magnitude. Thus COSMOS scale error is only expected to affect stars brighter than 19^m. For galaxies with their lower surface brightness this limit may be pushed even lower.

Figure 4.6 shows the graphs of COSMOS relative magnitudes plotted against the sequence photometry. Ideally lines through the points should have 45° slopes. The non-45° slope for bright images is partly due to COSMOS scale error. Fainter than this reasonably similar behaviour is shown by the sequences. The 45° line which most reasonably fits the points for both sequences past 19.5 crosses the $M_C - M_{Sky} = 0.0$ line at roughly 22.9 implying this as the value for M_{sky} on J3721. However, there is large uncertainty in this value. This uncertainty is caused by the known possible scale errors in the sequence and is increased because of the random errors in the COSMOS magnitude system.

There was also available photometry of the spiral galaxy NGC 253 (Pence, private communication) which lies in the field of plate J3721. PDS measurements of this plate by Drs. J Godwin and D. Carter (Oxford) gave $\mu_J^{Sky} = 23.0 \pm .2$mag arcsec^{-2} (see Fig. 4.7). This is a more reliable value than those obtained from the sequences and so we adopt this value for the J3721 sky brightness. Small overlap regions between J3721 and the other J plates allows us to calibrate their magnitude scales as well (see Table 4.2).

In the R band we are less well off for photometry. All that is available to us is the Hawkins electronographic sequence and the correction

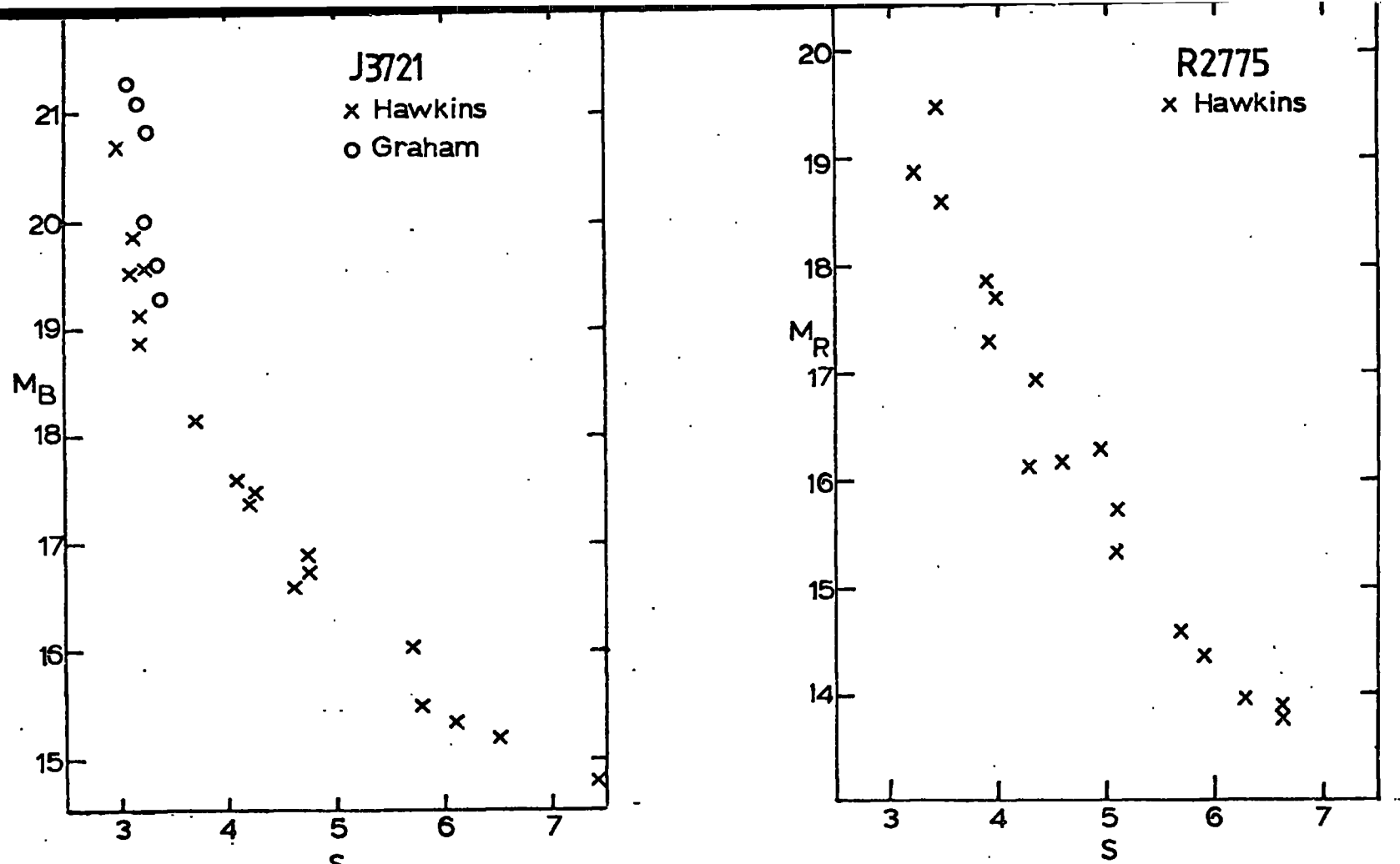

Figure 4.5 The Gaussian width parameter α plotted against magnitude for sequence stars on plates J3721 and R2775. For faint images (> 19.5^J mag,>18.OR mag) α is a constant independent of magnitude. However, for brighter images width increases with magnitude. This is an effect due to the presence of a "halo" around the COSMOS measuring spot and this produces a scale error in the COSMOS photometry of bright images.

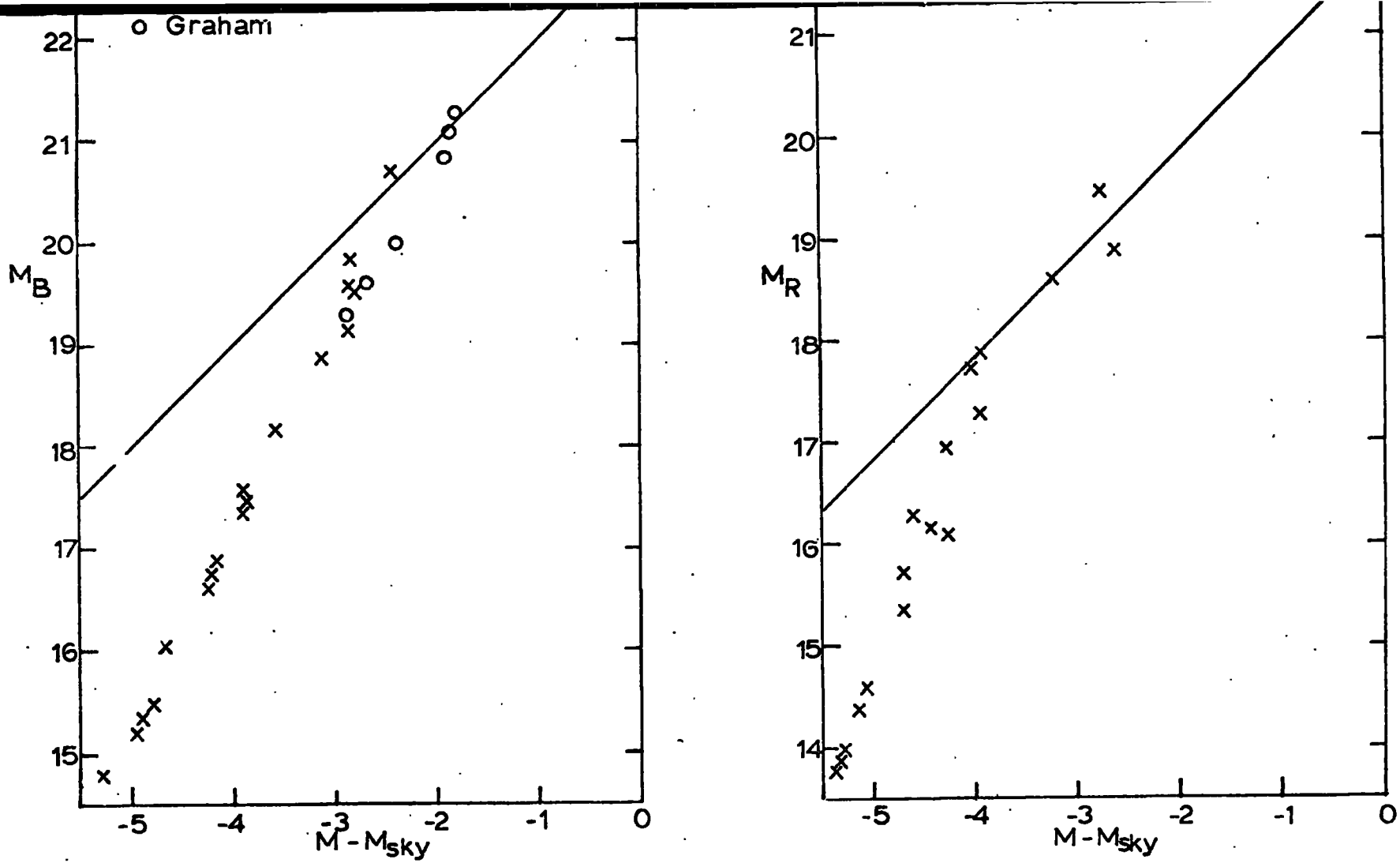

Figure 4.6 The relationship between sequence and COSMOS photometry of images on plates J3721 and R2775. The 45° line shown is fitted only to the fainter images that were shown from Figure 4.5 to be unaffected by COSMOS scale error. This line indicates that the sky brightness for plate J3721 is around 22.75 Jmag and 21.75 Rmag for plate R2775.

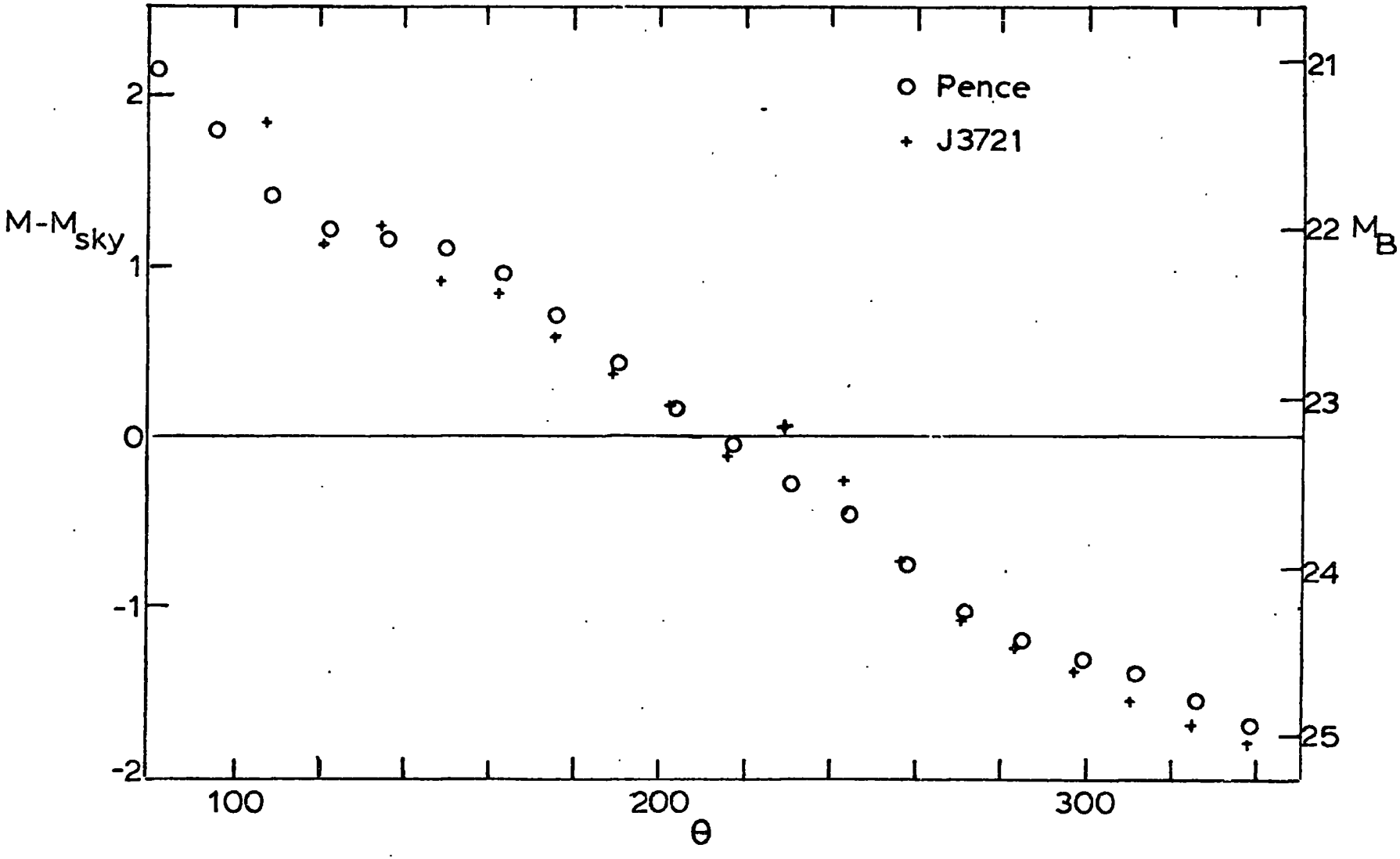

Figure 4.7 The comparison here of Pence absolute photometry along the major axis the galaxy NGC253 with relative PDS photometry of plate J3721 shows that this plate's sky brightness is 23.0 J mag arcsec^{-2}.

between his magnitude system and our own is uncertain. However, the value of μ_R^{Sky} this sequence indicates, 21.75 mag arcsec^{-2} , produces observed R number consistent with predictions (see Chapter 5) and so we tentatively use this value to give our absolute R scale. But the R photometry for these fields clearly requires much more investigation.

4.6 STAR GALAXY SEPARATION

The extension of our deep galaxy studies to larger areas of plate also meant that improvements had to be made in the automatic star-galaxy separation algorithsm. In the earlier work of Phillipps et al, 1978, the technique used was that of McGillivray et al. (1976) where the lower surface brightness of galaxies forms the distinguishing criterion. Here the same basic technique was used. A small area of plate is "eyeballed" and star-galaxy separated by eye. Differences in identification between different observers are small down to the 50 pixel limit with a 7% cut. A T_{min}-log A diagram (see Figure 4.8) is drawn for these images and the third order of polynomials fitted to the stellar objects by least squares. Good fits are obtained by splitting the curve into parts for fitting, then each part of the curve is moved to the right by an arbitrary amount to provide a good upper envelope to the observed star distribution. With perfect measuring the stars should lie on a line but random errors spread this line out. The horizontal part of the star curve at low values of T_{min} is caused by saturation due to the wide COSMOS spot more and more under-estimating the central transmission of brighter stars. The flattening of slope at the faint end is caused by the increased proportion of sky measured with each image.

This curve then sets the local star-galaxy separation criteria - above this curve all objects are galaxies, below stars. Errors involved in using this criterion rather than separating by eye run at the 5% level

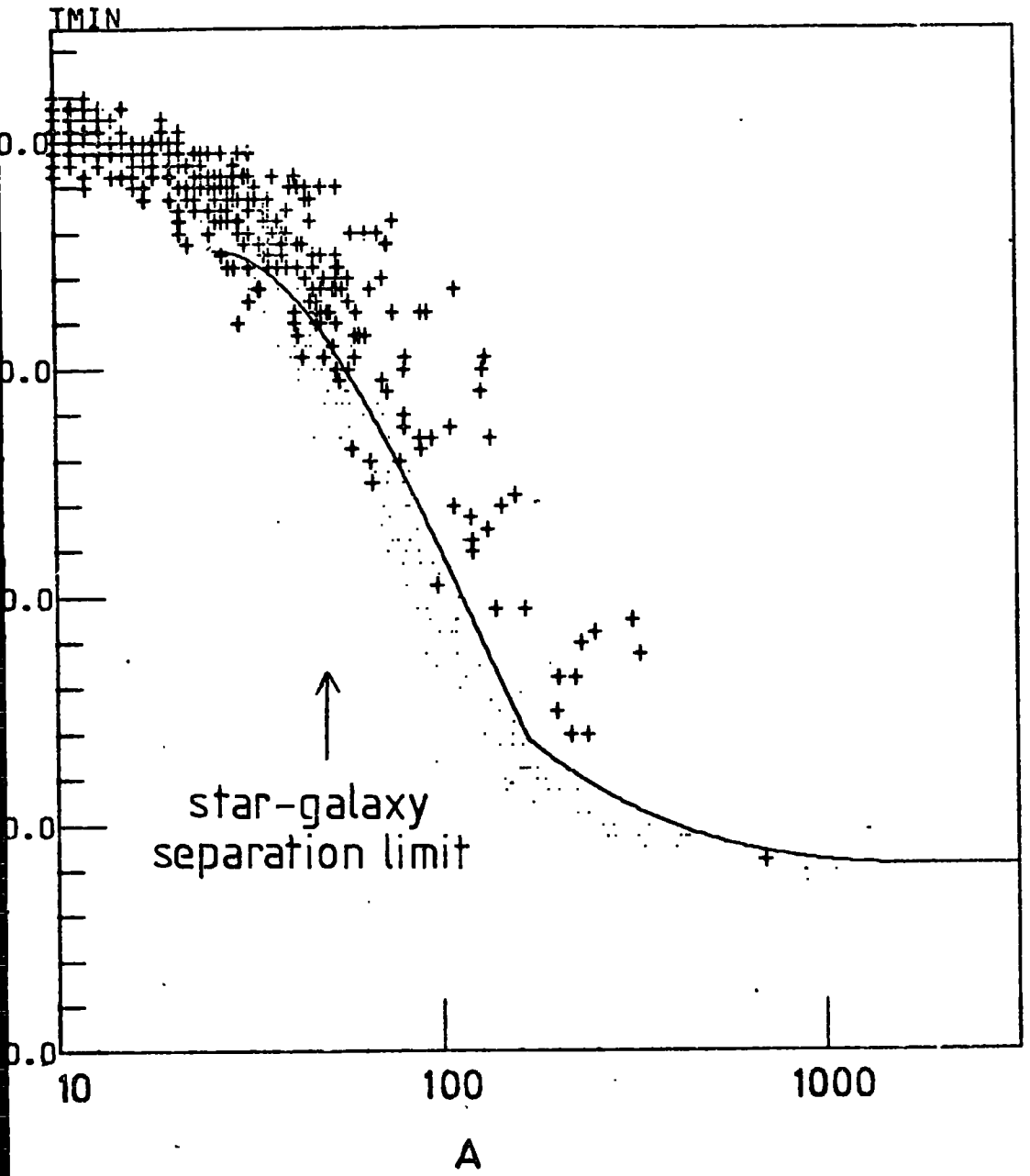

Figure 4.8 The distribution of minimum transmission, T_{min}, and isophotal area A for all images within a 1 cm^2 area of a J plate. Plus signs represent images classified by eye as galaxies; dots represent stars. The curve is the most successful set of cubics dividing the distribution with area $A \gtrsim 50$ into the two types.

when the curve is used locally.

The major possible source of error is introduced in using this star-galaxy separation over widely varying areas of plate. Two major corrections to the star curve have to be made. The first corrects the shape of the curve for changes in emulsion sensitivity. A brighter background than in the original eyeballed area pushes the fainter stars in Figure 4.8 downwards since the brighter background contributes to the measured T_{min} of these images. It can be shown, (Fong, private communication) that if the upper envelope from the original area (average background transmission To) is given by

$$T_{min} = g\ (\log A)$$

then in an area where the average background is T_1

$$T_{min} = \frac{g(\log A)\left[T_o T_1 - (A+B)\ T_1 + AB\right] - AB(T_o - T_1)}{g(\log A)(T_o - T_1) + T_o T_1 + (A+B)\ T_o + AB} \qquad (4.4)$$

where A and B are constants defined by the plate's characteristic curve and this is used in the new area as the criteria for star-galaxy separation.

As well as the variations in emulsion sensitivity, there is another effect which varies these star-galaxy separation criteria over the plate. The COSMOS spot has a constant depth of focus of roughly ± 25 μm but the plate to be measured can sag by ± 100 μm in the centre of the COSMOS plate-holder. This means that the effective atmospheric seeing for the plate is increased where images are relatively defocussed. This affects star-galaxy separation because the actual division between stars and galaxies is moved further to the right in Figure 4.8 than otherwise would be predicted.

This effect is taken into account by first drawing an effective "seeing" map for the whole plate. This is done by finding the median width of all images in each of 25 (= 5 x 5) 0.6 sq. deg. bins across the plate.

These median widths give an estimate of the relative amounts of sag in each part of the plate. A 2-dimensional interpolation is carried out between the bin centres on a 40 x 40 grid to smooth these estimates. The star-galaxy separation curve fitted in Figure 4.8 is then shifted along the log A axis by an amount $k\Delta S$ where ΔS is the change in median seeing in another area and k is a fitted constant for each plate.

The movement of the corrected curves for each plate was checked by plotting T_{min} - log A scatter plots and the predicted curves for small regions over the whole measured area. For J3721 extensive eyeball checks were also carried out to verify these procedures. The final overall proportion of bins identification by the automatic procedure was found to be 10%. Inevitably, this number of image misidentifications consisted of slightly different proportions of stars and galaxies in different regions but this did not bias the resulting distribution to any marked extent.

Shown in Figure 4.9 are the resulting correlations between number density and background transmission for stars and galaxies from 2 plates; these show no sizeable biases. Figure 4.10 shows the images classified as stars and galaxies on the 3 regions in J and R. The randomness of the star distribution as opposed to the clumpy galaxy distribution is further qualitative evidence for the success of the above methods. The number density of stars and galaxies detected to magnitude limits 21.5 in J and 19.75 in R for the various plates are also shown in Table 4.2.

Having defined our deep, magnitude limited galaxy catalogues thus we now move on to their statistical analysis.

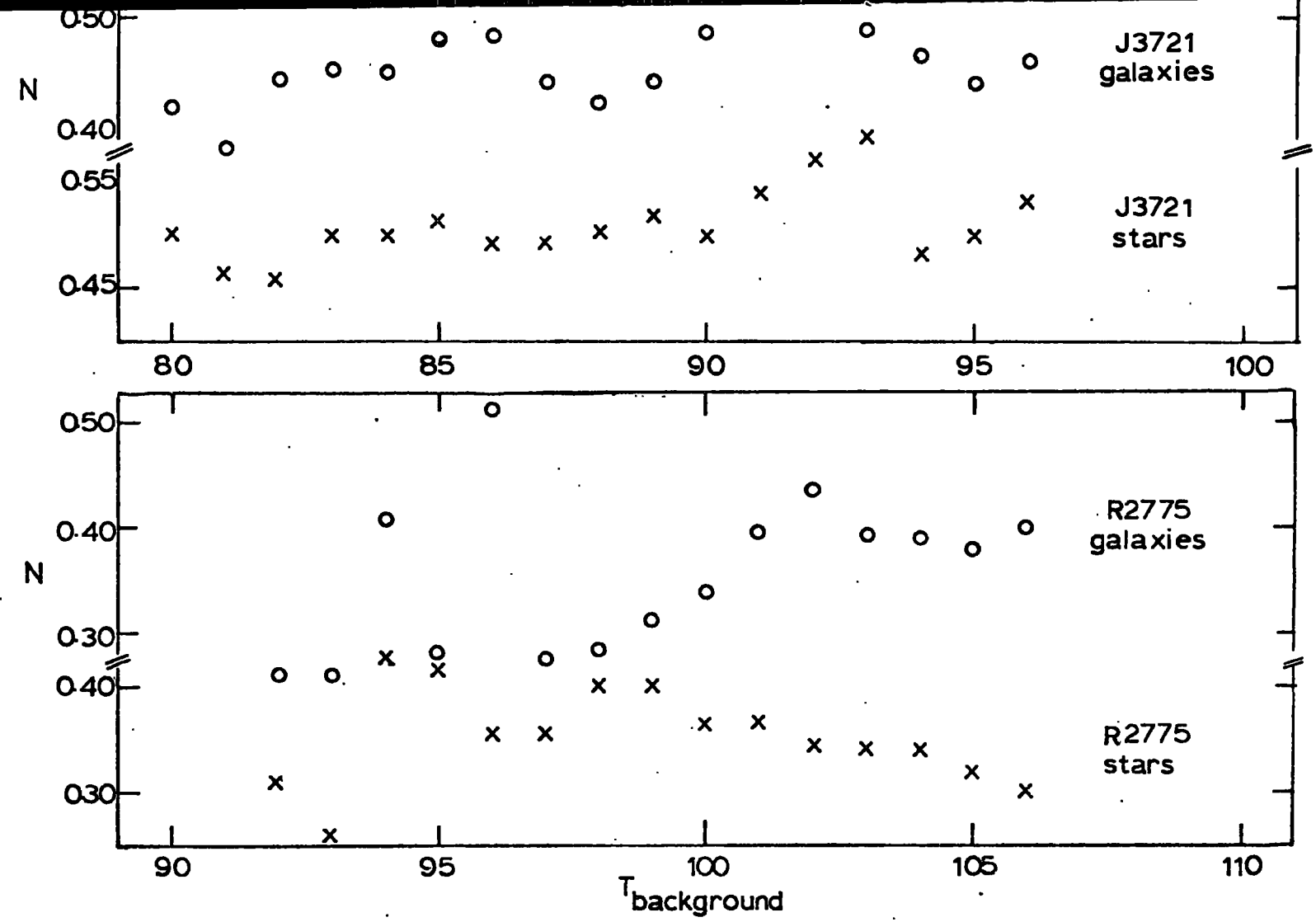

Figure 4.9 Number density, N, of stars and galaxies plotted against their background transmission, T_b, for plates J3721 and R2775. No significant biases are evident.

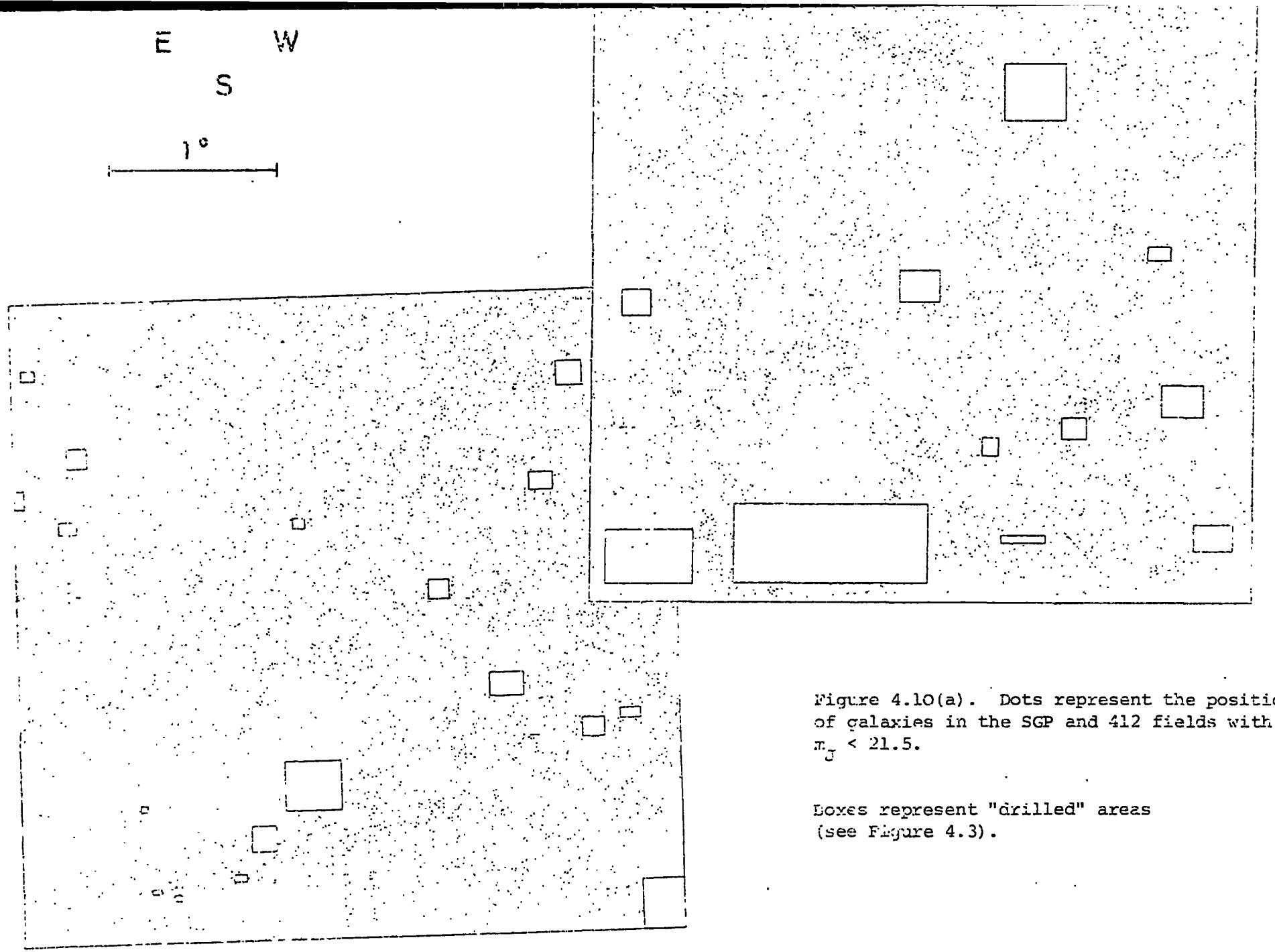

Figure 4.10(a). Dots represent the position of galaxies in the SGP and 412 fields with $m_J < 21.5$.

Boxes represent "drilled" areas (see Figure 4.3).

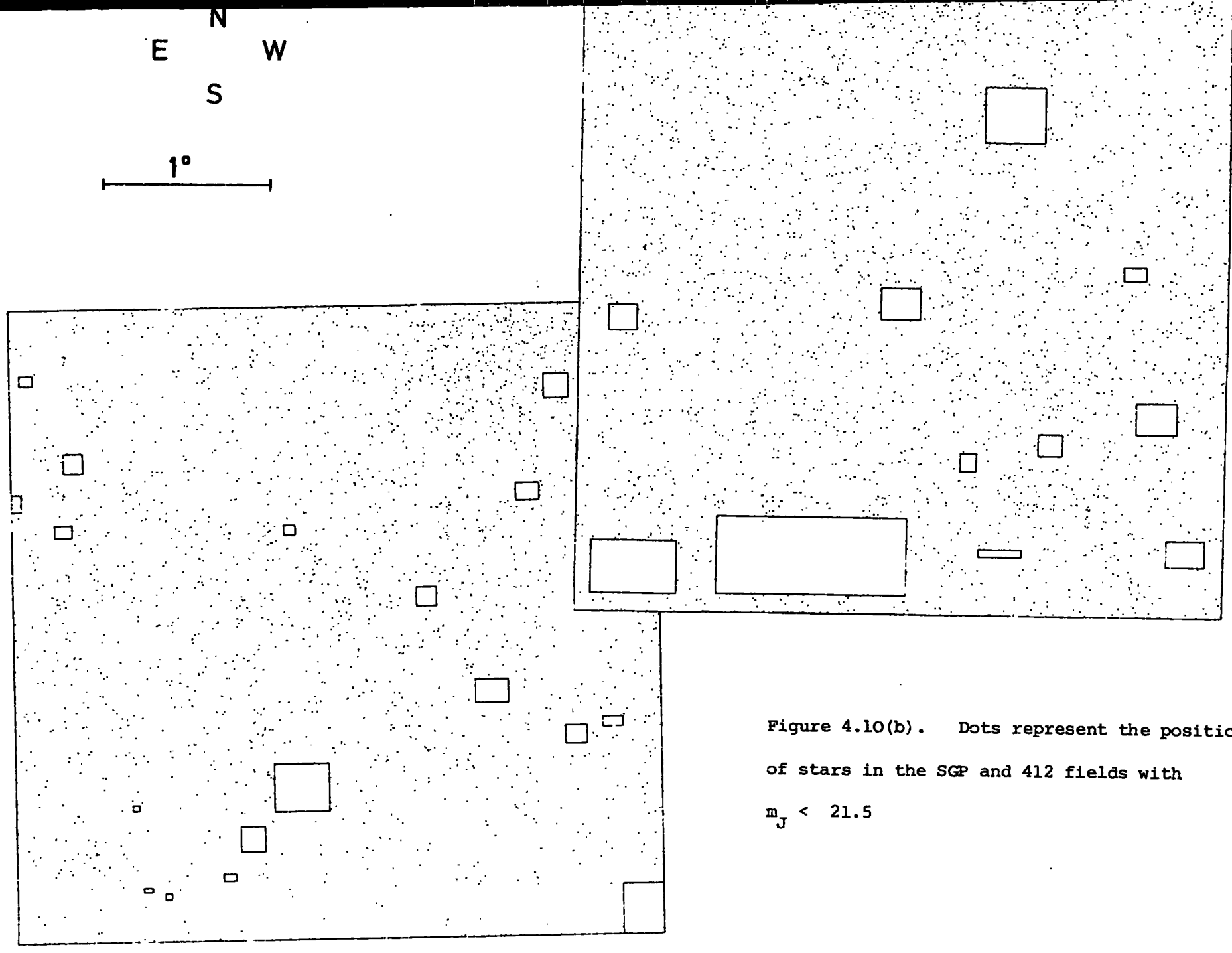

Figure 4.10(b). Dots represent the position of stars in the SGP and 412 fields with $m_J < 21.5$

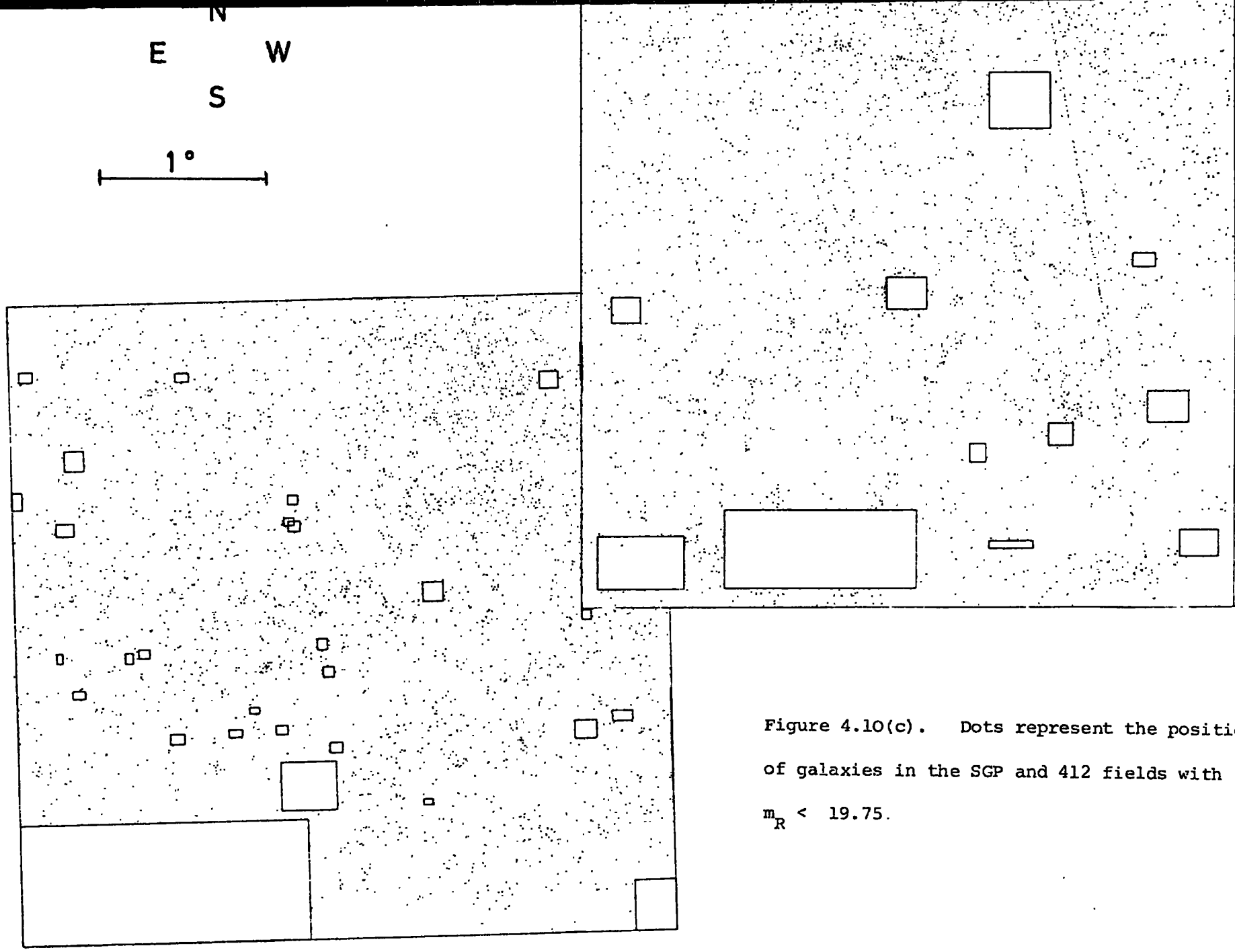

Figure 4.10(c). Dots represent the position of galaxies in the SGP and 412 fields with $m_R < 19.75$.

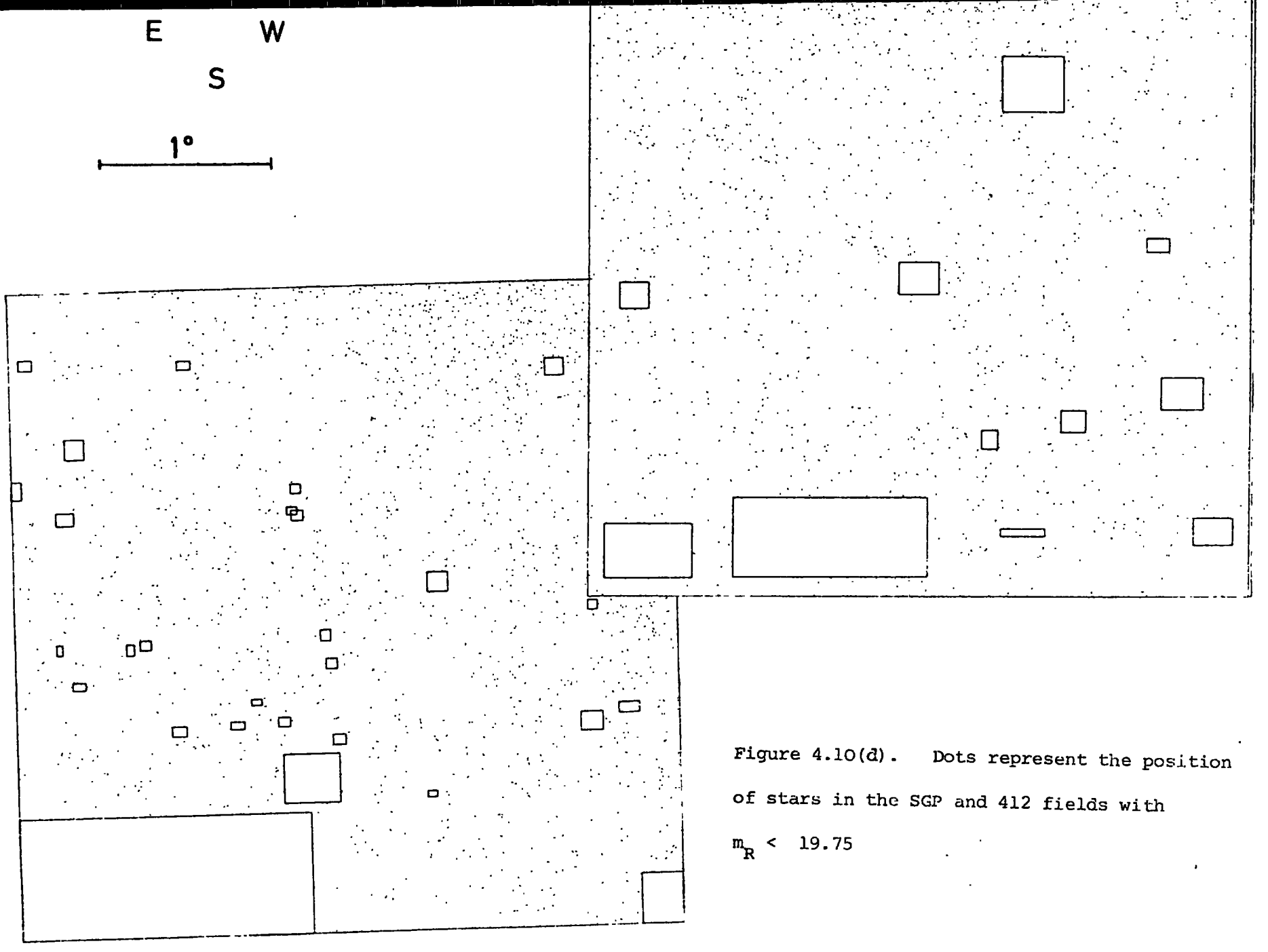

Figure 4.10(d). Dots represent the position of stars in the SGP and 412 fields with $m_R < 19.75$

CHAPTER FIVE

SELECTION EFFECTS OPERATING ON DEEP SCHMIDT PLATES

5.1 INTRODUCTION

To carry out comparisons of the correlations obtained from deep samples with those obtained from shallower catalogues we need to find an "average depth" for the deep samples. In the absence of redshift information for individual galaxies this depth must be estimated by considering the theoretical galaxy number-redshift relation, n(z), (or, equivalently the galaxy selection function, $\phi(z)$) for the sample. The selection of a galaxy at a particular redshift depends not only on the brightness limit of the sample but also on a number of other factors including the luminosity function of galaxies, their k-corrections, luminosity evolution and the relative proportions of their division into more phological types. Many different models for these galaxy properties have been suggested and all are subject to much uncertainty (see Ellis 1979) for a review.

Fortunately information about these parameters is contained in our samples, in a manner independent of the galaxy distribution. We can test between these models by seeing which combination best predicts the observed number-magnitude relationships. This approach is similar to that of Ellis et al (1977) who fitted the number-angular diameter relationship with the same aim. This approach will also be investigated here.

Another handle on these models can be gained through the observed galaxy number - (J-R) distribution. Thus we also discuss in this chapter the method of obtaining this distribution for one of the J-R plate pairs and the results from its subsequent modelling.

Having found the best fitting models we can calculate n(z) and $\phi(z)$ (see Peebles 1973, Phillipps et al, 1978). $\phi(z)$ is then used in

Limber's formula (see Chapter 2) to predict the correlation amplitudes expected at these depths.

Finally, we also discuss briefly the number-magnitude relations and colour distributions for the stellar samples. Although these have been produced almost by default, they contain, potentially much information both on stellar populations at the galactic poles,and quasars.

5.2 MODELS

We shall look briefly here at the input models from which theoretical number counts can be computed. Certain of the parameter choices are similar to those used in Ellis et al (1977).

We always adopt the Schechter form for the galaxy luminosity function (Schechter, 1976) with the values of his α and β parameters for the various galaxy types taken from Tinsley (1977) and shown in Table 5.1. The absolute normalisation fo this luminosity function was given by taking Schechter's ϕ^* to be 0.0022 as recommended by Felten (1977). This value has been corrected upwards for the effect of galactic obscuration which has been input into our models as 0.25^m in J and 0.12^m in R (at the galactic pole). The relative proportions of galaxy types was taken from Pence (1976) but the effect of assuming a mix more weighted towards late types (Tinsley, 1977) is also discussed (see Table 5.1). The value of Schechter's M^* was taken for these types also from Tinsley (1977). These magnitudes are isophotal and are corrected to total magnitudes using the relations

$$J_T = B(0) - 0.5$$

$$R_T = r(0) \qquad \text{(see Kron, 1978, Dixon,1978)}$$

The width of the luminosity function was cut for all types at $M^* \pm 4.0$ mag.

TABLE 5.1

Standard Astronomical Parameters

Galaxy Type	Proportion	M^*_J	α	J-R	$K_J(z)$	$K_R(z)$
E	12.5%	-20.70	1.25	1.65	$5.0z - 1.4z^2$	$1.09z + 1.28z^2$
SO	25	-20.70	1.25	1.65	$5.0z - 1.4z^2$	$1.09z + 1.28z^2$
Sab	25	-20.80	1.25	1.45	$4.0z - 1.5z^2$	$1.02z + 0.92z^2$
Sbc	17.5	-20.95	1.25	1.10	$3.2z - 1.4z^2$	$-0.03z + 1.23z^2$
Scd	13	-20.30	2.00	0.96	$3.0z - 2.0z^2$	$-0.21z + 1.11z^2$
Sdm	7	-20.35	2.00	0.85	$2.0z - 1.5z^2$	$-0.63z + 1.03z^2$

Notes:
1. All data assumes $H_o = 50$ km s^{-1} Mpc^{-1}.
2. Luminosity functions follow Schechter's (1976) relations with faint end slope α (see EFP eqns 3 & 4), $\beta = 0.025$.
3. K-terms as a function of redshift z, K(z), were calculated using data taken from Pence (1976).
4. Galactic absorbtion $A_J = 0^m.25$, $A_R = 0^m.16$ was assumed.
5. Felten's (1977) normalisation of $\Phi^* = 0.0022$ was taken for the luminosity function overall. This normalisation applies outside the Galactic poles, i.e. before any absorbtion correction.
6. Evolutionary corrections for the standard model were derived from the slow star formation models of Tinsley (1978).

The model for the galaxy k-corrections in J and R for the various types is taken from Pence (1976). These are less certain in J at high redshift than in R. The model for galaxy luminosity evolution was supplied by Tinsley (private communication) and features, in particular, evolutionary brightening of ellipticals and Sϕ's in J. This model is called a slow star formation (SSF) model and predicts much less brightening than Tinsley's previous "conservative" evolution used by Ellis et al, constraints on this model coming from observations on the night sky brightness (Dube et al,1977).

The colour indices of galaxies which allows us to convert M^*'s from J to R are again taken from Tinsley (1977) and are as shown in Table 5.1.

With these models theoretical number counts can then be calculated. This is done by computing from the luminosity function the number of galaxies at each redshift that are brighter than the sample limit (taking into account k corrections, evolution, etc). This general method applies whether the sample is limited in isophote and area or in apparent magnitude.

5.3 NUMBER-ANGULAR DIAMETER RELATIONS

In the work of Phillipps,etal(1978) the deep samples were limited by isophotal angular diameter. In Ellis et al (1977) the selection effects in such samples were examined. We can limit the present COSMOS samples either in angular diameter or in apparent magnitude. Limiting the samples by apparent magnitude is more conventional and makes easier any comparisons with shallower samples. It is worthwile, however, to first investigate how well we can model the distribution of angular diameters in these samples.

To do this we follow the same procedure as in Ellis et al in which reasonable galaxy luminosity profiles are convolved with a Gaussian "point spread" function and the image angular diameter calculated at the isophote

relevant for the sample. If this diameter falls below the sample size limit then the galaxy is excluded from the predicted counts (for fuller account see Phillipps 1979).

Presented in Figure 5.1 are the observed differential angular diameter counts, n(d), for our 5 samples. The angular diameters are calculated from the COSMOS image parameters according to the algorithm of Ellis et al. These counts are limited by the COSMOS 10 pixel detection cut off, but are uncertain at d $<$ 5'' because star galaxy separation was not verified by eye to such small scales. The slopes at large d are consistent among the J samples and also among the R samples. The larger numbers in the J3721 sample compared to the J1916/J1920 samples are as a result of this sample being complete to a fainter isophote, (see Table 4.2).

To illustrate the problems involved in this approach, we consider the modelling of the J3721 n(d). Here we are in a better position than Ellis et al because value for the threshold isophote can be determined from the absolute photometry (see Section 4.5). This value is calculated to be 25.75 mag arcsec^{-2} for the J3721 scan.

Ellis et al showed that the form of n(d) not only depended on the value for this isophote but also on the width of point spread function used. This width was estimated for these samples from fitting Gaussians to the central intensity and area, A, cf a number of stars (see e.g. Figure 4.4). The "seeing" width adopted for this plate was 3.2".

Using the parameters with the Pence mix and other parameter values in Table 5.1, the n(d)'s are predicted as shown in Figure 5.2. Curves are shown calculated both with and without SSF evolution.

As we shall see the parameters used in the solid curve give a good representation to the observed n(m) curves. However, Figure 5.2 shows that they give remarkably bad fits to the observed n(d)'s. The agreement is worst

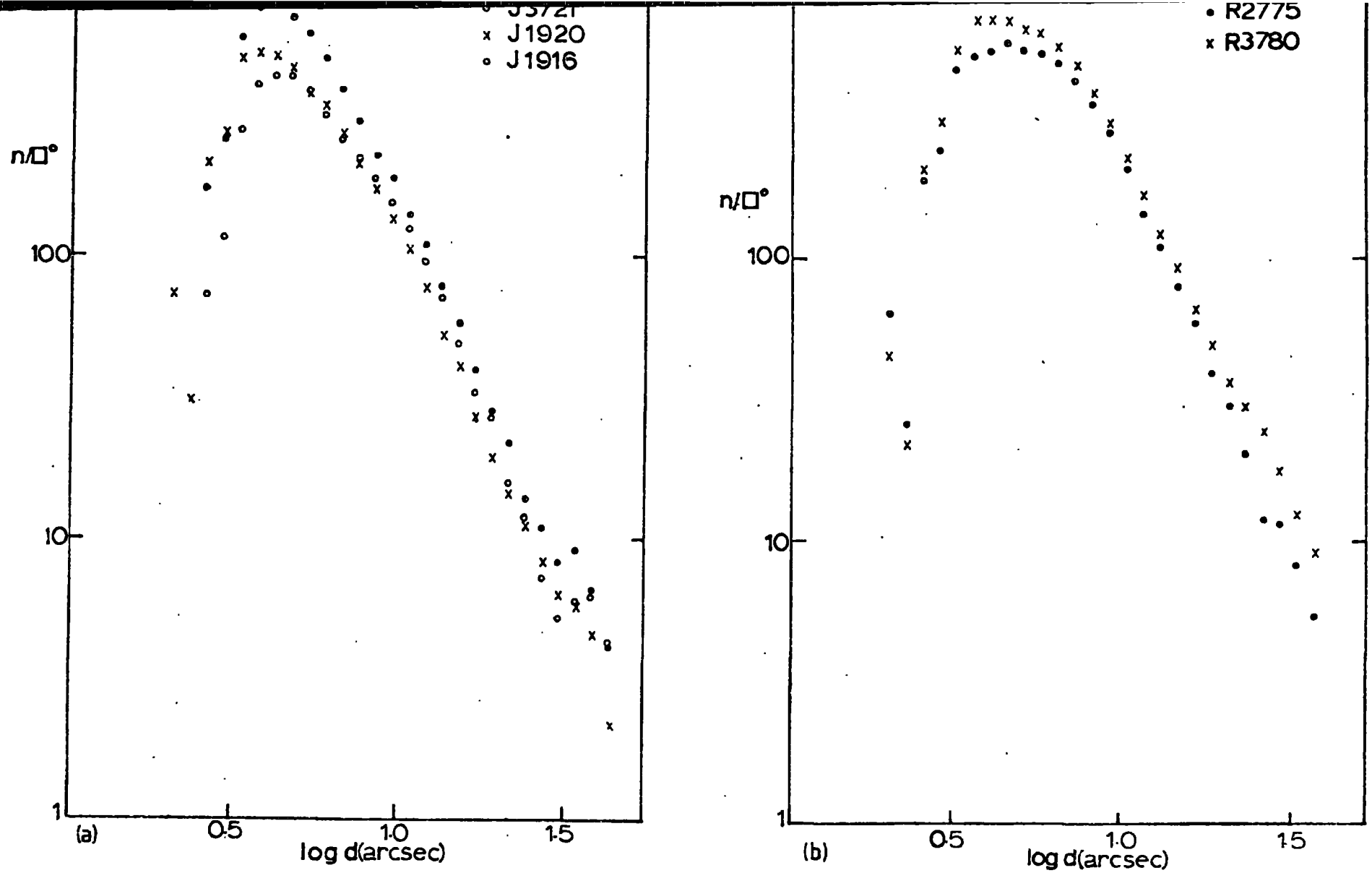

Figure 5.1 Observed differential angular diameter counts, n(d) for the galaxies from the 5 plates. The results are reasonably consistent from plate-to-plate .

(a) J plates (b) R plates.

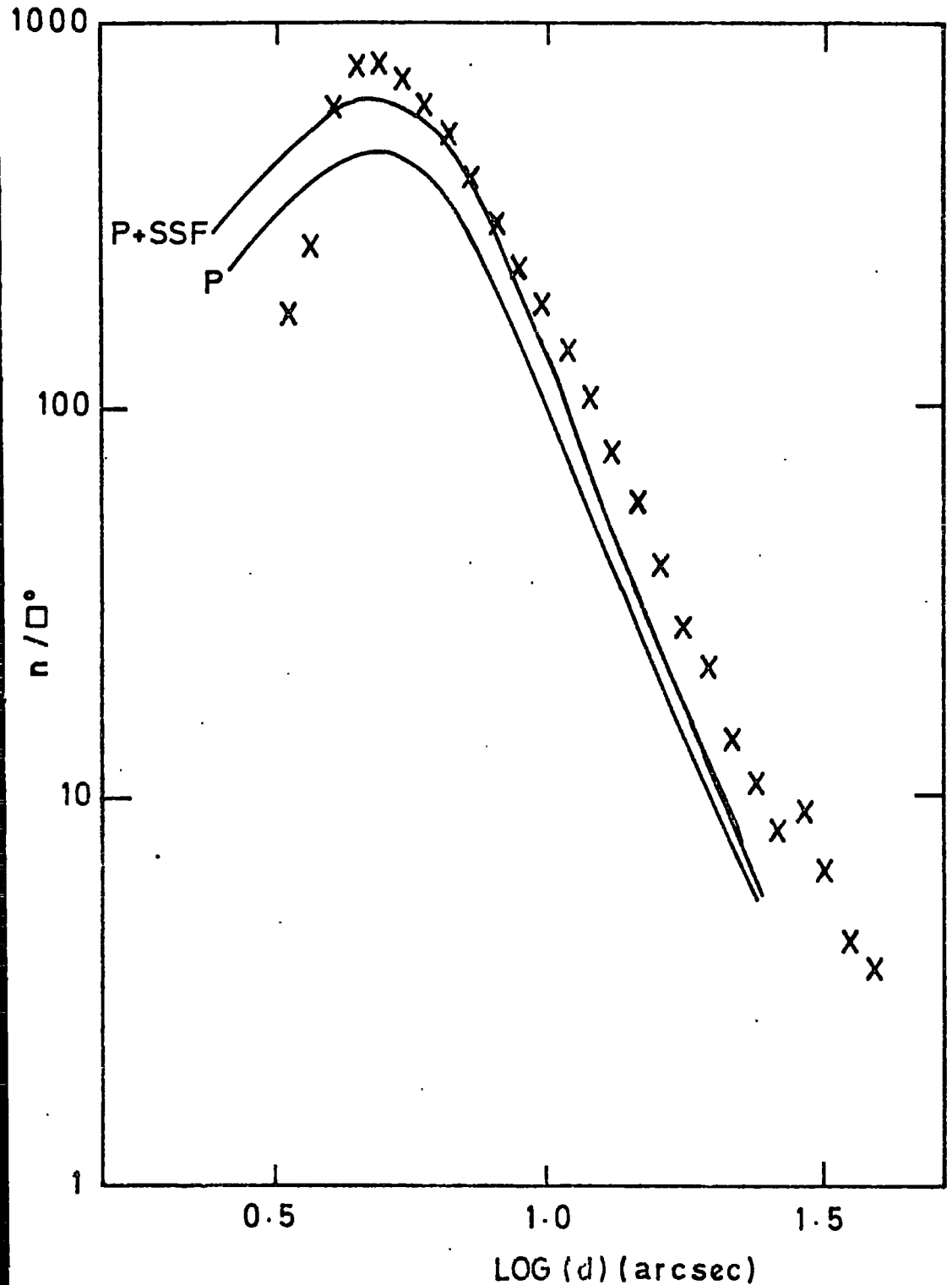

Figure 5.2 Predicted differential angular diameter counts for plate J3721. Curve P represents the prediction for the model using the Pence mix with no evolution and curve P + SSF the prediction for Pence mix with SSF evolution. The isophote used was 26.0 J mag arcsec^{-2} and the seeing was 3.2''.

at large d where neither the redshift dependent parameters nor seeing have much effect. The only way to produce agreement here would be to make the isophote fainter by up to 1.5 mag $arcsec^{-2}$ which is unquestionably too faint. It seems that images (at large d) as measured by COSMOS are just too extensive.

The probable cause is the halo around the COSMOS spot. Even when the spot centre is a substantial distance away, a bright object will still be making a substantial contribution to the measured light via this halo. This would make the angular size of bright images much larger than expected. The way to take account of this in the model would be by using a more realistic point-spread function than a Gaussian, but this is difficult because the exact shape of the COSMOS spot profile is unknown. Thus we prefer to model the n(m) curves to obtain our selection functions. As we have seen the effect of this halo is not as drastic on our magnitudes since these are weighted by the central intensity which is less affected by this problem.

5.4 NUMBER MAGNITUDE RELATIONS

Many observed number-magnitude relations have been presented in recent years using a variety of techniques. Presented first in Figures 5.3a and 5.3b are summaries of the integral results in the J and R passbands respectively (where results were obtained in different magnitude systems the usual approximate correction factors were applied). Most previous work has been done near the J band and although the counts seem reasonably consistent over the range of interest here, it can be seen that outside this range, there are some large variations between the different observers. Some of this variation is probably caused by inadequate corrections for the different magnitude systems ; the rest can only be caused by systematic differences in either photometric scale, or, perhaps, in star galaxy separation techniques. In the R band the variation between observers seems less. However

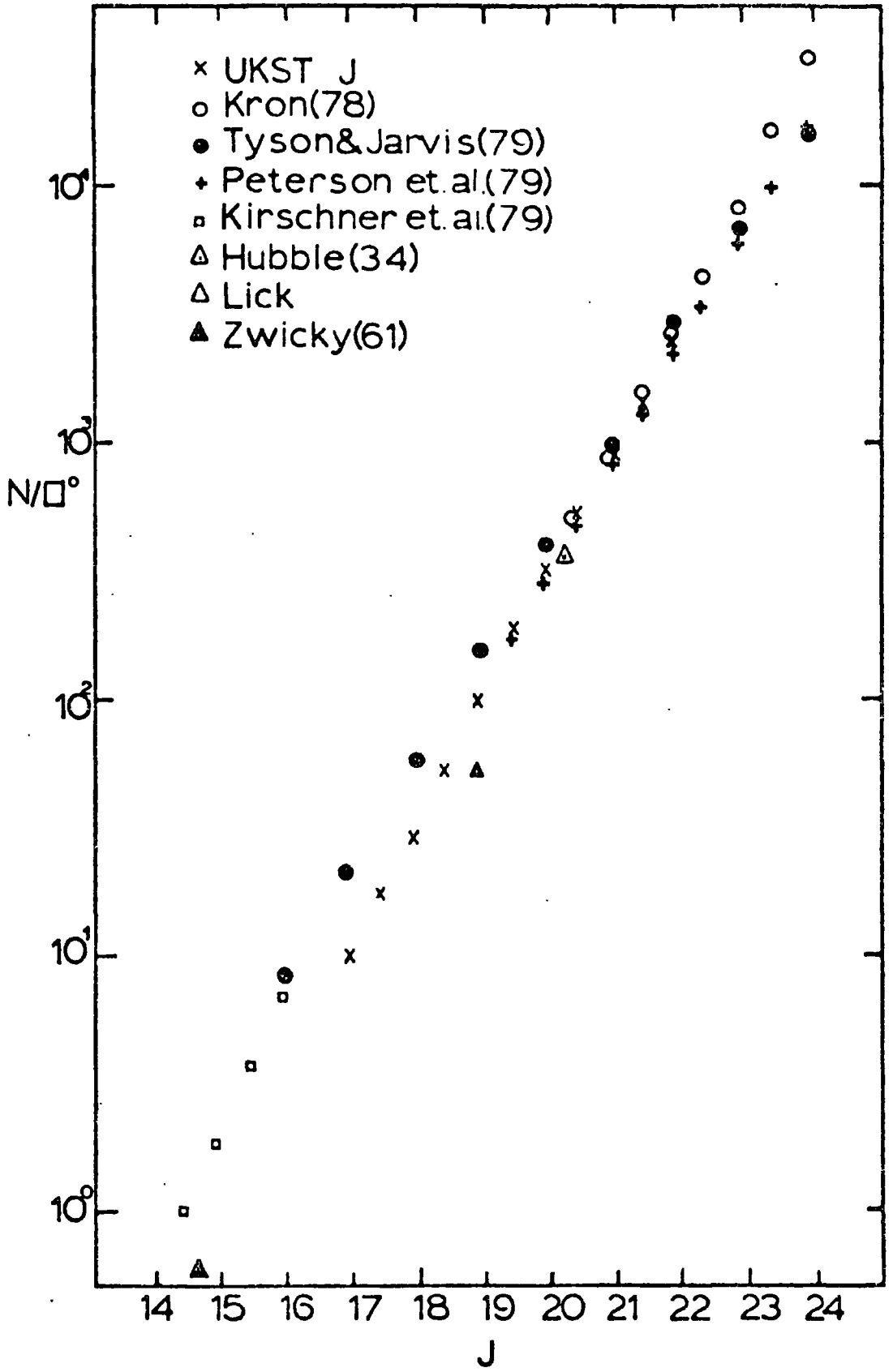

Figure 5.3(a) Observed J integral galaxy number magnitude counts from our UKST samples and the other samples referenced. These counts slopes agree reasonably over the short range of interest here (m_J 18 $\lesssim m_J \lesssim$ 21.5) but disagree at both fainter and brighter magnitudes.

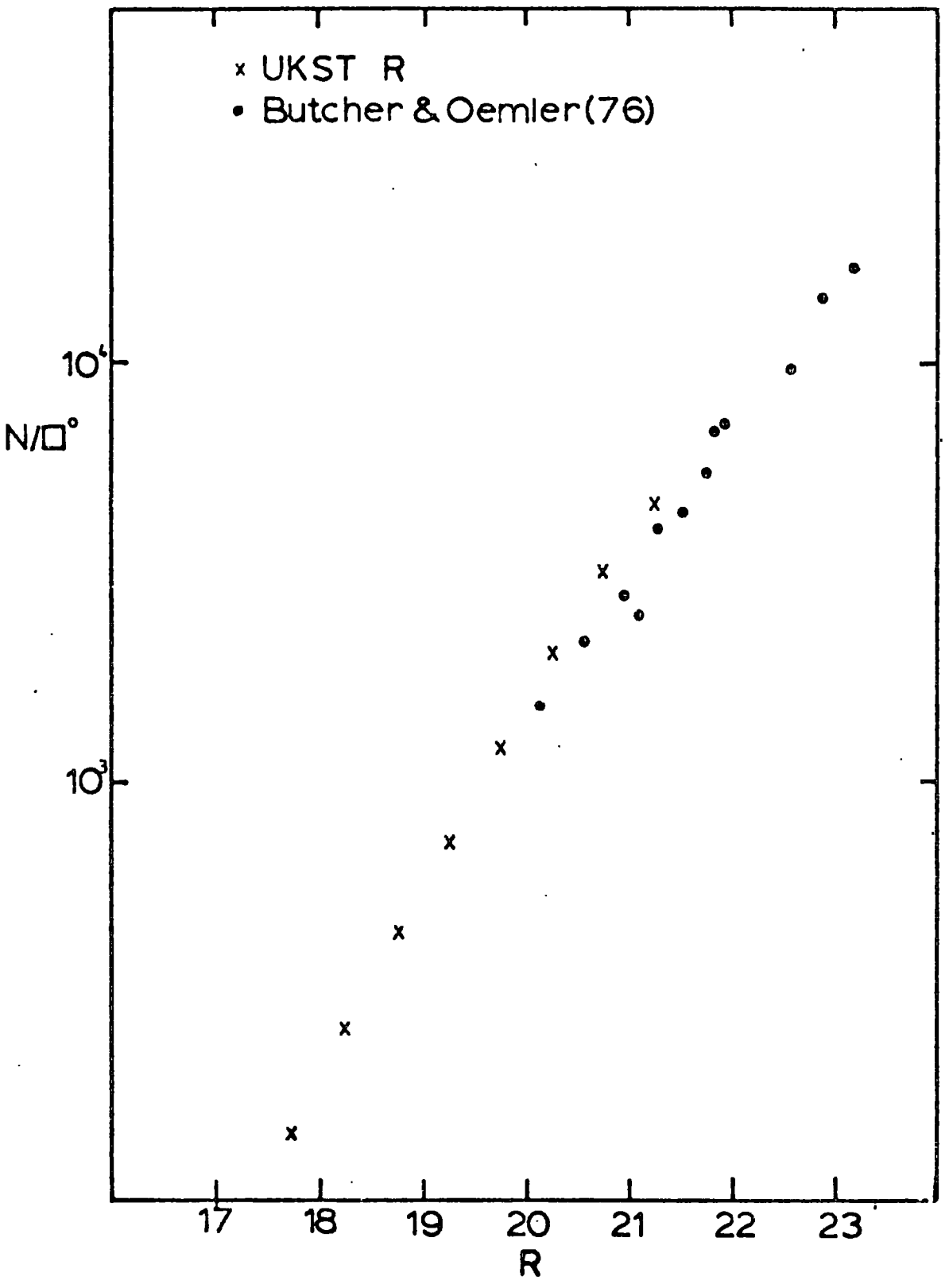

Figure 5.3(b) Observed R integral galaxy number magnitude counts from UKST and other samples.

this is probably only coincidence since the corrections for the various red passbands are even less certain than for the blue. Thus the point to be made before trying to model, for instance, the slope of the n(m)'s is that it is by no means certain what the observed n(m) slope actually is. Under these circumstances it is thought best to concentrate on modelling only our own results. This has the advantage of consistency and it also means that we will be better placed to allow in the modelling for the effects of any errors.

Presented in Figures 5.4a and 5.4b are the COSMOS number counts plotted in differential form. To give a wider baseline in J, the number counts of Kron (1978) are also plotted. The agreement between these two over their overlap region is good with the n(m) slope at m_J = 21.5 being measured as 0.44 in the logarithm. The first step is to find to what magnitude limit our samples are complete and unaffected by the COSMOS 10 pixel detection cut off. The dashed line in Figure 5.5 shows that a number magnitude prediction incorporating the size cut off at the appropriate isophote differs little from a prediction for a simple magnitude-limited sample to m_J = 21.5. Even past this point the data shows no fall off in the observed n(m). By similar considerations the R samples were also found to be complete at 19.75 mag.

The dashed line in Figure 5.5 was convolved with a Gaussian of half-width 0.3^m, the estimated average error in the magnitudes. This was done to check that the n(m) curves were not too sensitive to photometric error. The dot-dashed line in Figure 5.5 is the result and this shows negligible difference from the unconvolved prediction in the region of interest.

The observations in J are steeper than the prediction based on the Pence mix with no luminosity evolution. The inclusion of SSF luminosity evolution substantially improves the agreement. However, it cannot

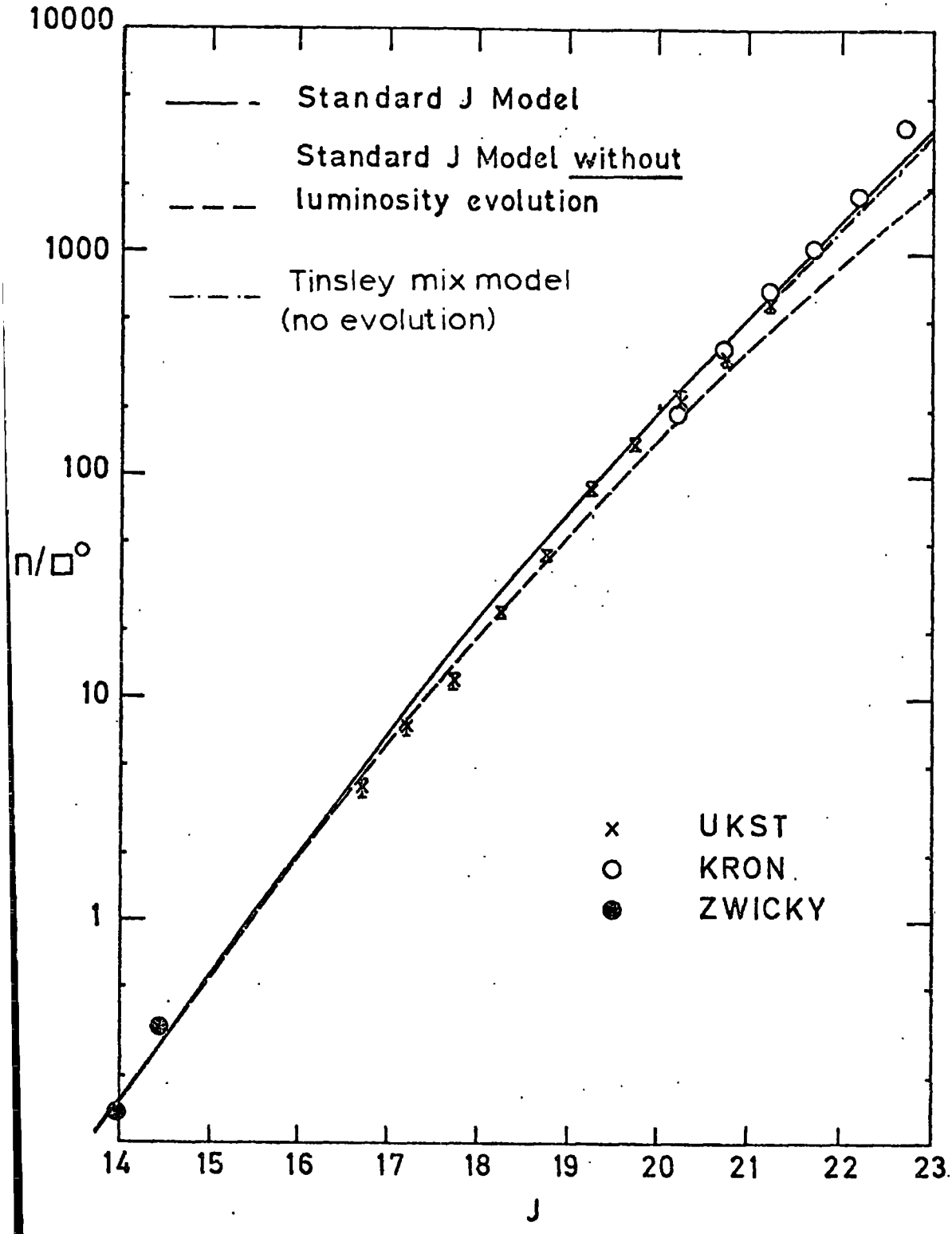

Figure 5.4 (a) Differential number counts per square degree for galaxies in 0.5 magnitude intervals plotted against J magnitude for various surveys. The UKST counts were taken from all 3 J plates. The solid curve is the prediction of the standard model. The dashed line has no luminosity evolution. The agreement between the UKST counts and other well calibrated data confirms the accuracy of our photometry.

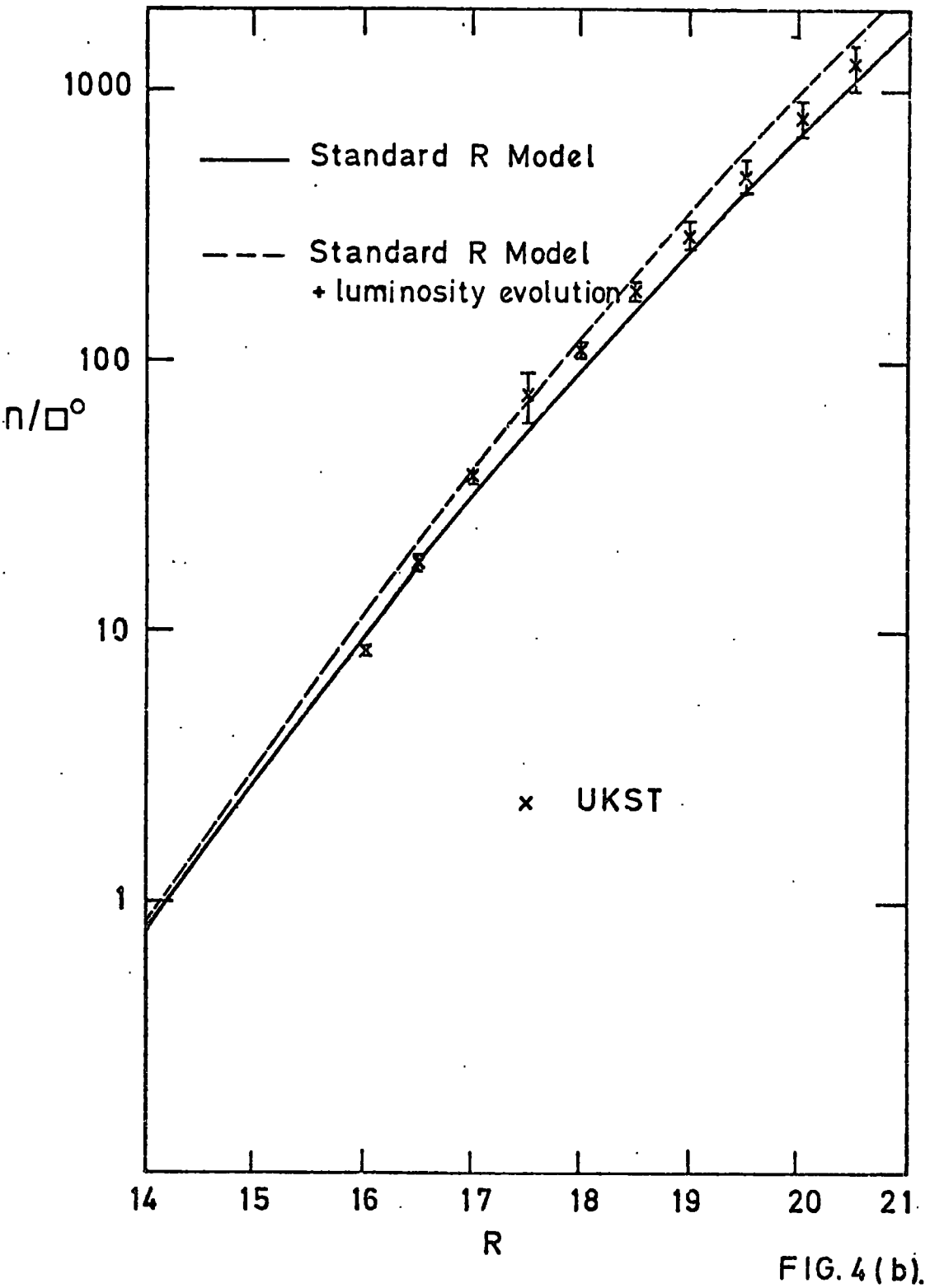

Figure 5.4 (b) As Figure 5.4(a) but for R counts. The UKST counts were taken from both R plates.

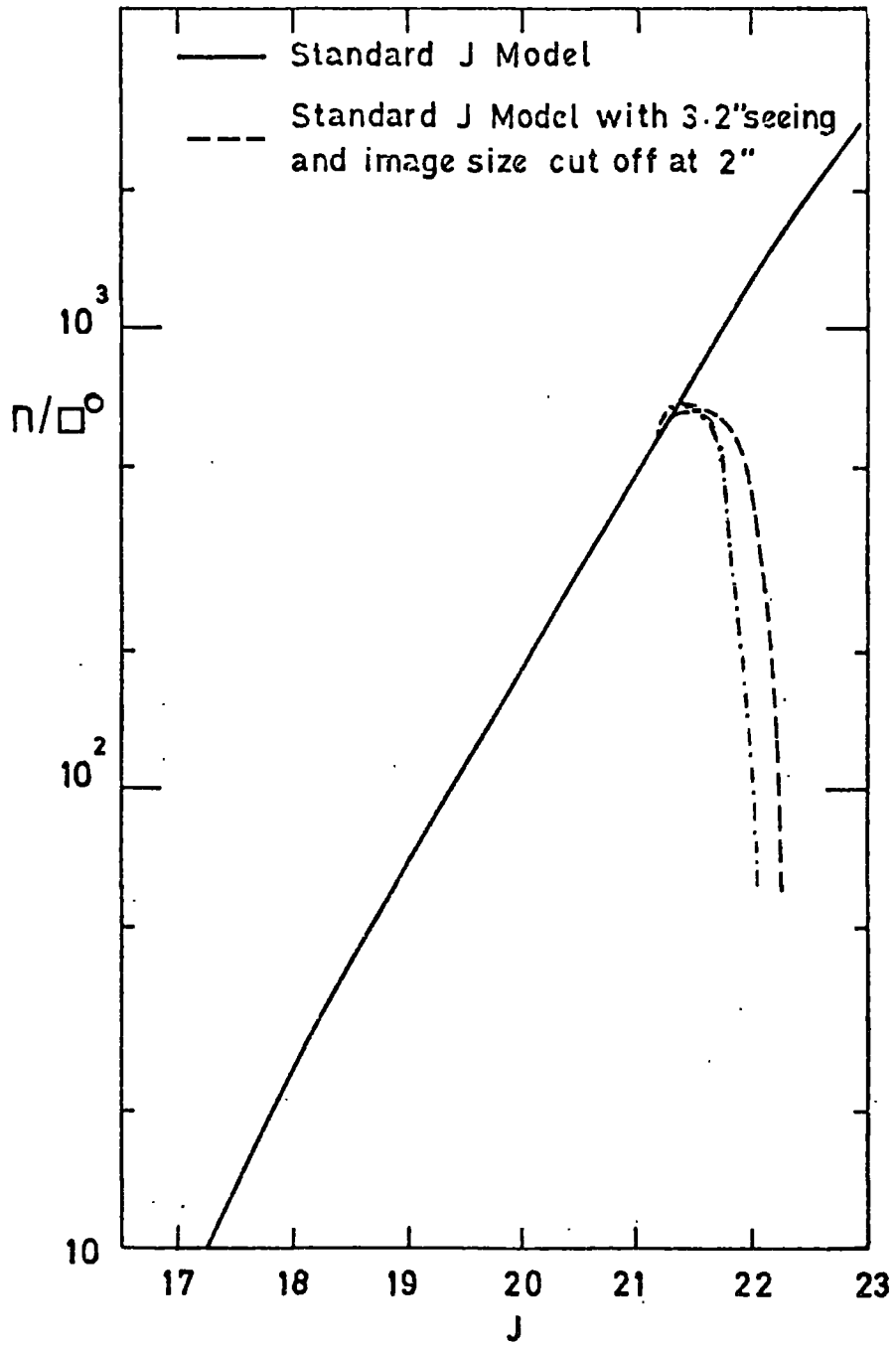

Figure 5.5 Predicted differential number magnitude counts for galaxies in the J band. The dashed curve applies to a sample defined by the COSMOS image size limit at the $\mu_J = 26.0$ mag. arcsec^{-2} isophote. The solid curve applies to a deep sample unaffected by such size and surface brightness selection effects. Both predictions use the standard model. The agreement for $J < 21.5$ indicates the COSMOS selection procedure does notbias our magnitude limited samples.

thus be concluded that these n(m) curves represent evidence for galaxy luminosity evolution. This is seen by considering the predictions from the Tinsley mix of galaxy types ; Figure 5.4a shows that a model using this mix and assuming no luminosity evolution gives just as good a fit to the data. Thus number counts by themselves cannot distinguish between the effects of luminosity evolution and varying the mix of galaxy types.

If we are only interested in predicting the amplitudes of correlation functions for the deep samples then this restriction is not too severe. What we need for this purpose from the number counts is an idea of the effective K-correction which includes the effects of K-dimming and luminosity evolution. This effective correction represents all the effects of increasing redshift on the absolute magnitude of a galaxy. This enables $\phi(z)$ to be calculated, irrespective of the source of redshift dependence. It shall be seen in Section 5.5 that combining the n(m) relations with colour information helps to isolate the mix dependence. For the moment we choose the Pence mix with SSF evolution as defining the effective correction. This will define our standard luminosity parameters in J ; standard in this context indicates that models based on the parameters fit the observed n(m)'s.

In the R band the number counts prediction based on the Pence mix show reasonable agreement with the data but the observations show no real preference between models with or without evolution. However, since the deeper counts show very flat slopes of around 0.40 at $m_R = 21.0$ (see Figure 5.1b) we adopt the no-evolution model as standard for the R passband. (Evolutionary brightening always steepens the n(m) slope).

The effect of varying another parameter, the width of the luminosity function cut off, was also investigated. Changing the width from M^* ± 4.0 to M^* ± 7.0 made no significant change to the n(m) predictions.

5.5 GALAXY COLOURS DISTRIBUTION

More information about the selection effects operating in these samples is offered through the distribution of J-R galaxy colours. A computer programme was written which identified an image on a J plate with an image on a companion R plate if the transformed coordinates of the centroids of the two images were the same (within a small tolerance). This programme was applied to the J-R pair J3721/R2775 and in this way found J-R colours for 95% of the J3721, $m_J \lesssim 21.5$ sample in a consistent fashion over the plates.

Figure 5.6 shows the J: J-R: number contour plot as measured for this sample. If allowance is made for the wider spread in (J-R) due to the larger errors in our photometry then there is reasonable agreement between these distributions and those obtained by Kron (1978). However, care must be shown in comparing these two because Kron's red passband is different from the red band used here.

Shown to the same scale in Figure 5.8a are the total n(J-R) results for stars and galaxies, $m_J \lesssim 21.5$. The galaxy colours peak at (J-R) $\sim$1.2 bluewards of the stellar peak at (J-R) $\sim$1.8. Shown in Figure 5.8 are the observed n(J-R) distribution for galaxies split into J magnitude bins as shown. This can be looked at as a series of cross-sections across Figure 5.6. To reduce the chance of COSMOS scale error affecting these results only images faintwards of $m_J = 19.5$ are considered. For comparison, Figure 5.9 a, b, c shows, as the solid lines, the equivalent predicted results for our three models. The results of convolving these plots with a Gaussian error function is shown here as the clashed lines. The width of the error function in (J-R) is 0.35^m, computing by multiplying the error in the individual magnitudes, 0.25^m (see Chapter 4), by $\sqrt{2}$ to obtain this error in the difference.

Despite this smoothing by our errors, it seems clear that <u>both</u> the models which fitted the J number magnitude counts seem inconsistent with the

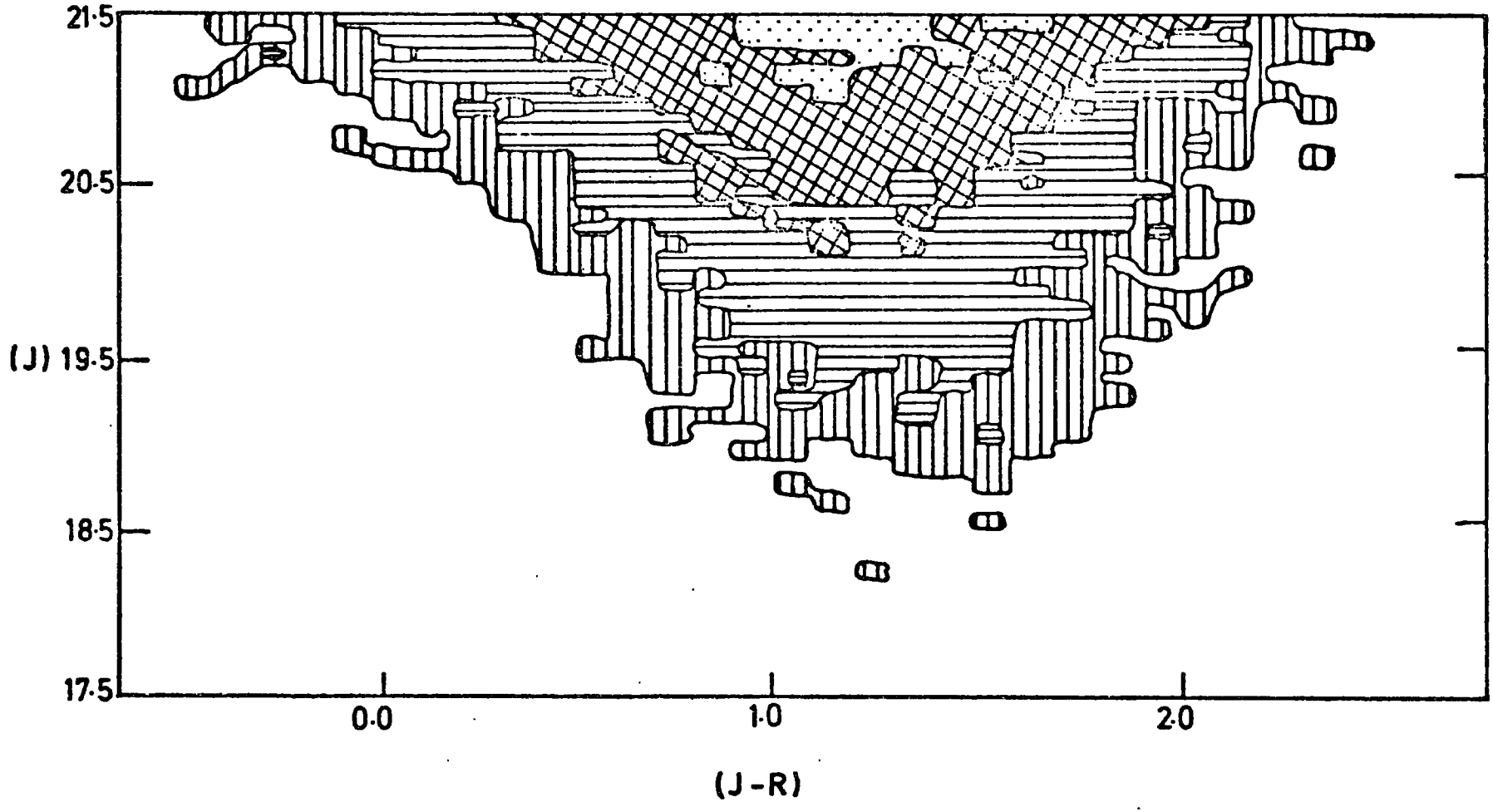

Figure 5.6 Number density contours for the galaxy colour-magnitude diagram for plate J3721. Density increases by factors of 2 towards centre . This distribution is in reasonable agreement with the findings of Kron (1978), showing a broad range of galaxy colours.

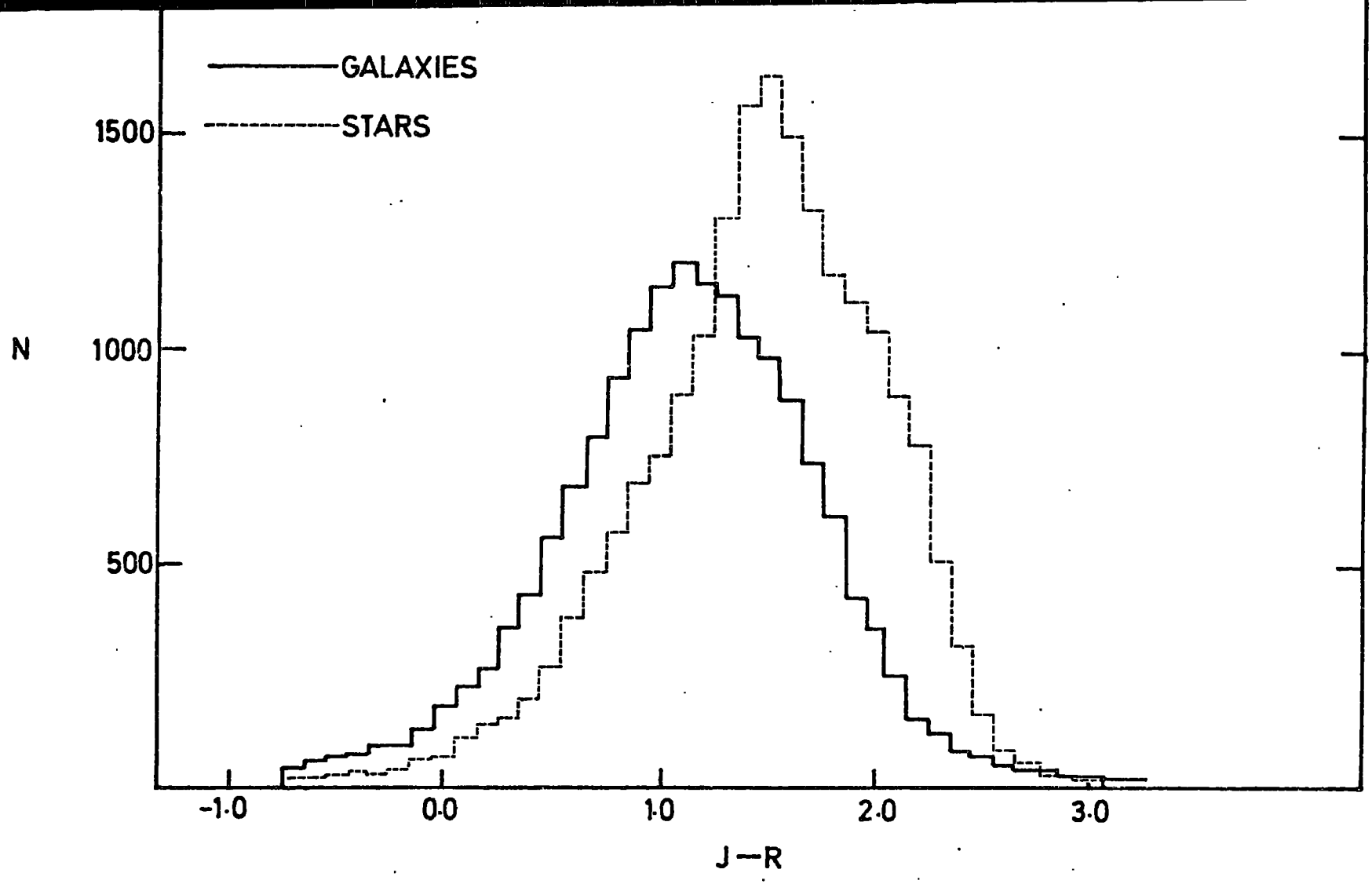

Figure 5.7 Integrated Number-Colour relations for galaxies and stars from plate J3721.

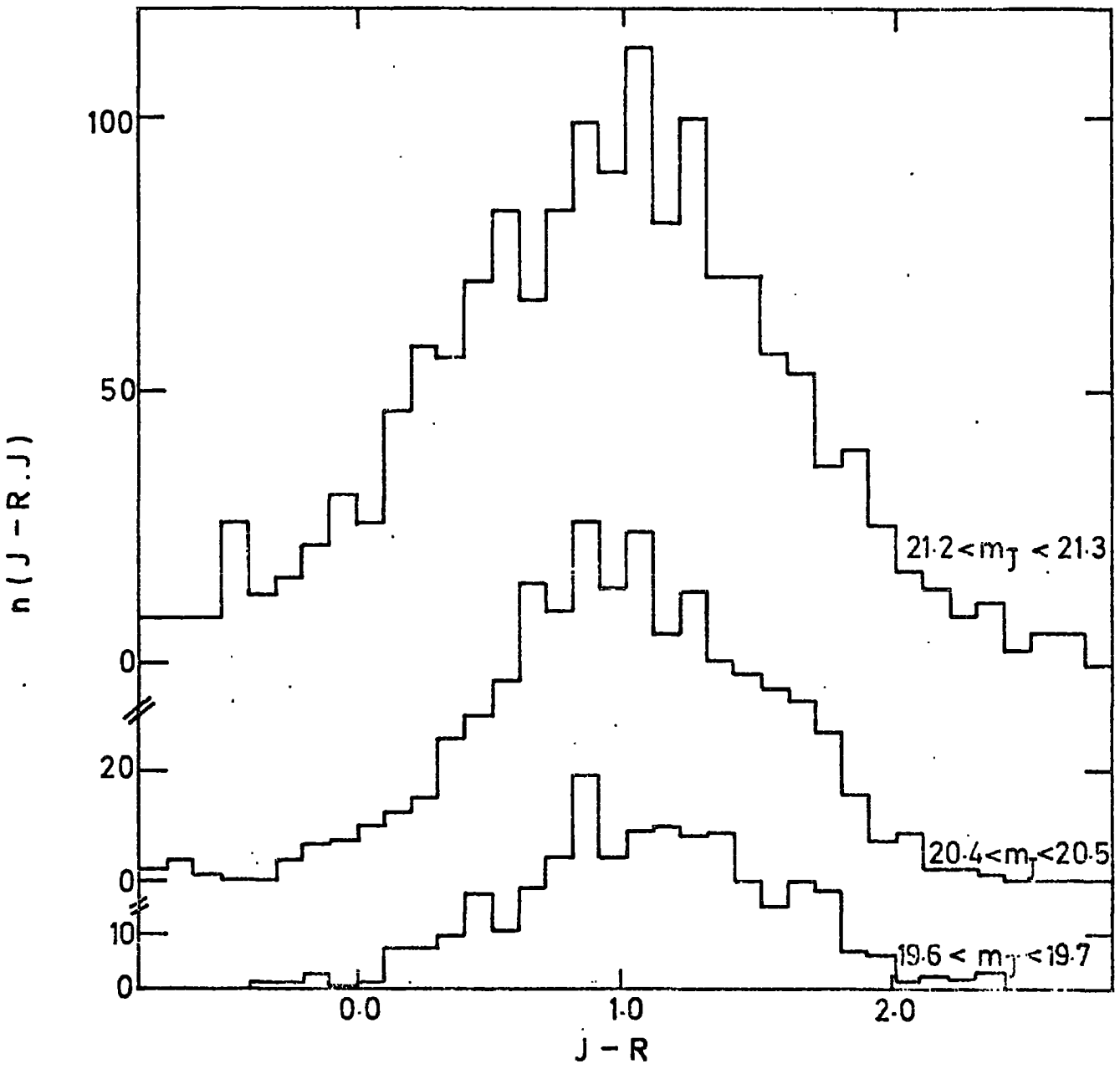

Figure 5.8 Observed n(J-R)'s in the J magnitude bins shown for galaxies on plate J3721. This can be looked on as a series of cross-sections across Fig.5.6.

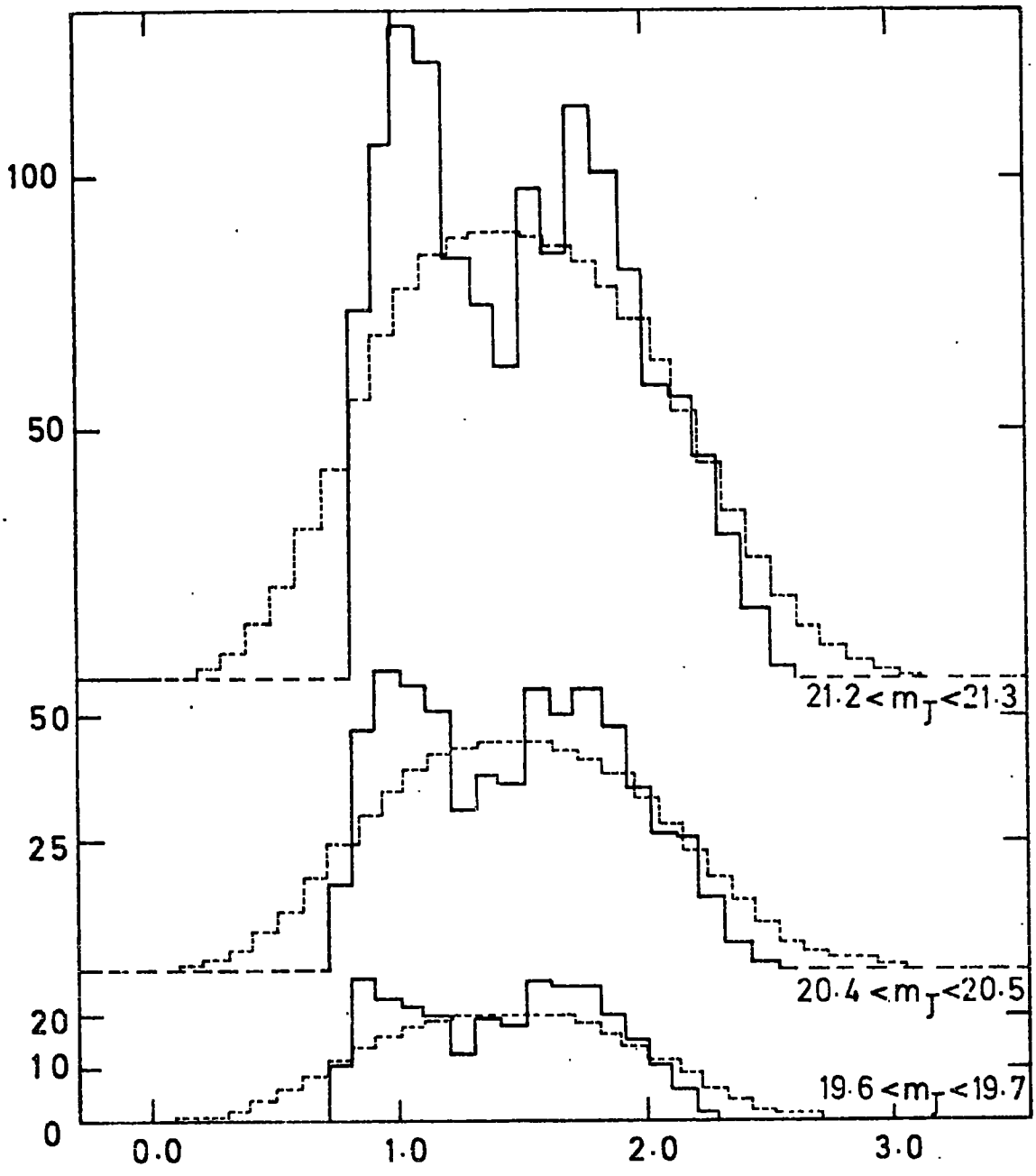

Figure 5.9a Predicted n(J-R)'s in J magnitude bins as shown, based on the Pence mix. Dashed line shows the prediction convolved with a realistic error function.

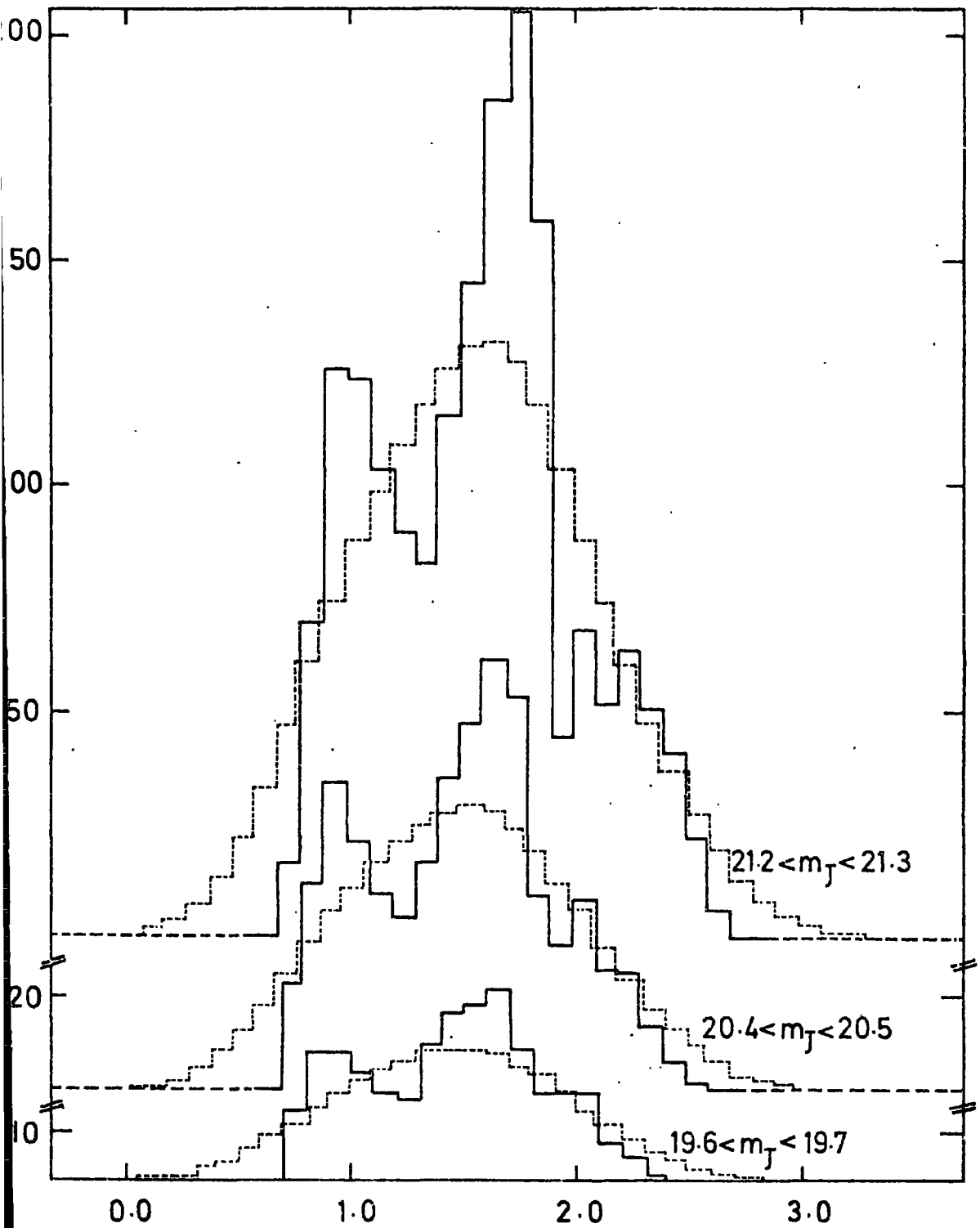

Figure 5.9b As 5.9(a) except predictions are based on the Pence mix + SSF luminosity evolution.

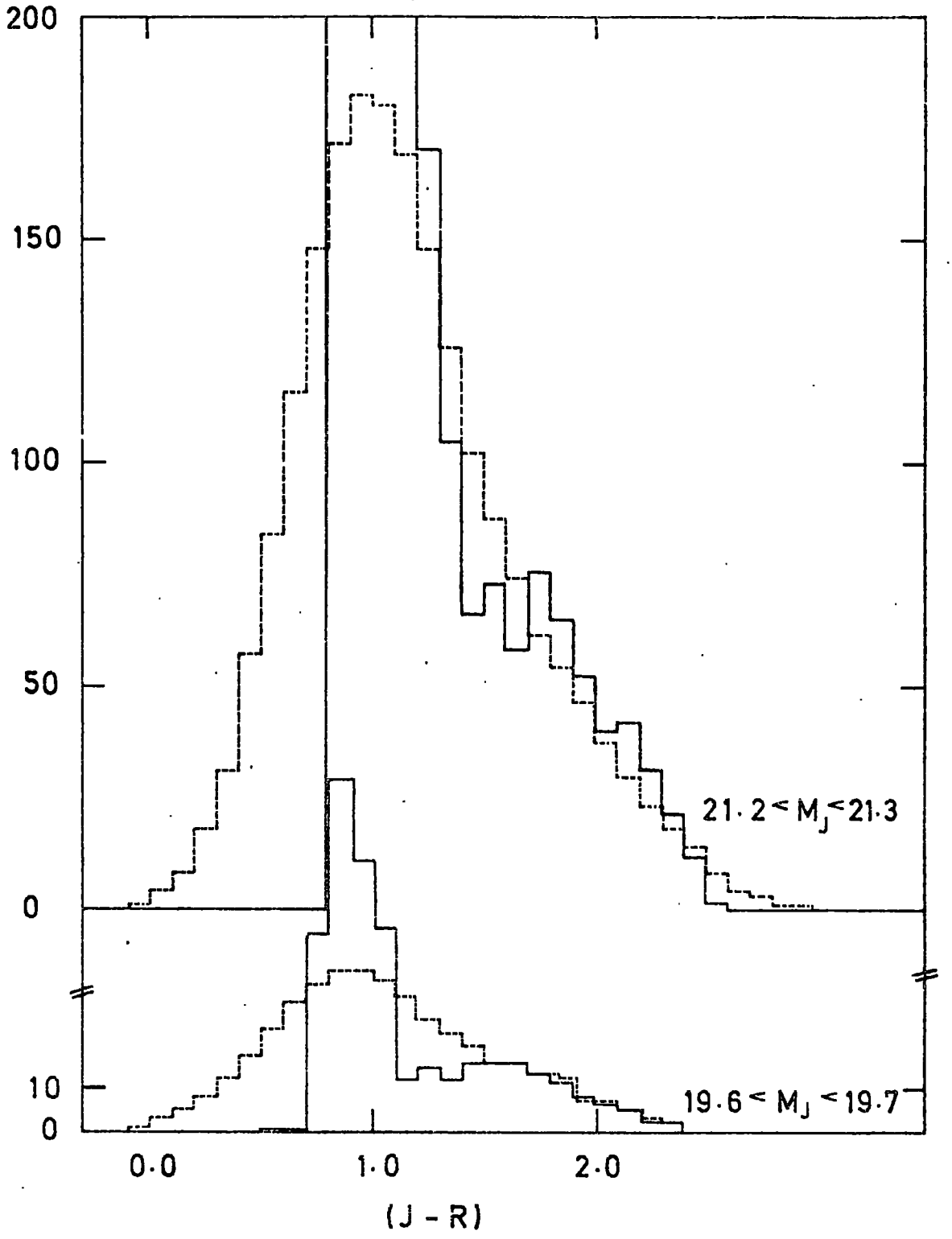

Figure 5. 9c As 5.9 (a) except predictions are based on the Tinsley mix (with no evolution).

data. The domination of blue late type spirals in the Tinsley mix produces too narrowly peaked a distribution at J-R = 1.0 for faint galaxies. The Pence mix with SSF evolution seems to produce too many red galaxies at faint limits because of its strong evolutionary brightening of ellipticals and SO's. The Pence mix with no evolution is the best of the three although it also peaks redwards of the observations. Because the effects of redshift are small at 19.5^m the difference between observation and theory here could be taken as evidence of an error in the absolute calibration in our (J-R) values of 0.2^m which would result in a redwards shift of the observed n(J-R) curves. Such an error is entirely possible in view of the uncertainties in our absolute calibration and is also suggested by comparison of our faint star colours with those of Kron (see Section 5.7). Even with this shift allowing the brighter galaxies to be fitted, the Pence mix still requires an evolutionary brightening in the blue passband of around 0.2^m for all galaxies to fit the n(J-R)'s at $m_J = 21.0$. Some sort of evolution was also required, it will be recalled, to fit the J number magnitude counts. Thus we may have some evidence from the galaxy colours that the form of the evolution is different from that predicted by Tinsley's SSF models. This evidence is made less strong because of the uncertainty in the accuracy of the K-correction models. However, the power of the galaxy colour distribution as a tool to investigate galaxy luminosity evolution has been shown. This power will be improved when machine measured plates in a wider range of colours become available.

Finally, since only an effective K correction term is required to scale the covariance functions we may, for this purpose, retain the Pence mix with SSF model as defining our standard J parameters.

5.6 GALAXY SELECTION FUNCTIONS

Using the standard parameters the n(z) diagrams are calculated (as in Ellis et al (1977)) and shown for samples limited at various magnitudes in J and R in Figures 5.10a, and 5.10b. Although the deep J and deep R samples contain roughly the same numbers of detected images it can be seen that the

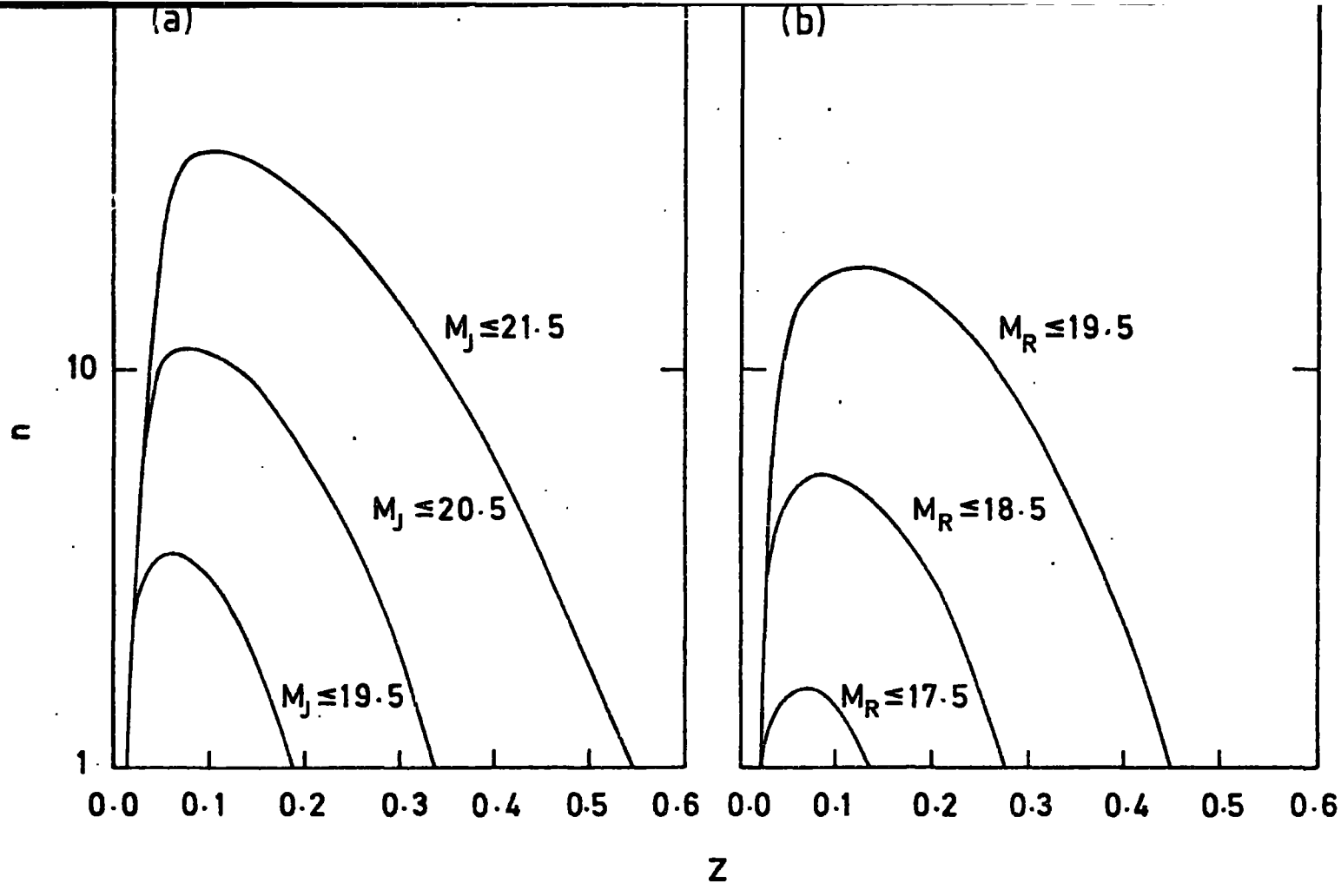

Figure 5.10(a) The number redshift relation predicted by the standard parameters for the J samples.

Figure 5.10(b) The number redshift relation predicted by the standard parameters for the R samples.

R n(z) peak is broader than its J counterpart. This is as a result of of the different effective K corrections in J and R. Also, it should be noted that especially in the deep samples the n(z) distributions are very wide.

Having obtained these n(z)'s the galaxy selection functions $\phi(z)$ for the samples can be calculated again as in Ellis et al. These are shown in Figure 5.11.

5.7 STELLAR n(m) AND n(J-R) RELATIONS

An interesting by-product of our galaxy cataloguing procedure is the creation of complete stellar catalogues. These are interesting because of the information they hold on stellar populations at the galactic poles. Much care must be taken with the stars since the COSMOS scale error has a worse effect on these than on galaxies. Therefore, we shall only consider stellar magnitudes fainter than 19.5^{m} in J where this scale error is small.

Firstly are presented the ensemble averaged n(m) counts for stars in J and R (see Figure 5.12). Comparing these two we see that at faint limits the R counts fall off substantially quicker than their J counterparts. This is consistent with the existence of a population of faint blue stellar images.

More evidence for such a population is brought out by considering the n(J-R) versus J diagram as shown in Figure 5.12. A double peaked colour distribution of stars with $m_J \lesssim 19.5$ can be easily seen. The movement of the bluer peak redwards at $m_J = 19.5$ is most probably the effect of the COSMOS scale error which becomes important for our J stellar photometry at about this point. However, the evidence for two populations of stellar images at fainter limits is clear. This result is consistent with the findings of Kron (1978) (again if allowance is made for the larger random

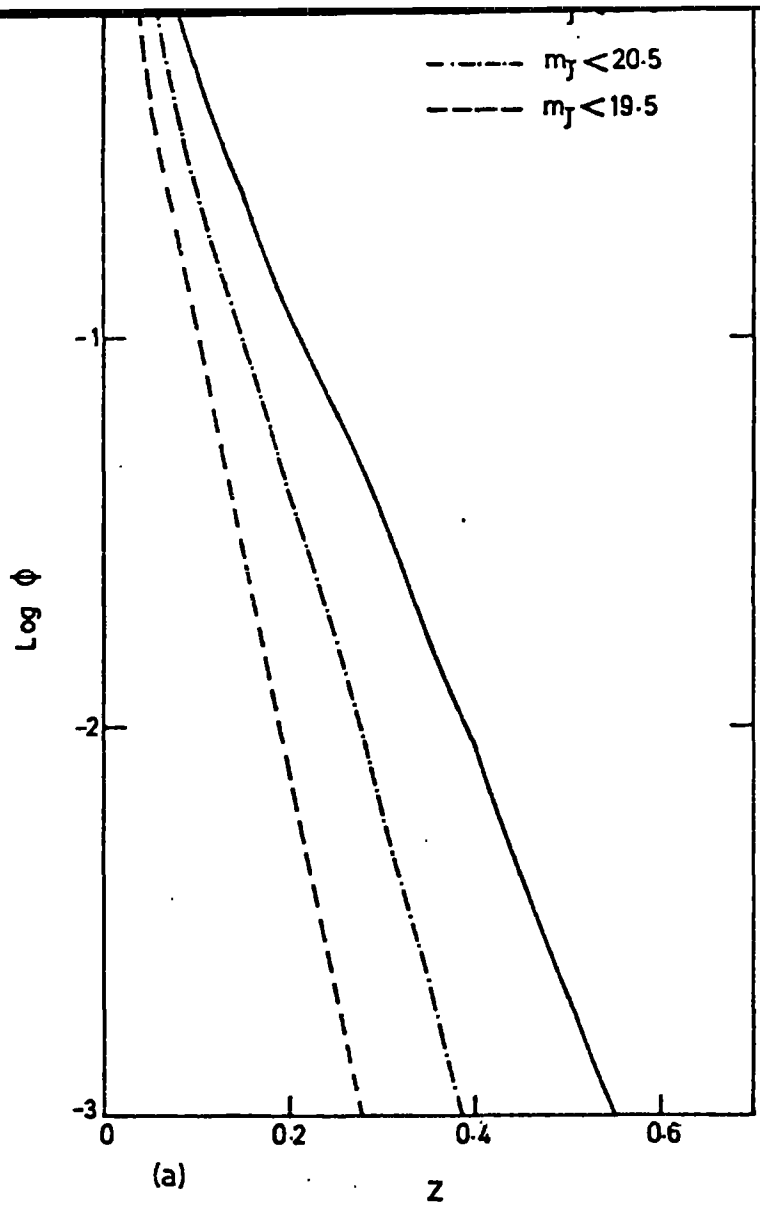

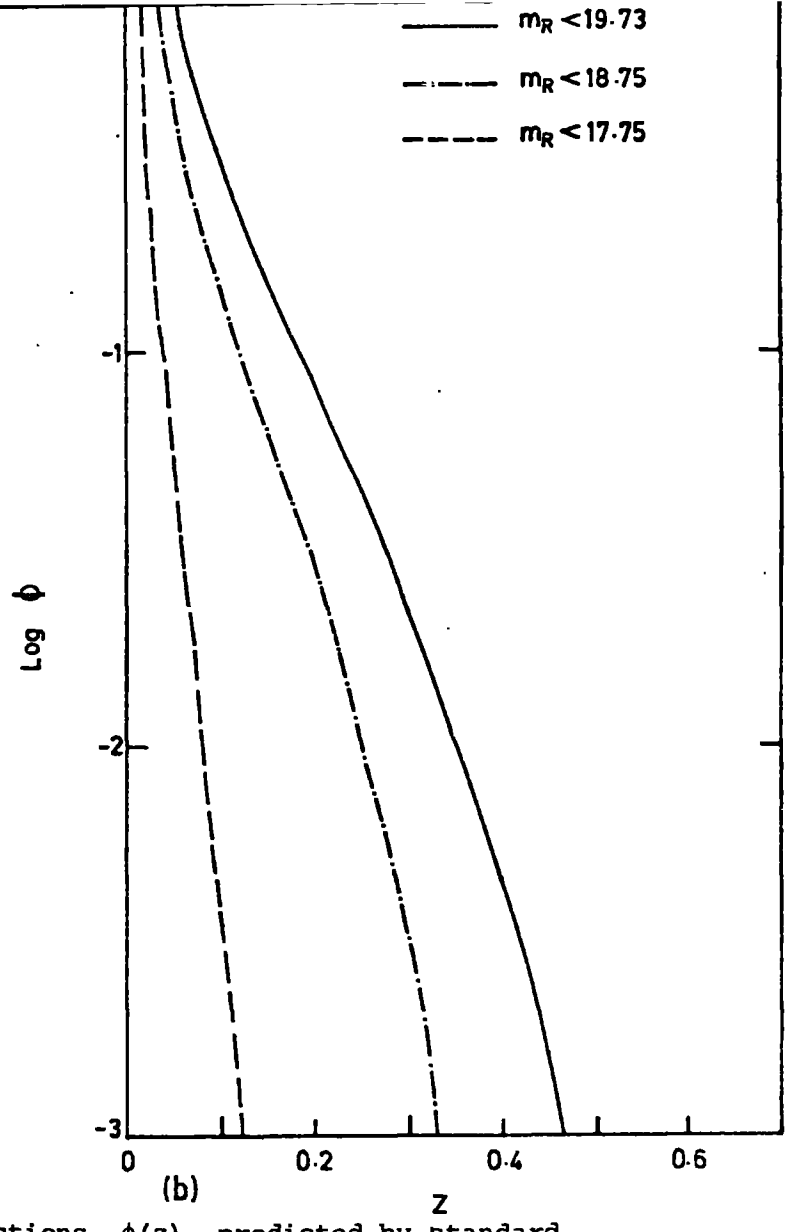

Figure 5.11(a) The selection functions, $\phi(z)$, predicted by standard parameters for the J samples.

Figure 5.11(b) The selection functions, $\phi(z)$, predicted by the standard parameters for the R samples.

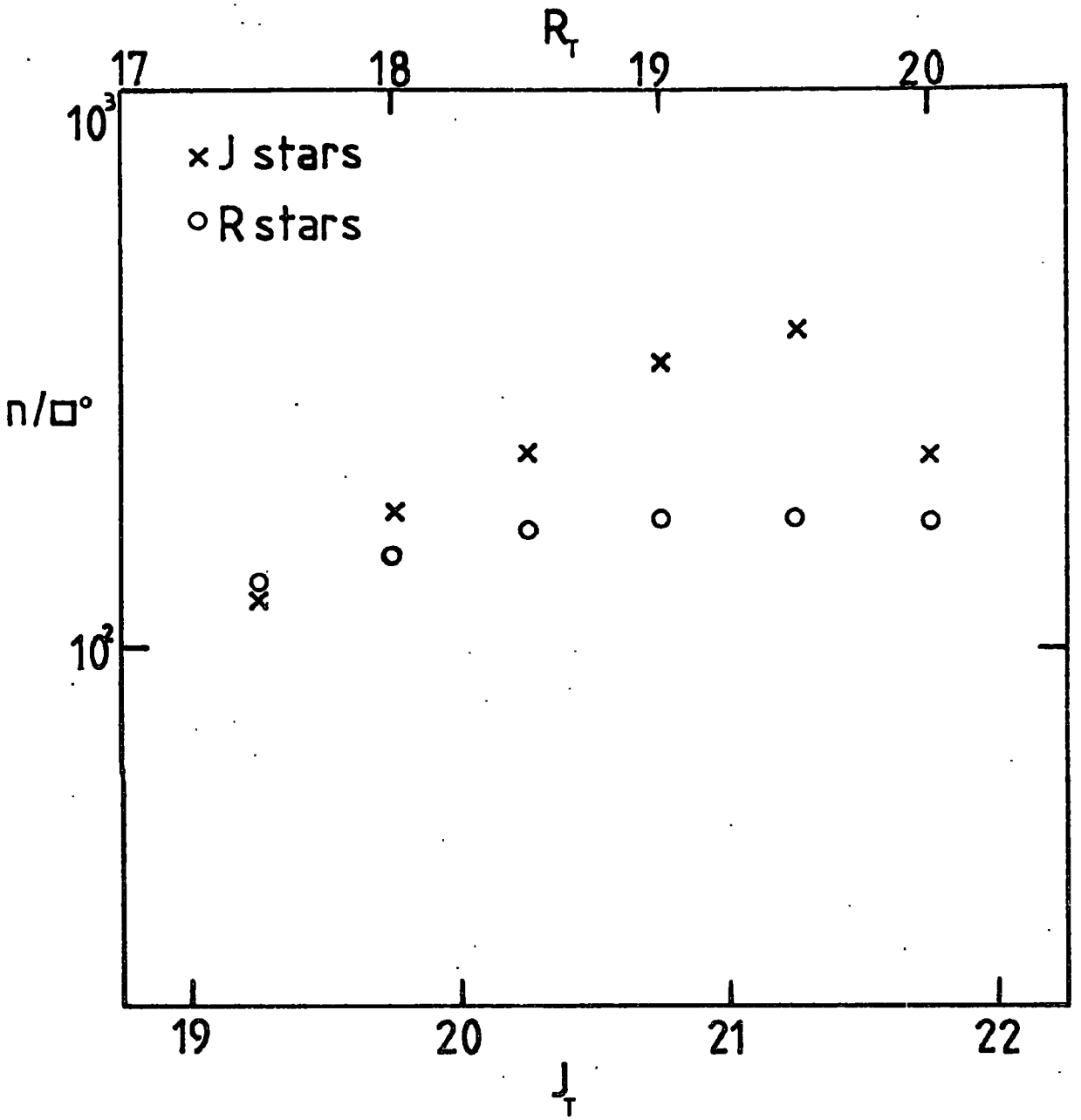

Figure 5.12 Observed, differential, stellar number magnitude relations in J and R from the UKST samples.

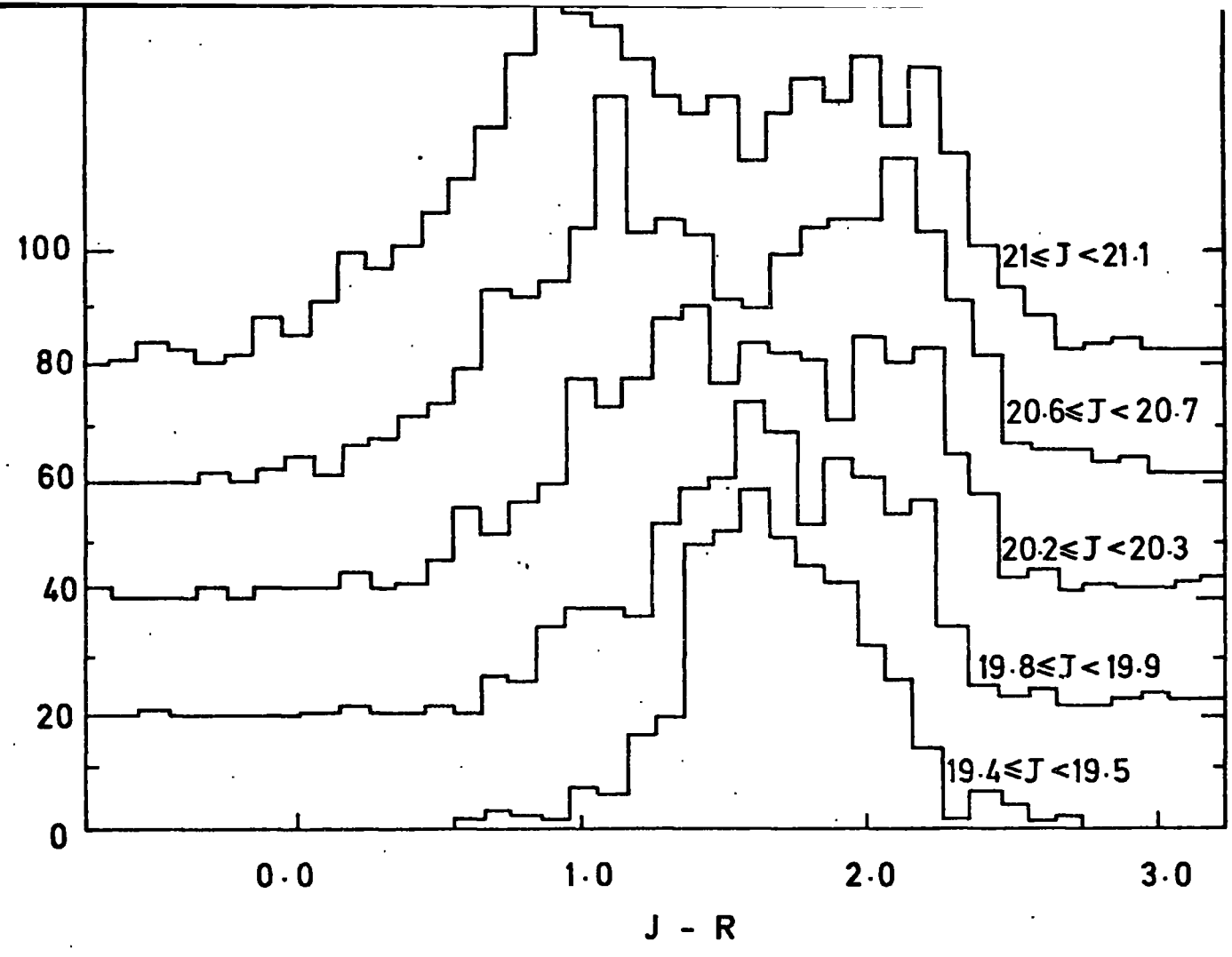

Figure 5.13 Observed n(J-R)'s in the J magnitude bins shown for stellar images on plate J3721. Note the double peaked distribution at faint magnitudes. This is consistent with the results found by Kron(1978).

errors in our photometry) who also found a double peaked distribution (see his Figure 26). The red peak in Kron's data occurs at B-V $\sim$1.6, suggesting that it may be identified with a population of main sequence M type dwarfs. These would have J-R $\sim$2.2 whereas the peak in the present data lies at J-R $\sim$2.0 supporting the possible 0.2^m absolute calibration error suggested earlier.

Initially, it was thought that the bluer peak might have consisted of quasars. However, the number of blue objects seen at m_J <20, is much more than the number of quasars expected at this limit. Also, inspection of some of the brighter images from this peak on an objective prism plate revealed that few of these images were quasar candidates. It is much more likely that these images are galactic stars. The blue peak here is centred on J-R $\sim$ 1.0 corresponding, roughly, to Kron's blue peak at B-V $\sim$ 0.6. Stars of this colour can be identified with G type dwarfs. The identification of these two populations of stars is supported by the findings of Morton and Tritton (1979) who, using various spectroscopic methods also find that the most numerous gypes of stars at faint apparent magnitudes are G and M types.

If this classification is correct then the M types have absolute B magnitude, 9^m, which if Kron's data is to be believed, places them at up to 10 kpc away from the galactic plane. The G types have absolute B magnitudes 5.5 which places them even further away, in the range 5 $\rightarrow$ 50 kpc. This is very good evidence for the existence of a large halo of old stars, extending to distances of 50 kpc above the galactic plane. The angular distributions of these two populations will be investigated in the next Chapter.

CHAPTER SIX

CORRELATION ANALYSES

6.1 INTRODUCTION

In this Chapter we investigate the distribution of galaxies in the deep catalogues by measuring the 2-point galaxy correlation function, $w(\theta)$. Much information of importance to cosmological theory can be gained by comparing the results obtained from the deep samples with those obtained in the shallower catalogues. These comparisons (sometimes called "scaling tests") are of interest both at small angle and at large angle.

At small angle the shallower catalogues give a reasonable -0.77 power-law for the dependence of $w(\theta)$ with θ and this is also the form expected from the $w(\theta)$ of the deep samples. Using the selection functions found in Chapter 5 it is possible to compare through Limber's formula the amplitudes of the power-law found in deep and shallow catalogues. Limber's Formula is derived making the assumption of the homogeneity of the galaxy distribution over the largest scales ($\gtrsim$ 50 h^{-1} Mpc) and thus scaling, at the broadest level, forms a test of this assumption. An example of the type of inhomogeneous model being tested is one where the nested clustering of the CH model is extended to arbitrarily large scales (see de Vaucouleur's (1971) and Wesson (1976) for discussion of this cosmological model).

At a more detailed level the scaling of the covariance amplitudes can test for dynamical evolution in galaxy clustering at small separations, over the lookback time of the sample. The successful execution of such a test demands high precision of the selection functions estimated in Chapter 5 from the number counts (and the remarks in Section 5.4 over the number counts reliability must be remembered here). Given this condition any

small discrepancy between prediction and observation could only be interpreted in terms of clustering evolution.

Phillipps et al (1978) considered a simple model for ξ's possible redshift dependence of

$$\xi(r,z) \quad \alpha \quad \left(1 + z \right)^{-\beta} \quad \xi(r) \qquad (6.1)$$

with β taking the values 0 or $\pm$ 1. We shall define β = 0 to be the no-evolution case. Here clusters stay fixed with time in proper coordinates. The value β = 1 corresponds to the case where clusters expand with the universe and β = -1 to the case where clusters are collapsing at the same rate as the universe is expanding. These latter two values for β are regarded as giving upper limits to physically acceptable models of clustering evolution. The β = 0, no evolution, case corresponds to the isothermal theory picture because this theory predicts that the most highly non-linear levels of its hierarchical galaxy distribution will be in virial equilibrium and therefore stable in proper coordinates. The adiabatic theory's predictions for clustering growth is more vague but it is felt that since the protoclusters collapse along only one axis, expansion with the Hubble flow may continue along the others and so perhaps the β= 1 value may be the most relevant here. Amplitudes of $w(\theta)$ in the deep samples can then be calculated for the different β values by inserting the appropriate $\xi(r,z)$ from equation (6.1) into the relativistic Limber's formula (see Phillipps et al).

These techniques were first applied by Phillipps et al to a sample of about 3000 galaxies contained in machine measured scans of a 2 square degree region of a J-R platepair of the same Schmidt field. Small angle scaling tests revealed a puzzling discrepancy of $\sim$ 2.5 in both passbands

in the sense that the deep samples appeared to be less clustered. The uncertainty in the selection effects was thought to be insufficient to resolve the discrepancy. Also the amount of evolution needed to fit the data was of such a size as to be entirely unphysical. It was concluded that sampling problems were the most likely explanation. Initially, it was not known how large an area of sky would be required to make a deep sample "fair" for this purpose. Here each of our samples comprise an area approximately 7 times that of Phillipps et al.

With this increase in sample size, it is now also possible to check the reproducibility of the feature at large angle found by Groth and Peebles' (1977) in their correlation analysis of the Lick Catalogue. The possible existence of such a feature is an exciting prospect for theories of galaxy formation since it may define a characteristic scale of clustering. As indicated in Chapter 1 both adiabatic and isothermal theories make q_o dependent predictions for the position of such a break. Assuming such a break exists then it is also important to investigate the asymptotic slope of $\xi(r)$ past the feature. In the isothermal theory, at least, this holds clues to the early distribution of matter in the universe. It is therefore very important to establish whether this feature is real, that is, produced by true spatial clustering, or whether it results from systematic effects operating in the Lick Catalogue (although Groth and Peebles give arguments against this latter possibility). In the long term, it may be possible to obtain $\xi(r)$ directly by analysing complete redshift catalogues (see Kirshner et al, 1979). However, present redshift samples are too small to allow an unequivocal estimate of $\xi(r)$ to be made at the scales of interest. Also estimation of $w(\theta)$ rather than ξ has the advantage that

its normalization (and thus its estimated form) is independent of assumptions about the absolute space density of galaxies although, of course, estimates via $w(\theta)$ of the spatial position of the feature are not . A crucial test of the reality of any feature found in this way will be to see how it scales both internally, within our deep samples, and also with the Groth-Peebles feature.

Thus our investigation into the behaviour of $w(\theta)$ at these depths divides principally into two parts, the behaviour at small angle and the behaviour at large angle. After first describing in Sections 6.2 to 6.4 the particular estimation procedure used for $w(\theta)$ we consider the small angle results, their scaling behaviour and implications of the results for theory in Sections 6.5 to 6.8. We then go on to discuss the estimates and scaling at large angle in Sections 6.9 to 6.11.

In addition, we also discuss in Section 6.12 the correlations found in colour subsamples of the galaxy samples. In Section 6.13 is presented a brief description of the correlations arising from the stellar images in the deep samples. Finally in Section 6.14, the main conclusions from the correlation analyses are summarized.

6.2 ESTIMATION OF THE ANGULAR CORRELATION FUNCTION

The estimation of the angular correlation function, $w(\theta)$, was done in two parts using two of the estimators described in Chapter 2. For angular separation $\theta<0.1^{o}$, we first computed the number of pairs of galaxies in bins of constant width $\Delta\log\theta$, excluding those galaxies which fell in the drilled regions. The same number of points were then randomly distributed over an identically drilled area and the procedure repeated.

The resulting estimator is

$$w(\theta) = N_d(\theta)/N_r(\theta) - 1 \qquad (6.2)$$

where N_d is the number of actual pairs at separation θ and N_r the equivalent for the random distribution.

For larger angles, $\theta > 0.1^\circ$, the galaxies were first binned into 64 x 64 bins of size $\sim$12 arcmin^2. Taking the galaxy separation as the distance between bin centres, the covariance function for this region was estimated using the relation

$$w(\theta) = N_p(\theta) \; / \; (N_b(\theta)\bar{n}) - 1 \qquad (6.3)$$

where N_p is the total number of pairs computed in the separation range $(\theta - \Delta\theta/2, \; \theta + \Delta\theta/2)$, $N_b(\theta)$ is the number of bins used to find N_p and $\bar{n}$ is the average number of galaxies per bin. Any bin that overlapped a drilled region was excluded.

6.3 UNFILTERED RESULTS

Using these estimators we obtain the correlation function given in Figure 6.1 for the 5 plates. Although the estimates agree at small angles they differ markedly for $\theta > 0.1^\circ$. In this region the correlation functions show a change to steeper slope for the pair J3721/R2775 and for J1916. However, the function here falls only slowly for the J-R pair J1920/R3780. The consistency of the J and R correlation functions for each field suggests that this difference is <u>not</u> an artefact of photographic or measurement faults on individual plates.

It might be argued that the difference is caused simply by statistical fluctuations in the distribution of galaxy clusters and

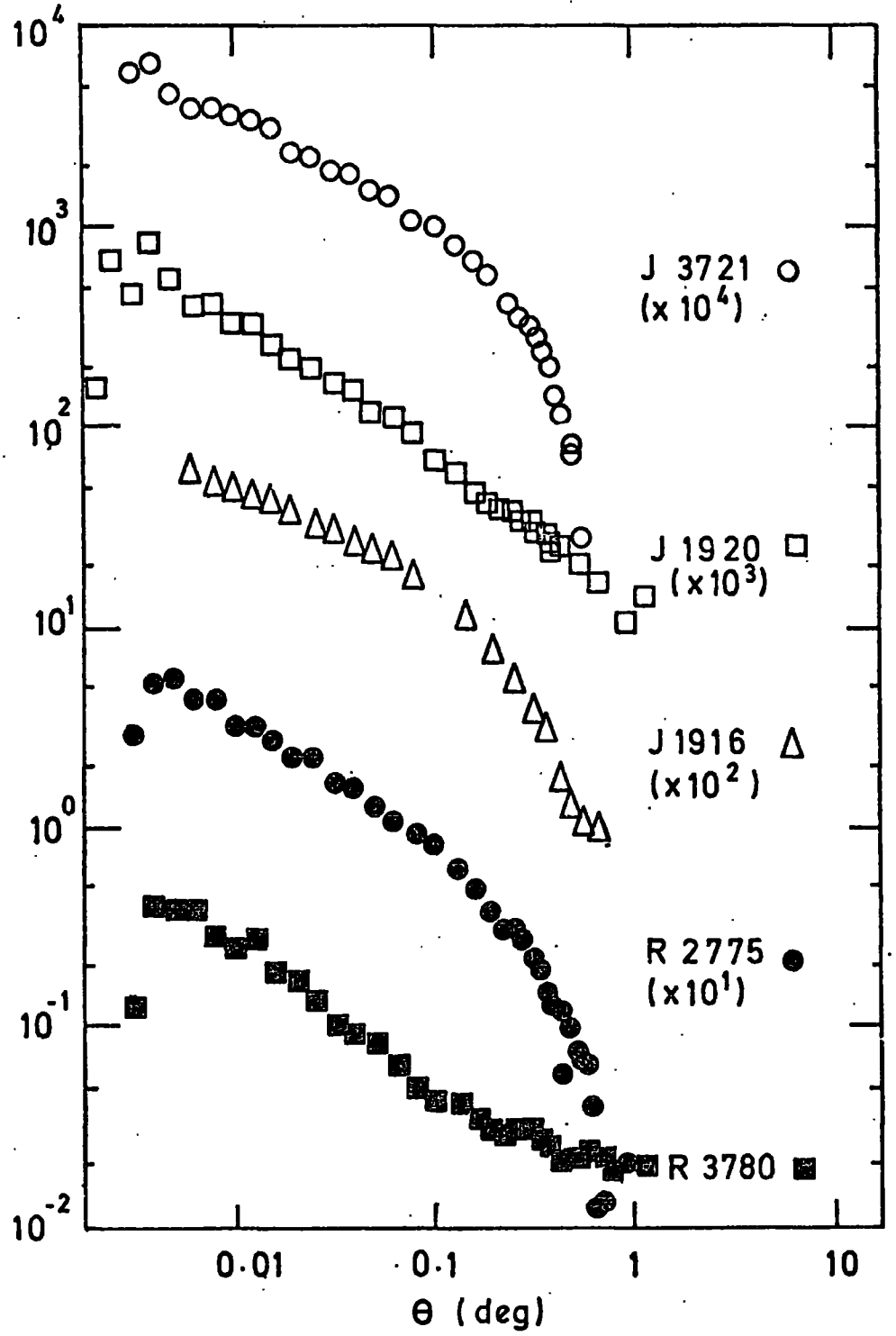

Figure 6.1 Unfiltered angular correlation functions for galaxies on the five plates listed in Table 4.2 The samples are limited at J = 21.5 and R = 19.75. The estimates are separated in the ordinate for clarity. Estimates of plates J1920 and R3780 (both field 412) show a different form to those for the other plates.

therefore only provides evidence that our samples are not "fair". However, this explanation is most unlikely since the difference occurs at a scale of only 0.1 times the dimensions of the measured area.

Figure 4.10a shows the galaxy distribution for plate J1920. It reveals a striking gap in the distribution of more than 3^{o} in length and 0.5^{o} in width stretching in a north westerly direction. This deficiency will make other areas of the plate look overdense on large scales and hence raise $w(\theta)$. The gap can also be seen in the galaxy distribution on plate R3780, though, in this case it is less pronounced. In contrast the galaxy distribution on plate J3721 is relatively flat on the largest scales.

To test whether an absorbing cloud may be responsible for this deficiency on the field of J1920/R3780, the extinction in the J and R passbands (C_J and C_R respectively) were calculated from number magnitude counts. Comparing counts inside and outside the gap we obtain $C_J = 0.25 \pm 0.05$ mag. and $C_R = 0.12 \pm 0.05$ mag., consistent with reddening produced by interstellar dust (Allen, 1973). If such an absorbing cloud does exist then the uniformity of the stellar distribution on this field suggests that it lies at some distance from the galactic disk. Efforts are now being made to obtain 21 cm observations which will hopefully clarify the origin of this interesting feature.

Thus there is some reason to believe that an effect not intrinsic to galaxy distribution is operating on the largest scales on the field of J1920/R3780. The best estimates of $w(\theta)$ are therefore, not given by Figure 6.1, but by an estimator applied to the data after it has first been filtered to remove this induced large scale gradient.

6.4 FILTERED RESULTS

A "moving average" filter was applied to the data by replacing n_{ij}, by the smoother counts

$$n'_{ij} = \bar{n}\, n_{ij}/f_{ij} \qquad i,j = 1, \ldots.64 \tag{6.4}$$

Here, $\bar{n}$ is the average count per bin over the entire area and f_{ij} is the average count per bin in the occupied area within the immediately surrounding 32 x 32 bins (i.e. 1.9° x 1.9° area). The estimator of eqn.(6.2) is then applied using n'_{ij}. For small θ the same f_{ij} is used, except that in this case, $\bar{n}/f_{ij}$ weights each point (both in the data and the random distribution) before applying eqn.(6.1).

Figure 6.2 shows the filtered estimates for $w(\theta)$. At small scales there is little change from the unfiltered results for any of the plates. As expected, the estimate for J3721 is unchanged even at large scales. However, the new estimates for J1920 and R3780 now correspond well with those from the other two fields.

The appearance of a change in slope at the same scale length as that seen on the other two fields is not formed by the action of filtering. We show this by considering averaged results from four 2-dimensional simulations. These simulations consist of distributing 20000 objects in uniform clusters with cluster centres randomly placed over an area similar to those of the samples. The clusters have 100 objects each and have diameters of 0.8°. The averaged $w(\theta)$'s computed from these simulations by our unfiltered estimator are shown in Figure 6.3 alongside and in agreement with the analytically calculated $w(\theta)$ for this model (see Section 2.3). These $w(\theta)$'s are of comparable magnitude to the observed. Simulations were also done which were similar to the above but contained

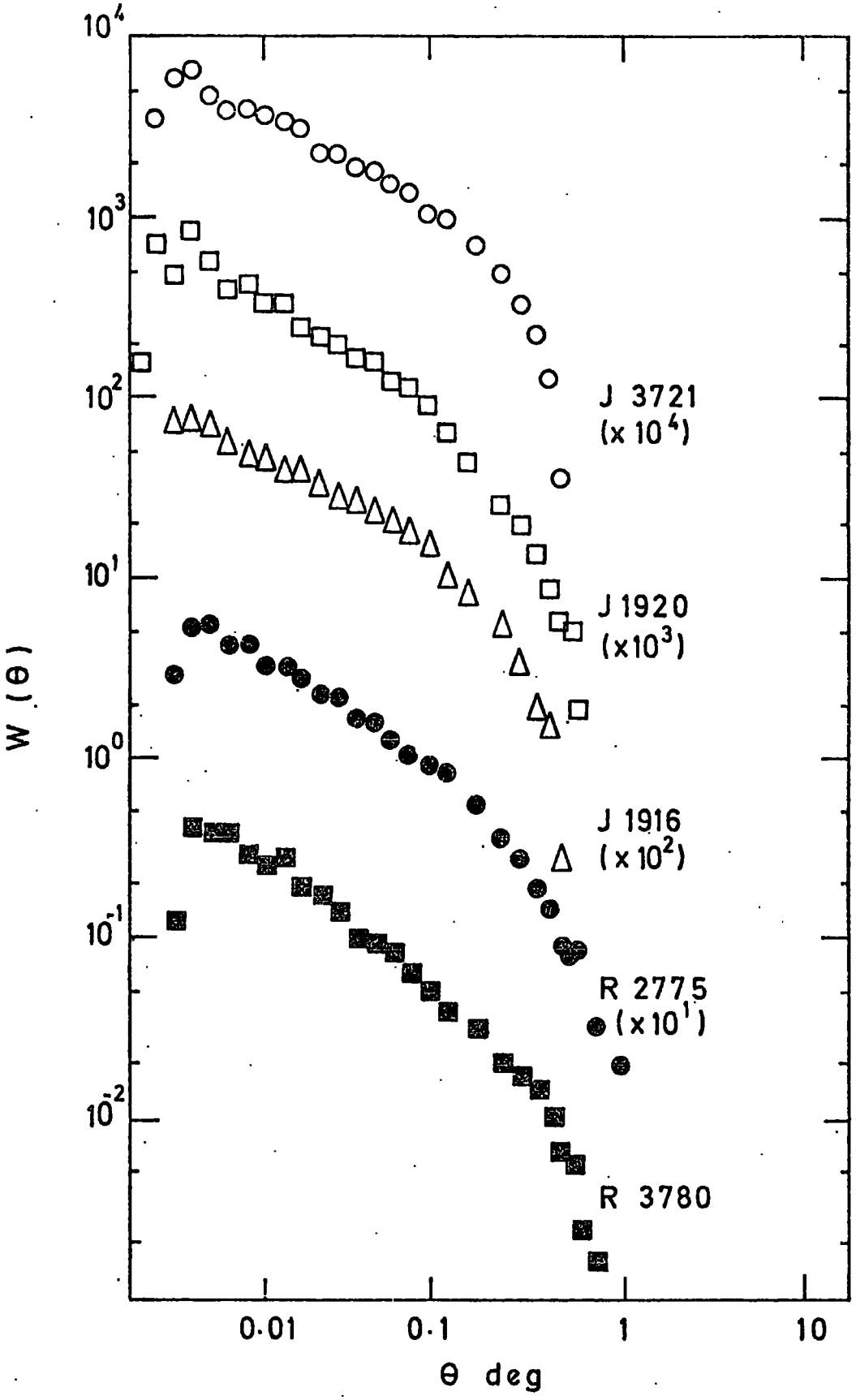

Figure 6.2 Filtered angular correlation functions for galaxies presented as in Figure6.1. Each estimate shows evidence for a feature at θ ∿0.3 degree.

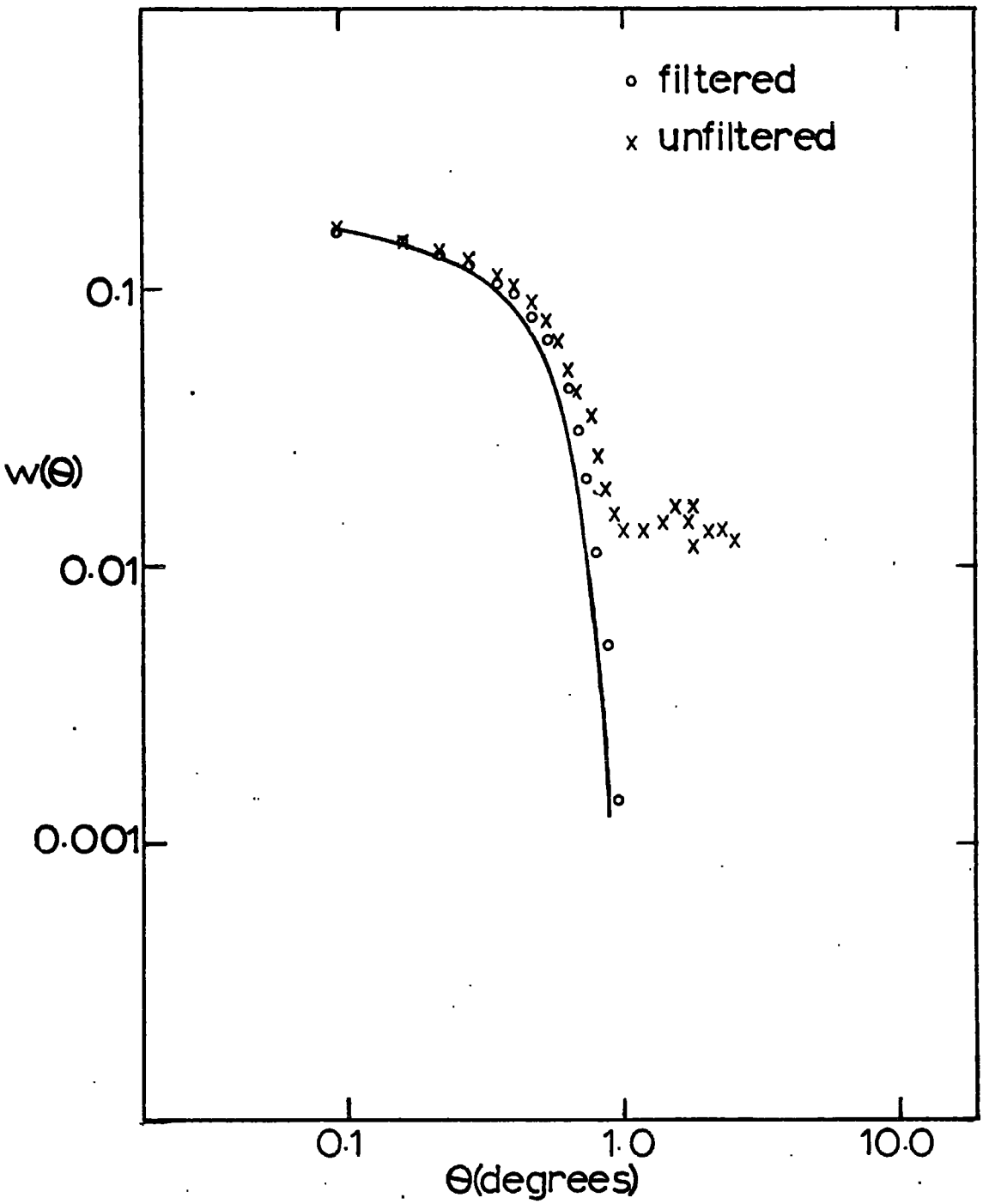

Figure 6.3 Testing the filter. The solid line represents the analytic result for a clustering process of randomly distributed 0.8° diam. clusters with 20 members uniformly distributed in 2-dimensions inside each cluster. The average density and level of clustering is similar to the data's. The crosses represent the average covariance function estimated from 4 unfiltered simulations of this process but which has a large artificial "zone of avoidance". The open circles represent the average covariance function obtained after filtering in the same manner as for the data.

a "zone of avoidance". This meant that in $\frac{1}{4}$ of the sample area there was only a $\frac{3}{4}$ chance of accepting a generated object. This gives rise to a large-scale density inhomogeneity, similar in size to that shown by the J1920 field. Thus shown also in Figure 6.3 are the estimates of $w(\theta)$ from filtered and unfiltered estimators. The unfiltered results display large scale behaviour like that found from the J1920 field whereas the filtered results show good agreement with the "true" $w(\theta)$ arising from the small scale clustering component even to scales as large as $\sim 0.8^{\circ}$. The filter has had only a negligible effect on scales smaller than this. It has certainly produced no break at $\theta \sim 0.3^{\circ}$ as was obtained from plate J1920 and thus this feature's existence seems independent of the filtering procedure.

Thus it appears that $w(\theta)$ is reproducible for $.005^{\circ} \lesssim \theta \lesssim 1^{\circ}$ on all 5 plates of 3 different fields. This, of course, does not preclude the possibility that some subtle systematic effect is conspiring to produce a common behaviour. The fact, however, that unfiltered results from J-R plate pairs of the same field give consistent results shows that if any such systematic effects are present, they do not dominate our estimates. Finally, it is worth noting that the same correlation results were obtained from independently reduced MM data for J3721.

In Figure 6.4 we show the ensemble averaged <u>unfiltered</u> correlation functions for the three J plates cut at limiting magnitudes of 19.5, 20.5 and 21.5. Their filtered counterparts are shown in Figure 6.5a. The similarity between the two sets is because the filtering is only necessary for one field. Figure 6.5b shows the ensemble averaged correlation functions for the two R plates at limiting magnitudes of 17.75, 18.75 and 19.75. In Figure 6.6 are also shown the filtered, ensemble averaged results for two J "slices" - samples limited in magnitudes, $19.5 \lesssim m_J \lesssim 20.5$

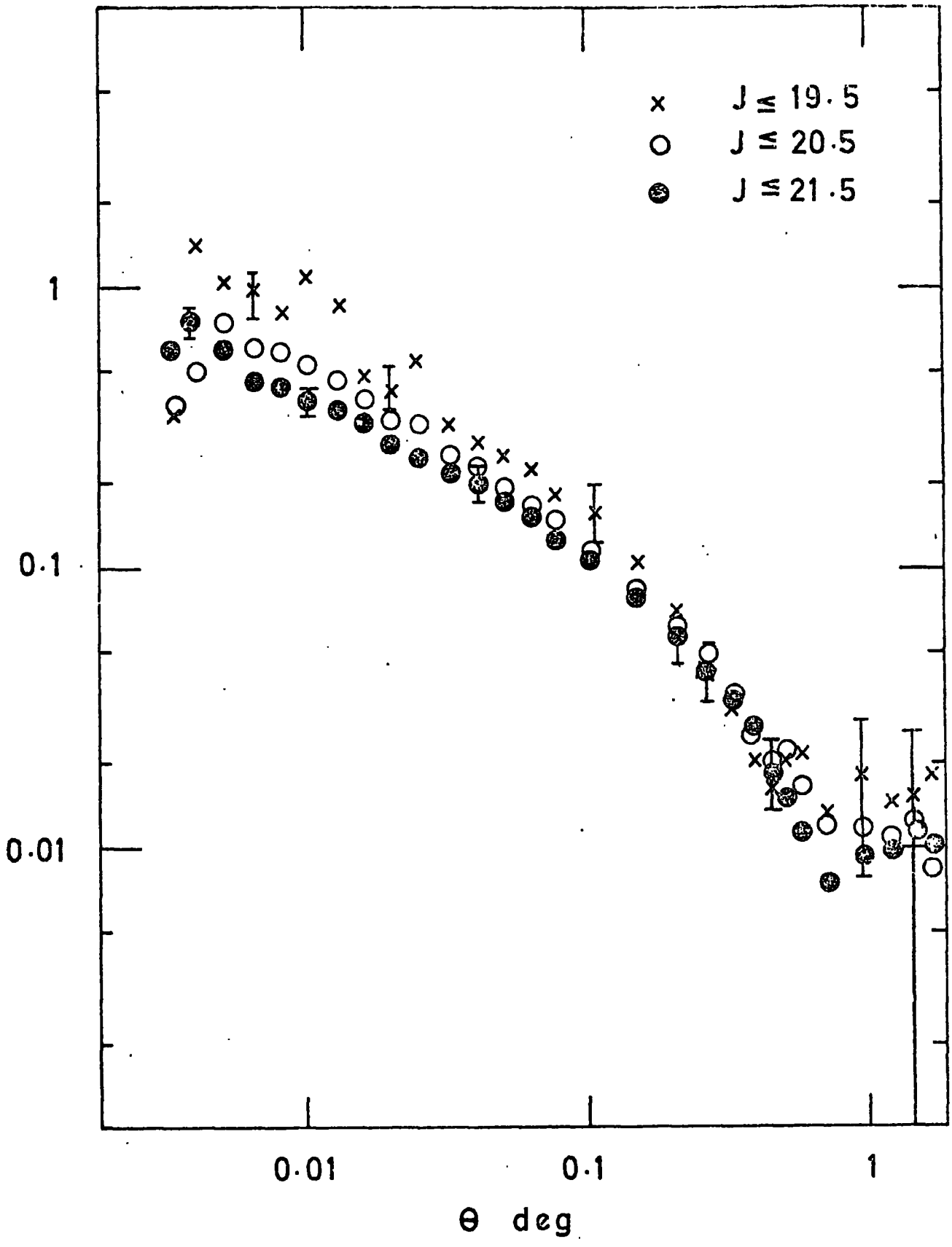

Figure 6.4 Unfiltered ensemble - averaged angular correlation functions limited at various magnitudes for the 3 J plates. Typical empirically-determined error bars are displayed.

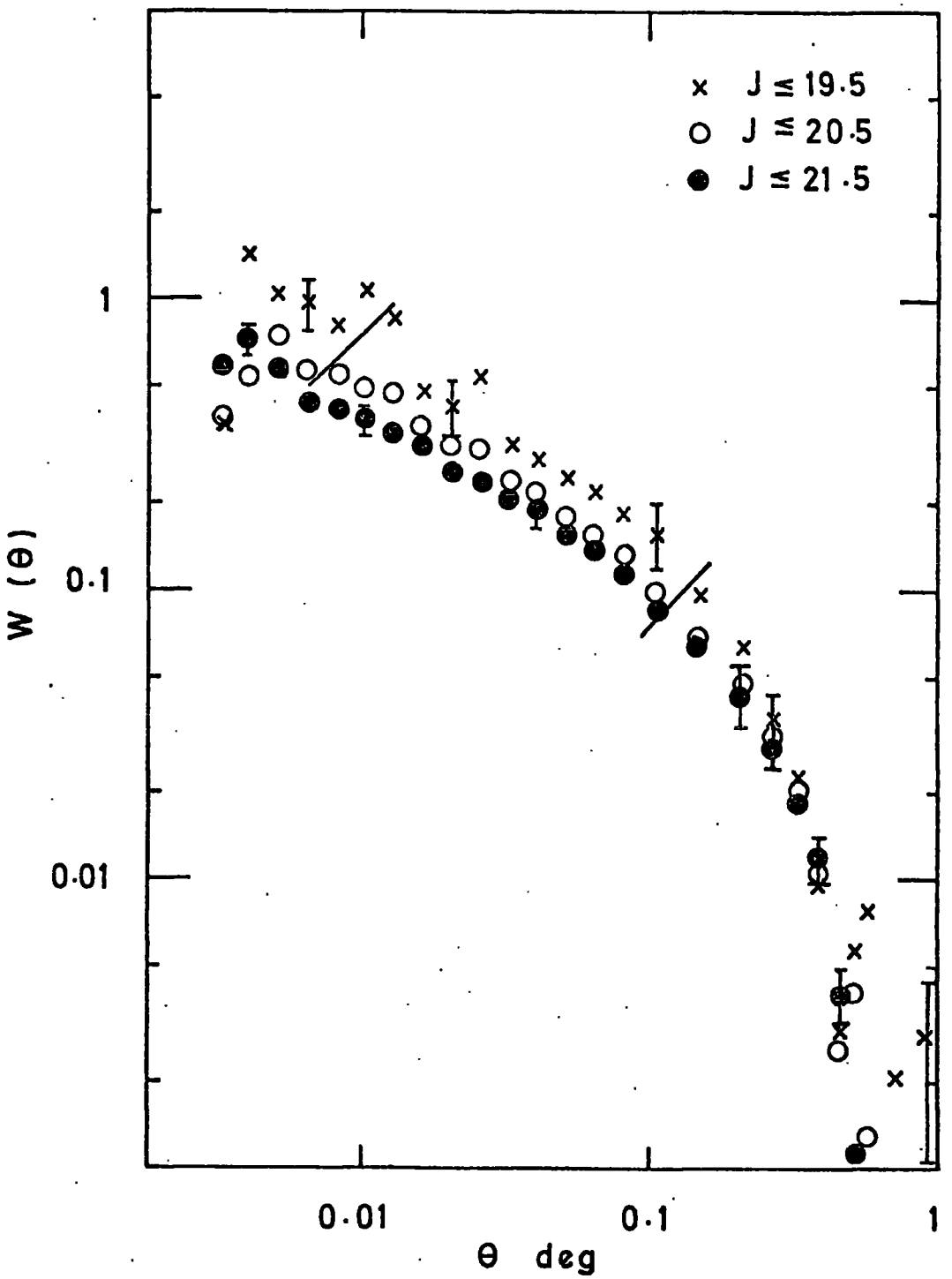

Figure 6.5 (a) Filtered ensemble-averaged angular correlation functions at various limiting magnitudes for three J plates. The solid lines show therange over which power-laws were fitted for the scaling comparisons.

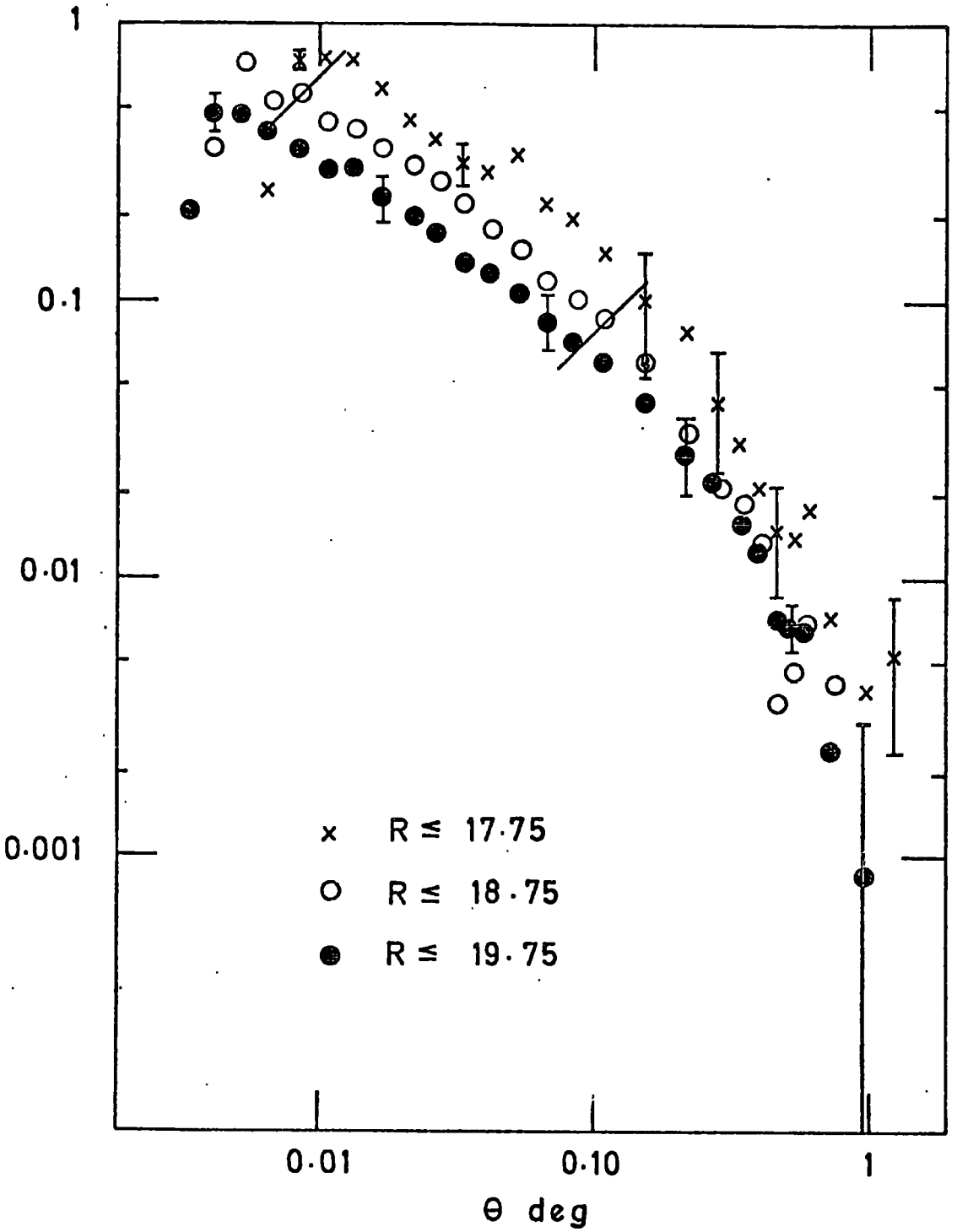

Figure 6.5 (b) As Figure 6.5(a) for the R plates.

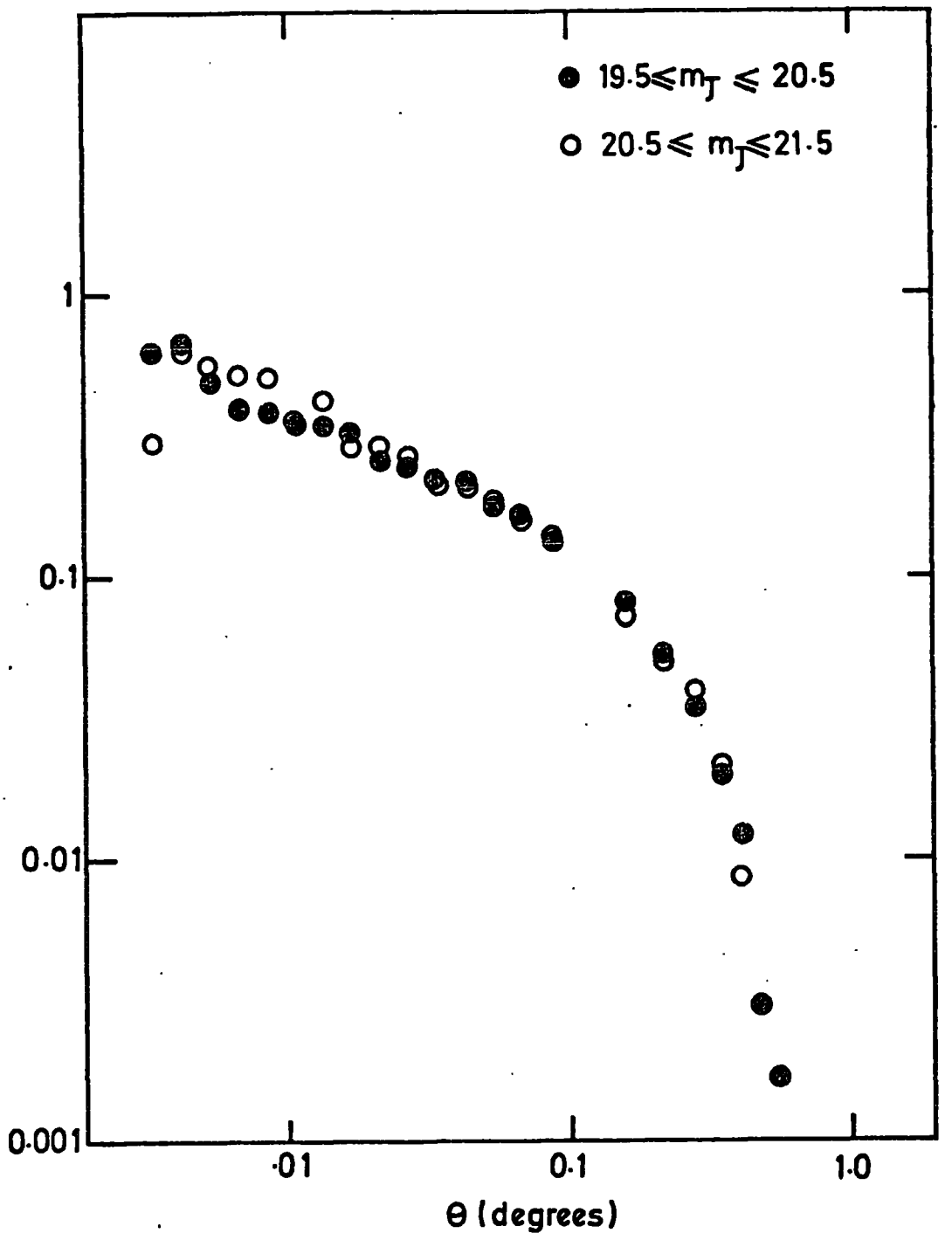

Figure 6.6 Ensemble averaged 2-point galaxy correlations for the J plates in the magnitude ranges shown. The small angle slopes here are much less steep than for shallower J samples (see Table 6.1).

and $20.5 \lesssim m_J \lesssim 21.5$. Empirically determined error bars are given where appropriate.

6.5 SMALL ANGLE POWER LAW FITS

It is important to compare correlations for the different samples in a consistent manner. This is difficult because, although power-laws always give reasonable fits to our results, the index of the best fitting power-law, is not always that obtained for shallow samples. To enable comparisons via Limber's formula, we fitted a -0.8 power-law at each depth over a fixed range of spatial separations. The spatial distances were calculated from the angular separations by assuming an effective angular diameter distance for each sample. The fitted range is indicated in Figures 6.5. The correlations at small angular separations should not be affected by machine problems since, even for the J <19.5 sample, 95% of the galaxies have an isophotal angular diameter greater than the lower θ limit. The large θ limit is carefully placed so as to avoid any problems with the steepening of $w(\theta)$ at large scales.

Table 6.1 gives the best fitting amplitudes A for the form

$$w(\theta) = A\theta^{-0.8} \qquad (6.5)$$

A was fitted using log-log least-squares techniques. The best fitting power-law indices δ, and their corresponding amplitudes B for the more general form

$$w(\theta) = B\theta^{-\delta} \qquad (6.6)$$

are also given in the Table. These were also fitted using a log-log least squares procedure. In most cases we give the empirically estimated standard errors found from averaging the individual fits to each curve

TABLE 6.1

Correlation Amplitudes

Sample	N	A(δ = 0.8) (corrected)	δ	B
J				
M_J<19.5	182.2± 1.5	(2.89 ± .467)x10^{-2}	-0.73±.076	1.41x10^{-2}
M_J<20.5	530.9±17.9	(1.88 ± .213)x10^{-2}	-0.67±.023	5.71x10^{-2}
M_J<21.5	1478.3± 83.9	(1.50 ± .166)x10^{-2}	-0.57±.025	8.24x10^{-2}
19.5<M_J≤20.5	358.2± 8.3	-	-0.55±.032	2.31x10^{-3}
20.5<M_J≤21.5	933.6± 41.8	-	-0.47±.032	1.19x10^{-3}
R				
M_R<17.75	146.5± 20.5	(2.93± 1.28) x10^{-2}	-0.69±0.06	1.01x10^{-2}
M_R<18.75	439.5± 34.5	(1.69± .433)x10^{-2}	-0.73±0.022	8.0 x10^{-2}
M_R<19.75	1225.0±125.0	(1.09± .202)x10^{-2}	-0.69±0.020	4.26x10^{-2}

Notes: The fits were done between the lines shown in Figures 9. The errors quoted for δ are least squares errors of fit. All other errors were empirically determined by averaging between plates.

The amplitude A has been corrected upwards by a factor of 1.23 to account for 10% contamination of the galaxy samples by stars during automatic star galaxy separation.

making up the ensemble.

Finally in Table 6.1 amplitudes are also corrected for contamination by stars due to the identification errors that must exist in any form of star-galaxy separation. Our stellar samples are effectively randomly distributed on all scales greater than the limit to which the power-laws were fitted. If w is the observed correlation function for a sample composed of fractions f_g and f_s for galaxies and stars respectively, then

$$w = f_g^2 \, w_{gg} + f_s^2 \, w_{ss} \qquad (6.7)$$

where w_{gg} refers to the true galaxy correlation function and w_{ss} to that for the accidentally included stars.
(We assume no cross-correlation between stars and galaxies). Eyeball checks show that f_g and f_s are about 0.9 and 0.1 respectively for all our samples. Thus if $w_{ss} \equiv 0$ for all θ in our range, $w_{gg} = w/0.81$ and the true amplitude is higher by 23%.

6.6 SMALL ANGLE SCALING COMPARISONS

The corrected amplitudes for the integral J and R ensembles are plotted together with the predictions in Figure 6.7. The amplitudes measured by Peebles and co-workers for the shallow catalogues are also shown.

The scaling behaviour of the deep samples agrees well with the predictions of the standard models described in Chapter 5 ; there is no large discrepancy such as that found for the samples of Phillipps et al (1978). With the exception of the deepest J cut, the amplitudes agree with the predictions of the standard models to an accuracy of better than 20% which is well within the indicated errors. (see Section 6.8 for a discussion of the results for the m_J <21.5 sample). Thus these amplitudes

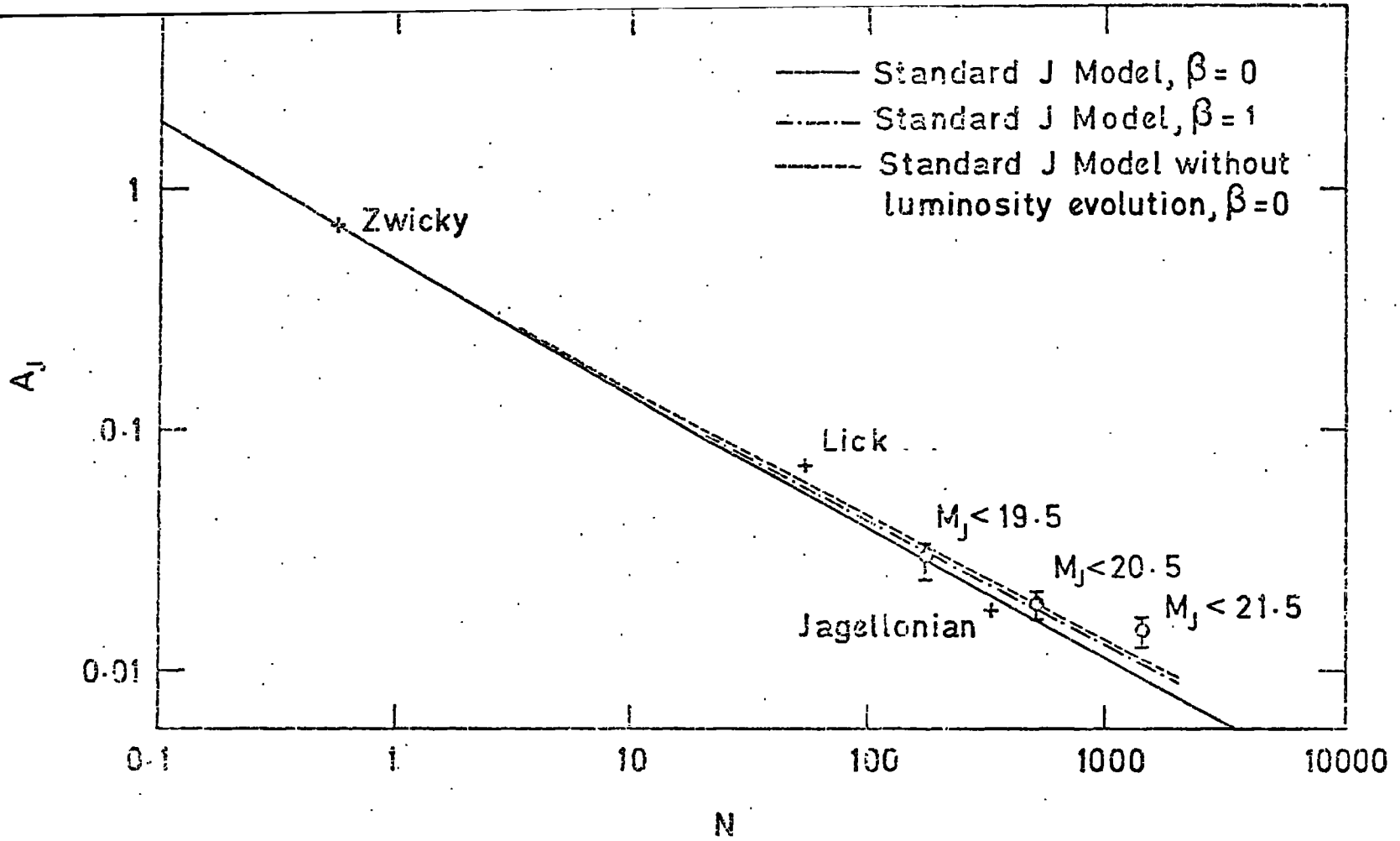

Figure 6.7(a) Amplitudes of -0.8 power-law fits to the galaxy angular correlation function plotted against galaxy surface number density per square degree. The observed amplitudes are to be compared with model predictions allowing for geometrical and projection factors. The solid curve uses the standard model. The dashed curve shows the effect of excluding luminosity evolution. The dot-dash curve allows clusters to be fixed in comoving space rather than in proper space ($\beta = 1$ instead of 0).

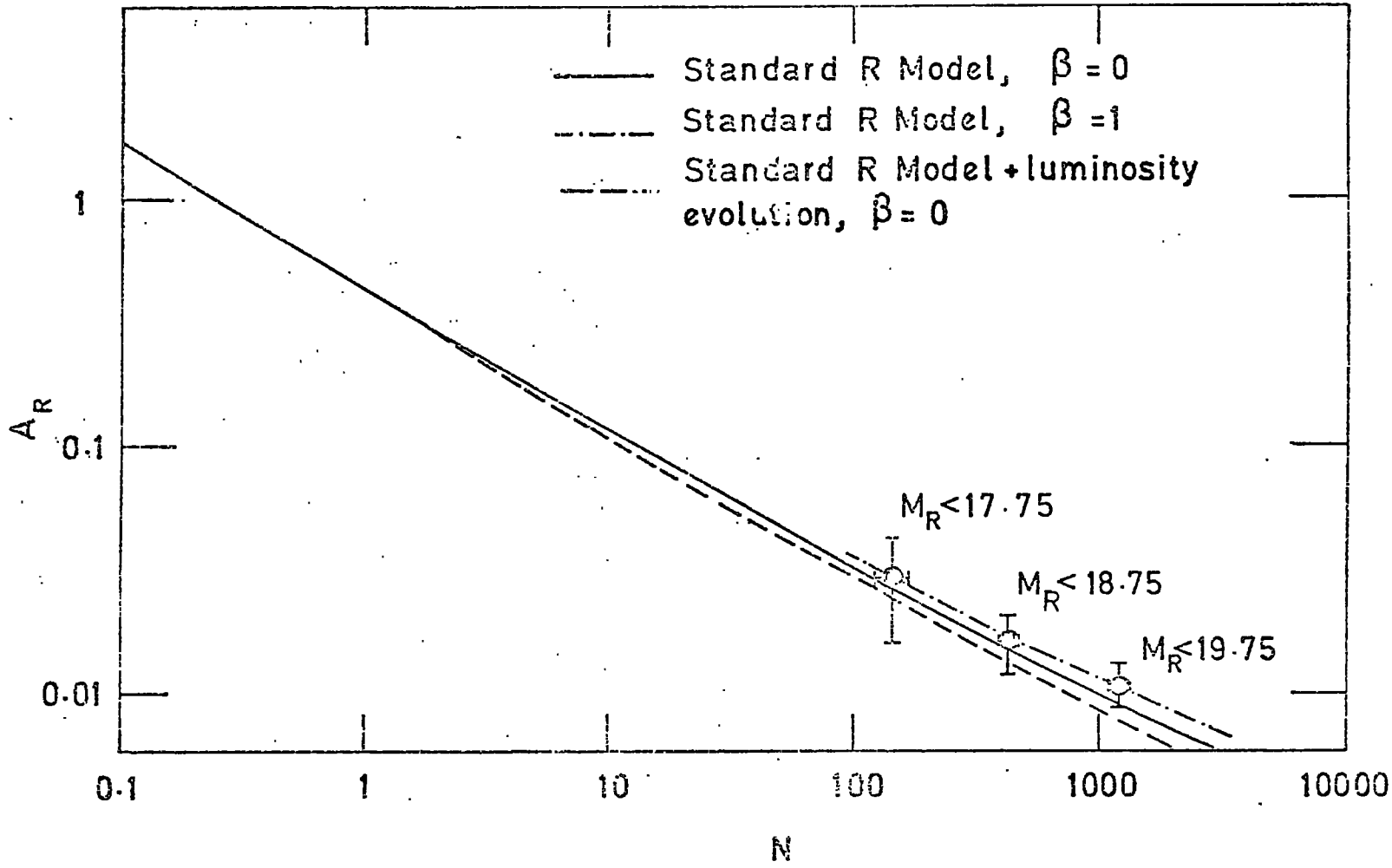

Figure 6.7 (b) As Figure 67 (a) for the R band.

scale to the Zwicky amplitude as well as those amplitudes obtained from the S-W and Jagellonian samples. This is an encouraging result in support of the basic cosmological assumptions of the homogeneity and isotropy of the universe on very large scales. It indicates that the same model of galaxy clustering is applicable out to a luminosity distance of $\sim 700\ h^{-1}$ Mpc. It is also encouraging to note that the standard parameters (Table 5.1) used to fit the galaxy number-magnitude counts reasonably explain the deep-angle correlation functions. The two tests are not identical, for the scaling relations depend critically on the shape of $\phi(z)$ being particularly sensitive to changes in K-corrections and luminosity evolution.

6.7 THE OBSERVED SLOPES

Table III shows that the best power-law index (eqn. 6.6) is sometimes substantially flatter than the value -0.77 ± 0.05 quoted by Peebles (1974a) for the local samples. The R plates and the shallowest J samples give a mean $\delta = -0.71 \pm 0.012$, which is reasonably consistent with the local value. The indices for the deeper J samples and especially for the J slices, however, appear to become flatter with increasing depth. A possible systematic machine effect is unlikely as only the J samples are affected.

A ready explanation of this phenomenon is provided by the preferential selection of spirals as the J samples reach fainter ; the E/SO K-correction in J is much greater than for spirals. Thus, considering that E/SO's are more highly clustered than spirals, the observed flattening is not surprising. We have further checked using the approximate correlation results of Davis and Geller (1976) for the different morphological types that the scaling carried out above is not seriously affected by this selection effect.

For the R passband, the difference between the K-corrections for E/SO's and for spirals is much less and, as observed, would then have little effect on the power-law index. More evidence for the truth of this explanation is presented in Section 6.12.

analysed.

6.8 DISCUSSION OF SMALL ANGLE RESULTS

The scaling discrepancy of Phillipps et al cannot be explained by contamination of the samples by stars, as f_s would then have to be 0.4 (equation 6.7). The discrepancy was thought to be due to the small areas covered ($\tilde{\sim}$ 2 deg^2), i.e. sampling problems. The amplitudes obtained by dividing plate J3721 of this sample into four areas of comparable depth and size gave a standard error of ± 20% in the fitted amplitude, which does indeed indicate that 2 deg^2 at these depths might not provide a fair sample for small-scale clustering analyses.

However, although the field of Phillipps et al could well be a rather special one, an additional explanation for the discrepancy may be that the photometry of the faintest images for those samples was much more inaccurate than for the present COSMOS runs.

Phillipps et al's smallest images would frequently consist of only $\tilde{\sim}$ 15 pixels (cf. 50 pixels here). Although Ellis et al (1977) showed such samples were reasonably well-defined, the models could not allow for the effects of random errors both in the COSMOS measurements and in the emulsion on the plates themselves. Fluctuations in image size at the limit could be so large as to contaminate the sample with galaxies actually much fainter than the supposed limit, thus broadening $\phi(z)$ and lowering the correlations.

This explanation is supported by experiments with COSMOS where the effective number of pixels per image was reduced. Discrepant

correlation amplitudes (to factors $\sim$ 2) were obtained at the faintest limits where previously the data had scaled reasonably accurately, and indeed, Phillipps et al did find a reduction in the discrepancy when analysis was confined to larger images.

As has been noted, the deepest J sample $w(\theta)$ amplitude does not scale as well as the amplitudes from the other 5 samples. The amplitude here is some 50% higher than is predicted with the standard J model. The size of the correlations being larger than predicted is slightly disturbing since, as we have seen, most errors tend to diminish the correlations. However, if we have overestimated the amount of star contamination in this particular sample then simply by omitting the corresponding correction factor we find that this deep result lies within one standard error of the prediction. Therefore, since the errors on the amplitudes may be larger than those indicated in Figure 6.7 because of such systematic effects, we shall not, at present, attach too much significance to this result.

A detailed interpretation of the present scaling results is difficult because the errors are often as large as the effects we might reasonably expect to detect. Nevertheless, it is worth noting the effect of varying some of the standard parameters on the fits to the observed amplitudes in Figure 6.7. Removing SSF luminosity evolution from the J standard model improves the fit to the J sample amplitudes (but, of course, produces a less good fit to the number counts of Chapter 5). The R amplitudes seem to prefer very little luminosity evolution in agreement with the rough indications from the COSMOS R number counts. Extending the width of the luminosity function from M^* ± 4.0 to M^* ± 7.0 had a negligible effect on these results in J or R. We note finally, that it is possible to further improve the model agreement in both J and R by introducing correlation evolution. This is done by putting $\beta = 1$ in the prediction

for the standard model, which corresponds to the case of clusters expanding with the Hubble flow. If the models of Chapter 5 were to be trusted then this would indicate that clusters are not in virial equilibrium. But clearly the size of the errors in Figure 6.7 means that such a detailed discussion must await machine measured data to fainter limits (a) to better define the galaxy number magnitude relations and hence the "effective" galaxy K-corrections and (b) to determine any evolutionary trends over a wider range in limiting magnitudes. This means that the test of isothermal clustering growth rates must await the availability of such samples as well. However, the present results should provide a firm base from which these investigations can confidently be extended to these deeper limits.

6.9 SCALING COMPARISONS AT LARGE SCALES

We have seen (Table 6.1) that at small scales the correlation estimates are well represented by a power-law of index ~ -0.7 or shallower. We turn attention now to the large angle results where the interest is in establishing whether the break away from this power-law behaviour, seen by Groth and Peebles in their analysis of the Lick Catalogue, is reproduced in the samples analysed here.

An inspection of Figures 6.5 show that for $\theta > 0.3^{\circ}$ the estimates break sharply away from the power-law and that after $\sim 0.5^{\circ}$ there are no $w(\theta)$ points significantly different from zero. Indeed points at $\theta > 0.3^{\circ}$ would have to be raised by over 5 empirically determined standard errors to maintain the power-law fits.

It may be thought that this feature is caused by an integral constraint which applies to our estimators of $w(\theta)$

$$\int_{\text{Sample area}}\int \hat{w}(\theta_{12})\, d\Omega_1\, d\Omega_2 \simeq 0$$

This relation arises because the average density, $\mathcal{N}$, required to obtain w (θ), has been estimated, not in ensemble average, but from the individual samples. However, this constraint has only a small effect on our estimates as can be seen by considering the $m_J \lesssim 21.5$ sample. If we use an ensemble averaged number density, $\mathcal{N}_{av}$, (= 1478.3 from Table 6.1) then it can be shown (see Groth & Peebles, 1977 eqn. 31) that the maximum difference that this makes to w(θ) for any of the individual plates is the addition of the term $\left(1 - \frac{1311}{1478}\right)^2 = 0.01$. The addition of this amount to the $m_J \lesssim 21.5$ w(θ) of Figure 6.7 has little effect and thus the feature has not been produced in this way.

The crucial test of the reality of this feature is to check whether it scales correctly with depth. To perform the scaling test we adopt the method of Groth and Peebles (1977), where a two power-law model is inserted in the relativistic version of Limber's formula. We choose the indices to be -1.8 and -2.8, but the required factors are insensitive to reasonable variations in these indices. Table 6.2 gives the values of the scaling factors x, y and D^*_{eff} at our various depths. These factors are defined exactly as in Groth and Peebles. To allow a fair comparison of the large scale behaviour of w(θ) we chose the parameters from Figure 6.7 which best described the small angle scaling behaviour. Since these do not adequately describe the small angle scaling result for the $m_J < 21.5$ sample, we have not used this sample in the diagrams that follow.

The results of scaling Figure 6.5 via Table 6.2 to the Zwicky depth are shown in Figure 6.8a. The scaling behaviour at large angle is seen to be less consistent than at small angles showing some slight systematic effects as the samples go deeper. However, in view of the uncertainties in the estimation we regard the scaling agreement shown in Figure 6.8a as remarkably good. In Figure 6.8b the deepest J and R cuts from Figure 6.8a

TABLE 6.2

Scaling Factors for the Feature

Samples	x	y	$h^{*}_{D_{eff}}$ (Mpc)
J			
19.5	0.920	0.780	336.1
20.5	0.888	0.721	479.5
21.5	0.853	0.665	668.7
R			
17.75	1.020	0.934	300.0
18.75	0.984	0.856	432.6
19.75	0.937	0.768	608.9

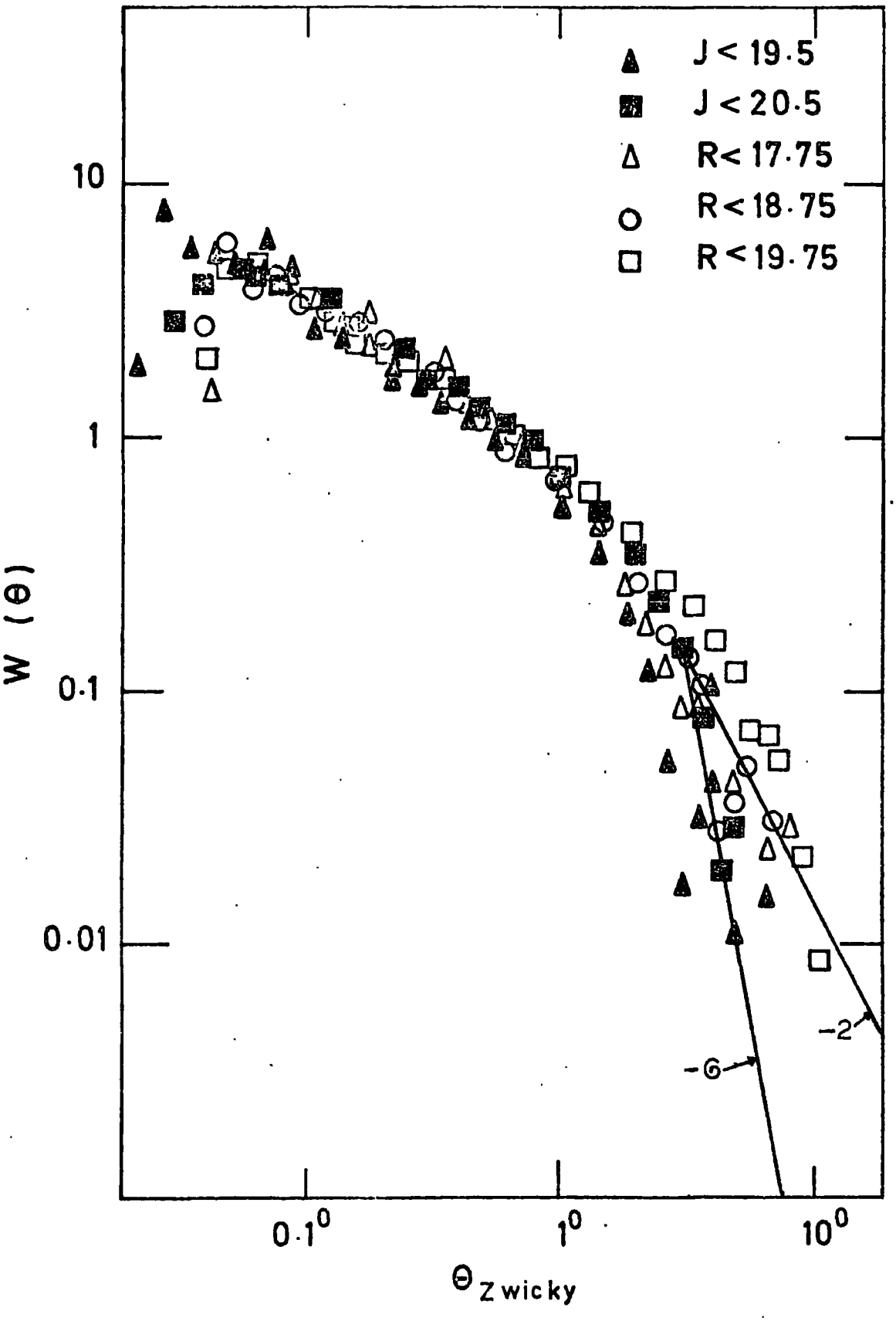

Figure 6.8 (a) Angular correlation functions for the ensemble-averaged samples scaled to the depth of the Zwicky catalogue.

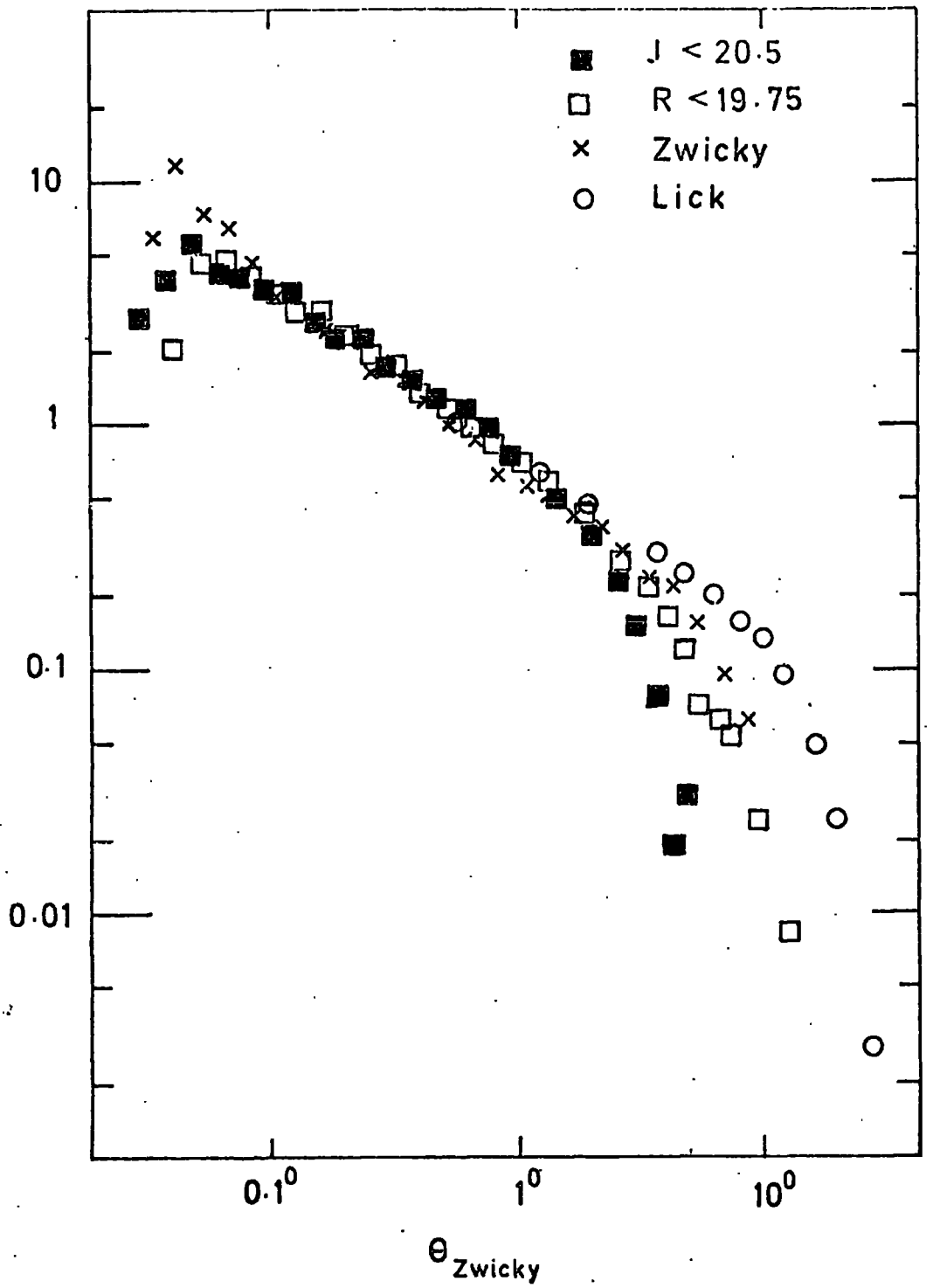

Figure 6.8 (b) Angular correlations functions for the deepest samples of Figure 6·8(a) together with the Zwicky and scaled Shane-Wirtanen results. The feature in the UKST samples occur at smaller separations.

are reproduced along with the results from the Zwicky catalogue and the scaled Lick counts (as estimated by Groth and Peebles). Although the agreement at large scales between the Zwicky catalogue and the deep samples is reasonable, the agreement is not so good with the S-W results. The feature in the S-W results occurs at $\theta_{Zwicky} = 10^{o}$ whereas in our sample it occurs at $\theta_{Zwicky} = 3^{o}$. Thus our estimate corresponds to a break in ξ at around $3h^{-1}$ Mpc instead of at $9h^{-1}$ Mpc. Since this discrepancy persists even in our shallowest sample whose limit is within 1^{m} of the S-W limit, the difference cannot be resolved by a judicious choice of any parameter in the scaling procedure.

Before discussing these results further we now demonstrate that there is no bias in our $w(\theta)$ estimators which artificially creates or moves the feature by showing that an independent statistical analysis, Mead's analysis, corroborates our large scale correlation estimates.

6.10 MEAD'S ANALYSIS

Mead's Analysis has been described in detail in Chapter 3. To recap briefly, a statistic $S(\theta)$, designed to reveal the angular size of any preferred scale in the galaxy clustering, is calculated. The statistic has the advantage that small estimates are unaffected by large scale number density gradients in the data. Thus, no filtering ambiguities are encountered. Now, if we were to interpret the feature discussed above to be the scale length of a preferred cluster size seen at an average distance for our sample, then we should also expect to see a peak in the $S(\theta)$ statistic at the appropriate angle.

The Mead's Analysis of the $J < 21.5$ ensemble is shown in Figure 6.9 The $S(\theta)$ statistic clearly peaks in the region 0.12^{o} to 0.24^{o} and falls sharply away for scales greater than the $w(\theta)$ break point of 0.3^{o}. Furthermore, $S(\theta)$ behaves no differently on J1920, the field we had to filter, than

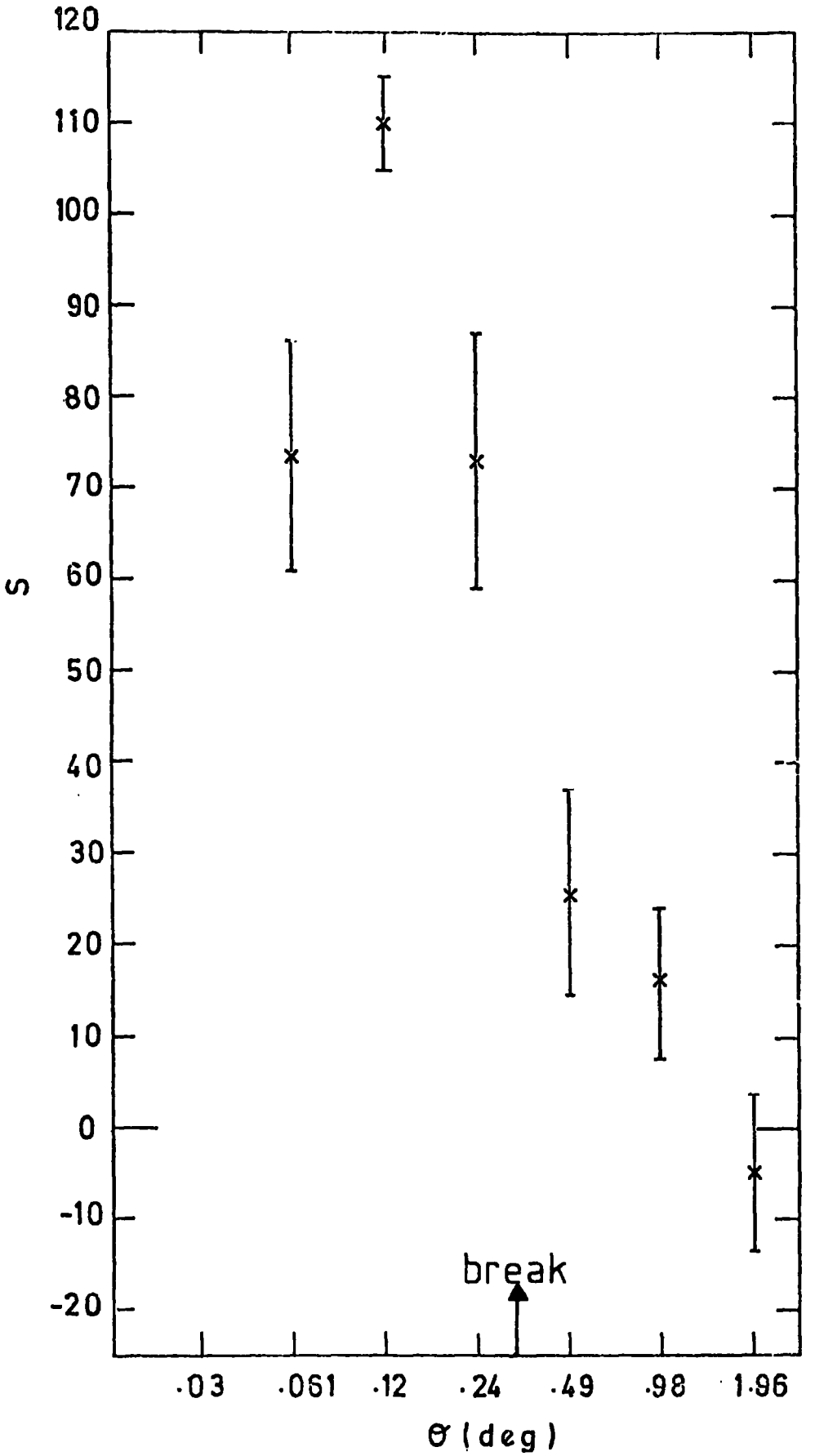

Figure 6.9 Mead's analysis of the ensemble-averaged sample limited at J = 21.5. The ordinate represents the degree of clustering at various angular separations. The peak in the statistic occurs at approximately the angle corresponding to the feature observed in the correlation function.

on J3721. The analysis, therefore, gives very convincing evidence in support of the reality of the feature. The small scale behaviour or S(0) also gives further support to the contention that the correlation statistics are more consistent with galaxies being distributed in clusters with power-law density fall-offs than in a hierarchical pattern (see Chapter 3).

6.11 DISCUSSION OF LARGE ANGLE RESULTS

Although we have shown in Section 6.6 that our small-scale $w(\theta)$ estimates are consistent with those expected from shallower catalogues, there is now some discrepancy between the large scale behaviour of the deep samples and that of the S-W counts. We have discussed carefully sources of possible error in our estimates. These include the possibilities that :-

(a) our sample is not a "fair" one on large scales (see Section 6.3).

(b) the filtering of J1920/R3780 has biased the results (see Sections 6.4 and 6.10).

(c) there is a "sample size" bias in our estimator of $w(\theta)$ on all the plates (see Section 6.10).

(d) some systematic error has been introduced into our galaxy distribution during, say, star-galaxy separation (see Chapter 4).

Arguments have been given against all these explanations and these become stronger when taken together with the fact that our samples scale reasonably well with respect to one another, and also by the fact that the filtered results are reproducible from one plate to another. If there is an error, we consider (d) to be the most likely source, since such effects are the most difficult to detect.

On the other hand, there are also serious difficulties in estimating the position of the feature on the shallower surveys. We have

already mentioned the difficulties encountered with Galactic obscuration. Although the feature is seen in the estimates for the Zwicky catalogue its position does not scale to better than a factor of $\sim$2 to the S-W feature (see Figures 13-14, Groth and Peebles 1977). Furthermore, the smoothing applied by Groth and Peebles to the S-W counts would not remove the effects of emulsion or obscuration variations over a single plate. If such "within-plate" effects were common, they would act like the obscuration on J1920, keeping the S-W correlations artificially high. A good check on contamination by small scale obscuration will be to apply the Mead's analysis to the S-W counts.

The implications these results have for galaxy formation theory run as follows. If the isothermal picture is assumed then the break corresponds to the transition between the linear and non-linear regions of galaxy clustering. If the true position of the feature is given by our estimates at $3h^{-1}$ Mpc then this destroys the agreement between observation and the prediction for $\xi(r)$ at large scales from the BBGKY equations in an $\Omega = 1.0$ universe (Davis et al, 1977). However, the feature at this position would possibly be consistent with isothermal theory in an $\Omega = 0.3 \rightarrow 0.5$ universe (see by comparing Figure 6.8 with Figure 2 of Davis et al). This may be consistent with statistical investigations of galaxy clustering dynamics using redshift catalogues from which estimates of Ω of 0.4 are obtained (Peebles, 1979).

The slope of the correlation estimates past the feature are also of interest in isothermal theory. Based on the -1.77 slope obtained for $\xi(r)$ at small separations isothermal theory predicts (Davis et al, 1977)

that at large angle

$$\xi(r) \alpha r^{-3}$$

and thus

$$w(\theta) \alpha \theta^{-2}$$

Drawn on Figure 6.8 are lines of slope -2 and -6. The points seem to much better fit the steeper slope. But before claiming that isothermal theory thus fails this observational test we would need to be more certain that systematic errors were not affecting our estimates of $w(\theta)$ at these large scales. This would demand much more precise scaling agreement between our large scale estimates of $w(\theta)$ than is shown in the present samples.

The adiabatic theory also makes predictions for the position of the break. Here this feature is a relic of the initially preferred clustering scale and Ω dependent predictions have been made for its size. (Doroshkevich & Shandarin, 1978). The value of Ω corresponding to a break at $9h^{-1}$ Mpc is 0.01 whereas at $3h^{-1}$ Mpc it corresponds to a value for Ω of 0.2.

Finally, although in theoretical and other aspects of this discussion we have emphasised the differences between our results and those of Groth and Peebles, it must not be forgotten that <u>both</u> analyses indicate the existence of a feature in $\xi(r)$. Considering the different methods of compiling the catalogues with all the difficulties involved, the discrepancy in position, in experimental terms at least, may not be too serious.

6.12 GALAXY COLOUR SUBSAMPLES

In the future with more sophisticated machine measurement of Schmidt plate fields it may be possible to obtain the individual correlation results for deep samples of elliptical and spiral galaxies. Davis and Geller (1977) found for individual local samples that the covariance functions of ellipticals and SO's were steeper than those of spirals. Ultimately it will be very interesting to scale these results to test if the correlation evolution of spiral galaxies differs from that of ellipticals.

In any such project a means of automatically separating out elliptical and spiral galaxies in deep samples would be needed. The J-R colour of the galaxies would probably feature prominently in any suggested separating algorithm since ellipticals and SO's are known to be intrinsically redder than spirals. With the present data, we can at least make some preliminary investigations by dividing the galaxies into subsamples on the basis of their colour and working on the assumption that the redder subsamples is more likely to be elliptical dominated.

Thus we divide the J3721, $m_J \leq 21.5$ sample into roughly equal halves at J-R = 0.0. The distribution of galaxies within each subsample is shown in Figure 6.10a and Figure 6.10b. A visual comparison immediately shows that the redder galaxies tend to be preferentially found in clusters consistent with their containing E and SO galaxies. The correlation function for the two subsamples are shown in Figure 6.11. Firstly, the redder galaxies have a much steeper correlation function slope at small scales than the blue galaxies, as might be expected from Figure 6.10. Since Davis and Geller's result showed similar differences in the correlation of the elliptical /SO and spiral galaxies the suggestion again is that the red sample is dominated by E's and SO's whereas the blue is dominated by spirals. The small scale differences in Figure 6.11 also confirm in a

(a)

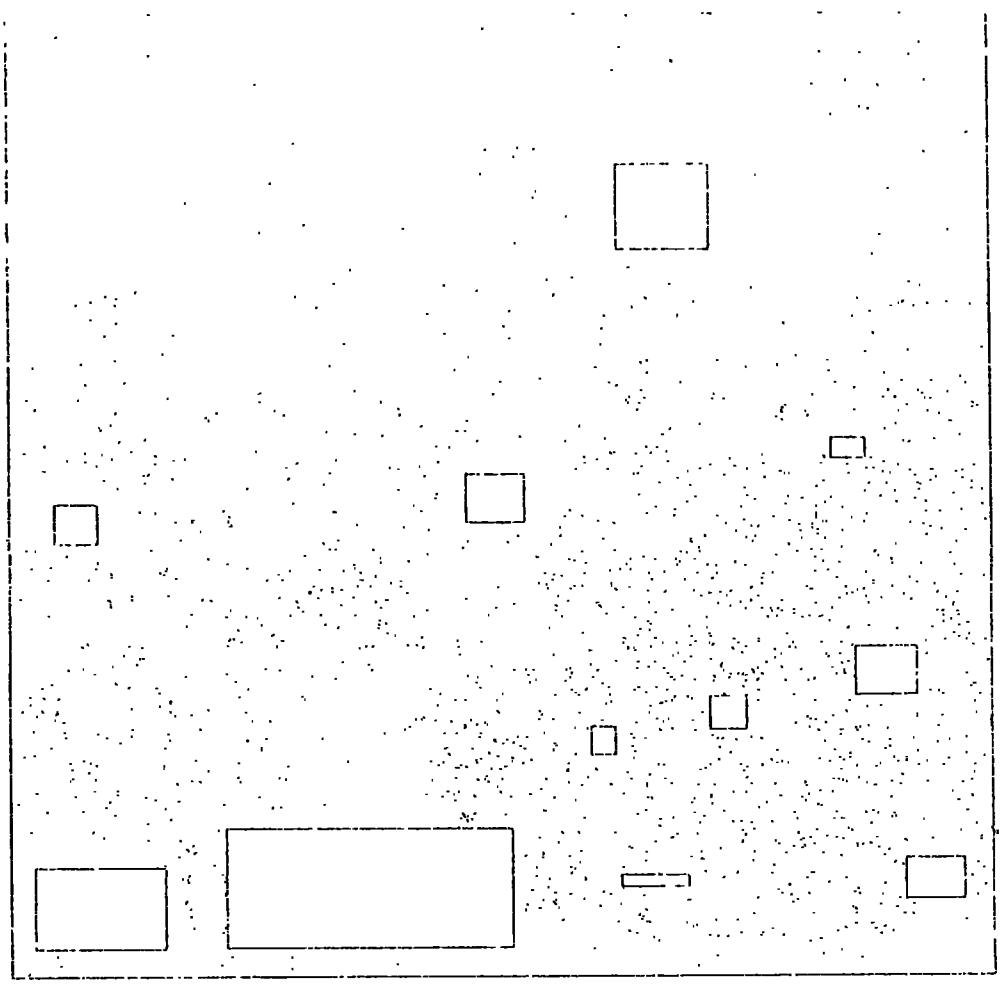

(b)

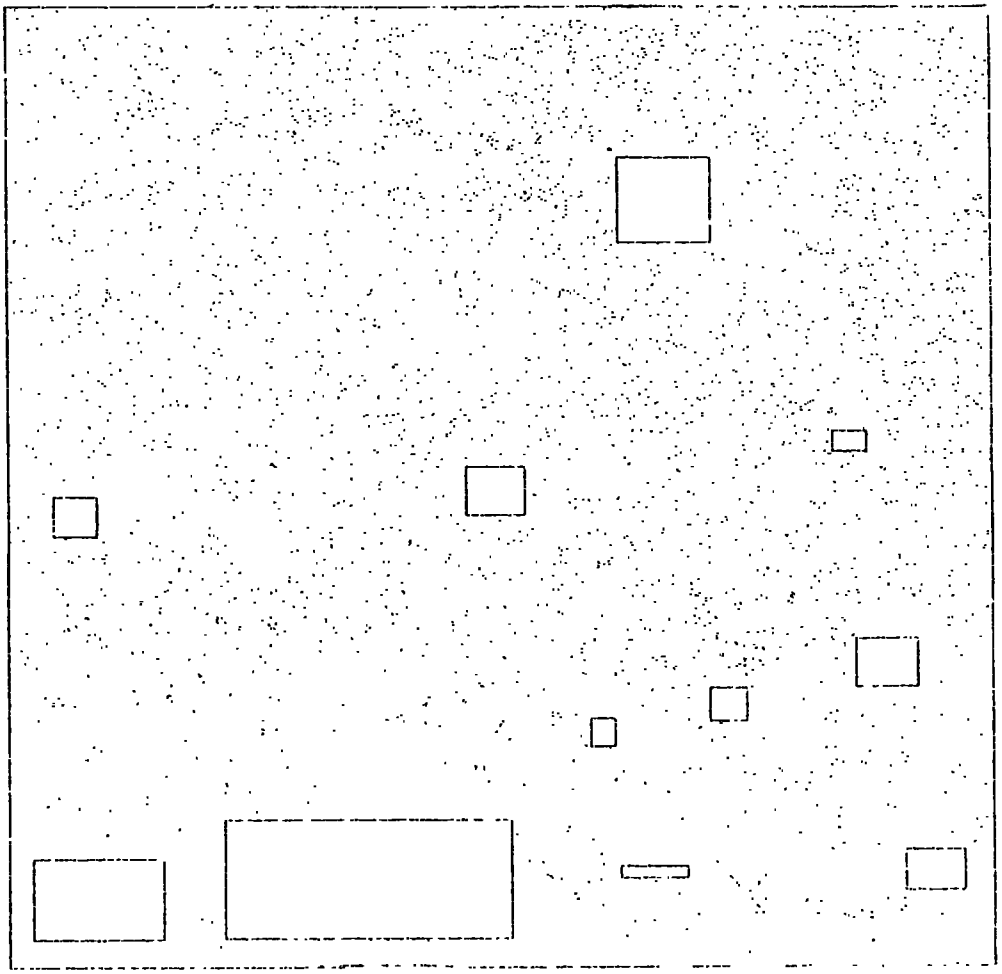

Figure 6.10 Distribution of galaxies on plate J3721 $m_J \leq 21.5$, with J-K (a) less than 1.56(b) greater than 1.56 . The bluer galaxies in Figure 6.10(a) are obviously less clustered.

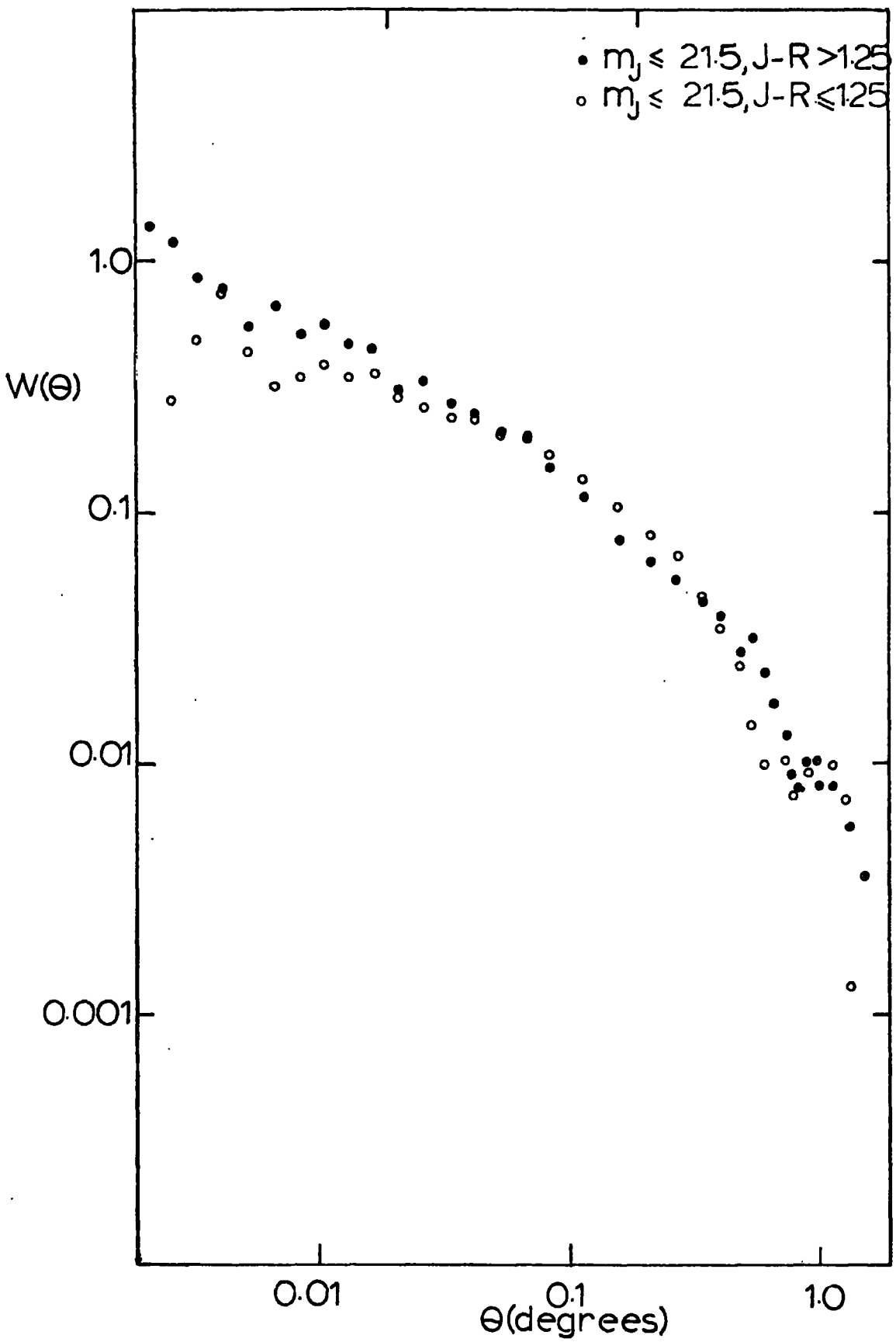

Figure 6.11 2-point correlations of galaxies on plate J3721 in J-R colour subsamples. The bluer galaxies show a shallower sloped covariance function than the redder galaxies.

rough way the tendency of the J $w(\theta)$ slopes to become flatter with depth. It will be recalled that it was suggested that this might be explained if spirals were less clustered than ellipticals because ellipticals are selected out of deep 5 samples because of their large K corrections. Figure 6.11 indicates, in a similar manner to the results of Davis and Geller that such a difference may well exist. It would be of interest to do scaling tests by also cutting the samples at brighter magnitudes. However, even internal scaling here is difficult because (a) the correlation functions for the various types from the local samples are not yet well enough established and (b) there are large uncertainties in the effective K-corrections for the subsamples since the number counts for these are less well established than for the complete sample. These difficulties with small angle scaling will only be resolved when it is possible to more precisely isolate the elliptical /SO population. The prospects for this project will be discussed in Chapter 7.

At larger angle it is interesting to note that the break for the blue,spiral dominated sample occurs at a smaller angle than for the redder sample. This result is slightly unexpected on the basis of the simple picture of galaxy distribution where ellipticals and SO's are preferentially found in the small central cores of clusters with spirals distributed around them in a larger, less concentrated halo. However, the difference between the break points is not too large and may possibly be accounted for by the different selection effects (K corrections etc) operating to produce different average depths in the two samples. This would mean that the larger angular position of the feature in the red samples did not necessarily imply a larger spatial position of the feature for ellipticals.

6.13 STELLAR SAMPLE CORRELATION ANALYSES

In Figure 6.12 are presented the ensemble averaged results from the J and R stellar samples limited at m_J = 21.5 and m_R = 19.75 respectively. The results in J and R are similar showing zero correlation on scales greater than 0.01° but showing evidence for anti-correlation over a range of scales smaller than this. Machine merging of images is undoubtedly causing some of this anticorrelation. However, it is interesting to consider if this is responsible for all of it. Shown in Figure 6.12 for comparison purposes are the ensemble averaged galaxy correlations at those depths. They show much less anticorrelation but this is an unfair test since it is known that the power-law behaviour of $w(\theta)$ extends to very small scales and this will cause many galaxy pairs to be formed. Apart from this indication it is difficult to test the reality of this feature, basically because the COSMOS output does not allow any clue as to the number of merged images in the sample.

It is also worthwhile to investigate the distribution of colour subsamples of the stellar images. Recalling the two peaked distribution found in the n(J-R) relation of Section 5 , the stellar images are divided into halves accoridng to their (J-R) being larger or smaller than 0.3, a value which bluewards contains the majority of the blue peak and redwards the majority of the red.

Dot plots of these two subsamples are shown in Figures 6.13a, b. There is some evidence for a slight density enhancement of objects in the SW corner of the blue sample but this was found to coincide with an area where defocussing of the plate appeared to be more of a problem (see Chapter 4) and this could easily have caused the slight bias towards higher densities here. This small inhomogeneity in the distribution will not cause too much of a problem, especially at the interesting smaller scales, for

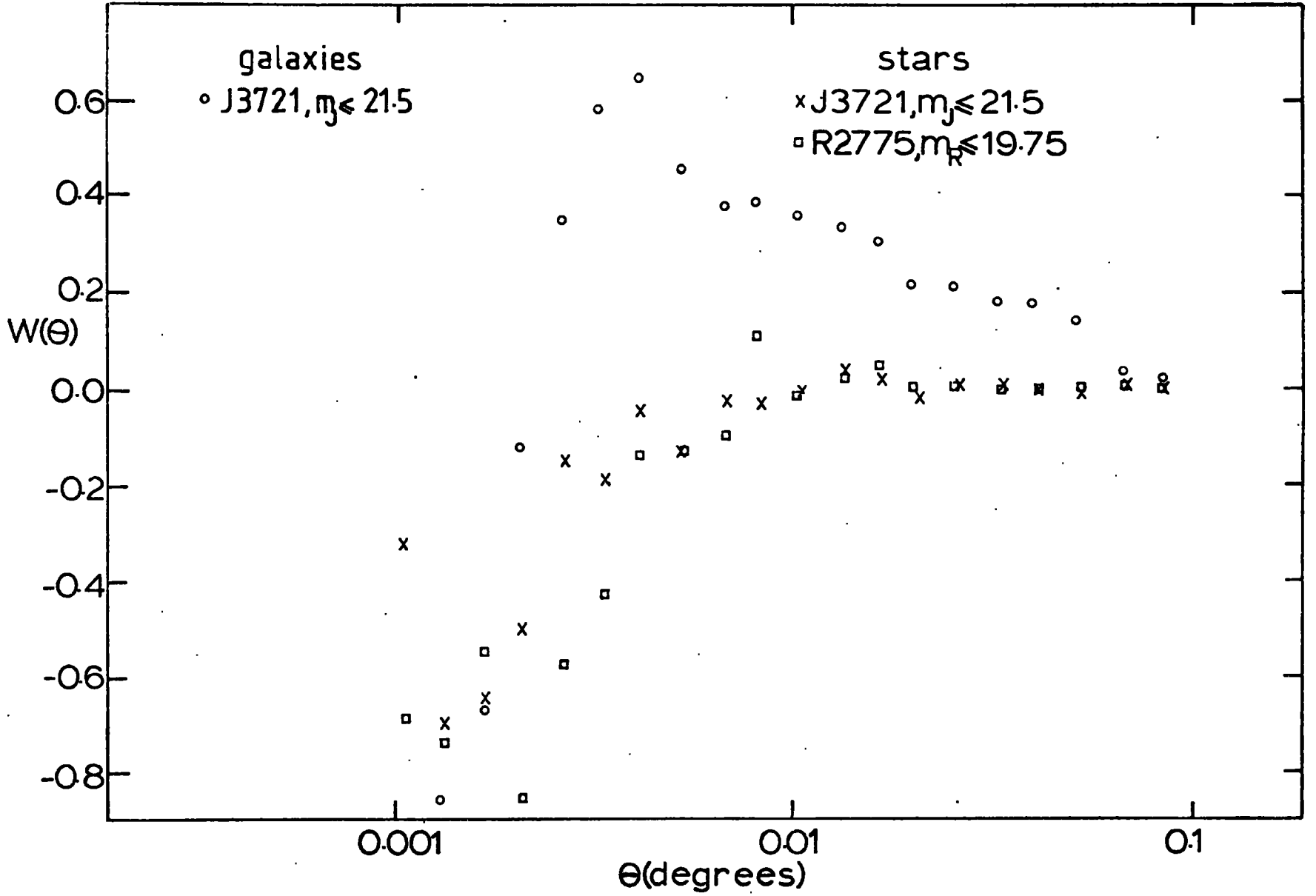

Figure 6.12 2-point stellar correlation for plate J3721 and R2775.

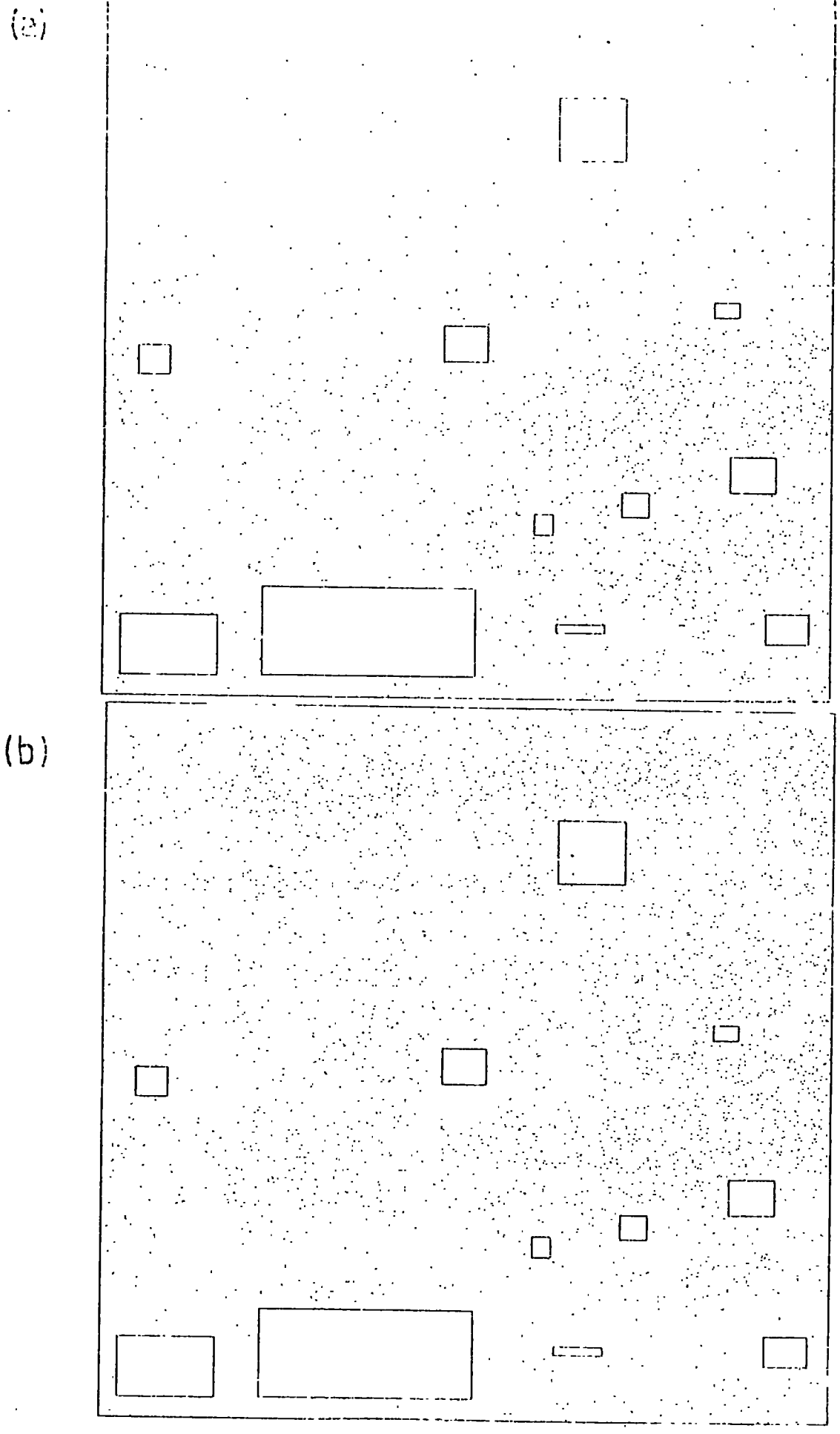

Figure 6.13 Distribution of stars on plate J3721, $m_J \leq 21.5$ with J-R colour (a) less than 1.5^m (b) greater than 1.5^m.

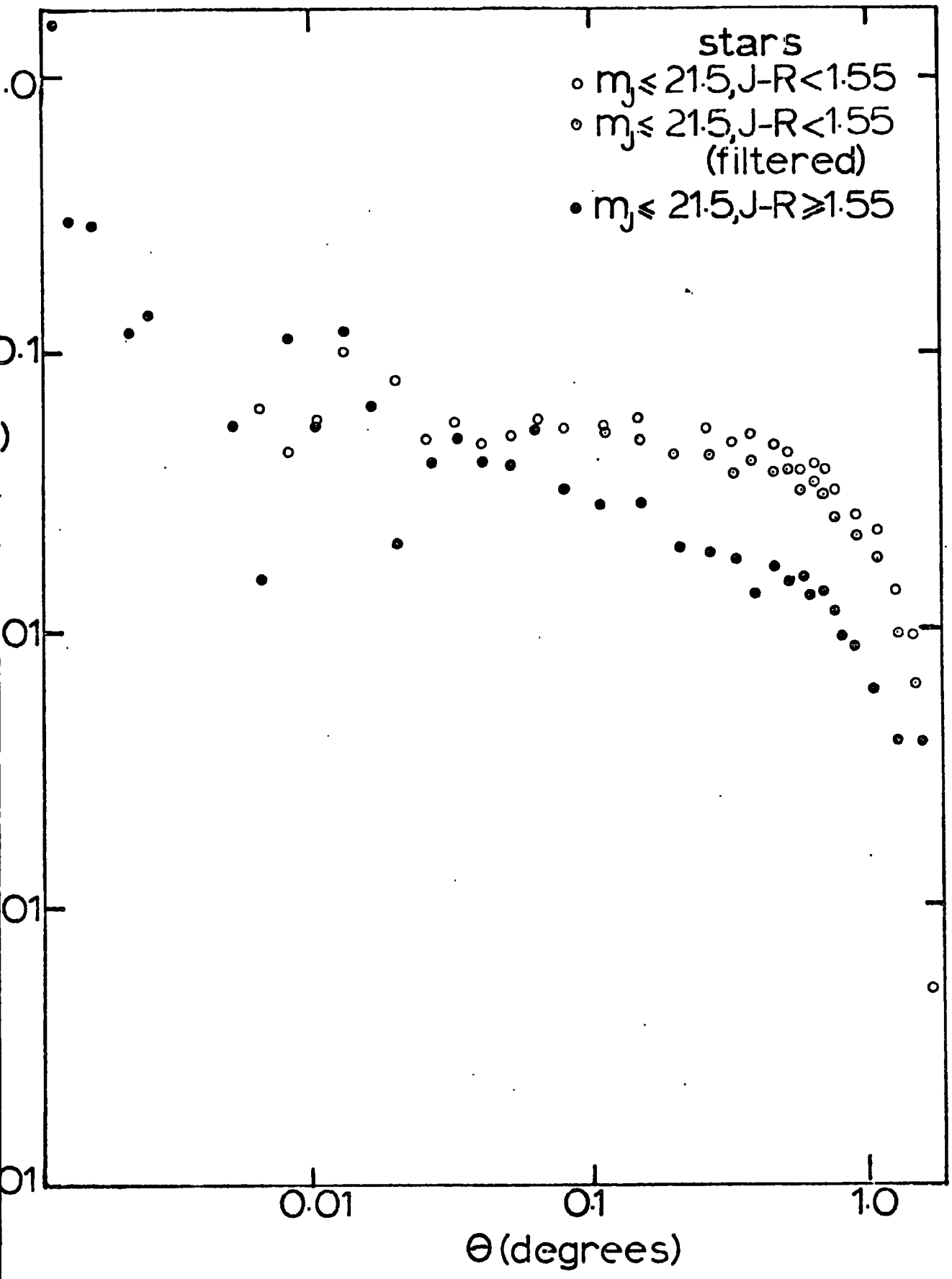

Figure 6.14 2-point correlation functions for stars on plate J3721 in the J-R colour subsamples.

the correlation estimates. These are shown for both the blue and red subsamples in Figure 6.14. Interestingly the red now shows no anticorrelation up to 0.01^{o} and indeed shows some evidence for positive correlations. The blue sample still shows strong anticorrelation over these small scales. It is possible to invent astronomical explanations for these phenomena such as the red sample being dominated by a population of redder stars which would be old enough to have formed many binary pairs. This type of explanation has possibly been made more likely because it is harder to explain on the grounds of simple machine merging why the bluer stars are affected more than the red. But machine effects are still the most likely reason for the stellar $w(\theta)$'s behaviour at small scales ; the number of pairs involved at small separation is so small that even a slight bias, say, in our matching procedures, could produce the observed difference between the blue and red subsamples.

6.14 CONCLUSIONS

We have seen from analyses of deep machine-measured samples of galaxies taken from 5 UKST plates of 3 fields around the South Galactic pole that :-

(i) The amplitude of the small scale galaxy correlations is in good agreement with that expected from the results of shallower surveys. This scaling was done assuming a galaxy luminosity function and an effective K-correction which were consistent also with galaxy number-magnitude counts presented here using COSMOS and from other sources. The scaling agreement is powerful evidence that the locally derived spatial correlation function is applicable to depths of $\sim 700h^{-1}$ Mpc. The errors are still too large to place useful constraints on clustering evolution.

(ii) On large angular scales the correlation functions show good evidence for a feature at separations corresponding to $3\ h^{-1}$ Mpc. Although the large angle correlations scale reasonably amongst our samples, this position is a factor of ~ 3 smaller than the feature found by Groth and Peebles (1977) in their analysis of the Shane-Wirtanen counts. However, considering the uncertainties involved such a discrepancy may not be too serious.

(iii) Bluer galaxies have been found to have a flatter $w(\theta)$ slope than redder galaxies, consistent with the idea that redder elliptical and SO galaxies are preferentially found in clusters.

The implications of these results in terms of the isothermal and adiabatic theories of galaxy formation have been discussed. The covariance results for the blue and red stellar populations have also been presented.

CHAPTER SEVEN

CONCLUSIONS

7.1 INTRODUCTION

To conclude the thesis, this final Chapter contains a summary of the results we have obtained from the statistical analyses presented in the preceding Chapters. A summary is also given of the implication of these results for standard galaxy formation theories.

Before this, however, we shall also look at the longer term prospects for continuing statistical investigation of galaxy properties. Thus in Section 7.2 we consider the possibility of obtaining complete redshift catalogues using spectroscopic methods and the results that may arise therefrom. In Section 7.3 we look at the exciting prospects for obtaining approximate redshifts of galaxies using photographic methods. Section 7.4 looks at how very deep correlation evolution tests may be possible using "catalogues" of galaxies arising from absorption line spectra of cosmological quasars. Finally, Section 7.5 contains the overall conclusions from the work presented in this thesis together with a discussion of methods whereby the questions more directly arising from this work may shortly be answered.

7.2 COMPLETE REDSHIFT CATALOGUES

At the moment much effort is being expended in using spectroscopic methods to obtain magnitude limited galaxy catalogues with complete redshift information Huchra et al (1979) obtained redshifts for and analysed the very shallow Shapley Ames catalogue. Kirshner et al (1979) have presented a deeper catalogue, containing 166 galaxies in 8 fields across the northern galactic hemisphere, limited at 15 mag. in J.

Tonry and Davis (1979) are endeavouring to produce a much more extensive catalogue (over 1000 galaxies) covering the area defined by $b_{II} \geq 40^{\circ}$ $\delta > 70^{\circ}$, to a slightly shallower magnitude limit, 14.5 mag. The Durham group is also producing a redshift survey to a much fainter limit, 17 mag in J, in the southern galactic hemisphere to try and eliminate any biases in the shallower samples due to the local supercluster. The statistical analyses of surveys such as these contain much potential information on the dynamics and the distribution of galaxies.

The dynamical information in such samples is contained in the average, relative peculiar velocity differences between pairs of galaxies, V_{21}. A variety of methods have been suggested for estimating this number. These include the comparing of correlations functions found in redshift space with those found in projection, and also the correcting of the observed histograms of the total relative velocity differences at various separations, for the effects of Hubble flow (see Davis et al, 1978, Geller and Davis (1978) for reviews). This average velocity can then be used in applications of statistical virial theorems to make estimates of Ω , the cosmological density parameter, on the assumptions that the galaxy distribution is a useful measure of the mass distribution and that the galaxy clustering is statistically stable. Preliminary estimates give Ω=0.2→0.7 from the sample of Huchra et al and Ω = 0.4 from the sample of Kirshner et al, (see Peebles 1979). It is also possible to make a test of the isothermal theory with these catalogues - isothermal theory predicts that the average peculiar velocity difference will stay constant as a function of separation. The velocity differences found at large separation will also test the hypothesis that superclusters have large peculiar velocities relative to each other (Rubin et al, 1974, Smoot et al 1978).

The redshift samples also provide extra information on the distribution of galaxies. They will make slightly easier the application to galaxy catalogues of statistics such as the multiplicity function that have bad projection properties (although there will still be difficulties because the samples are brightness rather than volume limited). This will enable more effective tests to be made between the hierarchical and power-law cluster models. Estimating the correlation at large scales will be easier with 3-dimensional data in the sense that the break point will be lifted higher above the statistical noise. The drawback here is that the background normalisation is much more difficult than for the 2-dimensional estimator of Chapter 6 and the form of the covariance function at large angles is very sensitive to this normalisation. However, it will be interesting to compare the results between the various methods of estimating $\xi(r)$. Complete redshift catalogues will also make possible more objective tests of "chains", "holes" and all structure which are claimed to be seen in the incomplete redshift catalogues available at present (Tifft 1978, Gregory and Thompson, 1978).

Finally complete redshift samples will allow other statistical investigations apart from those concerned with galaxy distribution. Most important amongst these other investigations is a more accurate determination of the luminosity function of field galaxies.

7.3 REDSHIFTS BY PHOTOGRAPHIC METHODS

Obtaining redshifts by spectroscopic methods is a slow procedure, consuming large amounts of telescope time. But these methods provide probably the only way to determine galaxy velocities accurately enough for the dynamical investigation (these require errors in velocity of under 100 $km\ s^{-1}$). However, the production of useful three-dimensional pictures of galaxy distribution demands less high precision in redshift determination

and it is interesting to consider if approximate galaxy redshifts could be found using faster methods.

One general method which has been suggested is to try and isolate galaxies redshift dependence in some multidimensional space of image parameters, measured on photographic plates by measuring machines. A particular example of this method might involve measuring plates for one field taken in 3 or 4 widely spaced, narrow, optical passbands. This magnitudes of an image measured in the different bands would be used to define an approximate image spectrum. Parameters relating to the width of the image profile would also be measured on one or more the plates. These profile parameters together with some of the colour information would first be used to separate early and late type galaxies, then best fits could be made to the rough colour spectrum based on the redshift dependent average K-corrections for the various types. This method would work better for elliptical galaxies which have more distinguishing features in their spectra than spirals. This would give, at least, a chance of determining reasonably accurate average redshifts for elliptical dominated clusters.

It is possible to make preliminary tests of this method with the present data. Here for the J3721 plate we have three useful parameters to work with - the J magnitude, the J-R colour and a width parameter $(\alpha')^2$. This width parameter is defined by the equation

$$(\alpha')^2 = \alpha^2 - S(x,y)^2$$

where α is the half width of the Gaussian fitted to the image central and threshold intensities (as in Chapter 4) and $S(x,y)$ is a normalising factor to account for the variation in image size over the plate because of plate sag. The value of $S(x,y)$ taken is that found by interpolating average

image widths in contiguous bins over the plate (see Section 4.4). The quantity $(\alpha')^2$ can then be plotted against J-R colour for all the J3721 galaxies for which colours are available. This is done in 0.5 mag bins in Figure 7.1. Contours have been drawn on this graph to pick out the areas most densely populated by galaxy images. Before looking at theoretical predictions for where ellipticals and spirals should lie in this diagram, it is immediately noticeable that the galaxies clearly divide into at least two populations - a broad band which runs diagonally from wider blue objects to narrower red objects and a narrower band which remains at constant width as a function of colour.

The theoretical predictions for this diagram were done in the case of ellipticals assuming the luminosity profile of Abell and Mihalas (1966) and Holmberg's (1969) absolute magnitude - profile relation. The equivalent relations for spirals were taken from Freeman (1970). These are the same laws as used by Ellis et al (1977) to predict number-angular diameter relations. Here both the apparent image angular diameter (at the isophote appropriate for the J-R sample) and apparent central intensity were calculated for galaxies of various types over a range of redshifts. Gaussians were then fitted to these, just as in the observations, to find the predicted $(\alpha')^2$ for these images. A theoretical diagram can then be produced (see Fig. 7.2) which can be compared directly with the observations. These comparisons are only valid for $m_J > 19$ mag. faintwards to avoid problems with the known scale error in the COSMOS magnitude system for brighter images.

This comparison shows a striking resemblance between theory and observation. The broad band found in Figure 7.1 is in the position predicted for spirals in the models, and the narrower band lies roughly in the region predicted for earlier types. Thus even with the limited data at our disposal here it seems that a rough separation of galaxy types may be possible. Also since the major component which causes the galaxy images to move across the

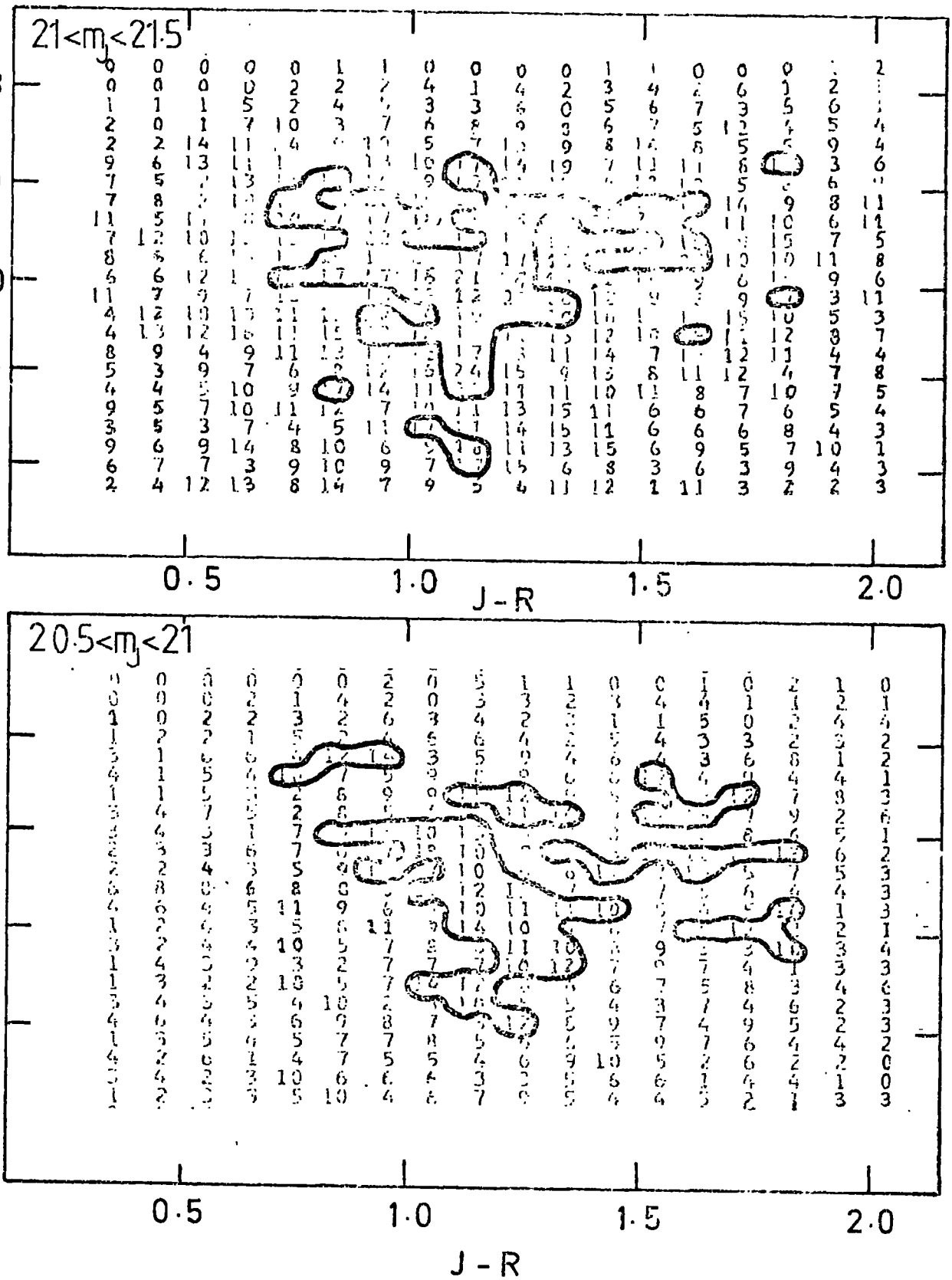

Figure 7.1 Gaussian width parameter α''^2 plotted against J-R colour for J3721 galaxies in two J magnitude bins as shown.

The isodensity contours show at least two populations of images. ($\alpha''^2 = \alpha'^2 - S(x,y)^2 + \bar{S}^2$ where $\bar{S} = 3.2''$, the average seeing for the plate)

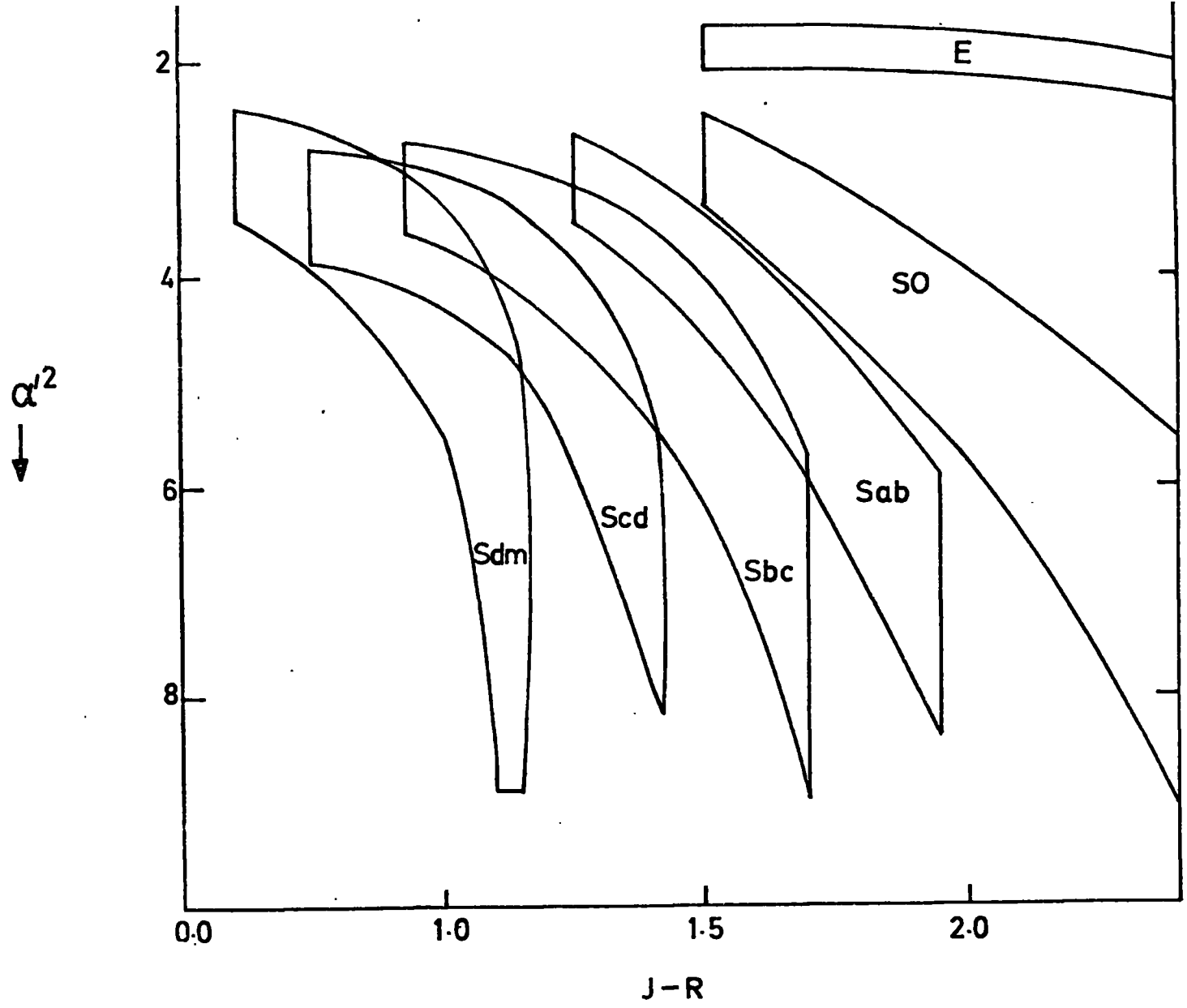

Figure 7.2 Theoretical relationship between galaxy width and J-R colour based on standard parameters for various morphological types. Note similarities between this and Figure 7.1.

theoretical colour width diagram is the galaxy's redshift and since this movement is visible in Figure 7.1 as well, there seems some hope that a small increase in photometric accuracy may make the obtaining of approximate redshifts a real possibility.

It is important to note that the random photometric errors in the present sample have not been enough to smooth the main features in Figure 7.1. This is because although the errors are large the statistical noise is small because of the large number of images involved. The identification of the trends in Figure 7.1 would have been much more difficult if only $\frac{1}{4}$ of the images had been measured, even if their photometry had been good to $\pm$ .05^{m}.

Thus there is cause for cautious optimism obtaining approximate redshifts by these techniques and it is hoped to try the method out with new measurements of the SGP field in J, V and R using a new set-up of the COSMOS machine which allows more accurate pixel integrated magnitudes to be outputted.

7.4 QSO SPECTRA

An exciting prospect for investigating galaxy distributions at very high redshift is based on the assumption that QSO's are at the cosmological distances implied by their redshifts. It has been suggested on this assumption that the many unidentified absorption lines seem shortwards of the Lyman α emission line in the spectra of quasars are hyman α lines produced by the absorption of light in hydrogen clouds attached to galaxies, intervening in the line of sight between ourselves and the quasar. The numbers of lines seen is consistent with such a hypothesis if galaxies have 50 Kpc haloes (Ellis 1978, Peterson 1978). If this suggestion is accurate then by converting the wavelength of these lines into redshifts and then into comoving coordinates,basically 3- dimensional galaxy covariance

function can be estimated for a nearly cylindrical volume around the light path from the quasar. This cylindrical volume will be of the order of 500 h^{-1} Mpc long (determined by the length of the Lyman α-Lyman β interval at the redshift of the quasar) at a redshift of 2.5 or more (it must be this large to allow the quasar's Lyman α emission line to be redshifted into the optical bands).

Very high resolution measurements of QSO spectra are needed for this project to succeed. This is to allow the differentiation of absorption lines from individual galaxies in the same cluster. These are important in defining the correlations on the very interesting smallest scales. At low resolution these lines may be merged into a single absorption line of larger equivalent width. However, if a good estimate of the spectral resolution is known it may be possible to use data of only moderately high resolution by correcting statistically for line merging.

Having obtained estimates of $\xi(r)$ in this way it would first be of interest to investigate if the correlation functions followed a -1.8 power-law on small scales. If this were to be found this would be a strong suggestion that the absorption did arise either in or around galaxies, then the task would be to compare the amplitude of the correlations with that derived locally. At such large redshifts this would form a stern test of theoretical predictions of clustering evolution.

Some work has already been done in this way by Sargent et al (1979) using moderately high resolution spectra. These authors find that the covariance functions of the Lyman α lines lie close to zero over a wide range of separations. However, preliminary investigations by the present author using reasonably high resolution spectra produced results which were consistent with a -1.8 power-law over the appropriate range of scales. Here estimation techniques were used which took accurate account of edge

and resolution effects. Using such techniques and spectra of the highest resolution exciting results may be possible in the near future.

7.5 SUMMARY OF CONCLUSION FROM PRESENT WORK

In the preceding chapters an account has been given of results obtained from statistical analyses of both shallow and deep galaxy catalogues. By applying the statistics reviewed in Chapter 2 to simulated shallow catalogues, it has been shown that these statistics may not provide as strong evidence for the hierarchical model as had previously been believed. This means that the evidence is also less strong for purely isothermal fluctuations in the early universe. A new statistical analysis, Mead's analysis, applied to a variety of catalogues showed that although the hierarchical model may represent well the distribution found in N-body simulations a simple power-law cluster model may better represent the observations. It has been argued that such a model with its definite preferred scale of clustering might well be consistent with the adiabatic theory of galaxy formation.

Further tests of the models of galaxy distribution could come from a detailed analysis of the Abell cluster catalogue. It has already been discovered that the correlations between clusters are ten times the size of those between galaxies (Hauser & Peebles, 1973). This is unexpected on the basis of isothermal theory which predicts that the clustering of clusters should have a similar form to the clustering of galaxies. It would be of great interest to see if Mead's analysis applied to this catalogue revealed that the distribution of clusters was hierarchical. This would be more evidence that the distribution of clusters was <u>different</u> from the distribution of galaxies and might indicate that the process which formed clusters of clusters was different from the process which formed clusters of galaxies, consistent with the predictions of adiabatic theory.

Methods have also been described for producing deep magnitude limited galaxy catalogues from areas the size of several Schmidt plates, using the COSMOS measuring machine. Selection functions for these samples have been derived from their number-magnitude and colour magnitude relations. These relations have been shown to be consistent with those obtained by other investigators.. The scaling tests of the small angle correlation functions for the deep samples show that the size of correlations found are consistent with predictions based on locally derived correlation functions, showing none of the discrepancies found in previous investigations. This scaling agreement is powerful evidence for the homogeneity of galaxy clustering on scales 50 h^{-1} to 700 h^{-1} Mpc. Detailed inspections of the observed scaling results shows a slight preference for models of clustering evolution where clusters expand with the universe. However, sampling and systematic errors are really still too large to exclude any physically feasible model of clustering evolution.

From colour subsamples of the catalogues, the result of Davis and Geller (1976) has also been confirmed, that early type galaxies have a steeper small scale covariance function slope than later types.

To continue the work of trying to put constraints on correlation evolution the next step is to apply the techniques developed here to 4^m plates. From the base provided by the present results, the wider range in limiting magnitude afforded by these deeper plates should allow any possible evolutionary trends to be better established.

The correlation functions at larger angles contain another major result in that a feature is found similar to that noted by Groth and Peebles (1977) in their analysis of the Lick catalogue. However, here the position of the break occurs at 3 h^{-1} Mpc instead of 9 h^{-1} Mpc. Although these results could well be considered in reasonable agreement taking account of

the large experimental errors, the difference is important in terms of theory and we have discussed the implications for galaxy function theories if the feature were to be found at smaller separation than had previously been believed. Our large angle correlation estimates are made more believable by virtue of their reasonably good internal scaling behaviour. The next objective for this particular project must be to similarly measure a different plate from a separate field with another machine such as the APM machine at Cambridge (Kibblewhite et al, 1979). If our large angle correlation function results were to be reproduced, this would be strong evidence indeed that systematic effects were operating in the analysis of the Lick catalogue.

Finally there have also been presented number magnitude counts and correlation analyses for the deep stellar catalogues which were produced at the same time as their galaxy equivalents. It seems certain that stellar images divided fairly sharply into two populations in terms of their (J-R) colour. The correlation results for the two populations have been analysed and their results discussed.

REFERENCES

1. Aarseth, S.J., Gott, J.R. and Turner, E.L., 1979, Astrophys. J, 228, 664
2. Abell, G.O., 1958, Astrophys. J. Suppl., 3, 211.
3. Abell, G.O., 1962. In Problems of Extragalactic Research, ed. G.C. McVittie (New York; McMillan).
4. Abell, G.O. and Mihalas, D.M., 1966. Astron. J., 71, 635.
5. Allen, C.W., 1973. Astrophysical Quantities, 3rd edition (London ; Athlone Press).
6. Bartlett, M.S, 1964. Biometrika, 37, 1.
7. Besag, J. and Diggle, P.J., 1977. Jl. R. Statist. Soc., C,26,237.
8. Bhavsar, S.P., 1979. Astrophys. J., 222, 412.
9. Binney, J., 1976. Mon. Not.R. astr. Soc., 177, 19.
10. Blackman, R.B. and Tukey, J.W., 1959. The measurement of power spectra (New York ; Dover).
11. Bogart, R.S. and Wagoner, R.V., 1973, Astrophys. J.,181, 609.
12. Bonnor, W.B., 1957, Mon. Not. R. astr. Soc., 117, 104.
13. Carpenter, E.F, 1938. Astrophys. J., 88, 344.
14. Chincarini, G. and Rood, H.J., 1976. Astrophys. J., 206, 30.
15. Cox, D.R.and Lewis, P.W., 1966. In Statistical Analysis of a Series of Events, (Methuen Monographs in Statistics).
16. Dautcourt, G., 1977, Astron. Nachr., 298, 141.
17. Davis, M. and Geller, M.J., 1976. Astrophys. J., 208, 13.
18. Davis, M., Geller, M.J., and Huchra, J., 1978. Astrophys. J., 221, 1.
19. Davis, M., Groth, E.J and Peebles, P.J.E., 1977. Astrophys. J. Lett., 212, L107.

20. Dodd, R.J., MacGillivray, H.T., Ellis, R.S., Fong, R and Phillipps, S., 1976. Mon.Not.R. astr. Soc., 171, 329.

21. Doroshkevich, A.G., and Shandarin, S.F., 1978. Mon.Not. R. astr. Soc., 182, 27.

22. Dube, R.R., Wickes, W.C., and Wilkinson, D.T., 1977, Astrophys. J. Lett., 215, L51.

23. Dixon, K., 1978, Thesis, University of Oxford.

24. Efstathiou, G., 1979, Mon.Not.R. astr. Soc., 187, 117.

25. Efstathiou, G., and Eastwood, J., 1979. preprint.

26. Efstathiou, G., Fall, S.M., and Hogan, C., 1979. Mon.Not.R.astr. Soc, submitted.

27. Ellis, R.S., 1978, Mon.Not.R., astr. Soc., 185, 613.

28. Ellis, R.S., 1979. Proc.Roy.Soc., in press.

29. Ellis, R.S., Fong, R. and Phillipps, S., 1977, Mon.Not.R.astr.Soc, 181, 163.

30. Fall, S.M., 1978, Mon.Not. R. astr. Soc., 172, 23P.

31. Fall, S.M., 1979, Rev. Mod. Phys., 51, 21.

32. Fall, S.M., and Tremaine, S, 1977, Astrophys.J., 216, 682.

33. Felten, J.E, 1977, Astron.J., 82, 861.

34. Freeman, K.C., 1970, Astrophys. J., 160, 811.

35. Geller, M.J., and Davis, M., 1978, Astrophys. J., 225, 1.

36. Gott, J.R. and Turner, E.L., 1977., Astrophys. J. 216, 357.

37. Gregory, S.A. and Thompson, L.A, 1978, Astrophys. J, 222, 784.

38. Groth, E.J. and Peebles, P.J.E, 1976, Astr. Astrophys., 53, 131.

39. Groth, E.J., and Peebles, P.J.E., 1977, Astrophys. J., 217, 385.

40. Groth, E.J., Peebles, P. J.E., Seldner, M. and Soneira, R.M., 1977, Sci. Am. 237, 76.

41. Hauser, M.G. and Peebles, P.J.E., 1973. Astrophys. J., 185, 757.

42. Holmberg, E., 1969, Arkiv. Astr. 5, 305.

43. Hubble, E.P., 1934, Astrophys. J., 79, 8.

44. Huchra, J., Davis, M., and Geller, M.J., 1979, in preparation.

45. Jones, B.J.T., 1976a, Rev. Mod. Phys., 48, 107.

46. Jones, B.J.T., 1976b. Mon.Not.R. astr. Soc., 174, 429.

47. Kiang, T., 1967. Mon. Not. R. astr. Soc., 135, 1.

48. Kibblewhite, E.J., Bridgeland, M.T., Hooley, T. and Horne, D., 1975. In Image Processing Techniques in Astronomy, Dordrecht : D. Reidel, p 245.

49. Kirshner, R.P. Oemler, A. and Schechter, P.L., 1979. Astron. J., 83, 1549.

50. Kron, R.G., 1978, Ph.D. Thesis, University of California, Berkeley.

51. Layzer, D., 1974. In Stars and Stellar System, Vol. IX.

52. Limber, D.N., 1953, Astrophys. J., 117, 134.

53. MacGillivray, H.T.,and Dodd, R.J., 1979, Mon.Not. R. astr. Soc., 186, 69.

54. MacGillivray, H.T., Martin, R. Pratt, N.M., Reddish, V.C., Seddon, H., Alexander , L.W.G., Walker, G.S. and Williams, P.R., 1976, Mon. Not. R. astr. Soc., 176, 265.

55. Mead, R., 1974, Biometrics, 30, 295.

56. Montgomery, D.C. and Tidman, D.A., 1974, In Plasma Kinetic Theory, (New York : McGraw Hill), Chap.4.

57. Morton, D.C. and Tritton, K., 1979. In preparation.

58. Nilson, P., 1973. Uppsala Astro. Obs. Ann., 6, (Uppsala General Catalogue of Galaxies).

59. Peebles, P.J.E., 1973, Astrophys. J., 185, 413.

60. Peebles, P.J.E., 1974a. Astr. Astrophys., 32, 197.

61. Peebles, P.J.E, 1974b, Astr. Astrophys., 32, 391.

62. Peebles, P.J.E., 1974c, Astrophys. J., 189, L51.

63. Peebles, P.J.E., 1975, Astrophys. J., 196, 647.

64. Peebles, P.J.E., 1978, Astron. Astrophys., 68, 345.

65. Peebles, P.J.E., 1979, Astrophys. J. in press.

66. Peebles, P.J.E., and Groth, E.J., 1975, Astrophys. J. 196, 1.

67. Peebles, P.J.E., and Hauser, M.G., 1974. Astrophys. J.Supp.,28,19.

68. Peebles, P.J.E. and Yu, J.T., 1970. Astrophys. J., 162, 815.

69. Pence, W., 1976. Astrophys. J., 203, 39.

70. Peterson, B.A., 1978. In I.A.U. Symp. No. 76. eds. Einasto, J. and Longair, M.S. (Reidel: Dordrecht).

71. Peterson, B.A., Ellis, R.S. Kibblewhite, E.J., Bridgeland, M.T., Hooley, T. and Horne, D., 1979. Astrophys. J. Lett., submitted.

72. Phillipps, S., 1979, Thesis, University of Durham.

73. Phillipps, S., Fong, R., Ellis, R.S., Fall, S.M., and MacGillivray,H.T, 1978. Mon. Not. R. astr. Soc., 182, 673.

74. Pratt, N.M., 1977. Vistas in Astr.

75. Pratt, N.M., Martin, R., Alexander, L.W.G., Walker, G.S., and Williams, P.R., 1975. In Image Processing Techniques in Astronomy (Dordrecht: Reidel).

76. Press, W.H. and Lightman, A.P., 1978. Astrophys. J, 219, L73.

77. Press, W.H. and Schechter, P.L., 1974. Astrophys. J., 187, 425.

78. Ripley, B.D., 1977, Jl. R. Statist. Soc., B, 39, 2.

79. Rubin,V.C, Ford, W.K., and Rubin, J.S., 1973,Astrophys.J.183,Llll.

80. Rudnicki, K., Divorak, T.Z., Flin, P., Baranowski, B. and Sandrakowski, A., 1973. Acta Cosmologica 1, 7.

81. Sargent, W.L.W., Young, P.J., Boksenberg, A. and Tytler, D., 1979 preprint.

82. Schechter, P., 1976, Astrophys. J., 215, 703.

83. Seldner, M. and Peebles, P.J.E., 1977. Astrophys. J. 215, 703.

84. Seldner, M., Siebers, B., Groth, E.J. and Peebles, P.J.E., 1977, Astron. J., 82, 249.

85. Shane, C.D. and Wirtanen, C.A., 1967. Publ. Lick. Obs., 22, Part 1.

86. Shapley, H. and Ames, A., 1932, Ann. Harvard Obs, 88, 43.

87. Sharp, N.A., 1979, Astr. Astrophysics.

88. Smoot, G.F., Gorenstein, M.V., and Muller, R.A., 1977. Phys. Rev. Lett., 39, 818.

89. Soneira, R. M. and Peebles, P.J.E., 1977. Astrophys. J.,211, 1.

90. Soneira, R.M. and Peebles, P.J.E., 1978, Astron. J, 83, 845.

91. Tifft, W.G., 1978, Astrophys. J., 222, 54.

92. Tinsley, B.M., 1977. Astrophys. J. 211, 621 (erratum, ibid, 216,349).

93. Tinsley, B.M., 1978, Astrophys. J., 220, 816.

94. Tonry, T. and Davis, M., 1979, preprint.

95. Turner, E.L. and Gott, J.R., 1976, Astrophsy. J.Suppl.Ser.,32,409.

96. Tyson, J.A., and Jarvis, J.F., 1979. Astrophys. J. Lett.,230,L153.

97. de Vaucouleurs, G., 1971., Publ. astr. Soc. Pac, 83, 113.

98. de Vaucouleurs, G., 1974. In Stars and Stellar Systems, Vol IX,Ch.17.

99. de Vaucouleurs, G., de Vaucouleurs, A., and Corwin, H.G., 1976, Second Reference Catalogue of Bright Galaxies, (Univ. of Texas:Austin).

100. Webster, A., 1976. Mon. Not. R. astr. Soc., 175, 61.

101. Wesson, P.S., 1976, Astrophys. Sp. Sci., 40, 325.

102. Zwicky, F., 1957, In Morphological Astronomy(Herzpringer Verlag: Berlin).

103. Zwicky, F., Herzhog, E., Wild, P., Karpowicz, M. and Kowal, C.T., 1961-68. Catalogue of galaxies and clusters of galaxies, in 6 vols., California Institute of Technology, Pasadena.

ACKNOWLEDGMENTS

I should firstly like to thank Dr. R Fong for his supervision of this thesis and for many lively and stimulating discussions over the past three years.

I am also indebted to my colleagues and friends in the Cosmology Group at Durham, Drs. G.Efstathiou, R.S. Ellis and S. Phillipps, who all had a large influence on the work presented here.

I thank Mr. J. Besag of the Mathematics Department at Durham for a very good suggestion (the application of Mead's analysis to galaxy catalogues) at a time when things were not going well.

Many thanks are also due to the COSMOS team at the Royal Observatory, Edinburgh, in particular Dr. H.T. MacGillivray, Mr. R. Martin and Dr. R. Stobie, for all their hard work at the machine itself. Thanks also go to the U.K. Schmidt Unit at R.O.E., in particular Drs. R.D. Cannon and T. G. Hawarden, for their help in obtaining the Schmidt plates used in this work.

I should also like to thank Drs. J. Graham (Cerro Tololo), M.R.S. Hawkins (R.O.E.) and W.D. Pence (Sussex) for providing sequence photometry prior to publication.

Many thanks also go to Drs. D. Carter and J. Godwin (Oxford) for their hard work in supplying P.D.S. photometry used here.

Very useful discussions were held with Drs. S.M. Fall, B.J.T.Jones and E.J.Kibblewhite at The Institute of Astronomy, Cambridge.

I thank the Physics Department of the University of Durham for its support, financial and otherwise, during my research, and in particular Professor A. W. Wolfendale for all his help and encouragement.

I also especially thank Drs. J.V.Major, F.D.Gault and Mr. A.P.Lotts for allowing me the use of the excellent computing facilities of the High Energy Nuclear Physics Group at Durham.

The Physics Department Drawing Office is thanked for its production of many of the diagrams in the thesis itself.

I am very grateful to Mrs.S. Mellanby of the Applied Physics and Electronics Department for her speedy typing of the text.

I was supported by S.R.C. and University of Durham grants for the period of the research.

Finally, my warmest thanks to my fiancée, Kathryn, for her everlasting patience while this thesis was being completed.